COUPLED ANALYSIS OF TWO-PHASE FLOW

IN

ROUGH ROCK FRACTURES

Thesis submitted in fulfilment of the

requirements for the award of the degree

DOCTOR OF PHILOSOPHY

From

UNIVERSITY OF WOLLONGONG

By

Jeffrey Richard Price, M Eng(Studies), MIE(Aust), FGS

School of Civil Engineering

2005

Thesis Certification

CERTIFICATION:

I, Jeffrey R. Price, declare that this thesis, submitted in fulfilment of the requirements for the award of Doctor of Philosophy, in the School of Civil Engineering, University of Wollongong, is wholly my own work unless otherwise referenced or acknowledged. The document has not been submitted for qualifications at any other academic institution.

Jeffrey R. Price

9 November 2004

ACKNOWLEDGEMENTS

In addition to the financial support offered by ARC (APAI) and Strata Control Technology (SCT), many people including colleagues and friends have assisted the completion of this project. Foremost, I gratefully acknowledge my supervisors Prof. Buddhima Indraratna and Dr. Winton Gale (SCT) for their support, encouragement and mentoring. I would also like to thank Prof. Robin Chowdhury, Assoc. Prof. Najdat Aziz and Dr. Phil Flentje for their interest, advice and motivation throughout the project. My fellow postgraduate students past and present, including Drs. Pathegama Ranjith, Senaka Welideniya and William Glamore, have also greatly assisted in the argument and crystallisation of my ideas. I would also like to thank Dr Barry and Margaret McMahon for their encouragement, the opportunity they provided and a valuable commercial geotechnical education.

A significant component of the research has relied upon the maintenance and development of specialised apparatus. The University Technical Officers and IT Technicians have offered continual, patient assistance, particularly Alan Grant, Bob Rowlan, Ian Bridge and Ian Kirby with Peter Turner, Leonie McIntyre and Des Jamieson keeping the computers running. Their constructive criticism during the laboratory equipment development and testing was invariably correct and immensely valuable. In addition, I am very grateful to Angus and Shane from New Dawn 3D for their assistance with the high-resolution laser scanning. Further mention should be made of all the Faculty administrative staff in the Engineering Enquiries Centre, particularly Mrs. Pam Burnham and especially Ms. Stacey Smith for their peerless understanding of the essential systems that seem beyond most mortals.

Finally and most significantly, I thank my wife Linda, for her patience, love, support and motivation, and my mother Mary for her encouragement. I dedicate this work to the memory of my father who was unable to see the conclusion of this project and to Peter Wiseman, a past colleague who personified enthusiasm and appreciation of the geological environment.

COUPLED ANALYSIS OF TWO-PHASE FLOW IN ROUGH ROCK FRACTURES

ABSTRACT

This research project has considered the impact of roughness on two-phase (air + water) flow in rough discontinuous geological media. Existing analytical approaches to two-phase flow tend to be highly theoretical and involve significant idealisation of the rock mass properties because of the variable distribution of rock mass discontinuities and the impact of fracture roughness. The anisotropic nature of fracture orientation, aperture topology and persistence combine to limit the coupled analysis of single and two-phase flow. The research has been driven by the need for improvements in the prediction of two-phase flows in the vicinity of underground mining development and infrastructure. The aim of the work has been to develop and verify robust simplified two-phase flow models that can be accurately applied to improve hydromechanical rock mass analysis.

Isothermal two-phase flow behaviour is encountered in geotechnical engineering particularly in underground construction and extraction associated in coal mining or in developments near to coal measures geological environment. The hazards presented by the potential for outburst can lead to loss of life as well as loss of production. The financial consequences of the loss of just a day of production from a typical Australian longwall mine in 2002 would lie within the range of 7000 to 20,000 tonnes (approximately A$ 0.25 to 0.5 million). The development of a simple coupled two-phase flow model would facilitate the ready quantification of geomechanical risks facing the industry.

A detailed review of the literature on two-phase hydraulics and fracture roughness has identified opportunities for the development of new analytical

techniques. Refined laboratory testing methods have been combined to gather high resolution roughness and aperture data. The resulting data have been used to study the nature of fracture roughness using Fourier series.

Specialised two-phase triaxial testing has been conducted and the test results have been analysed using the detailed knowledge of the fracture roughness and aperture to study the role of free fracture flow. The findings of the theoretical and laboratory testing schedule have identified the opportunity to characterise fracture roughness and to relate the results of the testing to hydraulic and mechanical apertures. The study has developed a new technique to assess the frequency composition of fracture roughness that can be related to the Joint Roughness Coefficient (JRC). Laboratory testing has also validated a proposed coupled annular two-phase flow model that is based upon the conservation of mass. The model relates the phase height parameters to the fracture mechanical aperture and enables the calculation of phase flow rates.

Consideration of hydromechanical analysis has lead to the development of a coupled homogenous fluid model that has highlighted the applicability of some of the study results to improve computer modelling capability using the existing UDEC code. Finite difference analysis has illustrated the development of non-parallel fracture flow and related the discretised mechanical aperture to the fracture hydraulic aperture. The homogenous fluid model has been found to enable hydromechanical analysis of rough fractures without the need for prior knowledge of the fracture JRC. These breakthroughs have revealed the potential for further application to field testing environments and improved hydromechanical modelling. Such an application of the study outcomes could increase the hydromechanical data that could be collected from borehole site investigation.

Publications arising from research project

The research milestones in this project have been published in two internationally recognised journals and six geotechnical conferences. Two more journal articles are yet to be published, with one of these in preparation at this time:

- Price J. & Indraratna B. (2004). Development of an equivalent homogenous fluid model for simplified two-phase (air + water) flow through fractured rock. *ASCE Journal of Geotechnical and Geo-Environmental Engineering, March 2004 –under editorial review.*
- Indraratna B, Price J, Gale W (2003). Laboratory Measurement and Analysis of Relative Permeability under Steady State Two-phase (air-water) Flow. *39th US Rock Mechs Symp, Cambridge MA, USA, Jun 2003 pp.1603-1611.*
- Price J, Indraratna B, Gale W (2003). Saturated steady state flow in rough rock fractures using Discrete Element Modelling. *12th Asian Regional Conference on Soil Mechs and Geotech Engg, Singapore, Aug 2003.*
- Indraratna B, Ranjith P, Price J, Gale W (2003). Two-phase flow of air and water through rock joints – Analytical approach and experimental verification. *ASCE Journal of Geotechnical and Geo-Environmental Engineering Oct 2003, 129(10): pp.918-929.*
- Indraratna B, Price J, Biswas S (2002). Keynote paper - Multiphase Saturated and Unsaturated Flow with Special Reference to Dam Filters and Jointed Rocks. *Indian Geotechnical Conference, Allahabad, India, 20 - 22 Dec. 2002, pp.713-727.*

- Indraratna B, Price J, Gale W (2002). Fourier description of fracture roughness. *Proc 5th North American Rock Mechs Symp, Toronto, Canada, 7 - 10 July 2002, eds. Hammah et al., Pub. University of Toronto Press, pp.35 – 44.*
- Indraratna B, Price J, Ranjith P, Gale W (2002). Some aspects of unsaturated flow in jointed rock. *Int Journ Rock Mech Min Sci, 39, pp 555-568.*
- Indraratna B, Ranjith P, Price J, Gale W (2001). A preliminary study of the relationship between two-phase flow (air-water) characteristics and fracture roughness. *Rock Mechanics in the National Interest, Washington DC, Jul 7-9 2001, eds. Elsworth et al., Pub. Swets Zeitlinger, Lisse pp.191-196.*

TABLE OF CONTENTS

LIST OF FIGURES

LIST OF TABLES

COUPLED ANALYSIS OF TWO-PHASE FLOW

IN

ROUGH FRACTURES

LIST OF NOTATION

NB: subscript *i* denotes generic notation for fluid phase and *m* denotes property belonging to fluid mixture alternatively, further subscripts apply specifically to *A* for air, *W* for water, *H* for a homogenous mixture and *f* for fracture. Fracture stiffness is described relative to fracture plane movement, i.e. *n* for normal and *s* for shear.

Abbreviation	Definition	Units
a	Empirical roughness coefficient (Louis, 1969)	
a_F	Forcheimer curve fitting parameter	
a_n, b_n	Fourier coefficients	
b_L	Langmuir slip factor	
b	Fracture normal spacing	m
B	Formation volume factor	
B_F	Fourar curve fitting parameter	
b_F	Forcheimer curve fitting parameter	
b_L	Langmuir slip factor	
c	Langmuir material Constant	
C	Concentration	kg m^{-3}
C_A	Isothermal compressibility of air	kPa^{-1}
C_{LM}	Chisholm modification to Lockhart-Martinelli pressure multiplier	
C_M	Missbach parameter	
C_W	Isothermal compressibility of water	kPa^{-1}
D	Coefficient of diffusion	
D	Fractal dimension	
d	Ratio of fracture contact area to fracture area	

Abbreviation	Definition	Units
def	Fracture normal deformation	m
D_h	Hydraulic diameter	m
D_L *or* $_G$	Equivalent hydraulic diameter for liquid or gas phase	m
e	Fracture aperture	m
e_h	Hydraulic aperture	m
e_{clip}	Mean mechanical aperture measured by clip gauge	m
$\hat{e}_w$	Mean aperture contacting wetting phase	m
$\hat{e}$	Mean aperture	m
$\overline{e}_{\log}$	Mean log normal aperture	m
e_m	Mechanical or physical aperture	m
E_m	Rock matrix Young's modulus	kPa m^{-1}
F	Force	kN
f	Aperture variability reduction factor (Witherspoon et al., 1981)	
$f(x)$	Fourier series for z as a function of x	
F_B	Buoyancy mass transfer force	kN
f_F	Fourar turbulent flow phase factor	
F_H	Hvorslev shape factor	
F_I	Interface mass transfer force	kN
f_L *or* $_G$	Lockhart-Martinelli friction factor for liquid or gas phase	
g	Gravitational acceleration	ms^{-2}
$G_i(f)$	Power spectral density function (PSD)	
h	Hydraulic head	m
H	Hurst index	
h_c	Water level during constant head test	m

Abbreviation	Definition	Units
h_F	Fourar curve fitting parameter	
J	Mass flux	kg s^{-1}
k	intrinsic permeability	m^2
K	Hydraulic conductivity	ms^{-1}
k_a	Apparent permeability (Klinkenberg effect)	m^2
K_e	Equivalent hydraulic conductivity	ms^{-1}
K_f	Rock fracture hydraulic conductivity	ms^{-1}
K_{mass}	Rock mass hydraulic conductivity	ms^{-1}
k_{max}	Maximum roughness amplitude	m
K_n , K_s	Fracture stiffness	MPa m^{-1}
K_p	Hydraulic conductivity in plane of borehole	ms^{-1}
K_r	Relative permeability	
l	Segment length	m
L	Reference length parallel to flow	m
M	Mass	kg
n	Porosity	
N	Number of fracture profile segments	
n	Number of data points	
N_{cap}	Capillary number	m/º
N_{TOT}	Roughness traverse total datapoint number	
P	Perimeter	m
p	Pressure	kPa
p_C	capillary pressure	kPa
$\overline{p}$	Mean pressure	kPa
Q	Flow rate	m^3s^{-1}
q	Specific discharge	ms^{-1}
R	Universal Gas Constant	
r_1, r_2	Radii of meniscus curvature	m
r_1, r_o	Radius of flow at origin and point 1	m

Abbreviation	Definition	Units
r_p	Pore radius	m
r_p	Pore radius	m
S	Surface roughness index	
s_h	Asperity height sample standard deviation	m
S_i	Phase saturation	
S_R	Scaling ratio	
s_θ	Chord angle sample standard deviation	º
T	Absolute temperature	K
T_s	Surface tension coefficient	mN m^{-1}
U	Velocity	ms^{-1}
u_p	Pore pressure	kPa
V	Volume	m^3
V_σ	Variance	
w	Fracture width in *y*-plane	m
X	Empirical Lockhart-Martinelli factor	
Z_2	First derivative of the roughness rofile	
$Z_i(f)$	Fourier transform of PSD	
A	cross sectional area	m^2
Δ_T	Total fracture deformation	m
Φ	Hydraulic potential function	
$\Phi_{L\ or\ G}$	Lockhart-Martinelli pressure drop multiplier	
Γ	Volumetric air phase fraction	
Π_m	Mean free path for a gas	
T	Tortuosity factor	
α	Lateral stress factor	
β	Fracture inclination from horizontal	º

Abbreviation	Definition	Units
β_T	Tilt angle	º
δ_n	Normal deformation of joint aperture	m
δ_s	Parallel deformation of fracture by shear displacement	m
ε	Absolute asperity height	m
ϕ	Friction angle	º
γ	Unit weight	kN m^{-3}
η_F	Fourar turbulent flow passability parameter	
$\imath$	Roughness angle	º
λ	Mean free path	m
λ	Pressure drop coefficient	
μ	Dynamic viscosity	kPa sec^{-1}
ν	Kinematic viscosity	m^2s^{-1}
θ	Wetting contact angle	º
ρ	density	tm^{-3}
σ	Standard deviation	
σ_n	Fracture normal stress	kPa
σ_1	Major principal stress	kPa
σ_3	Minor principal stress	kPa
τ	Shear stress	kPa
τ_{WJ}	Fracture wall shear stress due to water flow	kPa
ξ_{AC}	Air phase compression	m
ξ_{AD}	Air phase dissolution	m
ξ_{WC}	Water phase compression	m
ψ	Hydraulic streamline function	
ζ	Normal deformation phase proportioning factor	

Chapter 1

Two-Phase Hydromechanics

In Rough Discontinuous Media

1.1 Rationale

Two-phase hydromechanics applied to rough discontinuous geological media is very important in the field of geotechnical engineering, as is the role of fracture roughness in controlling rock mass behaviour in mechanical (Barton & Choubey, 1977; McMahon, 1985; Indraratna et al., 1995) and hydraulic terms (Louis, 1969; Witherspoon et al., 1980; Barton & Bandis, 1980; Brown, 1987; Indraratna et al., 2001). Two-phase flow is a complex discipline which becomes even more theoretically involved when combined with the nature of rock mass variability. Isothermal two-phase (air + water) flow in rough fractures is an area that has relatively recently begun to be explored. It is of considerable interest in underground engineering environments such as longwall coal mining, coal bed methane extraction, and underground storage of liquid petroleum gas. This topic has the potential to become more consequential by extension into areas of growing interest such as radioactive waste disposal, Hot Dry Rock energy projects and greenhouse gas storage. This research work builds on developments in petroleum engineering and industrial two-phase flow but from a geological engineering perspective.

1.2 Thesis outline

Subsequent chapters describe the development of the simplified two-phase flow models in relation to hydraulic and mechanical boundary conditions that can be measured in the

laboratory or field situation. This project attempts to extend our existing knowledge of idealised fracture flow behaviour and apply simplified geomechanical models that can be incorporated into larger numerical analyses. Each chapter introduces the particular phase of the research, describes and analyses the subject, and summarises the accomplishments, achievements and limitations of the proposed work.

A critical review of existing literature related to two-phase flow was undertaken in Chapter 2, to establish an understanding of the theory, with particular reference to discontinuous geological media. The review developed from the principles of general rock mass hydraulics and considered applications to in-situ testing and coal mining geomechanics and existing developments in petroleum engineering. The study showed that the structural complexity of the fractured rock mass often requires considerable assumptions to be made when formulating the problem analytically, which can invalidate a highly technical approach. Chapter 2 revealed the need for a detailed review of fracture roughness to define the significance of and approaches to the quantitative description of rock fracture roughness. Chapter 3 discusses the standard roughness profiles that form part of the recommended approach to rock mass description and classification (ISRM, 1978). A detailed topological study of the standard roughness profiles and real rock fracture surfaces was performed to establish a new objective technique for roughness description using Fourier series.

These critical reviews provided the basis for a theoretical consideration of separated continuous two-phase air and water flow, and the fracture surfaces were used to justify the proposed theoretical model. Theoretical functions for the fluid phase heights, and fracture wall and interface shear forces were developed from the concepts of conservation of mass and momentum. A simplified theoretical annular flow model based upon the combination of Darcy's and Poiseuille's law was developed.

The applicability of this simplified approach to rock fracture flow was studied in the laboratory using an analogue fracture apparatus with the details given in Chapter 5. The apparatus incorporated Perspex plates to control and record the two-phase flow and pressure variables and observe the flow behaviour. The results validated the simplified analytical approach for bubble and slug flow, as well as annular flow conditions. The acquired data also provided an improved realisation of the expected flow behaviour in actual rock fractures.

The simplified two-phase annular flow model was extended from the analogue environment to real rock fractures using the Two Phase High Pressure Triaxial Apparatus (TPHPTA). The TPHPTA was refined to improve the control and data monitoring equipment. Tests were performed under controlled triaxial conditions with independent injection of air and water over a range of fracture normal stresses. Fracture deformation and air and water flow behaviour were used to back-analyse the test results using the simplified annular flow model. The similarity between the calculated phase heights and measured average fracture aperture verifies the hydromechanical approach for the analysing discontinuous geological media.

The numerical analysis of fracture flow in Chapter 7 has been considered at a single and multiple fracture level. A 2-D finite difference scheme with a finely discretised grid of variable mechanical aperture elements will reasonably predict the fracture hydraulic aperture and illustrate non-parallel fracture flow. The impact of fracture roughness on UDEC calculations has revealed a limitation of the code in rough fracture hydraulics. However, an adaptation of the input code has improved the accuracy of the flow calculations. A further theoretical model is proposed based on a ‘homogenous fluid’ to allow numerical two-phase analysis. The development of this model is described and validated against hydromechanical laboratory test data.

Chapter 2

Literature Review

2.1 Introduction

Hydromechanics is concerned with the mechanical aspects of fluid flow (e.g. water, gas or oil) in engineering materials. Fundamentally, the hydraulics of geological materials can be addressed from either a porous or a discontinuous medium perspective. The fields of hydrogeology and petroleum engineering have considered this hydromechanical problem from the prime foci of their respective disciplines. Early studies of geo-hydromechanics have arguably developed from the study of fluid mechanics of pipes and channels. Geomechanics is a wide discipline that could include both of the above fields, as well as the geotechnical impact on civil and mining engineering projects. This work to addresses geomechanical literature, focussing on geotechnical issues and provides an overview of current geotechnical understanding of flow, particularly unsaturated isothermal flow, in fractured media. Flow is primarily considered to be influenced by a driving gravitational or pressure gradient occurring in fractures, rather than slow percolation affected by capillary effects. Similarly, flow is considered in terms of secondary porosity (i.e. in fractures) rather than through the porous matrix or combination of the two.

This chapter describes the fundamental constitutive expressions that govern fluid flow. Particular attention is given to the nature of gas flow, because it behaves as a compressible fluid and is subject to additional physical characteristics. The preferred

methodology incorporating gas phase compressibility in the development of the proposed two-phase flow model is described in detail in Chapter 4.

2.1.1 Constitutive relationships

The three fundamental constitutive models that can be applied to hydromechanical problems are the conservation of mass, momentum and energy. This study has concentrated on theoretical consideration derived from conservation of mass and momentum. The principle of conservation of mass is illustrated by considering a flow rate Q between two smooth plates at 2 separate locations. If each of these elements have respective cross sectional areas A and B, and there is no fluid lost from the system, then:

$$M = Q.\rho = U_a.A.\rho = U_b.B.\rho \qquad [2.1]$$

where M is the fluid mass, ρ is the fluid density and U is the mean elemental velocity.

The phase pressure drop can be calculated from the principle of conservation of momentum. The general equation for total phase pressure drop of each phase is a combination of the three respective right hand terms in Eq. 2.2, distinguished by separate subscripts: losses due to friction (f) with the fracture walls; acceleration (a) impacts from localised unsteady flow; and changes in elevation (g) across the area of interest.

$$\frac{dp}{dx} = \left(\frac{dp}{dx}\right)_f + \left(\frac{dp}{dx}\right)_a + \left(\frac{dp}{dx}\right)_g = -\tau_w \frac{P}{A} - \frac{M}{A}\frac{dU}{dx} - \rho\ g \sin\beta \qquad [2.2]$$

Specifically re-writing these terms, the frictional losses can be stated as a product of the shear stress (τ_w) at the fracture wall acting around the perimeter of the fracture (P) with a cross sectional area (A); the acceleration losses can be replaced in terms of the phase mass (M) per cross sectional area and the phase velocity gradient (dU/dx). The

elevation component of momentum losses can be represented as the product of the phase density (ρ) and fracture orientation (β) from the horizontal.

The preceding relationships are readily applied to an incompressible fluid such as water, as was the case in this research project. Where the fluid is a gas, compressibility must be accounted for in accordance with the physics of a compressible fluid.

2.1.2 Controls on the behaviour of gases

The following sections review the physical laws that govern gas behaviour. There is a discussion of diffusion, adsorption, and the Klinkenberg effect, although these phenomena are less significant in high permeability media. However, dual permeability models must account for these flow effects because of the high intergranular storage potential, for example when considering gas outbursts.

2.1.2.1 Gases at rest

The compressibility of gases requires different engineering assumptions to those applied for liquids. Steady flow can be considered in terms of a constant mass flow, providing the basis for the continuity equation:

$$\rho AU = M = \text{constant} \qquad [2.3]$$

The fundamental equations controlling gases are:

a) Boyle's Law, at constant temperature T -

$$pV = \text{constant} \qquad [2.4]$$

where p is absolute pressure and V is volume of the gas.

b) Charles' Law, at constant pressure or volume -

$$\frac{V}{T} = \frac{p}{T} = \text{constant} \qquad [2.5]$$

where, T is the absolute temperature.

For a mass of gas M with density ρ, volume is proportional to M thus:

$$\frac{pV}{T} = MR \qquad [2.6]$$

where, R is the universal gas constant. Alternatively, [2.6] can be re-written for a unit mass of gas to yield:

$$p = \rho RT \qquad [2.7]$$

2.1.2.2 Flow of gases

There are localised changes in pressure and density during isothermal gas flow because of the compressibility of fluid. Therefore, one approach when considering continuity in terms of mass per unit time (e.g. Schrauf & Evans, 1984) is to modify the Bernoulli equation to give:

$$g\delta z + U\delta U + \frac{\delta p}{\rho} = 0 \qquad [2.8]$$

Makurat (1982) & Somerton et al. (1975) discuss the issue of permeability with regard to a gas. The intrinsic permeability (k) of a rock core sample for gas flow can be calculated using the standard method defined by the ASTM (1990):

$$k = \frac{2Q_{out}\, p_{out}\, \mu L}{p_{in}^2 - p_{out}^2} \qquad [2.9]$$

where Q_{out} is the volumetric flow rate, L is the distance between the reference points, p_{in} is the inlet and p_{out} the outlet pressure. This methodology is applied to an intact core and considers the matrix or primary permeability of the rock specimen. Gas flow would be a relatively slow process through the network of intergranular pores and throats. Pore diameters can be as small as 0.005μm in sedimentary rocks such as coal (Harpalani & Chen, 1999) indicating a significant magnitude of pore fluid pressure required to enable flow.

Harpalani & Chen (1999) & Somerton et al. (1975) discuss the Klinkenberg effect, which is a molecular characteristic observed in gases where slip occurs during flow at the fracture wall or through a granular matrix. The effect depends upon the mean free path of the molecules and the pressure, temperature, and molecular weight of the gas, and increases the permeability particularly where porosity is low or pressure gradients are relatively small. The relationship between permeability (k) and the apparent permeability (k_a) allowing for the slip effect is given by:

$$k_a = k\left(1+\frac{b_L}{\bar{p}}\right) = k\left(1+\frac{4c\Pi_m}{r_p}\right) \qquad [2.10]$$

where, $\bar{p}$ is mean pressure, r_p is the pore radius, Π_m is the mean free path of the gas, b_L is the slip factor and c is a constant. The Klinkenberg Effect varies for different gases, depending on their molecular composition. Lama (1995) illustrated the variation in slip factor with a range of test results from Bulli Coal samples. The work also shows how the slip factor increased with stress (Table 2.1):

Table 2.1: Slip factor recorded by Lama (1995) for Bulli Coal samples.

Gas	**Stress (MPa)**	**Slip factor, b_L (bar)**
Methane - (CH_4)	0.5	7.46
	2.5	7.02
	5.0	7.34
	7.5	9.83
Carbon dioxide - (CO_2)	0.5	177
	2.5	41.2
	5.0	22.9
	7.5	11.61

Lama's results indicated that the slip factor is larger for CO_2 than CH_4 for all stress levels, i.e. the variation in gas permeability due to the Klinkenberg effect in relation to

gas pressure is greater at lower stresses. Harpalani & Zhao (1989) studied the relationship of permeability to confining pressure using cylindrical coal samples in a triaxial cell. Their results suggested that coal, unlike other rocks, has a negative Klinkenberg Effect (i.e. decrease in permeability with increases in gas pressure) with a gas like methane, i.e. once the gas pressure falls below the desorption pressure, it begins to desorb, increasing permeability and reducing rock volume.

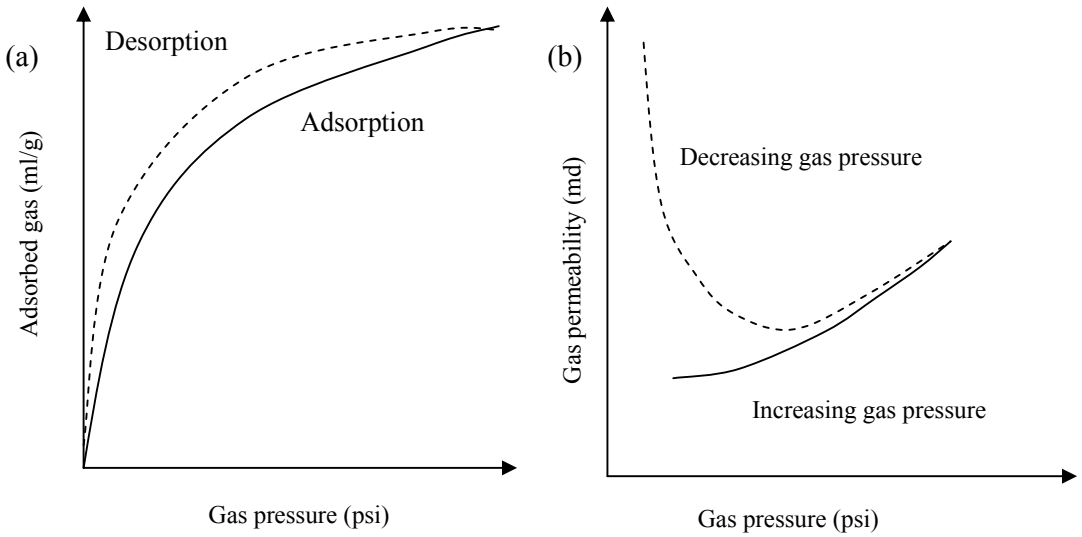

Figure 2.1: (a) A schematic adsorption / desorption isotherm for a coal sample up to 1000 psi. (b) A schematic plot showing the trend of gas permeability in relation to changes in gas pressure for a constant confining pressure (after Harpalani & Chen, 1989).

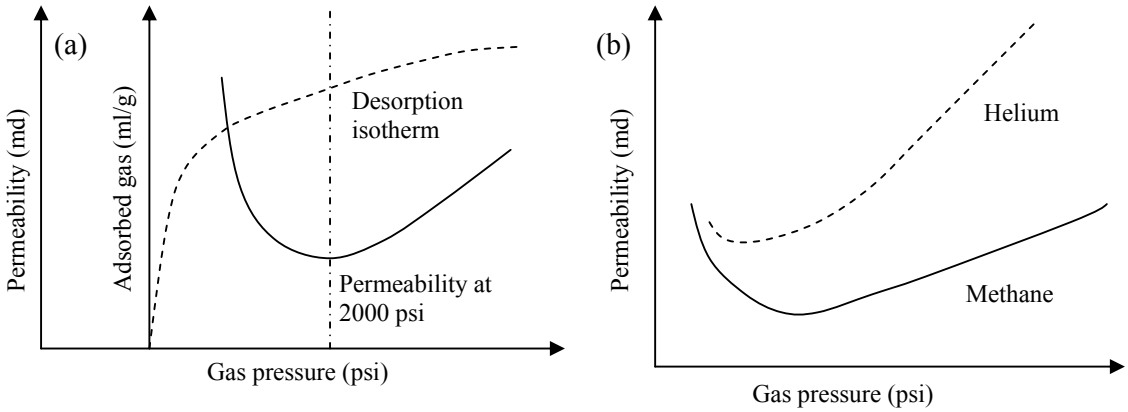

Figure 2.2: (a) Variation in permeability and adsorbed gas with decreasing gas pressure after (Harpalani & Chen, 1989). (b) Variation in coal permeability to helium and methane with decreasing gas pressure.

2.1.2.3 Adsorption

Adsorption allows rocks and soils to hold fluids within their mineralogical structure, e.g. water in certain clays or gases like methane within coal. The ability of rocks, such as coal, to adsorb gases is important, especially the affinity for methane. Other gases can be adsorbed, e.g. helium, nitrogen and carbon dioxide, although their affinity is significantly less than for methane (Fig. 2.3). It is accepted the gas is held at a molecular level within the micro-pores of the coal mass (Meaney et al., 1995), and is recognised to increase with coal maturity.

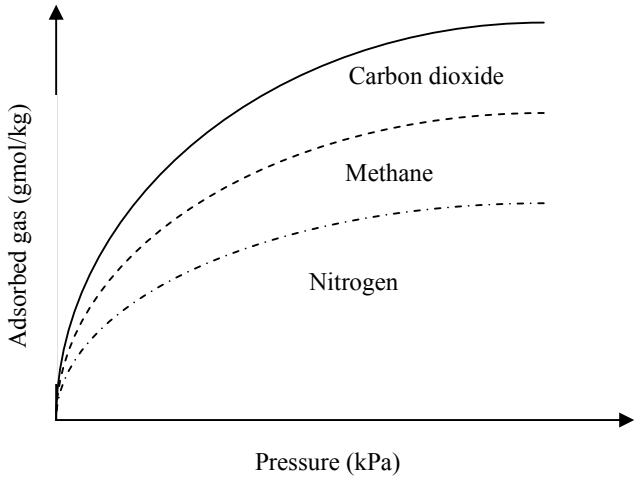

Figure 2.3: Examples of desorption isotherms for coals with respect to pure gases (Meaney et al, 1995).

Adsorption is usually defined using an adsorption:desorption isotherm (Fig. 2.1) which relates gas pressure to adsorbed gas content and confirms that decreasing trends in gas pressure reduce gas content. Figure 2.2a shows the increasing permeability associated with reduction in gas pressure and increase in the rate of change of adsorbed gas. This factor emphasises the significance of the fracture flow, whereby rock sample permeability becomes dominant with increasing matrix shrinkage.

Desorption test are used to calculate adsorption using Langmuir's equation:

$$V = \frac{V_L p}{p + p_L} \qquad [2.11]$$

where, V is the volume of the adsorbed gas, p is the gas pressure and V_L and p_L are the Langmuir volume and pressure constants respectively.

Desorption of gas from coal micro-structure is also responsible for matrix shrinkage at low gas pressures. Matrix shrinkage affects well production of gas and can be associated with changes in stress, which may further affect excavation support in underground coal mines (Harpalani & Chen, 1989). Harpalani & Chen (1989) observed rock mass shrinkage in excess of the expected elastic compression from the increased triaxial loading. They concluded that an increase in permeability below the threshold adsorption pressure was related just to gas desorption from the coal, as there was no mechanical change in the coal structure. They also noted that, if a coal seam had been subject to a historically higher gas pressure, then the permeability would be higher than expected indicating a hysteresis effect due to cyclic pressure variation.

2.1.2.4 Diffusion

Diffusion of a gas through water can be calculated using Fick's First Law by relating the concentration gradient to the diffusivity (D), represented by:

$$J = -D\frac{dC}{dx} \qquad [2.12]$$

where, J is the mass flux, C is the concentration gradient measured in the x direction and D is the diffusivity coefficient. The calculation of the rate of change of concentration uses Fick's Second Law in the equation:

$$\frac{\partial C}{\partial t} = D\left(\frac{\partial^2 C}{\partial x^2}\right) \qquad [2.13]$$

This mechanism has been effectively modelled in porous media where seepage velocity is low (Fredlund & Rahardjo, 1993). Fracture seepage velocity is often high but with flow still laminar, with the entrainment of air bubbles. Advection becomes more significant than diffusion in these cases and can be satisfactorily modelled using

conservation of mass and momentum principles for co- and counter-current flow (Wallis, 1969; Kostakis & Harrison 1999). The relatively large apertures and the high flow rates considered in this work minimise the significance of diffusion.

2.2 Single-phase fracture flow

This section considers the flow of a single-phase fluid through a fracture and investigates laminar and non-laminar flow through fractures and the rock matrix. The discussion provides a context for the research in this study.

2.2.1 Rock mass permeability

2.2.1.1 Introduction

The term 'rock mass permeability' often appears in discussions on groundwater flow and is essential in rock engineering problems. Permeability, better known as 'intrinsic permeability' defines the resistance to flow under an applied hydraulic gradient, being independent of fluid properties with units of (m^2). Strictly speaking, hydraulic conductivity should be used instead of permeability because in most cases, water is the permeant. Hydraulic conductivity (K) relates intrinsic permeability to fluid dynamic viscosity (μ) and is a function of permeant properties and pore geometry:

$$K = \frac{kg\rho}{\mu} = \frac{kg}{\nu} \qquad [2.14]$$

where, K has units of ms^{-1}.

The energy head causing water flow is calculated from Bernoulli's equation. In groundwater problems where the seepage velocity (U) is small, the effect of kinematic head can be ignored (i.e. assume that $U^2/2g \approx 0$). Thus, head (or total head) is defined as the sum of pressure head and elevation head above a given datum:

$$h = \frac{u_p}{\gamma_f} + z \qquad [2.15]$$

where, h is head (m), u = pore pressure (kPa), γ = unit weight of fluid (kN/m^3) and z is elevation above datum (m).

2.2.1.2 Primary and secondary permeability

Primary permeability and the material porosity are directly related, depending upon factors such as the rock type, geological history, and in-situ stress conditions. Porosity can vary between less than 1% for shales and granites up to 50% or more for some clays and sandstones. Secondary permeability is a function of fracture aperture and the degree of connectivity.

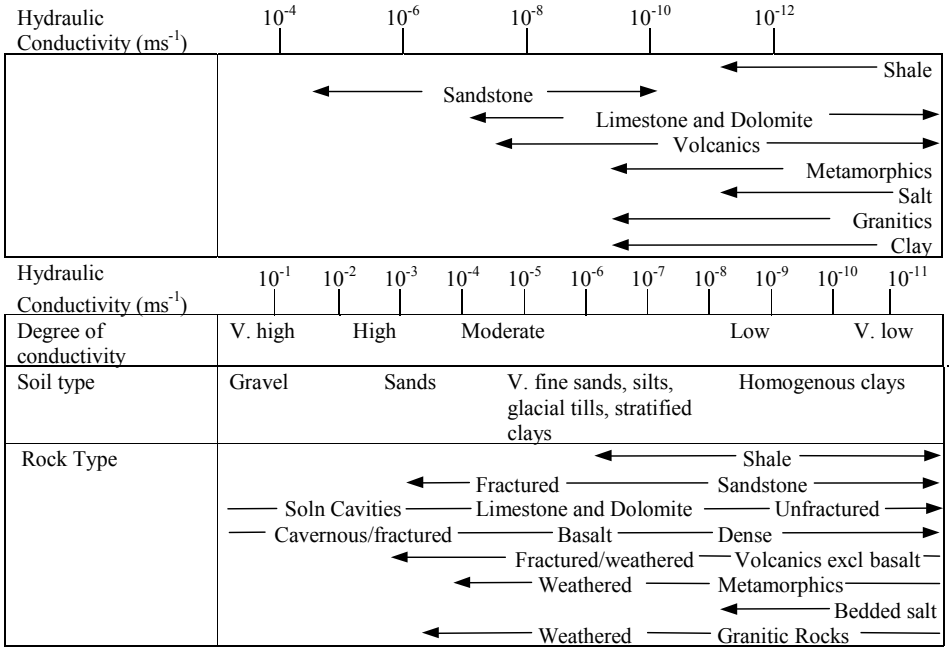

Figure 2.4: Typical values of primary and secondary hydraulic conductivity from laboratory and field tests (after Isherwood, 1979).

Water flow occurs in rocks through a combination of intergranular pores and interconnected fractures. Rock mass conductivity (K_{mass}) is, therefore, the sum of the matrix or primary conductivity (K_p) and the fracture or secondary conductivity (K_f). Both flow mechanisms occur in most rocks but due to the low primary porosity of many rocks, fracture flow is often the dominant mechanism:

$$K_{mass} = K_p + K_f \quad [2.16]$$

Equation 2.16 indicates that where primary permeability is about 2 orders of magnitude less than the secondary permeability, the primary permeability can be ignored for most practical engineering purposes. A typical variation in hydraulic conductivity for different rock types is illustrated by comparing laboratory tests and field test values shown in Fig. 2.4. This variation is a function of the size of the sample under investigation in relation to the scale of rock mass variability in the field.

Equation 2.16 can be re-written for an idealised case where regular spaced fractures intersect a rock mass. If the representative fracture aperture is *e* and the mean spacing is *b* then Eq. 2.17 can be proposed.

$$K_m = K_p + \frac{e}{b} K_f \quad [2.17]$$

The calculation of an equivalent rock mass conductivity representing the effect of primary and secondary porosity is a crucial but intractable problem. Previously, the Representative Elemental Volume (REV) was defined as a notional volume of rock that if tested would contain the intrinsic features of the rock mass. Theoretically, this would allow a rock mass comprising elements of primary and secondary conductivity to be considered as an equivalent porous media. Although a useful concept, in reality the actual volume varies with the rock type and location, and in certain circumstances may be indefinable. Preferably, a judgement-based approach should be used to complement the conductivity assessment and including an analysis of case history data where possible, so that the model could be calibrated to the site conditions.

2.2.1.3 Flow behaviour in hydromechanics

An analysis of fluid flow through a rock mass is a debate between the applicability of a porous or discontinuous medium approach, as summarised by Eq. [2.17]. Porous media approaches ignore the effects of rock mass defects, and consider flow through

intergranular void spaces, i.e. mainly concerned with primary or effective primary permeability. Discontinuous media approaches apply known locations and defect dimensions (i.e. secondary permeability) to analyse fluid flow, and can include or neglect intergranular flow depending upon the relative magnitudes of each permeability component.

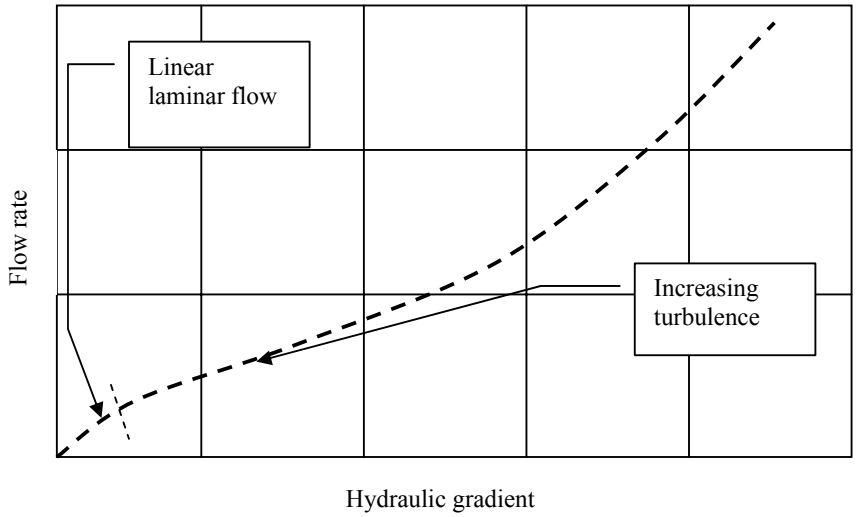

Figure 2.5: Illustration of the change in flow rate with hydraulic gradient

Each approach represents the ends of a broad spectrum of geological conditions to which either model is applicable to a degree. As discussed by various authors, eg. Gale (1990), stochastic fracture network models (eg. UDEC) present a third intermediate approach. Gale (1990) demonstrated close agreement between computed and measured inflow rates, but the mean fluid velocity contradicted tracer testing results. Gale (1990) demonstrates that accurate measurement of aperture, particularly residual aperture, is critical to the reasonable calculation of conductivity and fluid velocity. Others, including Brown (1987) have also used numerical modelling and fractal theory to carry out numerical studies of fluid flow that focus on the effect of surface roughness. The relationship between flow rate and hydraulic gradient is assumed to be linear during laminar flow, in accordance with Darcy's law. However, with the increase of frictional losses from the onset of turbulent flow, or flow separation from surface roughness and

inertial effects occurring from aperture variation, the relationship becomes increasingly non-linear (Fig. 2.5). Elsworth & Doe (1986) used alternative non-linear flow laws such as Missbach or Forcheimer, to analyse flow conditions.

2.2.1.4 Flow in Porous Media

Under the steady state flow conditions commonly encountered in engineering projects, seepage is intergranular, laminar and viscous, for which seepage can be calculated using Darcy's Law:

$$Q = KA\frac{\Delta h}{L} \qquad [2.18]$$

where, Q is flow rate, K is hydraulic conductivity, A is cross sectional area of flow and Δh is the change in head measured over a length L.

Darcy's law assumes the flow to be within a saturated homogenous isotropic media, and can be more formally written as:

$$q_i = -\frac{K_{ij}}{\gamma}\frac{\partial p}{\partial x_j} = -\frac{k_{ij}}{\mu}\frac{\partial p}{\partial x_j} \qquad [2.19]$$

where, q_i is the specific discharge, k_{ij} and K_{ij} are permeability and conductivity tensor components and $\frac{\partial p}{\partial x_j}$ is the pressure gradient causing flow. The flow rate can be written in terms of velocity (U). The velocity calculated from Darcy's Law is an 'average' velocity because it does consider the percolation path and seepage time.

When flow conditions are not linear, an alternative law is needed to perform engineering analyses. There are two particular approaches to calculate the flow behaviour under these conditions. The transition between linear and fully non-linear flow was well described by the Forcheimer's Law (Indraratna et al., 1994):

$$\nabla\phi = a_F U + b_F U^2 \qquad [2.20]$$

where $\nabla\phi$ is the hydraulic gradient, U is the average velocity and a_F and b_F are linear and non-linear constants.

The Missbach Equation is an alternative mathematical relationship for non-linear flow that has been more widely used in the analysis of pumping test data (Doe & Elsworth, 1986; Louis & Maini, 1972):

$$\nabla\phi = c_M U^m \text{ or } U = -K\nabla\phi^n \quad [2.21]$$

where, K is hydraulic conductivity, c_M is a constant, and n is 0.5 for turbulent and 1 for laminar flow.

2.2.1.5 Flow in Discontinuous Media

The Navier-Stokes equation can be used to develop the equation known as the 'parallel plate law' or 'cubic law' for linear laminar flow conditions, which assumes the fluid is viscous and incompressible, and flow occurs between two parallel smooth surfaces not in contact. Numerous studies have been conducted to establish the range of validity of the law to saturated flow and the applicability to flow in fractured media.

Lee & Farmer (1993) describe the evolution of fracture flow study and the application of Darcy's law from initial work by Romm (1966) and Lomize (1951). The former used two parallel glass plates with apertures as small as 0.2mm, with Romm (1966) concluding the formula was applicable to apertures of 0.2μm. The law is unsuitable for tight rough defects and for rough defects under high normal stress (Lee et al, 1993; Witherspoon et al. 1980). Lomize (1951) used marble and quartzite samples to demonstrate the cubic law validity for open fractures at low stresses, but with a departure at small apertures. Brown (1987) observed that the accuracy of cubic law predictions diminished when fracture surfaces became close, with flows about 50% of that predicted by cubic law theory. Brown (1987) found the Reynolds equation applicable in calculating flow using a numerical model, a fact confirmed theoretically

by Zimmerman & Bodvarsson (1996). Iwai (1976) and Witherspoon et al. (1980) considered the law valid for natural rough uneven and open discontinuities as narrow as 4μm. Witherspoon even developed Darcy's Law to include a term related to the fracture aperture discussed in Section 2.2.2. It is clear that fracture surface roughness significantly effects the linearity of flow, and is explored further in Chapter 3.

Cook et al. (1992) commented that "*changes in aperture of the void spaces between the two rough surfaces of a joint in partial contact with changes in stress are neither equal to nor proportional to changes in mean joint closure*." The change of contact area with increasing applied stress causes the mean void aperture to close more quickly than the mean joint closure. This result, plus an increasing flow path tortuosity with increasing stress, means that the laminar flow of fluid between fracture surfaces is no longer proportional to the cube of mean fracture aperture, as it would be for parallel surfaces, but to a higher and variable power. At high confining stresses, fracture flow is constricted by an irreducible hydraulic aperture or residual aperture (Indraratna et al., 1999b).

Flow through a fracture network is a development of single fracture flow concepts, for which various researchers have suggested new approaches (Indraratna et al., 1999a). Stochastic processes can be used to estimate flow characteristics, and when incorporated with mechanical analyses, increased connectivity can result in reduced rock mass stability. However, not all fractures within a network are conducting fractures (Lee et al., 1993; Long et al., 1985) and direct observation of defect orientation location and length is often needed for successful analysis. To calculate fracture flow using the cubic law is acceptable for most discrete fracture flow studies, however results should be interpreted cautiously because of the experience gained from the

DECOVALEX Project (Jing et al., 1996). Chapter 7 subsequently explores numerical analysis of fracture flow and illustrates flow estimation using a finite difference scheme.

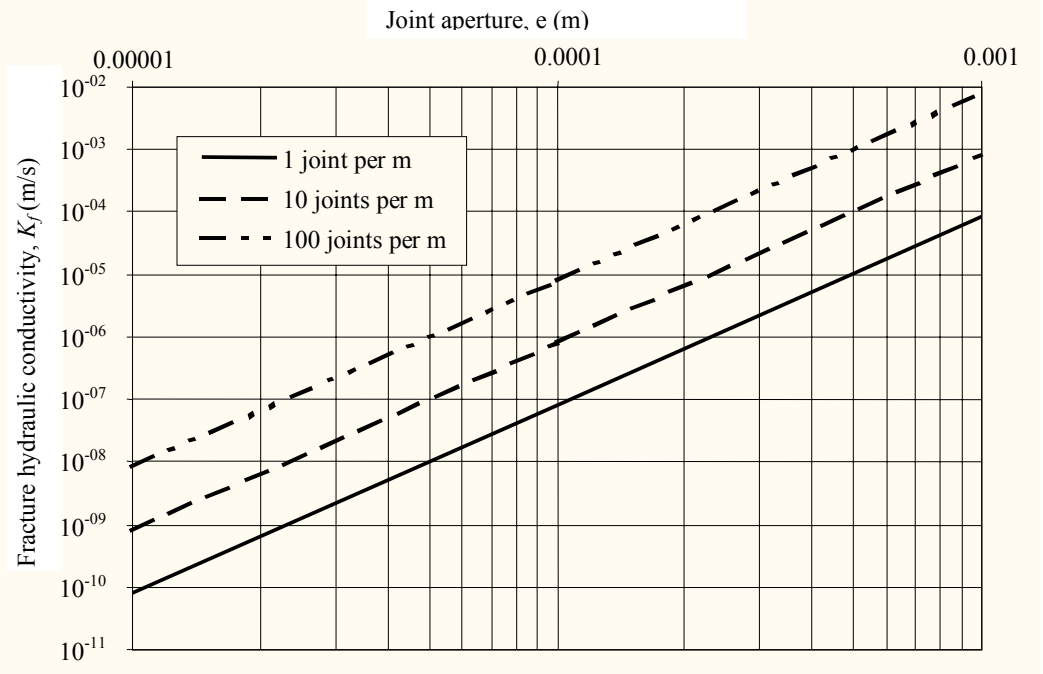

Figure 2.6: The influence of joint aperture (e) and joint spacing on hydraulic conductivity (K_f) in the direction of a set of smooth joints (after Hoek and Bray, 1981).

Flow is often idealised to occur between smooth parallel plates, on the assumption that flow is laminar and viscous. In such a case, the 'cubic law' gives hydraulic conductivity of a single fracture:

$$K_f = \frac{ge^3}{12\nu b} \qquad [2.22]$$

where, K_f is fracture conductivity, e is the hydraulic aperture, g is acceleration due to gravity, ν is the kinematic viscosity (1.01×10^{-6} m^2s^{-1} for pure water at 20°C) and b is the mean spacing between fractures (m). The sensitivity of fracture conductivity to aperture and fracture frequency in Eq [2.22] is plainly illustrated in Figure 2.6.

The impact of significant roughness or large pressure gradients were previously discussed (Fig. 2.7). In these circumstances, laminar flow behaviour can be replaced by transitional or turbulent flows. Early investigations (Louis, 1969) applied pipe hydraulics to fracture flow incorporating, the pressure-drop coefficient λ and Reynolds number Re, assuming that the hydraulic radius was 2*e,* where *e* is the fracture aperture.

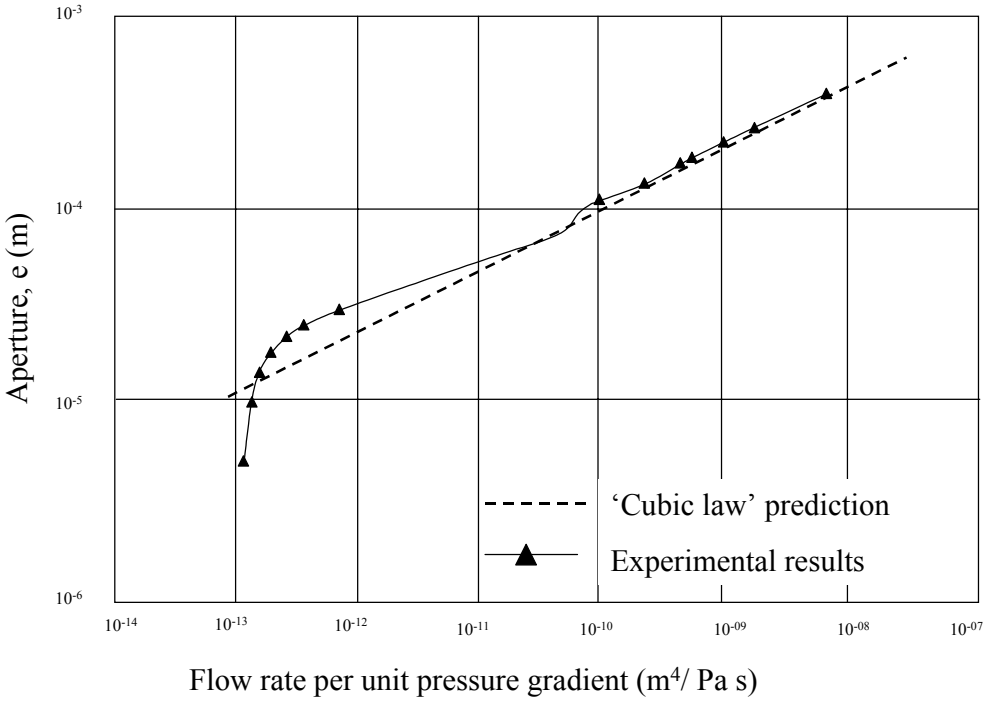

Figure 2.7: Sample plot showing the 'cubic law' validity, after Long et al (1996) and Cook et al. (1990).

Sharp (1970) reviewed the flow characteristics of fractures and summarised the theoretical flow laws depending upon the type of flow and relative roughness (k_{max}/D). This information is re-produced in Table 2.2 below. His work considered fracture roughness as an increase in the flow path length following the asperity geometry, compared to the overall length, measured as a straight line between the start and end of the flow path.

Table 2.2: Comparison of flow rate formulae for parallel and non-parallel flow (Sharp 1970).

Flow condition	Roughness	Equation
parallel flow (pipe flow)	$k_{max}/D_h <$ 0.033	$Q = \left[\frac{g}{0.079}\left(\frac{2}{\gamma}\right)^{0.25} e^3 J\right]^{4/7}$
		$Q = 4\sqrt{g}\log\left(\frac{3.7}{k_{\max}/D_h}\right)e^{1.5}\sqrt{J}$
non-parallel flow (joint flow)	$k_{max}/D_h >$ 0.033	$Q = 5.11\sqrt{g}\log\left(\frac{1.24}{k_{\max}/D_h}\right)e^{1.5}\sqrt{J}$
		$Q = 4\sqrt{g}\log\left(\frac{1.9}{k_{\max}/D_h}\right)e^{1.5}\sqrt{J}$

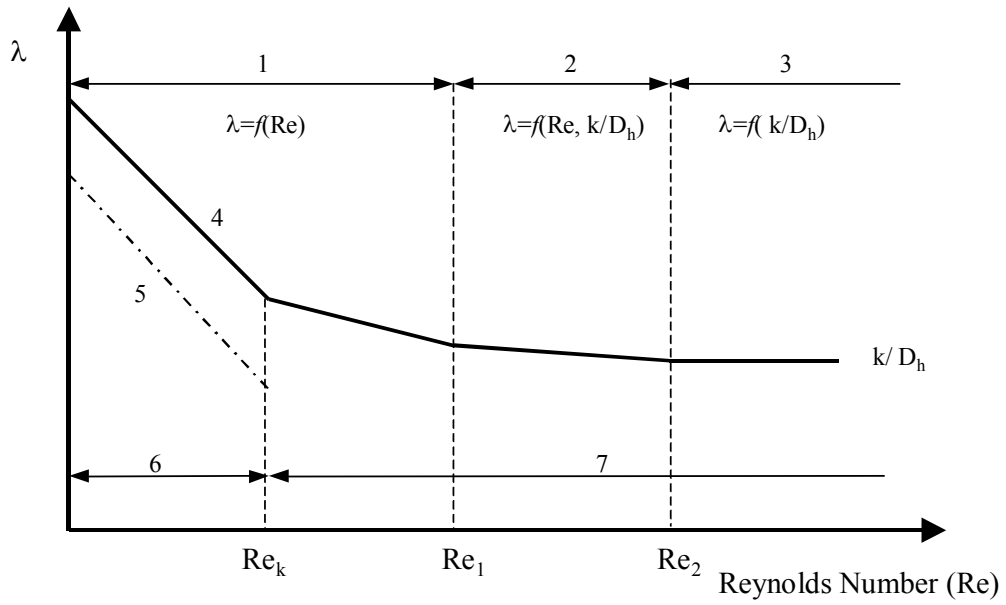

Figure 2.8: Plot of Pressure Drop Coefficient (λ) versus Reynold's Number after Louis (1976).

Louis (1968) developed relationships between pressure drop coefficient (λ), relative roughness (k_{max}/D_h), Reynolds number (Re) and unit flow rate for a laminar, transitional and turbulent flow. Louis (1968) quantified roughness using an empirical relative roughness coefficient defined as k_{max}/D_h where k_{max} is the absolute roughness (i.e. the maximum amplitude of the asperities measured parallel to the plane of the fracture).

Louis presented the relationship between the total energy gradient $\mathbf{J_c}$ and the pressure drop coefficient λ, where the velocity is constant along the flow path, $\mathbf{J_c} = \mathbf{J}$ thus:

$$\mathbf{J} = \frac{1}{D_h}\frac{U^2}{2g}\lambda \qquad [2.23]$$

The λ and Reynolds Number (Re) relationships for the range of flow types are given in equations Eqs. 2.24 to 2.26. Laminar flow extended to a critical Re of 2300 for hydraulically smooth surfaces ($k_{max}/D_h \leq 0.033$). The critical Re reduces for increasingly rough fractures.

$$\lambda = f(\mathrm{Re}) \qquad \text{hydraulically smooth flow} \qquad [2.24]$$

$$\lambda = f\left(\mathrm{Re}, \frac{k_{\max}}{D_h}\right) \qquad \text{transition flow} \qquad [2.25]$$

$$\lambda = f\left(\frac{k_{\max}}{D_h}\right) \qquad \text{completely rough flow} \qquad [2.26]$$

Table 2.3: Pressure drop coefficients and the unit flow rate for a single joint (Louis, 1976).

	Flow	Pressure drop coefficient (λ)	Unit flow rate (q)
Relative roughness $k_{max}/Dh \leq 0.033$ (parallel flow)	Laminar	I $\lambda = \frac{96}{\mathrm{Re}}$	$q = \frac{g}{12v}e_i^3 J_i$
	Turbulent	II $\lambda = 0.316\,\mathrm{Re}^{-0.25}$	$q = \left[\frac{g}{0.079}\left(\frac{2}{v}\right)^{0.25} e_i^3 J_i\right]^{4/7}$
		III $\frac{1}{\sqrt{\lambda}} = -2\log\frac{k_{\max}}{3.7D_h}$	$q = 4\sqrt{g}\left(\log\frac{3.7D_h}{k_{\max}}\right)e_i^{1.5}\sqrt{J_i}$
Relative roughness $k_{max}/Dh > 0.033$ (non-parallel flow)	Laminar	IV $\lambda = \frac{96}{\mathrm{Re}}\left[1+8.8\left(\frac{k_{\max}}{D_h}\right)^{1.5}\right]$	$q = \frac{ge_i^3 J_i}{12v\left[1+8.8\left(\frac{k_{\max}}{D_h}\right)^{1.5}\right]}$
	Turbulent	V $\frac{1}{\sqrt{\lambda}} = -2\log\frac{k_{\max}}{1.9D_h}$	$q = 4\sqrt{g}\left(\log\frac{1.9D_h}{k_{\max}}\right)e_i^{1.5}\sqrt{J_i}$

The flow type regions defined by Louis (1969) in Fig. 2.8 are labelled as 1, 2 and 3 corresponding to hydraulically smooth, intermediate, and completely rough, respectively. The range of laminar and turbulent flow is also indicated as domains 6 and 7 in Fig. 2.8. Fig. 2.8 also shows a similarity in flow response between the rock joints and conduits, in regions 4 and 5, respectively. The expressions from Table 2.3 allow construction of relationships between relative roughness and pressure drop, with Reynolds number for the range of identified flow types. These functions are plotted in Figs. 2.9 and 2.10.

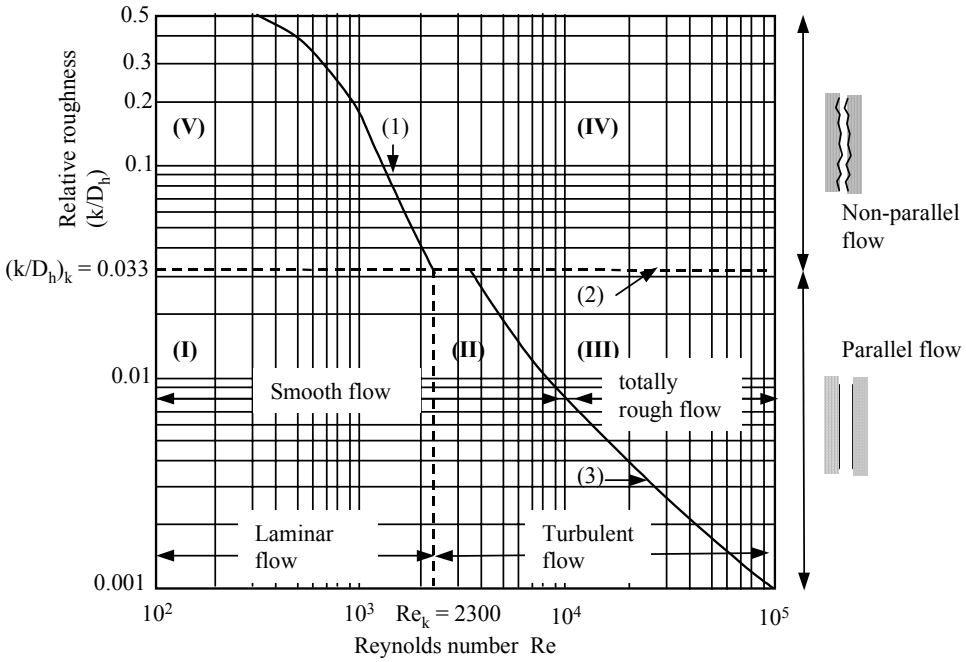

Figure 2.9: The relationship of flow behaviour to relative roughness and Reynolds Number, as defined by Louis (1968) and Thiel (1989).

Studies of single-phase non-linear flow (Schrauf & Evans, 1986) consider the effect of inertial losses and changes in flow velocity or direction and initiation of turbulent flow. The gas flow through fractures is tested and analysed by including a non-linear term related to the square of the velocity. The results show that the hydraulic aperture was less than the average measured fracture aperture, but fracture conductivity was well

predicted by empirical equations such as Louis (1968) and Barton (1982). Fracture deformation was well described by strain energy relationships without regard to fracture geometry. Flow rate through a fracture was found to be inversely proportional to the 4th power of the fracture aperture.

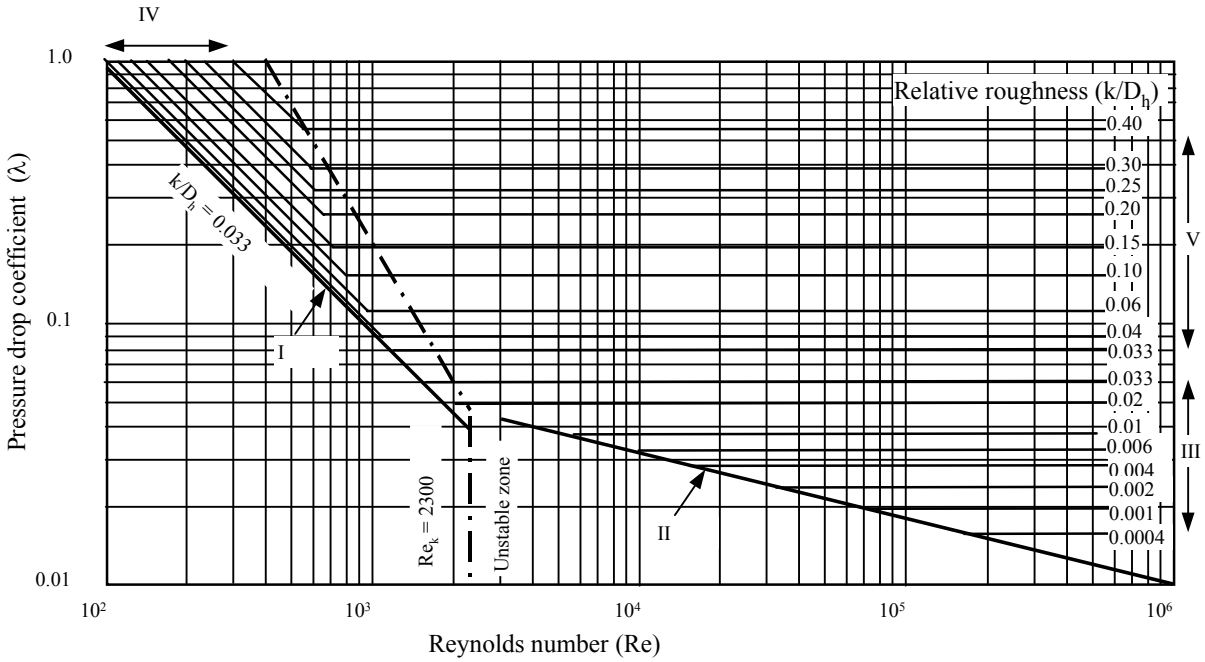

Figure 2.10: Joint flow relationships based on pressure drop coefficient, Reynolds number and relative roughness, after Louis (1976).

2.2.2 Geological factors impacting on flow behaviour

Engineering analysis often relies upon linear behaviour to predict the reaction of materials to changes in stress, deformation or flow. The following sections present explanations and discussions of geological factors that impact upon the observed single phase flow behaviour and complicate some of these linear simplifications.

2.2.2.1 Surface roughness

It is now widely accepted that the cubic law loses its validity at large pressure gradients, particularly in the case of tight and rough fractures. In 2-D, increases in roughness reduce the assumption of plate parallelism. In the third dimension, this results in further

increases flow path tortuosity in the fracture plane. As already stated, Louis (1968) developed empirical relationships between pressure drop coefficient *(λ)*, relative roughness, Re and unit flow rate for laminar, transitional, and turbulent flow. He quantified roughness using an empirical relative roughness coefficient defined as k_{max}/D_h, where k_{max} is the absolute roughness (ie. the maximum asperity amplitude measured parallel to the fracture plane) and D_h is the hydraulic diameter (ie. $2e$).

Louis & Maini (1972) relate fracture conductivity to joint surface roughness and contact area, thereby accounting for tortuosity in flow behaviour. This is achieved with the parameter κ – the degree of joint separation.

$$k_f = \frac{\kappa g e^2}{12 \nu C} \qquad [2.27]$$

where, κ is the open surface area of the joint divided by the total surface area, ν is the kinematic viscosity of water (1.2×10^{-6} m^2/s at 13˚C; 1.0×10^{-6} m^2/s at 20°C)' C is the roughness correction factor from Louis (1969). The roughness correction factor is further defined as follows:

For $k_{max}/D_h \leq 0.033$: $C = 1$ [2.28]

For $k_{max}/D_h > 0.033$: $C = 1 + a\,(k_{max}/D_h)^{1.5}$ [2.29]

In these equations, k is absolute joint roughness, D_h is the hydraulic diameter (or $2e$), a is a coefficient depending upon roughness type. Louis (1969) assumed $a = 8.8$.

Louis & Maini (1972) considered turbulent fracture flow and stated that was inapplicable due to an increase in energy losses resulting in a non-linear relationship between mean velocity and hydraulic gradient:

$$\overline{U} = k_j^1 \vec{J}^n \qquad [2.30]$$

where, k^1_j is the turbulent hydraulic conductivity of the joint, n is a factor varying from 0.5 for fully turbulent flow to 1 for laminar conditions.

They expanded this approach using the Louis (1969) results which included roughness and tortuosity in a formula for turbulent conductivity providing the formula:

$$k_j^1 = 4\kappa\sqrt{ge}\log\frac{d}{k_{\max}/D_h} \quad [2.31]$$

Such that:

For $k_{max}/D_h \leq 0.033$: $d = 3.7$ [2.32]

For $k_{max}/D_h > 0.033$: $d = 1.9$ [2.33]

Cornwell et al. (1985) used synthetic 'saw tooth' joint models to study fracture flow behaviour and showed that depending upon relative roughness, non-Darcy flow could be initiated for Re = 30. Ranjith (2000) tested relatively smooth, induced tensile fractures with Re ≤ 40 and identified laminar flow conditions during the test. Test results from the current study presented in Chapter 6 indicate that, non-linear flow probably develops for Re values similar to those encountered by Cornwell (1985).

Witherspoon et al. (1980) showed that a flow reduction factor *(f)* can be successfully applied to saturated flow problems with the cubic law for open, rough fractures, such that:

$$Q = \frac{1}{f}\frac{e^3}{12\mu}wi, \text{ and} \quad [2.34]$$

$$f = \left[1 + 6\left(\frac{\varepsilon}{e}\right)^{1.5}\right] \quad [2.35]$$

where, f is greater than or equal to 1 (such that 1 is representative of linear, laminar flow and f thus increases with turbulence), and ε is the absolute height of the asperities. Eq. [2.34] was found to be valid for $\varepsilon/e > 0.0065$. They considered confining stresses up to 20MPa and fracture apertures from 250μm down to 4μm, with the results showing that roughness reduced the flow by a factor of 1.04 to 1.65. Witherspoon et al. (1980) considered similar apertures to those of the samples tested in this project. Despite the

appeal of this methodology, there are practical problems with measuring absolute asperity height in the field where only a small exposure may be available to represent the larger fracture characteristics. The previously presented expression Eq [2.34] was extended by Cook et al. (1990) to also include tortuosity in terms of (1 - d)/(1 + d):

$$Q = \frac{1}{f}\left(\frac{1-d}{1+d}\right)\frac{e^3}{12\mu}wi \qquad [2.36]$$

The Cook et al. (1990) attempt was based upon a number of different void geometries made from agglomerations of regular shapes where *d* represented the proportion of contact area measured across the fracture surface.

Laboratory experiments (Witherspoon et al. 1980; Cook et al. 1990) showed that the back-calculated hydraulic aperture is less than the actual mechanical aperture under saturated conditions along a rough surface or in small aperture fractures. This discrepancy increases with increasing roughness. Barton et al. (1985) developed an empirical relationship between the hydraulic aperture e_h, mechanical aperture *e* and the *JRC* for the condition e $\geqslant$ e_h, as given below:

$$e_h = \frac{e^2}{JRC^{2.5}}, \text{ where apertures are measured in } \mu\text{m} \qquad [2.37]$$

This equation is based upon laboratory data and accounts empirically for non-parallel flow across a rough surface without recourse to topographic analysis parameters. The relationship of *JRC* to fracture roughness is described by the standard profiles proposed by Barton et al. (1977) and adopted by the ISRM (1978). Barton et al. (1997) proposed a new relationship between JRC, joint profile length *L* and the maximum fracture amplitude k_{max}. For a profile length of 100mm, the relationship is shown in Eq. [2.38]:

$$JRC = 400\frac{k_{\max}}{L} \qquad [2.38]$$

The issue of scale and the effect on *JRC* has been widely discussed and summarised by authors including Seidel & Haberfield (1995), and Indraratna & Haque (2000). Alternative approaches to modelling roughness include spectral analysis (Bonner & Durham, 1995), fractal analysis (Power & Tullis, 1991) or the Fourier series (Indraratna & Haque, 2000). The Fourier approach is very useful because of the mathematical simplicity that allows Fourier functions to be incorporated into the equations used to model rock mass behaviour.

Wei & Hudson (1988) proposed an alternative relationship between hydraulic and mechanical aperture (Fig. 2.11) which is represented by the following equation:

$$e_h = \frac{e_{ho}}{e_o}\left(e - e_{\min}\right) \qquad [2.39]$$

where, e_{ho} is the maximum hydraulic aperture, e_o is the closure of the joint when the hydraulic aperture is zero, e_{min} is residual mechanical aperture. The Wei & Hudson (1988) relationship is linear and attractive because of the simplicity the expression does not capture the non-linearity identified by the empirical Barton et al. (1985) equation that mimics observed fracture behaviour.

Lomize (1951) considered the effect of surface roughness on flow using glass plates with uniform glass beads glued to the surfaces. Cook (1992) credits Lomize with the following equation, which is an extension of the Reynolds equation multiplied by $1/f$:

$$Q = -\frac{1}{f}\frac{D^{*3}}{f}12\mu\frac{dp}{dx} \qquad [2.40]$$

where, f is a factor to account for the effects of surface roughness. Lomize (1951) verified the applicability of this equation to cubic law for fractures down to 4μm and confining stresses to 20MPa.

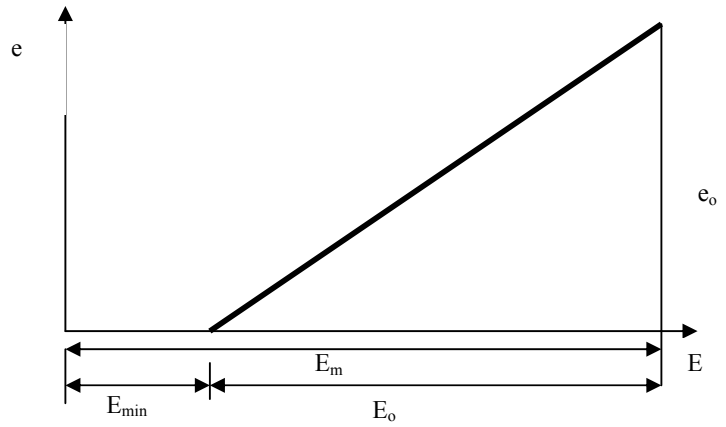

Figure 2.11: The proposed hydraulic and mechanical aperture relationship by Wei & Hudson (1993).

In his review of the hydraulic behaviour of rock joints, Gale (1980) summarised the primary difference in roughness assessments emerging between two principal bodies of workers. Louis (1969) and Rissler (1978) adopted relative roughness (R^*) as the ratio of the absolute height of asperities to fracture aperture. An alternative definition was used by Lomize (1951), where relative roughness was defined as the ratio of the mean asperity height ($0.5\ k_{max}$) over the hydraulic diameter (D_h, i.e. twice the fracture aperture). The difference in definition appears to originate from different experimental procedures applied by the workers. The former approach is limited by the dependence on surfaces with a uniform asperity height. The large number of parameters used to define roughness illustrates the difficulties in relating flow behaviour and rough surfaces to established flow laws. This divergence in roughness description exemplifies the ISRM in their 1978 standardisation of roughness in terms of the Joint Roughness Coefficient, *JRC*. This act allows a unified description of roughness and assessment of hydromechanical behaviour provided the issue of scale is accommodated.

2.2.2.2 Aperture variability

Indraratna et al. (1999) and Zimmerman & Bodvarsson (1996) stress the role of aperture variation in flow behaviour, where in reality the aperture is rarely uniform, contrary to

an assumption of the parallel plate law. They feel that it is acceptable to account for variation in mechanical aperture by using the log-normal mean hydraulic aperture in calculations based upon parallel plate theory. The term 'equivalent hydraulic aperture' is used to define the 'parallel plate' opening predicted using the 'cubic law'. This is in keeping with the definitions described by Tsang (1984) in relation to the 'cubic law'. The relationship between mechanical and hydraulic apertures is essential when analysing hydromechanical behaviour.

Variable aperture models have been developed by Neuzil & Tracy (1981) and Tsang (1984), among others. They commonly consider flow through small consecutive parallel plate elements with the elemental aperture related by an aperture function *f(e)*; Neuzil & Tracy (1981) propose a development of the parallel plate law as follows:

$$Q = LJ\frac{\gamma}{12\mu}\int_0^\infty e^3 f(e)de \qquad [2.41]$$

Where changes in aperture from element to element are small, Zimmerman & Bodvarrson (1996) indicate that the 'cubic law' generally provides an acceptable solution. Fracture aperture is the key parameter in calculating conductivity and flow. Aperture distributions have been predicted from several laboratory studies and mathematical models, and aperture distribution is well predicted if a log normal distribution is used (Hakami et al, 1990; Zimmerman & Bodvarson, 1996).

2.2.2.3 Fracture stiffness

Fracture stiffness parameters are crucial for controlling the coupled stress:flow behaviour of a fracture. This study is primarily concerned with fracture normal stiffness since the test apparatus prevents any shear displacement of the sample. Several authors have studied the relationship between stress and conductivity, including Carlsson (1990) and Indraratna et al. (1999). Carlsson (1990) tested sandstone and coal samples and found that there is a marked reduction of conductivity for rocks with a lower initial

permeability value. Carlsson (1990) does not compare rock type UCS or Young's modulus with initial conductivity, or conductivity rate of change. The elastic properties of the different rock types have a fundamental impact on the rate of change of conductivity. Aperture closure is directly related to the elastic properties of the rock substance and the fractures. Brace (1975) considered fracture orientation, and concluded that fractures parallel to the maximum principal stress would tend to dilate, whereas perpendicular fractures tended to close as loads increased.

Fracture deformation occurs from shear or normal deformation of the fracture walls. Shear test results reported by Makurat et al. (1990) indicated that conductivity increases of up to 2 orders of magnitude could occur, but as deformation increased, conductivity should decrease because of the formation of gouge material blocking the flow paths. Beyond a high threshold normal stress, the aperture does not reduce any further, i.e. after achieving the residual aperture (Indraratna & Ranjith 1999; Cook et al., 1990). Residual aperture depends on initial aperture as well as rock type and roughness profile. Cook et al. (1990) and Sharp (1970) postulated that deviation from the cubic law was a function of long wavelength un-correlated roughness (i.e. out of plane tortuosity between unmated fracture surfaces) which increases the flow path beyond the physical distance between two points. Tsang (1984) used an electrical resistance model to study aperture variation and tortuosity, and study established a number of conclusions, one being that increased tortuosity during defect deformation could reduce conductivity by 2 or 3 orders of magnitude. This conclusion seems highly likely given common encountered aperture variability and fracture stiffness of rock fractures.

Fracture behaviour is related to aperture through elastic theory using their normal and shear stiffness (K_n, K_s) as explained by Brady & Brown (1994). The contact

force (normal or shear) is related to the corresponding displacement by a linear relationship:

$$F_n = K_n \delta_n \quad [2.42]$$

$$F_s = K_s \delta_s \quad [2.43]$$

where F represents the force, δ is the displacement, and the subscripts s or n represent shear or normal orientations.

Chen et al. (1989) considered idealised fractures when assessing the impact of contact area on flow behaviour. They studied flow through an element of propped parallel plate used a boundary element with a smooth parallel plate model including several irregular contact areas of known area. They compared computed results with those recorded in laboratory experiments as well as the predicted impact using the Walsh-Maxwell approach. If the contact area was included irregular asperities, as would be expected for naturally rough surfaces, then the Walsh-Maxwell approach under predicted the fracture flow by as much as 30%. The equivalent aspect ratio of the contact area had to be included to make the analytical results agree with laboratory testing.

2.2.2.4 Gas Outbursts in mining

Gas outbursts are dangerous events in coalmines with the sudden and violent release of toxic and possibly flammable gases causing mechanical failure of the rock mass (Lama & Bodziony, 1996). The death of personnel, losses to production and damage to machinery and infrastructure are some of the consequences of these events. Outbursts are often associated with low permeability anomalies such as geological structures, including dykes or sills or alteration zones. These features inhibit gas drainage and elevate pore pressure gradients. In locations of low rock mass strength, the reduced effective stress conditions provide high risks of gas outburst. The violence of these

events is exacerbated by increased permeability as the fracture pore pressure drops below the rock matrix desorption pressure, as discussed in Sections 2.1.2.2 and 2.1.2.3 and illustrated by Harpalani & Chen (1999).

The geological and hydromechanical complexity of the mining environment means that very few researchers have actually gathered data showing the variations in gas pressure ahead of a long wall face in an undisturbed coal rock mass. There are two main factors in any analysis of gas pressure distribution ahead of an advancing face:

- change in coal conductivity, and
- change in flow field structure with advance of the face.

These factors have driven much of the work in this current project at the University of Wollongong and the industrial partners associated with the research. This project considers the flow behaviour associated with macroscopic structures. Another project to consider the hydromechanical behaviour of the coal microstructure is currently underway.

2.3 In-situ single-phase testing

In-situ testing under saturated or 'single-phase' conditions have been used for some time to gather real data on rock mass hydromechanics. Depending upon the application, water or gas can be used as the permeant depending upon the expected rock mass conductivity and special considerations, e.g. health and safety legislation. Typically, the apparatus is required to inject and hold water at different pressures until the flow rates attain constant values.

Rock mass hydraulic conductivity is routinely measured as part of the geotechnical field investigations. Common industry methods include open borehole tests (constant or falling head), or packer tests where an isolated section of a borehole is subjected to pressurised pumping. Test interpretation requires care, because field trials

can be affected by smearing of clay-rich material at the borehole wall, resulting in pores and fractures clogging and under-estimation of the field conductivity. The drilling method and test section should be carefully selected and prepared to minimise the smear effect. Evaluation of design parameters should be based upon a number of tests, and combined with careful borehole logging so that the variability in conductivity can be assessed and analysed.

2.3.1 Theoretical considerations

Considering laminar flow during water pressure testing, the associated general theory from Darcy's Law can be applied where the hydraulic gradient is a function of elevation and pressure head:

$$\vec{U} = -K_j \nabla\left(z + \frac{p}{\gamma_w} \right) = -K_j \Phi \qquad [2.44]$$

where, Φ is the hydraulic potential at the point of consideration.

The problem can be envisaged as a network of hydraulic potentials *(Φ)* oriented perpendicular to flow direction and streamlines *(Ψ)*. Louis & Maini (1972) describe the general equation for laminar flow in an idealised inclined joint as comprising radial and gravitational flow components.

For radial flow:

$$\Phi_r = \frac{q/b}{2\pi K_j} \log r + \text{constant} \qquad [2.45]$$

$$\Psi_r = \frac{q/b}{2\pi K_j} \beta \qquad [2.46]$$

For gravitational flow:

$$\Phi_g = (\sin\alpha) x + \text{constant} \qquad [2.47]$$

$$\Psi_g = -(\sin\alpha) y \qquad [2.48]$$

Flow and total hydraulic potential are modelled by considering both flows acting during a test on an inclined fracture:

$$\Phi = \Phi_r + \Phi_g = \frac{q/b}{2\pi K_j}\log r + (\sin\alpha)x \qquad [2.49]$$

$$\Psi = \Psi_r + \Psi_g = \frac{q/b}{2\pi K_j}\beta + -(\sin\alpha)y \qquad [2.50]$$

If there is a natural flow, inclined at an angle other than coincident with the coordinate axes (x and y), then Eq. [2.49] and [2.50] can be written as presented below. If there is no natural flow, the formulae simplify to just the radial flow terms.

$$\Phi = \frac{q/b}{2\pi K_j}\log\frac{r}{r_0} + J_x^0 x + J_y^0 \qquad [2.51]$$

$$\Psi = \frac{q/b}{2\pi K_j}\beta - J_y^0 x + J_x^0 y \qquad [2.52]$$

Where there are kinetic energy losses, the term ($U^2/2g$) can be introduced to the potential equation. The losses are negative for extraction and positive for injection pumping.

$$\Phi = \frac{q/b}{2\pi K_j}\log\frac{r}{r_0} \pm \frac{U^2}{2g} \qquad [2.53]$$

The kinetic energy losses within a system can be estimated from the equation:

$$\Delta\left[\frac{U^2}{2g}\right]_1^2 = \frac{q^2}{8g\pi}\left[\left(\frac{1}{er}\right)^2\right]_1^2 \qquad [2.54]$$

Pump pressure can result in coupled deformation of the rock mass, which can affect the interpreted fracture conductivity. Louis & Maini, (1972) related the test conductivity at a pressure p to that at a pump pressure of zero in their equation:

$$(K_j)_0 = \frac{1}{\left(1 + \frac{\alpha p b}{E_m e}\right)}(K_j)_p \qquad [2.55]$$

where, p is the mean water pressure between the 2 reference points, α is a lateral stress factor (1 if lateral stresses neglected, 0.5 to 0.9 if considered), E_m is the Young's modulus of the rock matrix.

The effect of entrance losses has been considered by Rouse (1961) such that:

$$\Delta\Phi = \xi \frac{U^2}{2g} \qquad [2.56]$$

where, ξ is approximately 0.5 for water (i.e. = 2.5m head of water for a flow of 10 ms^{-1}).

2.3.2 Constant or Falling Head Tests

These simple tests are quick and easy to perform and do not require specialised drilling equipment. A thorough discussion of head tests is given by Hvorslev (1951), and a summary of the main points is produced herein. The test methodologies apply to saturated ground conditions and involve the following techniques:

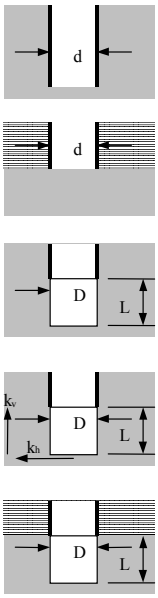

End conditions	Shape Factor F
Casing flush with end of borehole in soil or rock of uniform permeability. Inside diameter of casing is d cms.	$F_H = 2.75\ d$
Casing flush with boundary between impermeable and permeable strata. Inside diameter of casing is d cms.	$F_H = 2.0\ d$
Borehole extended a distance L cm beyond end of casing. Borehole diameter D in cms.	$F_H = \frac{2\pi L}{Log_e(2L/D)}$ for $L > 4D$.
Borehole extended a distance L beyond the end of the casing in a stratified soil or rock with different horizontal and vertical permeability. Borehole diameter is D.	$F_H = \frac{2\pi L}{Log_e(2mL/D)}$ where $m = (k_h/k_v)^{0.5}$ for $L > 4D$.
Borehole extended a distance L beyond the end of the casing which is flush with an impermeable boundary. Borehole diameter is D.	$F_H = \frac{2\pi L}{Log_e(4L/D)}$ for $L > 4D$.

Figure 2.12: Details of shape factor calculation for falling and constant head test, after Hoek and Bray (1981)

- maintaining a constant head of water in a borehole (using a constant inflow or extraction rate) over time, or
- adding or extracting a known quantity of water from the borehole, and monitoring the water level recovery in the borehole.

Assumption of the borehole geometry and the geological conditions of the test section enables conductivity to be calculated, as explained below. Rock mass conductivity (K_{mass}) is calculated from 'falling head' tests using either of the following equations:

$$K_{mass} = \frac{A}{F_H\left(t_2 - t_1\right)} \log_e \frac{h_1}{h_2} \qquad [2.57]$$

or from 'constant head' tests, using:

$$K_{mass} = \frac{Q}{F_H h_c} \qquad [2.58]$$

where, A is the borehole cross sectional area, F_H is Hvorslev's dimensionless shape factor for different test section conditions Fig. 2.12, h is the head at time t from the standing water level in the borehole, Q is the constant flow rate. The term h_c is the head maintained during the constant head test.

2.3.3 Packer Tests

Packer tests (otherwise called pressure or Lugeon tests) consist of pumping water into the test sections in stages at constant pressures whilst recording flow conditions until the flow rate becomes constant. The test section is isolated from the rest of the borehole by inflatable packers. The test results are described in Lugeon units (L), where a Lugeon is defined as the water loss of 1 l/min per 1m of test section at an effective pressure of 1 MPa. Moye (1967), Maini et al. (1972) and Houlsby (1971) have described the use and interpretation of the Packer test whilst Fell et al. (1992) provide a comprehensive discussion of the test, the related equipment and analysis.

Various relationships between the Lugeon value flow rate and an equivalent conductivity (K_e) have been suggested. Hoek and Bray (1981) suggested relationships based on the availability of an observation borehole because often only a single borehole, so the Hvorslev (1951) method for a constant head test using a shape factor applicable to a stratified rock mass provides an approximate solution:

$$K_e = \frac{QLog_e(2mL/D)}{2\pi Lh_c} \qquad [2.59]$$

where Q is the pumping rate needed to maintain a constant pressure over the test section, $m = (K_e/K_p)^{0.5}$, K_e is conductivity perpendicular to the borehole, K_p is conductivity in the plane of the borehole. The mathematical formulation assumes that $K_e > K_p$.

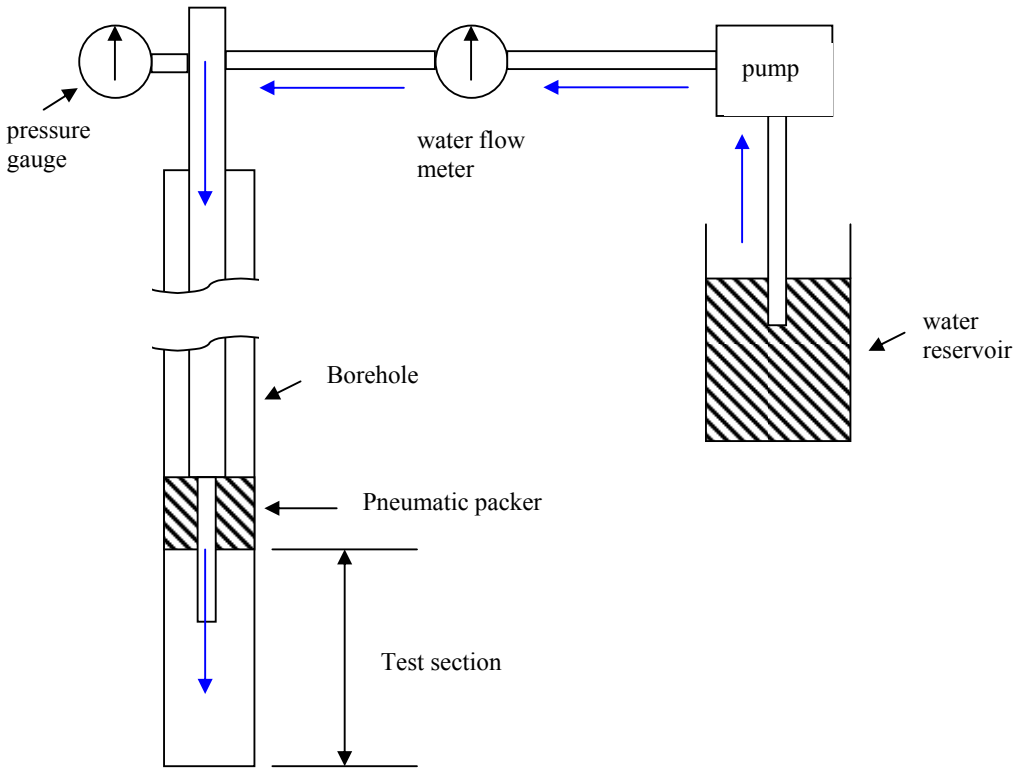

Figure 2.13: Schematic apparatus used for water pressure testing

2.3.3.1 Test equipment and procedure

A basic list of equipment needed to carry out water pressure tests is summarised by Fell et al. (1992) and includes:

- an inflating packer to seal off the borehole test section (either single or double packer combinations have been designed to overcome side leakage risks);
- air injection line and pump to inflate the packer to a pressure greater than test injection pressure;
- a pressure gauge to measure injection pressures for packer and test section;
- a flowmeter to measure water flow from the reservoir via the test section in to the rock mass.

A test assembly, similar to Fig. 2.13, is calibrated prior to testing to estimate friction losses at different pressures and flows. A range of test pressures should be selected to span the likely in-situ permeability without causing hydraulic fracturing. Fell et al. (1992) recommended an injection pressure of less than overburden pressure, assuming as a rule a unit weight of approx 22 kN/m^3. In low rock mass strength strata, lower injection pressures may be necessary. The actual test pressure is equal to the gauge pressure plus the water pressure in the line between the gauge and the static groundwater level.

To maximise accuracy, test records should detail:

- static groundwater level,
- period of borehole flushing to remove cuttings,
- depth and geological log of the test horizon,
- packer inflation pressure and check for side leakage, and

- sequence of test pressures (a, b, c, b, a) and recorded flow rates.

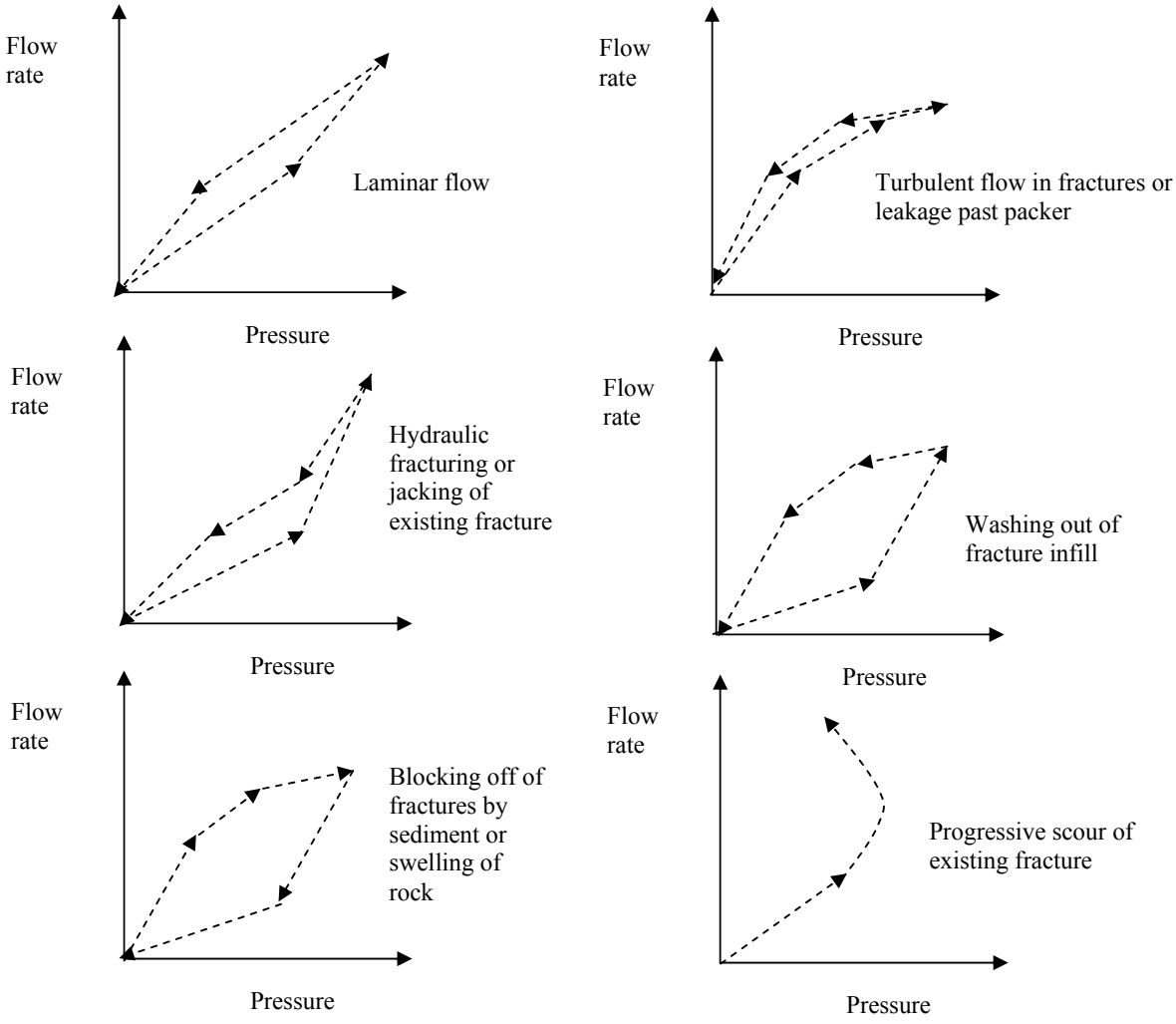

Figure 2.14: Typical test results from water pressure testing (after Fell et al., 1992).

2.3.3.2 Test results and single phase data analysis

Test result plots show the rock mass response to the fluid injection with a range of possible results presented in Fig. 2.14. The fracture and rock mass response is interpreted by comparing the change in conductivity with flow rate to infer behaviour such as laminar flow, erosion of infill or fracture plugging. Moye (1967), Houlsby (1972) and Fell et al. (1992) have comprehensively written on the test interpretation. The graph shows a range of flow rate versus pressure sequences that can be used to identify rock mass behaviour.

Moye (1967) and Hoek & Bray (1981) have published relationships between the Lugeon value and equivalent rock mass conductivity (K_e) by idealising radial laminar flow conditions in a homogenous isotropic rock mass (Table 2.4). The Hoek & Bray (1981) approach allows for anisotropic conductivity parallel and normal to the borehole (denoted K_e and K_p respectively).

Table 2.4: Analytical techniques for calculating hydraulic conductivity from in-situ testing.

Moye (1967):	**Hoek & Bray (1981):**
$K_e = \frac{Q\left(\frac{1+\ln(L/D)}{2\pi}\right)}{Lh}$	$K_e = \frac{Q\ln(2mL/D)}{2\pi Lh}$ where $m = (K_e/K_p)^{0.5}$

Fell et al. (1992) note that as a general rule of thumb, for $K_e/K_p \approx 10$ over 5m test sections for NMLC holes (75mm diameter) 1 Lugeon is approximately equal to a K_e of 1.6×10^{-7} m/s.

2.4 Two-phase Fracture Flow

2.4.1 Theoretical background

The general theory of isothermal, two-phase flow is well-established (Wallis, 1969; Hewitt & Naylor, 1976; Govier & Aziz, 1972), although to a lesser degree in geomechanics. The complexity of phase interaction compared to single-phase conditions, challenges a clear analytical description of behaviour. Several flow behaviour classifications exist in analogue fractures or pipes to improve overall understanding of flow (e.g. Mishimi & Hibiki, 1996; Fourar et al., 1993). This approach is subjective and can be affected by the particular experimental apparatus, e.g. the fracture aperture and phase injector design. However, the classifications allow identification of general characteristics and the tests provide a useful qualitative means to describe the problem.

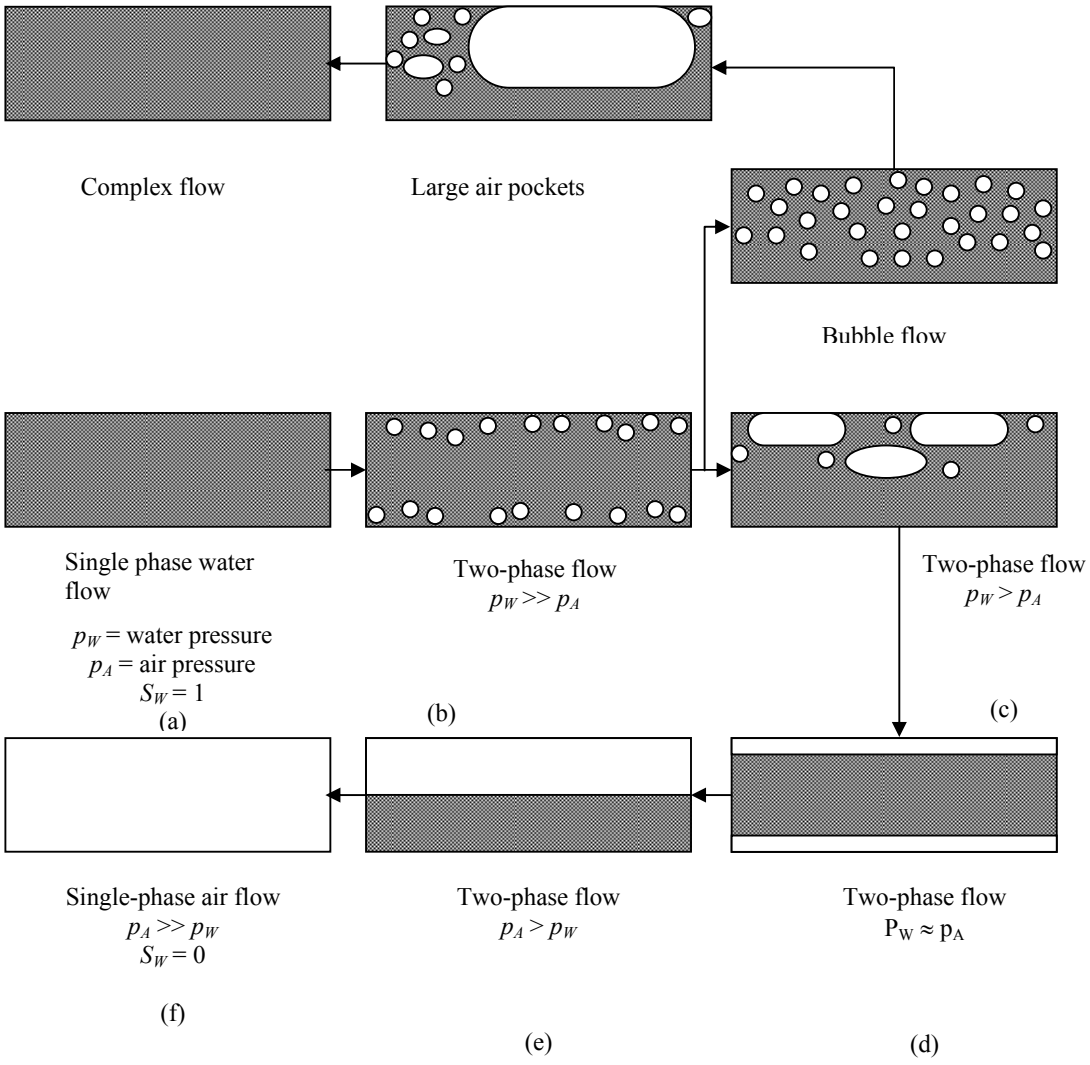

Figure 2.15: Simple joint elements showing potential two-phase flow patterns and water phase saturation S_W that could be encountered in the geological environment.

Fluid behaviour is influenced by phase velocity and mixture composition, giving rise to a particular flow pattern. Injecting air at increasing rates can lead to the simple two-phase flow patterns similar to Fig. 2.15 developing. Water flows exhibit a transition from saturated ($S_W = 1$) to bubble flows as air phase injection pressure increases. Small, rounded and finger-shaped bubbles develop as S_W decreases. The pattern evolves to comprise larger cap-shaped geometries with smaller rounded bubbles entrained in the intervening water slug. Increasingly complex bubble patterns can develop into a froth

pattern containing relatively small volumes of intervening water phase. As the air pressure drops, continuous air flow paths can develop in an idealised fracture to create a stratified pattern where the denser fluid occupies the lower part. Alternatively, denser water films can remain in contact with the fracture surfaces, whilst a core of air flows through the fracture, provided air velocity and surface tension can maintain the denser phase in contact with the upper surface.

2.4.1.1 Two-phase Hydraulics

Two-phase hydraulics is governed by the conservation of mass, momentum and energy. Physical processes such as phase change, capillary effects and the phase interface are significant in certain circumstances. The most simplistic two-phase flow model is the homogenous fluid concept, which represents both phases as a single equivalent fluid with fluid properties related to the relative proportions of each phase. This approach approximates the solution to the flow problem, however, a more accurate result can be achieved if the phases are considered separately.

Under 1-D laminar flow, a modified Darcy's Law is applicable to flow calculation, where matrix (or primary) permeability is neglected.

$$Q_i = \frac{K_{ri} e^3 w}{12 \mu_i} \left(\frac{dp_i}{dx} \right) \qquad [2.60]$$

The variables in Eq. [2.60] define flow rate Q_i in terms of K_{ri} and μ_i, relative permeability and kinematic viscosity for a fracture aperture e and width w acted on by a phase pressure gradient dp_i/dx. The subscript i attributes the variable to either the air A or water W phase.

The phase pressure drop can be calculated from the conservation of momentum. The general equation for the total phase pressure drop of each phase is a combination of the three respective right hand terms in [2.61]: losses due to friction (f) with the fracture

walls; acceleration (a) impacts from localised unsteady flow; and changes in elevation (g) across the area of interest.

$$\frac{dp_i}{dx} = -\tau_w \frac{P}{A} - \frac{M_i}{A}\frac{dv_i}{dx} - \rho_i g \sin\beta = \left(\frac{dp_i}{dx}\right)_f + \left(\frac{dp_i}{dx}\right)_a + \left(\frac{dp_i}{dx}\right)_g \quad [2.61]$$

The frictional losses can be re-written as a product of shear stress (τ_w) at the fracture wall perimeter (P) with cross sectional area (A); acceleration losses can be replaced in terms of phase mass (M_i) per cross sectional area and phase velocity gradient (dv_i/dx); and the elevation component of momentum losses as the product of phase density (ρ_i) and fracture orientation (β) from the horizontal.

Flow behaviour and phase interaction can be analysed individually in terms of conservation of momentum. Thus, total mixture pressure drop can be written in one equation, with the volumetric fraction of the air phase is denoted by ζ and the fracture perimeter in contact with air P_{air}:

$$\frac{dp}{dx} = -\left(\tau_{wW}(P - P_A) + \tau_{WA}P_A\right) - \frac{1}{A}\frac{d\left(M_W U_W - M_A U_A\right)}{dx} - \left(\rho_W(1-\zeta) + \rho_A\zeta\right)g\sin\beta \quad [2.62]$$

Greater accuracy is achieved in the general equation [2.65] if phase change and interfacial shear force F_{int} are considered. The phase change process can be represented as a change in mass per unit flow length related to the change in momentum i.e.,

$$\left(U_A - U_W\right)\frac{M}{A}\frac{dx}{dz} \quad [2.63]$$

The drop in momentum due to phase change is proportional to the air and water phases in general terms η and $1\text{-}\eta$. Further manipulation of Eq. [2.62] forms a separate expression for the effects of relative phase motion, and assists assessment of 'slip' or 'hold up':

$$\rho_W U_W \frac{dU_W}{dz} - \rho_A U_A \frac{dU_A}{dz} = \left(\rho_A - \rho_W\right)g\sin\beta - \frac{\tau_{wW}\left(P - P_A\right)}{1-\zeta} + \frac{\tau_{wA}P_A}{\zeta} + \frac{\tau_{\text{int}}P_{\text{int}}}{\zeta(1-\zeta)}$$

$$-\frac{M}{A}\frac{dx}{dz}\left(\frac{1-\eta}{1-\zeta}-\frac{\eta}{\zeta}\right)\left(U_A-U_W\right) \qquad [2.64]$$

2.4.1.2 Physical processes affecting fracture behaviour

A number of physical processes affect facture flow, including capillarity, phase compression and solubility, and fracture dilation in response to changes in the effective stress environment.

2.4.1.2.1 Capillary impacts

Water percolates between fracture surfaces, driven in fingers by gravity, surface tension and capillary pressures, where capillary flow dominates. This mechanism is different to the 'free' flow concept in the proposed simplified two-phase flow models. Capillarity is increasingly significant for smaller aperture fractures, given the established inverse relationship shown in Eq. [2.65]. Capillary pressure (p_C) results in a curved "interface" related to surface tension (T_s) and the meniscus curvature at the air-water interface, following Pruess & Tsang (1990).

$$p_C=\left(T_s\cos\theta\right)\left(\frac{1}{r_1}+\frac{1}{r_2}\right) \qquad [2.65]$$

Assuming conservatively, that the water is pure and temperature constant, surface tension remains unchanged (72.75mN/m at 20°C, Fredlund & Rahardjo, 1993). However, it is quite likely that the water will contain impurities, which will significantly reduce T_s. The terms r_1 and r_2 are the radii of curvature of the meniscus, measured perpendicular and parallel to the fracture plane, respectively. Assuming the contact angle θ to be zero, $r_1 = e/2$ and r_2 is very large, the above equation simplifies further:

$$p_C=\left(2T_s\right)/e \qquad [2.66]$$

Equation [2.66] shows that capillary pressure is increasingly important for narrow fractures, especially where phase pressures drops are relatively small. The capillary

pressure defines the entry pressure above which imbibition of a phase can occur. If three fluid phases are present, the lower T_s value determines the displacement preference in an situation where phase pressure gradients are increasing. Different percolation scenarios can be compared by calculating the capillary number N_{cap} (Keller, 2000) defined by the dynamic viscosity μ and unit weight γ of the permeating fluid, the flow rate Q and fracture cross sectional area A.

$$N_{cap} = \frac{\mu Q}{A\gamma \cos\theta} \qquad [2.67]$$

This concept was extended by Hardisty et al. (2003) for the flow of light non-aqueous petroleum liquid (LNAPL) in saturated and unsaturated rock fractures. Where a fluid is percolating in an inclined fracture (β), access to the adjacent fracture element can occur if the weight of the saturated fluid column in the fracture (γh) exceeds threshold capillary pressure of that fracture element, hence,

$$\gamma h \sin\beta = \left(2T_s\right)/e \qquad [2.68]$$

When capillarity is significant, it is unlikely that stratified flow could occur; in such a case, flow would be by gradual percolation and pore invasion depending upon the interaction of gravitational and capillary forces. Application of the proposed stratified theory to the numerical analysis of single- and two-phase flow through fractures is described in Chapter 6 and 7. The proposed application concerns steady state and active flow for both phases rather than passive imbibition of the wetting phase into a fracture containing the non-wetting phase or a combination of the both.

2.4.1.2.2 Phase compressibility impact on two-phase flow

Fluid phase compressibility should be included in any two-phase model when approximating the physical reaction. This phenomenon is most notable for the air phase because of the lower viscosity, due to changes in phase pressure or in-situ stress.

Indraratna & Ranjith (2001) found that for an idealised fracture, the total normal deformation (Δ_T) of the aperture can be related to the compressibility of air (ξ_{AC}) and water (ξ_{WC}), the solubility of air in water (ξ_{AD}) and the mechanical normal deformation (δ_n) due to changes in stress, whereby:

$$\Delta_T = \xi_{AC} + \xi_{AD} + \delta_n - \xi_{WC} \quad [2.69]$$

The volumetric compression per unit fracture area ξ_{ic} of the i phase is related to the change in volume (ΔV) in the x-y (fracture) plane. The compression of each phase can be calculated using the isothermal compressibility of air and water (C_A and C_W), and the phase volume V_i,

$$C_i = \frac{1}{V_i}\frac{dV_i}{dp_i} \quad [2.70]$$

thus,

$$\xi_{ic} = \frac{\Delta V}{y.x} = \frac{C_i V_i dp_i}{y.x} \quad [2.71]$$

For a fracture containing a fluid with bubbles of gas, phase pressures rapidly equilibrate as the phase volume (V_i) and saturation (S_i) change in response to the pressure variation. Where the difference in elevation is small, and 'slip' or 'hold up' is assumed negligible, one can assume $dp_A = dp_W = dp$.

Indraratna & Ranjith (2001) showed the solubility of air in water (V_{Dt}) can be described by the Ideal Gas law and Henry's law at certain pressure and temperature conditions. Thus, for a joint of length x and width y, the change of equivalent air phase height ξ_{AD} due to dissolved air may be written as follows:

$$\xi_{AD} = \frac{V_{Dt}}{x \cdot y} \quad [2.72]$$

Air is known to dissolve in water to occupy a maximum of 2% volume. The coefficient of solubility and the volumetric coefficient of compressibility for different gases could be applied if methane (CH_4) was considered instead of air.

2.4.1.2.3 Fracture-normal mechanical deformation

The mechanical change in fracture aperture can be related to normal fracture stiffness (K_n) and change in applied normal stress ($\Delta\sigma_n$). This should be written in terms of effective stress since the mechanical reaction of a water filled fracture will be mitigated by the fluid mixture with a pore pressure p, particularly where $p \approx \sigma_n$:

$$\delta_n = \frac{\Delta\sigma_n'}{K_n'} = \frac{\Delta\sigma_n - p}{K_n'} = \frac{\left(\Delta\sigma_1 \cos^2\beta - \Delta\sigma_3 \sin^2\beta\right) - p}{K_n'} \qquad [2.73]$$

A change in normal stiffness can be assessed from clip gauge deflection data in response to changes in confining stress and pore fluid pressure.

2.4.2 Two-phase flow in geological media

In spite of the foregoing assumptions, experience tells us that flow occurs between surfaces that are neither smooth nor parallel. To analyse fluid flow in fractured rock, the spatial distribution of interconnecting fractures and the spatial variability of fracture apertures must be accommodated. Where apertures are assumed to be relatively uniform and the fracture network idealised to a simple geometry (e.g. Snow, 1968), analysis can be relatively straightforward for single-phase fluids. The realities of the geological environment make such simplifications both necessary and limited in their application. For single-phase flow problems, it is often difficult to obtain sufficient field information on fracture network geometry and connectivity without access to a considerable area of rock exposure.

For two-phase flow problems, data collection is even more difficult, with most investigations restricted to collecting total flows per unit area from faces in underground

excavations (Kissell & Edwards, 1975), rather than isolated detailed records of flows from a particular fracture. Sometimes borehole investigations using cross-hole techniques and relatively small borehole separation can succeed in single-phase testing (Hsieh et al., 1983; Di Biagio, 1973), where there is good intersection with the fracture network. This thesis is confined to the fracture level and does not consider fracture network flow in detail.

2.4.2.1 Fracture Roughness

In geomechanics, roughness is referenced to standard 100mm long profiles (ISRM, 1978) by the Joint Roughness Coefficient (*JRC*). In this study, rock samples were selected to be 100mm long so that the 'scale effect' did not complicate the interpretation. Longer wavelength roughness (relative to fracture length) impacts upon water flow (Barton et al., 1985). Fracture roughness has a smaller impact on air flow (Di Biagio, 1973).

Small-scale roughness relates to capillarity and surface tension effects, which is significant when applying a two-phase conceptual flow model, because the microscopic scale roughness for most medium- and fine-grained rocks traps water within the intergranular pores exposed at the fracture surface. This means the fracture surface remains wetted except under high temperature or very high velocity gas flows at low S_W. Feasibly, stratified flow could only feasibly occur over relatively short fracture lengths in sub-horizontal fractures where the rock matrix is coarse-grained with low porosity, e.g. for coarser grained, low porosity igneous or metamorphic rocks such as granites, gabbros or gneiss. This observation is a phenomenon encountered in wider engineering situations (Wallis, 1969) and not confined to geomechanics. This realisation means that actual stratified flow as described by the simplified stratified model cannot occur very widely in the geotechnical environment.

2.4.3 Numerical simulations of fracture flow

2.4.3.1 Percolation flow in fine fractures

As summarised by Long et al. (1996), numerical simulation has been an effective method for investigating two-phase flow of immiscible liquids, and phase interference, and trapping, particularly for flow in relatively narrow fractures affected by capillary pressure. Fracture discretisation and the 'phase accessibility' concept (Pyrak-Nolte et al., 1990) enable study of the potential for phase occupancy of any fracture element under the imposed pressure conditions. For specified fracture aperture geometry, the resident phase displacement occurs where the imbibing phase pressure exceeds the capillary pressure associated with the local fracture aperture and the resident pore fluid.

Two-phase flow analysis of a 2-D discretised fracture can be performed by assuming the aperture distribution, negligible curvature of the interface in the plane of the fracture and phase accessibility is not affected phase distribution. These simplifications allow consideration of rough walled fractures with variable aperture. Pyrak-Nolte et al. (1990) successfully applied this approach to horizontal analytical models with verification by electrical resistivity analogue testing.

Glass & Norton (1992) studied the development of wetting structure in a rough walled fracture and recorded numerical and visual data as one surface of a transparent fracture replica was slowly flooded with water through a porous matrix. The aperture distribution for these tests is not reported, although their preliminary conclusions identify the development of trapped phase regions within the fracture plane and a hysteresis in the filling – draining occupancy. Their reported test fracture attained a maximum wetting phase saturation of just 60%. This highlights the role of roughness in disrupting the idealised parallel flow mechanism between smooth plates.

Norton et al. (1993a) reported on studies of the formation of gravity driven fingers at particular fracture orientations and the interplay of gravity and capillary forces

for an initially dry fracture. The purpose was to examine infiltration mechanisms in a transparent rough walled analogue fracture comprising two sheets of textured glass 30cm by 15cm. They make detailed observations of the development and saturation characteristics of dendritic flow structures. These studies mainly consider transient behaviour at water flow rates < 14 ml/min applied using a syringe pump.

Glass (1993) considered the curvature of the in-plane air-water interface on the phase accessibility law by calculating the form of gravity driven fingers of water flowing in a rough fracture replica. Glass (1993) demonstrated the proposed refinement resulted in greater computational accuracy of the saturation front location. Despite this improved agreement, the modified accessibility law did fully not replicate experimental observations. It appears that further improvement in theoretical understanding is necessary, and to better account for fracture roughness. The test fracture had a modal aperture of 0.215mm with approximately 2% of the surface area associated with an aperture of 0.02mm. Fracture apertures tested in this thesis have similar statistics and test behaviour was well predicted by the proposed macroscopic flow models.

Glass (1993) was also able to estimate the phase relative permeability by using percolation theory at particular capillary pressures indicating that two-phase flow was inhibited by phase interference. The work illustrated that the correlation length relationship with aperture distribution will have a significant effect on the ability of the fracture to transmit both phases. This work concentrated upon horizontal fractures and neglected gravity in the analysis.

Additional work by Norton et al. (1993b) considered phase distribution and development in a pre-wetted rough-walled analogue fracture. The fracture was saturated before the starting the test and allowed to drain under both gravity and capillary action. Drainage produced moisture field of isolated ‘islands’ of water

indicating lower levels of residual saturation with increased inclination (from the horizontal). A uniform wetting front was injected at the upper surface of the fracture and the flow patterns were observed to form unstable gravity driven fingers of water that would join and bifurcate as flow connection adjacent pockets of fluid. The residual saturation and distribution of the moisture field were found to have a significant effect on the development of finger flow. These studies consider a different hydromechanical aspect to this thesis, and are particularly applicable to the environment of narrow fractures with relatively low hydraulic or pressure gradients.

Norton & Glass (1994) considered the imfluence of saturation on wetting phase relative permeability. Flow visualisation testing showed the complex interaction of moisture distribution (channelling) and saturation for low Q_W in analogue rough walled fractures. Wetting phase saturation and average wetting phase aperture were found to be inadequate to model K_{rw} for $S_W < 60\%$). They also concluded that S_W was a good indicator of K_{rw} for $S_W > 90\%$. However, the range of applicability may well be larger, since there were no published test results for S_W in the range 60 to 90%. The work published by Glass and his co-workers in the period 1992 to 1994 concentrates on low volume flows of water through a fracture under a variety of initial moisture distributions. The work conceptualises flow through a fracture exposed in a weathered sub-crop, at the interface between rock and overlying soil strata. A periodic infiltration source is used to replicate rainfall effects. Their research activities are different to those in the work presented in this manuscript, although their work is applicable in particular where fracture injection pressures are low. Their work does not reference fracture roughness to an identifiable standard that allows application to different locations. The proposed two-phase flow models in this thesis suggest that K_{rw} is an adequate predictor for S_W lower than 60%, dependent upon the fracture roughness.

Pruess et al. (1990) assume linear laminar flow conditions to model the phase interference observed in their testing. The S_W conditions under which both phases were mobile were restricted to between about 5% and 30%, which they indicate to be both relatively large and understandable in terms of the 2-D nature of their approach. They explain that a 3 - D approach provides an extra dimension for flow to deviate around closed local apertures, enabling individual pores to have an affinity for one particular phase. Their saturation values are 'average' or macroscopic values for the test, rather than representative of saturation of that particular pore. Their approach is another example of a simplified technique and does not account for the potential of phase change. In a development at a larger analytical scale, Rasmussen (1991) considered a discrete fracture network and the air-water interface in a solution using the Boundary Integral Method (BIM). Rasmussen (1991) used an idealised Darcy's Law with smooth fractures and built upon concepts previously developed by Long (1986). There is no case history observations against which the results can be compared.

Keller et al., (2000) reports on tests and modelling of pore-scale two-phase flow at low flow rates and phase pressures. Analytical saturation-relative permeability-capillary pressure functions were constructed for the fractures under test, using aperture distribution results from CT scanning (Keller, 1997) and phase injection experiments. The results are applicable to microscopic flow behaviour of the particular fracture during multiphase injection. The Keller technique is related to fine aperture fractures and lies outside the scope of this thesis. Macroscopic flow behaviour represents an alternative analysis of two-phase flow that is the subject of subsequent two-phase flow discussion.

2.4.3.2 Free flow in large aperture fractures

The preceding debate on capillary effects concluded a diminishing impact on flow behaviour with increasing fracture aperture. Fourar et al. (1993) contemplated fracture flow as a limiting case of porous medium, pipe flow, or homogenous flow analysis with the equation:

$$U_{iS} = -\frac{kK_{ri}}{\mu_i}\frac{dp_i}{dx} \qquad [2.74]$$

where, i indicates either the liquid or gas phase, U_{iS} is the superficial velocity (flow rate per unit cross sectional area of the sample), p is the pressure, μ_i is the viscosity, k is the intrinsic permeability (single phase) and K_{ri} is the relative permeability. Phase interference is denoted by (liquid and gas) phase relative permeability assuming the Romm (1966) postulation that $K_{rL}+K_{rG} = 1$. This assumption limits the analysis since work performed as part of this research project confirms that $K_{rL}+K_{rG} \neq 1$.

Fourar et al. (1993) observed dynamic two-phase flow structures for smooth and slightly rough planar fractures between fine-grained clay bricks. Their study considered flow through artificial, rather than the larger grained natural fractures used in this study. For low gas velocities, dispersed small gas bubbles flowed in the liquid. The bubble size and complexity was proportional to gas velocity and at low S_W gas occupied the majority of the fracture with a liquid film observed along the walls. The liquid phase dispersed within the as the liquid velocity decreases. They observed only one phase to flow continuously and that no trapping occurred (with their analogue testing). Further investigation of relative permeability, phase occupancy and fracture orientation has been performed as part of this project and is presented in Chapter 5.

Fourar et al. (1993, 1995) present a semi-empirical analysis of pressure gradient data for rough fractures and acknowledge the deviation from linear, single- and two-phase flow conditions for rough walled fractures. The test equipment was not

sufficiently sensitive to measure air-pressure gradient but it was assumed that the phase-pressure gradients were equal. The non-linearity occurs from inertial forces proportional to the mixture superficial velocity and the mixture density (ρ_H) and can be written using Forcheimers Law:

$$-\frac{dp}{dx} = \frac{12\mu_H}{h_F^{\,3}} Q + B_F \frac{\rho_H}{h_F^{\,3}} Q^2 \qquad [2.75]$$

where, Q is the volumetric flow rate per unit width, B_F is a dimensionless function of the roughness. Values of h_F and B_F are calculated by fitting the parabolic curve produced from the lab data and from a *dp/dx* versus Q plot. The calculated aperture generally agreed with the experimental aperture used for both smooth and rough fractures and they concluded that relative permeability was related to saturation and unspecified additional factors. Their observed impact of fracture roughness contradicts the views of some researchers on single-phase flow (e.g. Louis, 1969; Witherspoon et al., 1981) as well as the results of work performed during this study. Their testing considers relatively small degrees of roughness, or maximum fracture amplitude, which restricts their conclusions to smooth or relatively smooth fractures, and not necessarily applicable to fractures of greater roughness.

Fourar et al. (2000) applied a petroleum engineering approach in a model for turbulent flow using a development of Forcheimer's equation with the passability parameter (η_F):

$$-\frac{dp}{dx} = \frac{\mu_i}{k}\left(f_F U_{iS}\right) + \frac{\rho_i}{\eta_F}\left(f_F U_{iS}\right)^2 \qquad [2.76]$$

where, f_i is a function that depends upon phase saturation and the other parameters are already defined. Further analysis related f_i to phase saturation, relative permeability and the Lockhart-Martinelli relationship. This development appears to allow accurate calculation of pressure gradient or relative permeability and reveals the relationship

between two-phase Reynolds number and relative permeability to within 9% of the measured values in the environment where inertial flow forces are dominant. This model appears to work well within the constraints of their single fracture model and the range of testing. The wider application to naturally occurring fractures of different orientation is problematic since the Lockhart-Martinelli relationship was developed for horizontal pipe flow (although Fourar et al. (1993, 1995) illustrated the applicability to relatively smooth fractures i.e. wide small apertures channels). The correlation also requires single-phase and two-phase flow and pressure-drop data, which may make the correlation less useful in the field, rather than laboratory, environment.

Kostakis & Harrison (1999) presented a novel constitutive model representing the isothermal counter-current flow of a gas bubble in flowing water. The model considered free flow with fracture apertures between 80μm to 300μm and neglected capillary effects. Their formulation considered fractures in rocks with negligible matrix permeability where water flowed under a strong downward hydraulic gradient for Reynolds numbers between 1 and 100. Kostakis & Harrison (1999) devised a simplified equation to represent the conservation of momentum for the gas phase in terms of the hydraulic gradient, the drag force acting on the bubble and the decrease in water momentum due to collision with the bubble (by considering the virtual mass term), the wall and buoyancy forces,

$$\frac{\partial\left(\rho_G U_x U_y\right)}{\partial y} = \frac{\partial p}{\partial y} + \frac{\partial \tau}{\partial x} + F_I + F_B \qquad [2.77]$$

where, F_I and F_B represent the interface mass transfer terms: F_I is a combination of the drag force the virtual mass force and the wall force; and F_B accounts for the weight of the water and the buoyancy of the gas. This solution tracks the rise of a single bubble through a vertical rough fracture containing counter-flowing liquid, and represents a microscopic flow solution to a two-phase flow problem.

2.4.4 Established two-phase fluid models

2.4.4.1 Introduction

Two-phase analytical models for steady state flow conditions were first developed for pipe hydraulics problems. The principal 1-D models were described comprehensively by Wallis (1969). This review describes the differences and main assumptions behind the three fundamental flow models that can be used for two-phase flow analysis applied to rock fractures.

1-D models are appropriate where flow is principally in one direction and relatively laminar. These models are suited to environments where fracture apertures are small and the out-of-plane dimension of a fracture is finite. However, where a rock mass comprises numerous rock 'blocks' bounded by fractures, then a 2 or 3-D approach could be necessary. The drawback with complex approaches is the difficulty in the definition of hydraulic conductivity for a fractured rock mass (Barton, 1973; Jing et al., 1996) for each of the phases and the pore pressure conditions. The pore pressure must be defined for each phase as functions of conductivity, relative permeability and saturation. The discussion within this context focuses on 1-D two-phase flow scenarios because of the similarity with the boundary conditions of the triaxial testing apparatus.

Multiphase flow analysis considers the simultaneous flow of several different phases, where a phase represents the physical state of a fluid, e.g. gas or liquid. A component defines a physical compound, e.g. water. Thus, steam and water are different phases but just one component. For the purposes of this research there is no distinction drawn between the consideration of two phases (eg. steam and water) or two components (e.g. air and water). The applicable analytical models for this particular problem are:

- Homogenous flow and,
- Separated flow.

The discussion includes special developments of the separated flow approach: the idealised stratified UoW model (Indraratna & Ranjith, 2001); and the semi-empirical Lockhart-Martinelli pipe hydraulics approach that has been to rock fractures by Fourar et al. (1993, 1995).

2.4.4.2 Homogenous flow model

This is a relatively simple multiphase technique using average values for the fluid mixture properties and applying single-phase mechanics. The velocity, viscosity and density are defined for a single equivalent phase based upon the weighted averages of the individual phase properties. It is assumed that equilibrium is reached during flow with interphase momentum- and mass-transfer occurring rapidly. Sudden changes in acceleration or pressure introduce errors that invalidate the assumptions. The continuity and conservation of momentum equations for steady state conditions in a smooth fracture element can be written (after Wallis 1969) as presented earlier in Eq. [2.1] and [2.2]. Chapter 7 explores the specific application of the homogenous fluid model to rough fracture flow.

2.4.4.3 The UoW Stratified flow model

In a recent development at the University of Wollongong (Indraratna & Ranjith, 2001), a constitutive model has been proposed as an adaptation of Darcy's law to two-phase (air-water) stratified flow). This work has been extended to include the concept of relative permeability in the work of Indraratna et al. (2003a). The original approach considers each of the phases separately as two stratified phases occurring as continuous layers of a particular phase height or "thickness". The model allows for the effect changes in flow rate and pressure over time. The phase height term includes terms for phase compressibility, solubility and the mechanical deformation of the joint aperture. The principle of conservation of momentum was applied to each of the phases and was

adapted to include phase change. This development of the original equations was modified (Indraratana et al., 2003b). This original model did not consider the capillary effects associated with fracture wall dry out. This limitation and the coupling of changes in fracture normal stress change to phase height for smooth and rough fractures are discussed in Chapters 4 and 6.

2.4.4.4 Lockhart-Martinelli Model

Lockhart & Martinelli (1949) developed a pressure drop correlation for two-phase flow for small diameter horizontal pipes that finds application in chemical engineering. Chisholm (1963) proposed modifications for pressures greater than 360kPa The original relationship has been widely applied in pipe hydraulics but also to flow in rock fractures by Fourar et al. (1993, 1995, 2000). This approach has not been applied to fractures tested in this project. The assumed limitation to horizontal orientations is considered complicates the use of the correlation for inclined fractures. In addition, the relationship requires single- and two-phase data for flow and pressure drop, which limits the application to laboratory consideration unless extensive field testing is available and a pre-defined fracture network geometry. The common complexity of geological environment comprising rock mass fractures of variable inclination would compromise the model due to unquantifiable elevation impacts. Nonetheless, the published application to geotechnical engineering warrants a brief discussion of the relationship.

The main assumption in the correlation is that the pressure drop for the liquid phase must equal the pressure drop for the gas phase, irrespective of the flow pattern, so long as capillary pressure is low, thereby:

$$\left(\frac{\Delta p}{L}\right)_{twophase} = 2 f_L \left(\frac{\rho_L U_L^2}{D_L g}\right) \qquad [2.78]$$

where, D_L is the equivalent hydraulic diameter of the section flowing with liquid, f is the friction factor of the liquid or gas phase (subscript L or G). Similarly for the gas phase:

$$\left(\frac{\Delta p}{L}\right)_T = 2 f_G \left(\frac{\rho_G U_G^2}{D_G g}\right) \quad [2.79]$$

This means that the model is not applicable to situations where inter-phase 'slip' is significant. The average phase velocities (U_i) can be related to the mass flow rate (M_i) by the following formulae:

$$U_L = \frac{M_L}{\alpha_{LM} \frac{\pi}{4} D_L^2 \rho_L}, \text{ and} \quad [2.80]$$

$$U_G = \frac{M_G}{\beta_{LM} \frac{\pi}{4} D_G^2 \rho_G} \quad [2.81]$$

where, the Lockhart-Martinelli parameters α_{LM} and β_{LM} account for the relative motion between the fluids and differences in flow geometry. The friction factors f_L and f_G are related to Reynolds numbers (Re) using the generalised Blasius form using the constants B_L and B_G:

$$f_L = \frac{B_L}{\mathrm{Re}_L^n} = \frac{B_L}{\left(\frac{4M_L}{\alpha_{LM} \pi D_L \mu_L}\right)^n} \quad [2.82]$$

$$f_G = \frac{B_G}{\mathrm{Re}_G^m} = \frac{B_G}{\left(\frac{4M_G}{\beta_{LM} \pi D_G \mu_G}\right)^m} \quad [2.83]$$

Assuming that B_L and n, and B_G and m are the same in both single and two-phase flows, then the ratios of two-phase to single-phase pressure drops for each phase can be written as:

$$\phi_L = \sqrt{\frac{\left(\Delta P / L\right)_T}{\left(\Delta P / L\right)_{SL}}} = \alpha_{LM}^{(n-2)/2} \left(\frac{D}{D_L}\right)^{(5-n)/2} \quad [2.84]$$

$$\phi_G = \sqrt{\frac{\left(\Delta P / L\right)_T}{\left(\Delta P / L\right)_{SG}}} = \beta_{LM}^{(m-2)/2}\left(\frac{D}{D_G}\right)^{(5-m)/2} \quad [2.85]$$

The original work classified the flow patterns of each phase as either turbulent or laminar, and related them to the two-phase Reynolds number as follows:

Laminar – laminar $\frac{DU_{SL}\rho_L}{\mu_L}$ and $\frac{DU_{SG}\rho_G}{\mu_G} < 1000;$

Laminar – turbulent $\frac{DU_{SL}\rho_L}{\mu_L} < 1000, \frac{DU_{SG}\rho_G}{\mu_G} > 1000;$

Turbulent – laminar $\frac{DU_{SL}\rho_L}{\mu_L} > 1000$ $\frac{DU_{SG}\rho_G}{\mu_G} < 1000;$

Turbulent – turbulent $\frac{DU_{SL}\rho_L}{\mu_L}$ and $\frac{DU_{SG}\rho_G}{\mu_G} > 1000.$

Lockhart & Martinelli (1949) proposed ϕ_L and ϕ_G as functions of X. The parameter X is an empirical ratio of the single phase liquid and gas pressure drops where:

$$X = \sqrt{\frac{(\Delta P/L)_{SL}}{(\Delta P/L)_{SG}}} = \frac{U_{SL}}{U_{SG}}\sqrt{\frac{\rho_L f_{SL}}{\rho_G f_{SG}}} \quad [2.86]$$

The pressure gradient is what would occur if the liquid were flowing alone at a velocity equal to the phase superficial velocity, and f are the single phase friction factor. Alternatively, X can be defined by a property-modified velocity ratio, whereby:

$$X = \left(\frac{U_{SL}}{U_{SG}}\right)^{7/8}\left(\frac{\rho_L}{\rho_G}\right)^{3/8}\left(\frac{\mu_L}{\mu_G}\right)^{1/8} \quad [2.87]$$

Fourar et al., (1995) proposed that for laminar flow:

$$\left(\frac{dP}{dx}\right)_G = \frac{-12\mu_G U_G}{h^2} \quad [2.88]$$

$$\left(\frac{dP}{dx}\right)_L = \frac{-12\mu_L U_L}{h^2} \quad [2.89]$$

Thus, the X can be given by:

$$X = \sqrt{\frac{\mu_L U_L}{\mu_G U_G}} \qquad [2.90]$$

Further modifications by Chisholm (1963) were suggested as part of a more rigorous derivation of the model. He recommended a relationship between the liquid-phase pressure drop multiplier and the Martinelli parameter for each of the basic flow configurations using the expression:

$$\phi_L^2 = 1 + \frac{C_{LM}}{X} + \frac{1}{X^2} \qquad [2.91]$$

where, C_{LM} is defined below depending upon the flow types:

Laminar – laminar	$C_{LM} = 5$
Laminar – turbulent	$C_{LM} = 10$
Turbulent – laminar	$C_{LM} = 12$
Turbulent – turbulent	$C_{LM} = 20$

For the laminar flow regime with negligible capillary pressure, Fourar et al. (1995) found that for all flow patterns except annular flow, the gas (ϕ_G) and liquid (ϕ_L) phase friction multipliers are linearly related to the Martinelli parameter X, hence:

$$\phi_G = 1 + X \qquad [2.92]$$

$$\phi_{L:} = \frac{1 + X}{X} \qquad [2.93]$$

They did not relate the friction multiplier to X for annular flow. They also derived the following expressions for the liquid volume fraction (or saturation) S_L, and related the relative permeability to the phase friction multiplier.

$$S_L = \left(\frac{X}{1 + X}\right)^2 \qquad [2.94]$$

$$\phi_G^2 = 1/K_{rG} \qquad [2.95]$$

$$\phi_L^2 = 1/K_{rL} \qquad [2.96]$$

Recent work by Lee et al. (2001) found that the simple approximation relating C_{LM} to the Martinelli parameter for flow in narrow rectangular ducts required a more comprehensive handling than previously suggested. The C_{LM} = 20 relationship that is usually recommended was found to be appropriate where both phases were turbulent. Alternate values for C_{LM} were proposed for other combinations of flow type as summarised in Table 2.5. It is interesting to note the relatively high laminar:turbulent transition Re value attributed for this work, which is high, even for relatively smooth surfaces. The Re values encountered in hydraulic testing of relatively smooth rock fractures tend to show the transition occurring at values < 100. Indeed, in some of the work reported in Chapter 6, the Re transition values were < 50. It would appear that the Lockhart-Martinelli correlation should be used cautiously when applied to rock fractures, and that the use should be limited to situations where inclination effects are insignificant.

Table 2-5: Values of constants and exponents for Martinelli *C* as proposed by Lee et al. (2001) (NB: laminar:turbulent boundary defined by Re = 2000).

Please see print copy for Table 2.5

Despite the frequent application of the Lockhart-Martinelli relationship to engineering analysis of two-phase flow, the issue of roughness and Reynolds number will impact on

the suitability of the approach and would need extensive testing on rough fractures o develop new correlations for C_{LM}. This fact, and the consideration of primarily horizontal flows will mean that direct application to rock fractures will be problematic, especially where large elevation differences are present.

2.4.5 Coupled two-phase analysis

Chapter 7 presents a specific discussion of computational and coupled two-phase flow analysis. However, a brief review of the status of the literature is warranted because of the importance of numerical analysis in coupled rock engineering. Computational techniques allow lengthy coupled two-phase flow calculations to be preformed increasing quickly. A refined constitutive relationship between stress and permeability would represent a considerable development in the analysis of hydromechanical behaviour. This goal is obstructed by the variability of fracture topography, stiffness and scale.

Nguyen (2001) considered the Japanese international engineering DECOVALEX II project and benchmarked available modelling packages each other to compare predictions and calibrate results to saturated and fractured rock conditions observed in the field. Nguyen reported that the outcomes from the different codes showed significant variation and implied the poor performance of finite element techniques since they had limited ability to identify fractures within the rock mass. Only one of the reviewed computer codes accommodated unsaturated flow and the detailed definition of fracture conductivity, mechanical apertures and connectivity were limited. Nguyen concluded there remained potential to develop more accurate computer models for coupled two-phase analysis of discontinuous rock masses.

Subsequent to the DECOVALEX II project, a recent version of FLAC (ITASCA, 2000) has been developed that can to model two-phase flows using a finite

difference technique. However, with only limited case history data available at this time, it is believed that this model is more appropriate to a porous rather than discontinuous media approach. At this stage, there are no coupled two-phase flow models known to the author, that competently model flow in discontinuous geological media. Computational codes such as UDEC (ITASCA, 2000) can be modified to consider variations to Newtonian fluid flow, and potential application of this code to two-phase flow problems is discussed in Chapter 7.

Recently Choi & Wold (2001) presented the theory behind their continuum-based computer code that can be used for analysis of gas outburst in underground coal mines. They have developed a 3-D model that is part of a coupled geomechanical flow model. The model is reported to combine large strain deformation, gas sorption, two-phase flow and stress dependent permeability using a ubiquitous and discrete jointed mesh. This computer code was developed by essentially combining the SIMED and FLOMEC codes. However, the ability of the code to model a fractured rock mass has not been it is not clearly explained, and the literature suggests that it is likely that some kind of tensorial analysis would be needed to develop the 3-D permeability model,

The Choi & Wold (2001) formulation for two-phase flow assumes Darcy's Law for both fluids, and uses relative permeability ($0 \leq k_{ri} \leq 1$) as well as saturation S_i in developing a set of coupled non-linear partial differential equations, given by:

$$\nabla\left(\frac{kK_{rG}}{\mu_G B_G}\left(\nabla p_G - \gamma_G \nabla d\right)\right) - Q_S = \frac{\partial}{\partial t}\left(\frac{nS_G}{B_G}\right) \qquad [2.97]$$

$$\nabla\left(\frac{kK_{rW}}{\mu_W B_W}\left(\nabla p_W - \gamma_W \nabla d\right)\right) - Q_S = \frac{\partial}{\partial t}\left(\frac{nS_W}{B_W}\right) \qquad [2.98]$$

where, k is the absolute permeability, γ is the density, S is the degree of saturation, B is the formation volume factor, t is the time, μ is the dynamic viscosity, d is the distance above a datum, n is the porosity, Q_S is a source or sink term.

The phase fluid pressures for gas (G) and water (W) are related by the equation for capillary pressure (p_C), where:

$$p_C = p_G - p_W \quad [2.99]$$

and the saturation relationship is given by:

$$S_W + S_G = 1 \quad [2.100]$$

The relationship between permeability and changing stress field applies an empirical relationship from work on well testing and hydraulic fracturing, given by:

$$k = k_0 e^{-\alpha \Delta J_1} \quad [2.101]$$

where:

$$\Delta J_1 = \left(\Delta \sigma'_1 + \Delta \sigma'_2 + \Delta \sigma'_3\right)/3 \quad [2.102]$$

and α is a site specific variable. As well as the representation of fracture permeability, the stress versus permeability relationship is perhaps the main limitation on their model, in terms of explaining the geomechanical processes involved in coupled two-phase flow, and requires careful calibration of the model to site conditions to ensure the model predictions. The stress:permeability relationship for water and gas could be investigated by a targeted field investigation programme using packer tests.

2.5 Summary

A review has been carried out of the leading literature on rock mass hydraulics, considering the flow of water and gas (in particular, air) through rock fractures. It is concluded from the review that engineering flow calculations rely upon significant simplifications because of the difficulty in solving the Navier-Stokes relationship when

applied to a natural variable environment like that of a fractured rock mass. One of the main outcomes is that engineering interpretations of fracture flow problems idealise fractures as smooth discontinuities within a rock matrix formed by parallel surfaces. The applicability of these assumptions appears valid (Zimmerman & Bodvarsson, 1986) where the aperture difference between adjacent fracture elements is small, but there is judgement involved in the assessment of the size, or scale, of the appropriate element size and the relative difference in aperture. Paradoxically, interpretation and simplification of fracture characteristics are necessary in the development of an analytical geotechnical model. Geological characteristics such as fracture roughness and aperture variability have been identified as key features in the correct interpretation of hydraulic and mechanical rock mass response under different pore pressure and in situ stress conditions. The numerical generation of the spatial extent and distribution of fractures within the rock matrix is subject to much statistical interpretation e.g. Long (1986) and ITASCA (2000). The predictions arising from applications of these methods depend as much on the fracture distribution and extent, as upon fracture flow behaviour. The real spatial distribution of rock mass fractures and the statistical techniques used to generate fractures in codes require careful inspection of the calculated results and may require several different models to be run when analysing a hydromechanical problem. This thesis focuses on the macroscopic flow behaviour of two-phase fluid in a single fracture. An improved understanding of the hydromechanics of two-phase flow will enable improved calculation accuracy and comprehension of hydromechanical behaviour. A detailed assessment of fracture roughness is needed to quantify the effect on flow. This aspect of the study is considered subsequently presented in Chapter 3 and a new application of Fourier series theory is used to develop an objective assessment of fracture roughness.

Chapter 3
Description & Implications
Of Rock Fracture Roughness

3.1 Introduction

Fracture description is of key importance in understanding the behaviour of all jointed rock masses. Representative fracture properties including orientation, persistence, spacing and aperture (ISRM, 1978) should be recorded in all engineering site investigations because of their influence on the mechanical and hydraulic performance of the rock mass. The spatial variation of fracture roughness is another quantity that should be noted to quantify the likely rock mass hydromechanical response, and is the focus of subsequent text.

This chapter presents a review of the significance of fracture roughness, and provides a background to the fracture roughness study that formed part of this research project. An innovative development of a mathematical technique applying a power-based, Fourier series analysis is shown to provide an objective and reproducible method of roughness assessment. The measurement of roughness and aperture is illustrated using different apparatus, culminating with a high-resolution laser scanner. Analysis of the roughness results with the Fourier technique provides mathematical data that are used to validate hydromechanical observations presented in Chapters 6 and 7.

Standard roughness profiles were proposed (Barton & Choubey, 1977) and adopted by the ISRM (1978) as part of their suggested rock mechanics guidelines. Each of the ten profiles represents a sequential increase in Joint Roughness Coefficient (*JRC*)

ranging from 0 to 20 in order of increasing roughness (Fig. 3.1). A digital technique to accurately record the topography of the selected profiles was used to gather data for analysis using a spreadsheet to fit a Fourier series. The resulting Fourier coefficients can then be used to reproduce profiles of an identifiable and controlled roughness. This approach, if it were incorporated into geomechanical computer applications, would improve control of the hydro-mechanical properties and performance of a modelled rock mass.

3.2 Engineering significance of roughness

3.2.1 ISRM definitions and profiles

To provide a standard upon which roughness could be universally assessed, the profiles proposed by (Barton & Choubey, 1977) were adopted in the ISRM Suggested Methods (ISRM, 1978). Each of the ten 100mm long profiles is attributed a range of Joint Roughness Coefficient (*JRC*) from 0 to 20, representing a sequential increase in roughness. Fracture persistence is not limited in reality, to an idealised reference length, and the relationship between the standard roughness profiles and real fracture profiles, or the 'scale effect', has been discussed, among others e.g. Lee & Farmer (1993). A detailed review of the scale effect is not part of this work, since the reported study tested specimens equal to the standard roughness length. However, Barton & Bandis (1980) proposed a relationship that accounted for the scale effect between the JRC standard profile (JRC_o) for a 100mm sample length and the equivalent roughness of a profile of length L.

$$JRC = JRC_o \left(\frac{L}{L_o} \right)^{-0.02 JRC_o} \qquad [3.1]$$

where, L is the sample profile length with subscript 'o' indicating the original (100mm) condition. This correction is necessary where large-scale roughness is considered for samples greater than 100mm length, because standard profiles would not capture the surface features. Any estimation made on the mechanical properties of the surface would tend to over-estimate the effect of roughness.

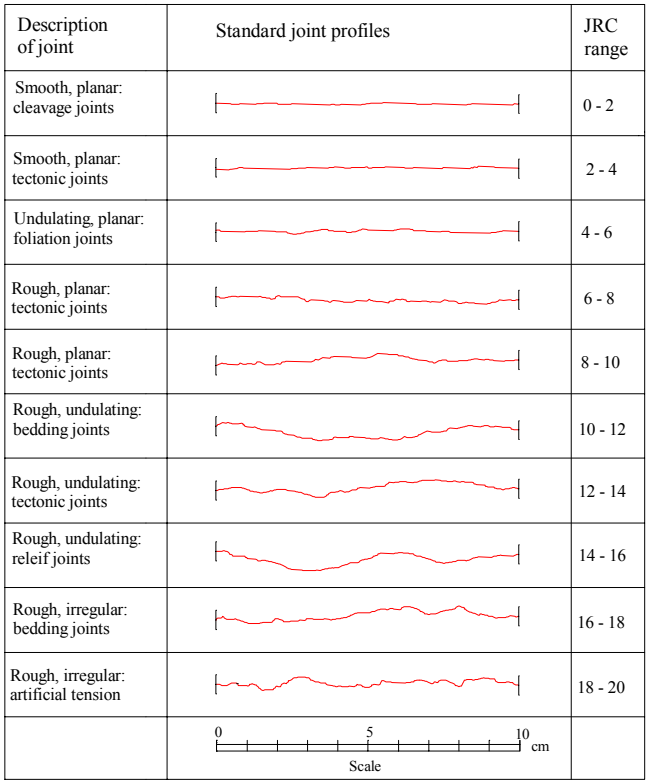

Figure 3.1: Standard Joint Roughness Coefficient profiles for the range $0 > JRC > 20$ after Barton & Choubey (1977), as modified in Indraratna & Ranjith (2001).

This can be illustrated by using Eq. [3.1] for a fictitious profile which has $JRC_0 = 10$. When the profile length is extended from 100mm to 500mm, the JRC value reduces to 7.25, showing the decreasing significance of the smaller scale roughness when the length of profile is increased.

3.2.2 Mechanical impact

The degree of fracture roughness has a significant impact on the mechanical and hydraulic properties of an in-situ and interlocked rock mass. The ISRM (1978) defines

roughness to incorporate components of a large-scale waviness and smaller scale unevenness. Waviness commonly results in interlocking of fracture surfaces and is associated with dilation during shear displacement. Waviness is also attributed to the observed increase in shear strength above the laboratory ultimate (or 'residual') friction angle (McMahon, 1985) where large-scale wavelength is defined as equal to at least 2% of the observed failure surface, hence:

$$\tau = \sigma_n \tan(\phi_{ult} + i) \qquad [3.2]$$

In this case, the angle i is the roughness angle, i.e. the angle between mean dip angle of the discontinuity and the flattest dipping section of the required wavelength, τ and σ_n are the shear and normal stresses (kPa) acting on the discontinuity and ϕ_{ult} is the ultimate friction angle determined in the laboratory using for example, the direct shear apparatus. Unevenness, being of smaller scale, tends to be abraded by the crushing of asperities during shearing, and in the field has less impact on the shear strength of the discontinuity. The role of scale is important when understanding the role of roughness on mechanical properties relating to field studies, because it is arguably the impact of unevenness that is measured in laboratory specimens, with waviness occurring in outcrop on a field scale. Where laboratory studies alone are being carried out, large-scale wavelengths would be greater than a few millimetres long. Given the method of analysis presented in this chapter, these results would have to be extended to include field data, if it was required to apply this approach to represent large-scale waviness. This could be easily added to a standard site investigation discontinuity mapping procedure. Studies on synthetic jointed blocks with regular saw tooth profiles suggest that i can be presented as the angle of the asperities (Barton et al., 1985). When considering natural surfaces, discontinuities are not necessarily mated so that the

roughness angle (i) should be related over the distance between asperity contacts, negating the impact of small-scale roughness on the mechanical fracture characteristics.

3.2.3 Hydraulic impact

The hydraulic impact of roughness on flow was discussed earlier in Chapter 2. Fracture flow is commonly analysed for steady state laminar flow conditions of an incompressible Newtonian fluid using a combination of Poiseuille's and Darcy's laws as described below in Eq. [3.3]:

$$Q = \frac{e_h^3 w}{12\mu}\left(\frac{dh}{dx}\right) \qquad [3.3]$$

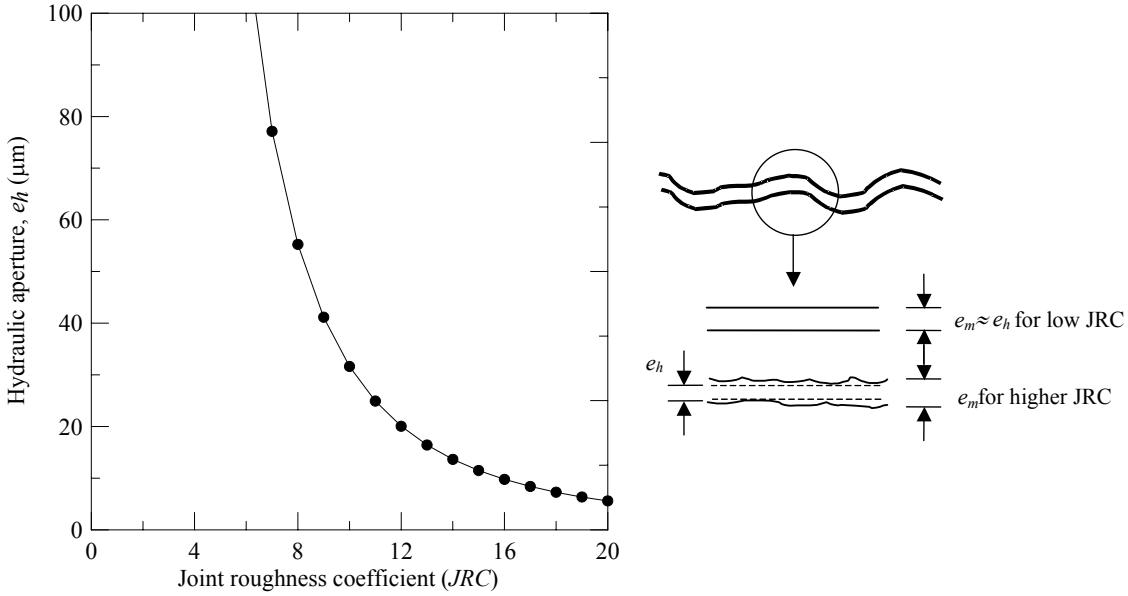

Figure 3.2: Relationship between hydraulic aperture (e_h) and joint roughness coefficient (JRC) for hypothetical fracture with mechanical aperture (e_m) of 100μm.

where, Q is flow rate, e_h is fracture hydraulic aperture, w is the fracture width, μ is the kinematic viscosity, and dh/dx is the hydraulic gradient. It is expected that increased roughness will have a major affect on flow since Eqn. 3.3 likens the fracture to a pair of smooth parallel plates. Fracture roughness promotes frictional losses and reduces the flow rate of groundwater seepage.

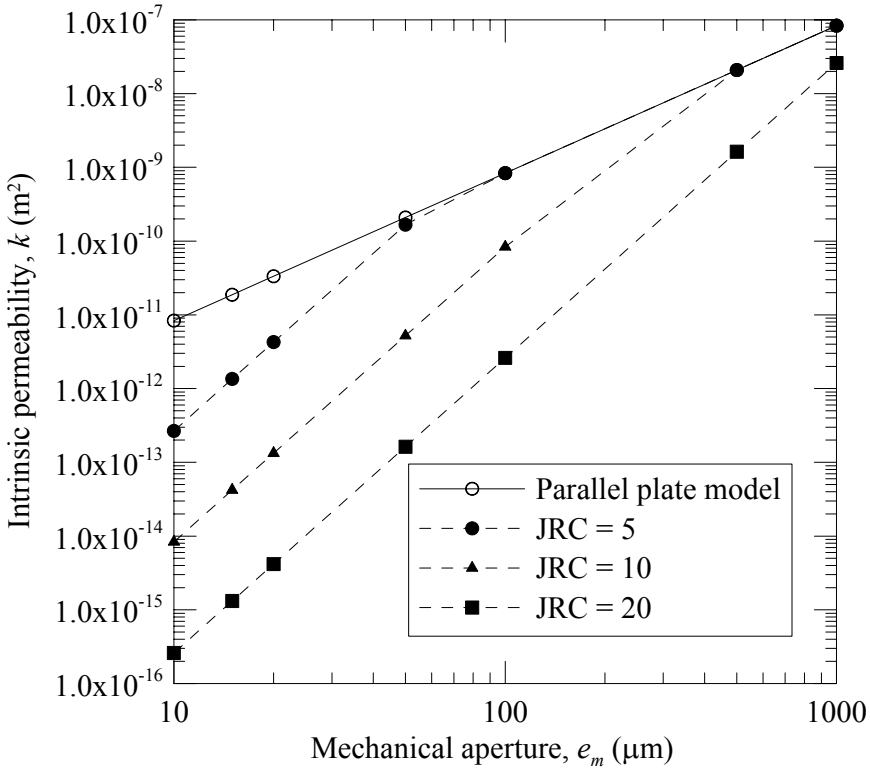

Figure 3.3: Graph showing relationship between mechanical aperture (e_m) and intrinsic permeability (k) for different fracture roughness (JRC).

As illustrated in Fig 3.2, surface roughness increasingly impacts upon the continuity and thickness of the fluid boundary layer at the fracture wall, leading to increased flow path tortuosity and the development of localised turbulence. This behaviour causes the discrepancy between the actual or 'mechanical' aperture of a fracture and the hydraulic aperture that would be back-calculated from Poiseuille's law, when the hydraulic gradient and the flow rate are known. This characteristic is demonstrated by the relationship between hydraulic aperture (e_h), mechanical aperture (e_m) and *JRC* as proposed by Barton et al. (1985). The relationship in Eq. [3.4]. is empirical and aperture measurements are in microns and is valid for $e_h \leq e_m$. In practice, smooth fracture JRC (i.e. low roughness) can be approximated by $e_h = e_m$.

$$e_h = \frac{e_m^2}{JRC^{2.5}} \qquad [3.4]$$

Figure 3.3 also illustrates the effect of increased roughness by the reduction in intrinsic permeability (k). The permeability (parallel plate model) calculated using the mechanical aperture (e_m) for the condition $e_m = e_h$ is compared with the permeability calculated using the corresponding e_h from Eq. [3.4]. The graph shows roughness impacts more severely on the intrinsic permeability for small aperture defects by more than 4 orders of magnitude.

Fracture topography is really three dimensional, extending in both planes of the opposing fracture surfaces. Non-parallel unmated surfaces in a fracture cause the flow path to deviate laterally in the fracture plane. Walsh (1981) considered several circular inclusions in an idealised smooth-walled parallel plate fracture and found permeability was reduced by a factor $(1 + d)/(1 – d)$, where d is the ratio of the included area to the total plate area.

$$Q = \frac{e_h^3 w}{12\mu}\left(\frac{1-d}{1+d}\right)\frac{dh}{dx} \qquad [3.5]$$

Eq. [3.5] allows for contacting asperities within an idealised fracture plane. This reduces a 2-D problem to one dimension. In reality, assessment of d is problematic and does not account for narrowing of the aperture, as opposed to that of asperity contact. Estimation of the parameter d requires detailed observation and even separation of the fracture surfaces, and may only be feasible in the laboratory.

The development of the Louis (1969) Relative Roughness Index was described in 2.2.2. The maximum amplitude k_{max} can be easily calculated where automated surface measurement techniques are employed. Aperture variability was also considered by Witherspoon et al. (1980) when the Darcy's Law equation was modified by the factor $1/f$. This development is discussed with particular reference to fracture flow in 2.2.2.1.

3.3 Descriptive techniques

A wide range of techniques have been applied to the measurement of rock fracture roughness. A number of the pertinent approaches are discussed in the following paragraphs covering a range of complexity. The purpose behind this roughness assessment approach was to devise a technique that could be applied in the field equally as well as in the research laboratory.

3.3.1 Observational Approach

The simplest roughness assessment technique is inspection, whereby natural fractures are compared to the standard profiles (ISRM, 1978) as shown in Fig. 3.1. This approach is very subjective relying upon visual or tactile assessment of the degree of roughness. This flaw means the same or different operators cannot guarantee the repeatability of the assessment. Milne (1990) recognised this and proposed a an objective photographic method involving the illumination and projection of the measured roughness profile. The roughness was assessed using the maximum difference in asperity height along the fracture length, and then related to *JRC* using an empirical relationship. The technique relied upon casting a shadow of the fracture profile at the desired location and recording a picture of the image. Comparison of the picture with the standard *JRC* profiles and measurement of the maximum asperity height measurement were used to relate the trace length to the *JRC*. This technique is well suited to field investigations with large sample block sizes or surface exposure, and benefits from the relatively low technology apparatus, which would be well suited to demanding field conditions. The Milne (1990) correlation provides a relationship between the maximum amplitude and JRC which is almost identical to that discussed by Barton & de Quadros (1997) for 100mm long samples.

The alternative empirical relationship is proposed by Barton & de Quadros (1997) and relates the maximum roughness amplitude a to the profile length L to calculate JRC:

$$JRC = 400\frac{a}{L} \qquad [3.6]$$

where, the constant is 400 for a 100mm profile. The advantage of this methodology is the simple equipment to measure the maximum roughness amplitude over the selected profile length, and has the benefit of being objective. However, this approach is very simplistic in the consideration of the profile maxima and minima, with no regard for variation in inclination of the intermediate points.

3.3.2 Mechanical Testing

Barton & Choubey (1977) propose more scientific assessment methods to account for the macroscopic impact of surface roughness. The Tiltmeter was specially developed for use with one of these methods. The meter allowed the controlled and progressive inclination of an axially fractured core specimen. The methodology required both complimentary parts of a fractured sample so that the specimen could be gradually tilted until the upper sample fragment slid over the lower fragment. Tilt tests apply the principle of Constant Normal Load (CNL) and the results used to back-calculate JRC:

$$JRC = \left(\beta_T - \phi_r\right)\frac{1}{\log\left(JCS \big/ \sigma_{n0}\right)} \qquad [3.7]$$

where, the tilt angle is β_T, ϕ_r is the residual friction angle, JCS is the joint compressive strength and σ_{n0} is the effective normal stress acting on the fracture. This method requires additional assessment of JCS and ϕ_r, and can result in the introduction of errors in JCS unless the Schmidt Hammer is used carefully. A Schmidt Hammer needs

particular care if the fracture surfaces are weathered, whereby the compressive strength has been altered from the fresh in-situ conditions.

Barton & Choubey (1977) found tilt tests worked well for relatively smooth fractures. However, rough fractures required a different approach because of the significant asperity interlock at low confining stress. To overcome the higher shear strength of such surfaces (*JRC* > 8), Barton & Choubey (1977) proposed 'Push' or 'Pull Tests' with the discontinuity inclined in the horizontal that could be performed in a shear box, where the normal load applied to the fracture surface is the self weight of the upper portion of the sample. These restrictions limit these methods to laboratory environments.

3.3.3 Digital Surface Measurement

Detailed fracture surface examination provides a further opportunity for roughness assessment, and these methods are becoming increasingly popular due to technological advances. The first step in undertaking roughness analysis is acquiring digital elevation data of the surface of interest. The form of data collection (1- or 2-D) and the reading frequency or interval are key in digital surveys. It is established in the literature that roughness should be regarded as heterogeneous and anisotropic (Yang & Di, 2000). Thus, careful measurement is essential so that the roughness impact on engineering analysis can be assimilated into the typical 1-D (plane strain) environment used in many engineering solutions. Digital surface measurement is particularly suited to some mathematical analyses, which are described in the following text. The methods are compared to illustrate the relevance of the preferred method.

3.3.3.1 Statistical analysis

Fundamental statistical studies of rock surfaces have been conducted, summarised by Tse & Cruden, (1977) and Krahn & Morgernstern (1979). Tse & Cruden (1977) used

the ISRM (1978) standard profiles measured at 1.27mm intervals to develop regression functions between the *JRC* and 8 different statistical variables. The work considers roughness as a function measured relative to a reference datum, or in terms of a spatial relationship of a location to the adjacent data points. Their work concentrated on variables that were related to the root mean square (*RMS*) and the auto-correlation function (*ACF*) – Eqns. [3.8] and [3.9]:

$$RMS = \left[\frac{1}{n} \int_{x=0}^{x=n} z^2 dx \right]^{0.5} \quad [3.8]$$

$$ACF = \frac{1}{L} \int_{x=0}^{x=1} f(x) f(x + \Delta x) dx \quad [3.9]$$

where, n is the number of measured points, z is the roughness amplitude about the centre line, dx is the interval between amplitude readings, $f(x)$ is the roughness amplitude at the distance x along a profile of length L such that Δx is the a constant distance lag. From the study of *JRC* profiles, Tse & Cruden (1977) concluded that the most correlated variables for surface roughness description were the mean square of the first derivative of the profile (Z_2) and the structure function (*SF*):

$$Z_2 = \frac{1}{L} \int_{x=0}^{x=L} \left(\frac{dz}{dx} \right)^2 = \sqrt{\frac{1}{n(\Delta x)^2} \sum_{i=1}^{n} (z_{i+1} - z_i)^2} \quad [3.10]$$

$$SF = \int_{x=0}^{x=1} \left(f(x) - f(x + \Delta x) \right)^2 dx \quad [3.11]$$

Their work highlighted the potential for systematic roughness measurement to be related to the established *JRC* system, and acknowledged the need to provide an quantitative description of what was sometimes a purely qualitative parameter. For rough surfaces in low normal stress environments Tse & Cruden (1977) summarised their study in 2 equations:

$$JRC = 32.2 + 32.47 \log Z_2 \quad [3.12]$$

$$JRC = 37.28 + 16.58 \log SF \qquad [3.13]$$

The derived relationships demonstrated high correlation coefficients of > 0.98 for a linear log regression. The Z_2 parameter is related to the chord angle between successive readings. The Structure Function *SF* is related to the auto-correlation function (*ACF*).

3.3.3.2 Fractal analysis

The impact of surface roughness on mechanical and hydraulic properties have also been analysed using fractal methods by several authors, including Power & Tullis, (1991), Seidel & Haberfield (1995), Kulatilake et al. (1998) and Yamatomi et al. (2001). Fractal theory was first developed from mathematical study of coastlines (Richardson, 1961) before being applied by Mandlebrot (1983) as a technique for modelling natural processes. Rock fractures are usually described as self-affine (Seidel & Haberfield, 1995) since disproportionate orthogonal scaling is necessary to maintain statistical similarity when the profile is extended.

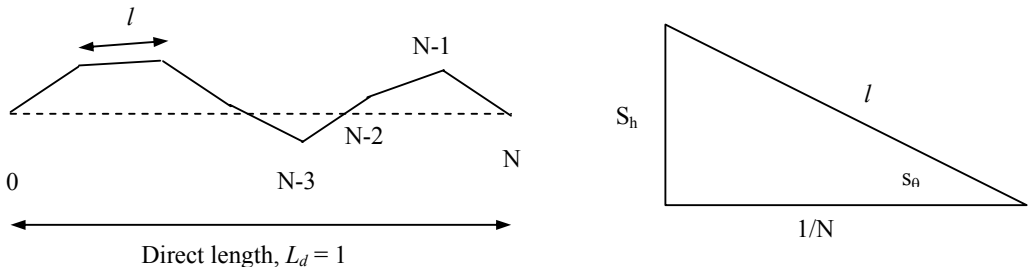

Figure 3.4: Left - definition of a fracture profile comprising *N* segments of length *l*. Right - defintion of standard deviation of chord length (modified from Seidel & Haberfield 1995).

Seidel & Haberfield (1995) developed the fractal technique in considering rock surfaces as self-affine surfaces and defined a relationship with chord inclination between adjacent readings and *JRC*. This approach is pictured in Fig. 3.4 showing their model joint surface profile comprising *N* segments of length *l* and an overall direct length L_d. For a large data population, the standard deviation of the asperity height s_h and the

chord angle s_θ have been approximated by the simple trigonometrical relationship between l and the fraction of the direct length ($1/N$).

$$s_\theta \approx \cos^{-1}\left(N^{(1-D)/D}\right) \quad [3.14]$$

$$s_h \approx L_d\sqrt{N^{-2/D} - N^{-2}} \quad [3.15]$$

Often these approaches use data from a fully automated, high-resolution optical scanning apparatus, capable of reading sub-millimetre frequencies; e.g. Jermy (1995) and Archambault et al. (1997) measured at 0.25mm and 0.5mm intervals, respectively. The success of a proposed technique partly relies upon the applicability to a wide range of situations. This is a function of the reading frequency or spacing, since a method that has a finer tolerance would be more suited to the controlled environment of a research laboratory, rather than a field scenario. Where such apparatus is not available or time constraints are too restrictive, it is believed that the method proposed in this chapter presents a viable alternative because of the relatively small number of datapoints. Seidel & Haberfield (1995) require 2^7 readings (i.e. 128 chord lengths) to create their profile, whereas the proposed method needs 50 data points for the 100mm sample). Seidel & Haberfield (1995) related their strong correlation between the measured and predicted profiles due to the similarity of their average reading frequency (0.78mm) to the average displacement at peak shear strength (0.95mm) observed in the original Barton & Choubey (1977) testing. The most useful outcome from the Seidel & Haberfield (1995) work is their direct relationship between *JRC* and the standard deviation of the chord angle. Seidel & Haberfield (1995) state that this relationship is maintained for reading intervals up to 6mm.

Yang & Di (2001) considered 2-D surface roughness using an extension of the fractal method. They used two-variable (self-affine) fractal Brownian motion theory to determine the relationship between the asperity height increment ($\Delta z_{x,y}$) of adjacent

points and the Hurst Index (H). Their model assumed a normal distribution of asperity height increment with a zero mean such that:

$$z(x+\Delta x, y+\Delta y) - z(x,y) \cong \frac{1}{S_R^{\mathrm{H}}}\left[z(x+r\Delta x, y+r\Delta y) - z(x,y)\right] \quad [3.16]$$

The Hurst Index is also related to the measured data and the variance V_σ from the equation,

$$V_\sigma = \sigma^2\left(\sqrt{\left(\Delta x^2 + \Delta y^2\right)^{2H}}\right) \quad [3.17]$$

where, σ is the standard deviation and S_R is the scaling ratio (a real number). The Hurst index, H is defined by scaling factor applied to the data to ensure maintenance of the self-affine properties. The main advantages of their method were: that the Hurst index could be calculated uniquely, rather than from fitting a tangent to the non-linear log-log plot of the variogram and the lag distance; and that the analysis could take account of the 2 dimensional roughness of the surface. H was related to the Fractal Dimension D with the formula:

$$D = 2 - H \quad [3.18]$$

The disadvantage was that although this approach was successful as an academic exercise, the two-dimensional Hurst Index could not be independently related to *JRC* and is dependent upon the user-defined eigen-directions applied to the analysis.

3.3.3.3 Spectral analysis

Piggott & Elsworth (1995) compared several approaches to modelling roughness, including a spectral analysis using a discrete Fourier transform to construct a semi-variogram function for naturally fractured samples. Durham & Bonner (1985) discussed the application of a power spectral density (PSD) analysis to the surface of three Westerly granite samples. Their work illustrates the ability of such techniques to reduce the complexity of fracture surface and void variation using spectral estimation:

$$G_i(f) = \frac{l^2}{L}\left|Z_i(f)\right|^2 \qquad [3.19]$$

The relationship relates the estimates of PSD $G_i(f)$ for each profile to the sampling interval l over a profile L long to the fast Fourier transform of the discretely sampled profile $Z_i(f)$.

3.3.3.4 Fourier series analysis

An alternative approach is to analyse the natural fracture surface using the Fourier series. The procedure can be applied to natural rough surfaces using lower frequency data acquisition methods than needed for fractal or spectral analyses. Discussions of the suitability of the technique have been presented elsewhere by this writer and others and included in several publications, e.g. Indraratna et al. (2002) and (1995); Indraratna & Haque, (2000). The Fourier method can be applied to either periodic, or single impulse functions, provided they are piecewise and continuous. The technique reduces a series of regularly spaced *x-z* data to a combination of 2 coefficients, related trigonometrically to an identified period or impulse bandwidth. This is achieved by considering the superposition of a number of harmonic frequencies to provide a realistic level of correlation with the original profile data. The degree of small scale refinement is enhanced by consideration of increasingly higher harmonic frequencies in the calculation of *f(x)*. These mathematical properties make the technique suitable for analysing the ISRM (1978) roughness profiles (Fig. 3.1) as well as natural rough surfaces. The Fourier series equations with the appropriate substitution of the relevant coefficients, can be used to accurately reproduce interfaces with realistic roughness profiles, and could be incorporated for example in computer modelling applications. Analysis of synthetic saw tooth profiles shows that the magnitude of the Fourier coefficients tends to decrease with each successive harmonic frequency (Indraratna et

al., 1995). This trend is more muted for natural fracture profiles but it is found to significant enough for *JRC* interpolation.

A description of the fundamentals of Fourier series can be found in standard texts, e.g. Spiegel (1974). The approach defines a variable as a function *f(x)*, in this case the asperity height (*z*) is defined in terms of the horizontal distance along the

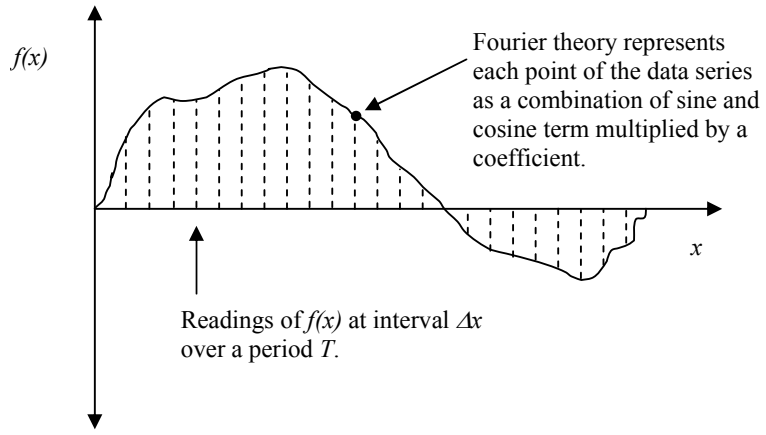

Figure 3.5: Schematic definition of a function *f(x)* comprising n harmonics and measured at a frequency *1/T* that could be approximated using Fourier theory.

profile *(x)* over a profile period *T*, or *2L*, i.e. in this case 100mm. In this instance, it is useful to write the function as a trigonometric series comprising sine and cosine terms calculated over *n* harmonic frequencies between limits of integration, which, here are *0* and *2L*. The series is defined graphically in Figure 3.4 and mathematically in Eq. [3.20].

$$f(x) = \frac{a_o}{2} + \sum_{n=1}^{\infty}\left(a_n \cos\frac{n\pi x}{L} + b_n \sin\frac{n\pi x}{L} \right) \qquad [3.20]$$

where, *f(x)* is a periodic continuous function measured at regular intervals, Δx, within the period 2*L*, with the coefficients a_n and b_n for $n = 0, 1, 2$ .... defined in Eq. [3.21] and [3.22] as:

$$a_n = \frac{1}{L}\int_0^{2L} f(x)\cos\frac{n\pi x}{L}dx \qquad [3.21]$$

$$b_n = \frac{1}{L}\int_0^{2L} f(x)\sin\frac{n\pi x}{L}dx \qquad [3.22]$$

The number of harmonics that are required to replicate the profile depends upon the profile intricacy and the sampling interval frequency. It is useful to calculate Parseval's identity ($\bar{y}^2$) Eq. [3.23] to assess the relative power dissipation of each of the harmonics and to understand the significance of particular harmonics in the optimal approximation of the profile.

$$\bar{y}^2 = \frac{1}{L}\int_0^{2L}\{f(x)\}^2 dx = \frac{{a_0}^2}{2} + \sum_{n=1}^{\infty}\left(a_n^2 + b_n^2\right) \qquad [3.23]$$

Eq. [3.20] shows that Parseval's identity is the sum of the squared coefficients, a_n and b_n for the harmonic frequencies n = 1 to ∞. The contribution of each harmonic frequency to $\bar{y}^2$ decreases with the magnitude of the coefficient. This shows how many harmonic frequencies are needed in the replication of surface profiles when using the Fourier series approach.

Yang & Di (2001b) postulated a relationship between the sum of the Fourier coefficients and *JRC* when considering the first 20 harmonic frequencies in the profile analysis. Their conclusion are not ultimately supported by this project, despite encouraging preliminary results (Price & Indraratna, 2003). For the purpose of this research, it is suggested that this hypothesis should be modified in accordance with Bendat & Piersol (1986). In such a case, the definition of a discrete profile would require consideration of n_{max} harmonic frequencies where $n_{max} = N_{TOT}/2 - 1$, where N_{TOT} is the total number of data points in a traverse. There does not appear to be a simple relationship between *JRC* and Fourier coefficients given the superposition of different

wavelength roughness functions. However, this study has identified a relationship between Parseval's Identity and *JRC* that is expanded upon in Section 3.4.

The main advantage of this approach is the low density of data needed compared to, for example, the fractal method and the potential to use different survey methods depending upon the location and scale of appliction. The primary control on accurate surface replication is the data collection interval (Δx). It is also important that the sampled length is long enough to capture the representative roughness wavelengths. This technique could be applied to field measurements be taken over a 10m to 15m period if large scale engineering problems are to be analysed. Care should be taken to record measurements over a period that will accurately model roughness of the wavelength pertinent to the problem.

A further advantage of this method is that it can be extended to functions in 2 dimensions with the use of double Fourier series. Thus, a function *f(x,y)* could be represented by a Fourier series of the form:

$$f(x,y) = \sum_{n=-\infty}^{\infty} \sum_{m=-\infty}^{\infty} Y_{n,m} e^{2n\pi i(x/c_1)} e^{2m\pi i(y/c_2)} \qquad [3.24]$$

where, x and y represent to two perpendicular directions measured at intervals Δx and Δy, n and m represent the series harmonics in x and y respectively, c_1 and c_2 are the limits in integration in the x and y direction respectively, and $Y_{n,m}$ is a coefficient defined as

$$Y_{n,m} = \frac{1}{c_1 c_2} \int_0^{c_1} \int_0^{c_2} f(x,y) e^{-2\pi(x/c_1)} e^{-2\pi(y/c_2)} dx dy \qquad [3.25]$$

Furthermore, the application of Fourier series allows potential combination with other existing Fourier applications applied to geomechnical behaviour, e.g. relating the fracture topography with the prediction of peak shear and dilation developed in jointed rock (Indraratna & Haque, 2000). The inter-linkage of geomechanical joint properties

would provide a powerful analytical tool for computational analysis, where a good roughness estimate or even measured data were available.

3.4 Preferred methodology

Several measurement techniques have been employed in this project for obtaining point information to describe the roughness profile. The different methods are briefly discussed in the following sections. A preferred method was ultimately adopted so that successive sets of readings for the test profile could be used to identify both the roughness characteristics of the surfaces, and the spatial variability of the fracture aperture. With the launch of proprietary laser or digital 3-D survey equipment e.g. Cyrax systems by Leica or Sirovision by CSIRO, there is a potential for future developments to provide very high reading accuracy over considerable areas. Such site-wide data acquisition systems could provide detailed roughness analysis and improved scale effect assessment.

3.4.1 Apparatus

Three methods were applied to measure roughness and aperture characteristics for the test fracture. These are discussed in the order of increasing technological complexity and automation. The more advanced methodologies provide the benefit of acquiring large volumes of test data in short time periods. A drawback of these techniques is that they often require carefully maintained laboratory environments and, unlike the more simple methods, are not well suited to field application. One of the aims behind the development of a methodology was to identify a process that could be easily adapted to use in the field and the laboratory. For example, simple apparatus such as feeler gauges and rudimentary survey (e.g. string line survey) could allow satisfactory data acquisition in the most adverse site conditions likely. These factors have to be considered when selecting an appropriate survey method.

3.4.1.1 Manual equipment – feeler gauges

Manual point measurement of fracture aperture can be made using automotive feeler gauges. Such a tool will measure to a minimum aperture of at least 50μm. The roughness can be estimated by recording asperity offset from a measured datum line at each of the measuring locations. The measuring interval is limited by the width of the feeler gauges and would be of the order of 5 to 10mm. By placing both pieces of the sample together in a loading frame, the change in aperture can be measured as the fracture-normal load is varied in order to provide an indication of the joint normal stiffness. This technique provides a simple check on aperture back-calculation, although the level of accuracy is restricted by the thickness of the finest feeler gauge, the feeler gauge width and the limitation on the number of points that can be sampled. The ability to only measure points at the edge of the sample may also bias the calculated results.

For example, a sample can be placed in a load frame with the fracture plane perpendicular to the direction of loading. If the normal load is increased in stages from 0 to 1MPa, the change in aperture can be determined by locating measuring locations at equally spaced intervals around the sample. The fracture normal stiffness can be estimated from a plot of the average aperture at each stress increment (Fig. 3.6). This method is labour intensive and limited in the accuracy and density of readings that can be recorded, e.g. using the average of 24 measuring points the average aperture increases following the confining stress increment from 0 to 500kPa. However, such simple techniques become more attractive in adverse field conditions where relatively limited data collection is required.

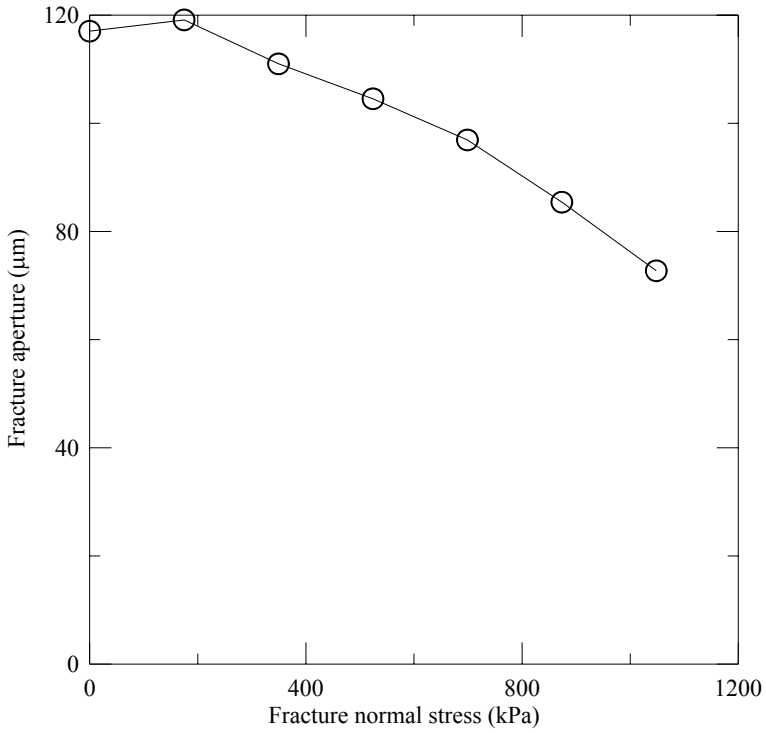

Figure 3.6: Fracture normal stiffness measurements using feeler gauges.

3.4.1.2 Contacting surface measurement apparatus

Coordinate Measuring Machines (CMM) can be used to mechanically measure surface roughness. These machines can be manual, semi-automated or automated and typically use a Renshaw probe or a stylus, to either lightly contact the rock surface using an up and down movement, or by trail lightly across the surface.

The measuring tip movement can be controlled to a tolerance of a few microns. Fractured rock specimens used on this project were digitised with a Ferranti U900 CMM (Fig 3.7). A sampling technique was developed combining digital data acquisition from the U900 to a personal computer. The sequence of operations is described in Appendix B.

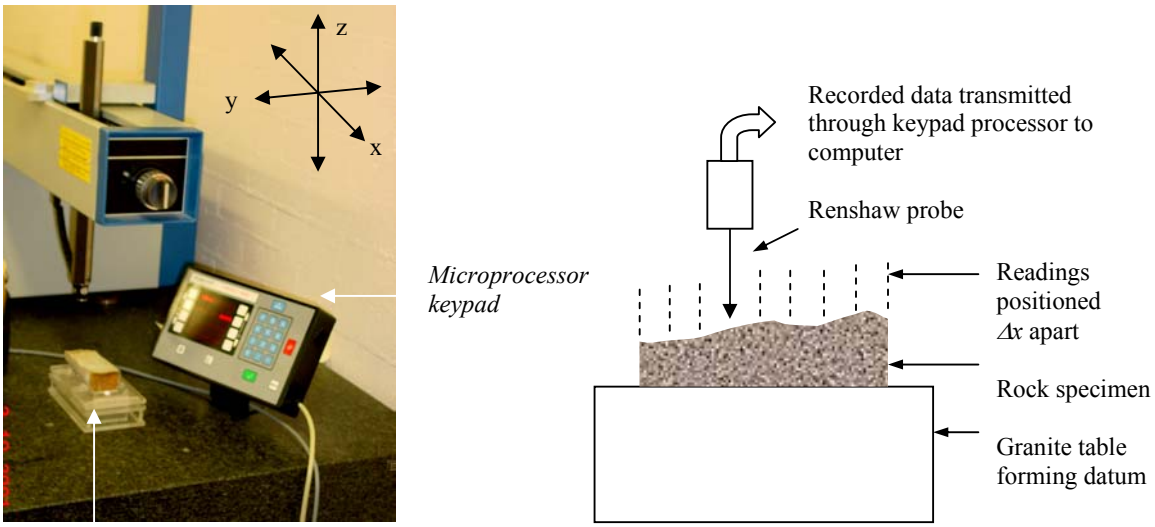

Figure 3.7. Photograph and schematic diagram of the Coordinate Measuring Machine showing use of equipment on a naturally fractured sample.

The Ferranti CMM provides highly accurate data, although the level of automation restricts the speed of operation and requires the operator to be present. This technique is very useful where a few short profiles have to be measured. Initial attempts at roughness measurement used the Ferranti CMM, were reported by the writer in Indraratna et al. (2002). As such, a mathematical approach was adopted to optimise the surface roughness measurement the widest possible sampling interval. The reading interval was selected to make the semi-automated data collection process as time efficient as possible, whilst providing satisfactory topographic detail so that the key features of the profile could be reliably replicated. In addition, this reading frequency is considered one that could be satisfactorily obtained in the field from available survey techniques. An interval of 2mm was finally selected such that for a 100mm long sample, 51 (i.e. N_{TOT}) data points would be recorded.

The specimen must be positioned and clamped in place so that the CMM can be used to measure the 3-dimensional topographic data to a theoretical accuracy of ± 3μm. The U900 was linked directly via the communications port to a computer, and

Microprocessor Keypad Programming was used for data capture using Windows Hyperterminal ©. This data was then imported to Excel and processed using Microsoft Visual Basic macros to allow analysis using the aforementioned spreadsheet functions.

An alternative to this equipment could be the use of 3-D industrial design milling and scanning equipment, which would be suitable for short sample profiles of the order of 160mm by 220mm. This type of apparatus, like the Roland MDX-20 (Fig. 3.8), will scan at 50μm intervals across a surface measuring to a vertical accuracy of 25μm, whilst operating automatically at > 4mm/sec. A further advantage arising from this apparatus is the opportunity to mill a 3-D replica of the measured surface, which could then be used for mechanical testing, e.g. in a shear box.

Figure 3.8: The Roland MDX-20 Desktop 3-D Milling and scanning equipment of potential use in geomechnical research.

This automated apparatus provides independent acquisition at a reading density of 20 points per millimetre, although at a slightly lower vertical tolerance than for the U900. This tool provides potential for the analysis of a significantly larger sample area, which

largely offsets any disadvantage in reduced data reading density or tolerance. This is especially so where larger scale waviness features, rather than small scale unevenness, is the focus of the study.

3.4.1.3 Non-contacting surface measurement

The most complex surface roughness measurement apparatus considered in this study is a computer controlled laser scanner, such as the Minolta Vivid 910 High Resolution non-contact 3-D Laser Scanner. This equipment pictured in Fig. 3.9, shows the sample placed in a Perspex cradle with the fracture plane approximately perpendicular to the axis of the laser.

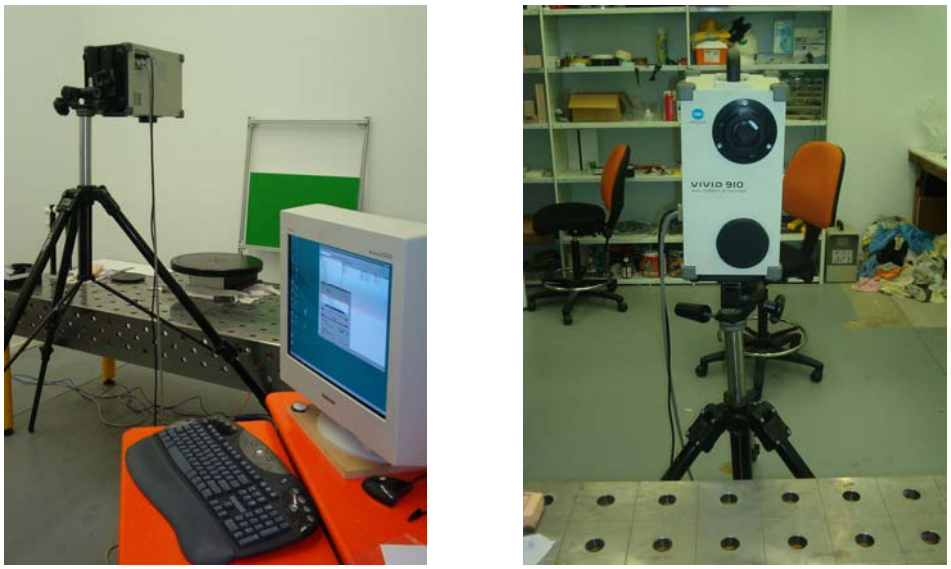

Figure 3.9: Minolta Vivid 910 high-resolution laser scanner apparatus showing the tripod supported CCD camera and the workstation used to control the camera and manipulate the scan data.

Laser power and focal length settings were finely adjusted to optimise data recovery and to minimise the number of "fly-off" data points (i.e. minimise error). Scans were automatically recorded at 0.1mm intervals in the *x*-*y* plane (i.e. parallel to the fracture plane) to a vertical (*z* plane) precision of ± 0.008 mm. The scan is performed using Laser triangulation, where a laser light plane is directed across a mirror that is precisely rotated over the subject. One of the advantages of data captured from the apparatus is

that any parallax error has been removed. The resulting reflected light pattern is used to develop high resolution contours of the specimen. The scanned coordinate data was saved in ASCII format allowing data processing and analysis. The scanning technique uses a synthetic fracture cast which is scanned in place in the manner described elsewhere (Indraratna et al., 2002). The approach uses a Dow Corning Silastic 'rubber' or ERA two-part polyurethane resin compound to form a cast of the fracture, by preparing both fracture surfaces with a release agent before applying the casting agent. Following application, the two portions of the rock specimen are mated in their recovered position, taped together and left for curing. The outside edges of the fracture were closed to prevent leakage of the compound out of the fracture before curing could occur and any excess compound removed. Once cured, the upper portion of the specimen could be removed so as to expose the upper surface of the cast to the laser scanner. After measurement, the cast was carefully removed so that the underlying rock surface could then be scanned. By measuring using the same interval and coordinate system, simple arithmetic data manipulation allows calculation of the physical or 'mechanical' aperture e_m. These two sets of measurements provide data on the topography of each fracture surface as well as the aperture, i.e. if two opposing fracture surface traverses are both defined by separate Fourier series - $f(x)_{upper}$ and $f(x)_{lower}$ - the fracture aperture function $\Phi(x)$ can equally be defined by a third Fourier series, such that:

$$\Phi(x) = f(x)_{upper} - f(x)_{lower} \qquad [3.26]$$

For a cylindrical sample 110mm high, the weight of one half of the sample acting normally at the fracture plane would be equivalent to a stress of less than 1kPa. The small magnitude of this normal stress means that the situation is effectively the same as zero confining stress condition. Zimmerman & Bodvarsson (1996) showed that fracture

apertures could be approximated by log-normal distributions. Thus, the average log-normal aperture can be calculated from the exponent of the average log aperture value, and also represents the average mechanical aperture at zero normal stress, i.e. $\bar{e}_{\log} = e_{m0}$.

3.4.2 Standard roughness profile analysis

The ISRM standard profiles (ISRM, 1978) in Fig. 3.1 were scanned and digitised using a personal computer, a flatbed scanner and proprietary graphics software. The data points were analysed for each *JRC* profile with a spreadsheet to obtain the Fourier coefficients using Eqs. [3.20], [3.21] and [3.22]. Spreadsheet formulae were written to integrate the x values for each harmonic (n) term by term, so that the Fourier coefficients (a_n and b_n) could be calculated. When the coefficient analysis was complete for each profile, the calculation was verified by using the computed coefficients to back calculate the values of $f(x)$ at the original measured interval (Appendix B). The results of the mathematical analyses are shown in Figure 3.10 and Table 3.1 summarises the Fourier coefficients for $0 > n > 5$:

Table 3.1: Summary of *JRC* Fourier Coefficients for harmonics $0 > n > 5$.

Fourier Coefficient	Joint Roughness Coefficient (JRC)				
	0 - 2	4 - 6	10 - 12	14 - 16	18 - 20
a_0	1.72	-0.336	3.225	-3.434	1.523
a_1	-0.307	0.077	-0.97	0.797	0.081
b_1	-0.029	0.261	-0.657	-1.58	-1.101
a_2	0.268	0.111	0.294	1.704	-0.297
b_2	-0.256	0.441	-0.506	1.005	-0.389
a_3	-0.617	-0.095	-0.317	-0.374	0.25
b_3	0.234	-0.035	-0.321	-0.452	-0.55
a_4	0.014	-0.098	-0.134	-0.293	-0.282
b_4	-0.165	0.057	-0.031	0.311	0.229
a_5	-0.121	-0.186	0.071	0.265	-0.602
b_5	-0.118	-0.108	-0.299	0.095	0.031

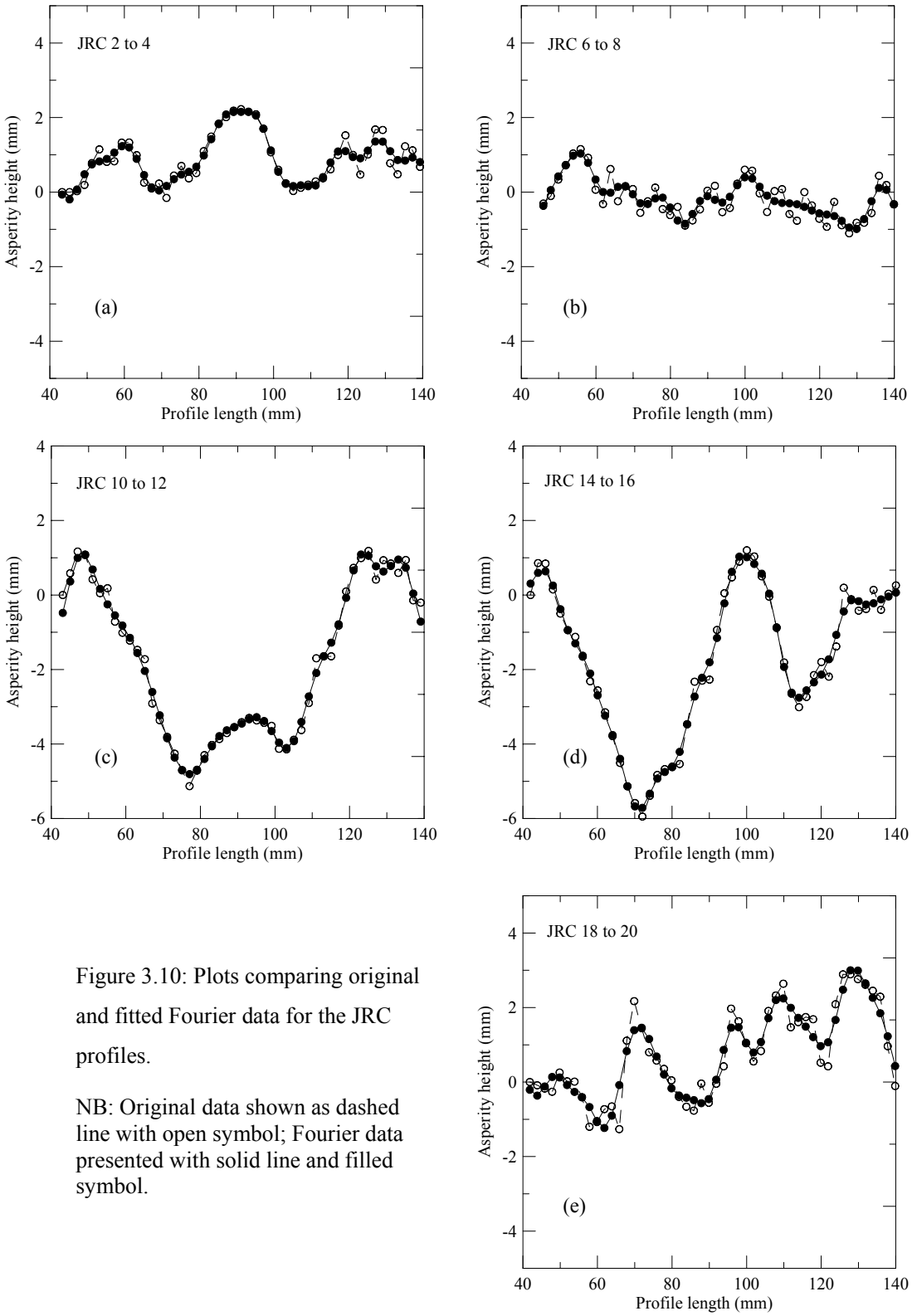

Figure 3.10: Plots comparing original and fitted Fourier data for the JRC profiles.

NB: Original data shown as dashed line with open symbol; Fourier data presented with solid line and filled symbol.

Five plots over the full range of ISRM (1978) roughness profiles have been presented to summarise the results of the analysis and to show the high level of agreement that has

been achieved between the measured data and the predicted Fourier data. The predicted data series reasonably identify the significant topology i.e. the major peaks and troughs for the measured profiles, e.g. Fig 3.10(b) for *JRC* 6 – 8 and Fig 3.10(e) for *JRC* 18 - 20. However, some of the smaller wavelength variations are not so well reproduced for the selected reading frequency, e.g. Figure 3.10(c) for *JRC* 10 to 12. The data replication could be improved at this fine scale if a reduced reading interval were applied, although the significance of any misfit is considered minor in relation to any estimation of empirical hydromechanical properties.

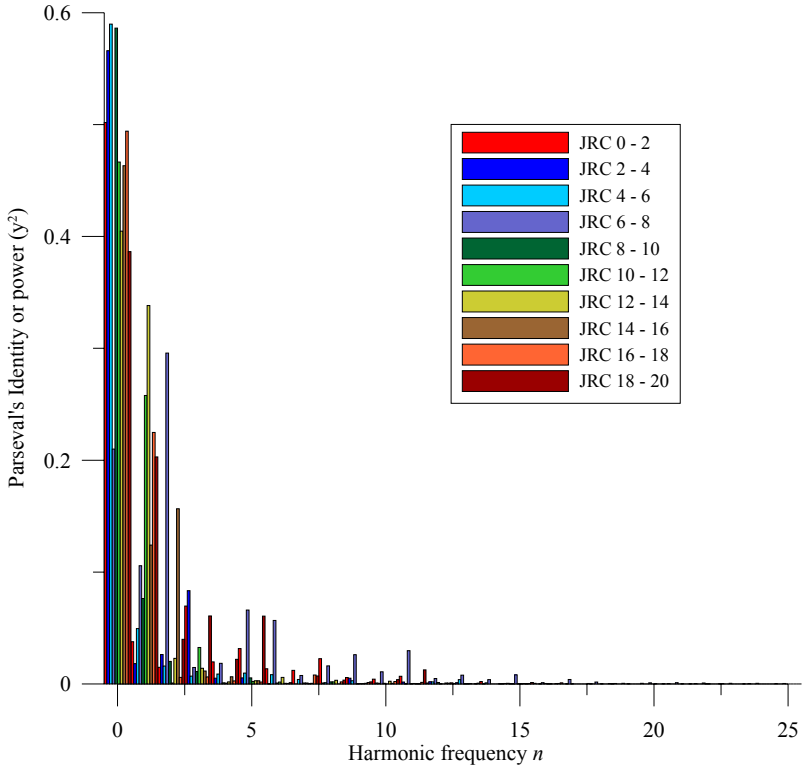

Figure 3.11: Plot of harmonic frequency power for JRC standard profiles.

The results of the power analyses (Figure 3.11) show that although the Fourier coefficients calculated for harmonics more than $n = 5$ are numerically small, they are significant in distinguishing between individual profiles. The tabulated coefficients (Table 3.1) can be substituted in to the Fourier series equation Eq. [3.20] and *f(x)*

calculated using a suitable period. This analysis has shown that the Fourier method is suitable for calculating a series of data points of a specific *JRC* for a profile idealised as either a periodic or impulse function. This could be combined with a set of aperture measurements in order to provide a realistic distribution of both roughness and aperture.

The tabulated data in Table 3.1 shows a complex relationship whereby the coefficients vary with *JRC* and harmonic frequency. The relationship is clarified if Parseval's Identity is calculated for each profile using Eq. [3.23] to plot a histogram of y^2 against n. Fig 3.11 presents this relationship, and the general trend of reducing power with increasing harmonic frequency is clear. Inspection reveals that there is a unique relationship between harmonic frequency and power for each profile for this particular reading interval. This relationship is an improvement on the identification of the *JRC* and provides a calibration for roughness assessment of real rock profiles.

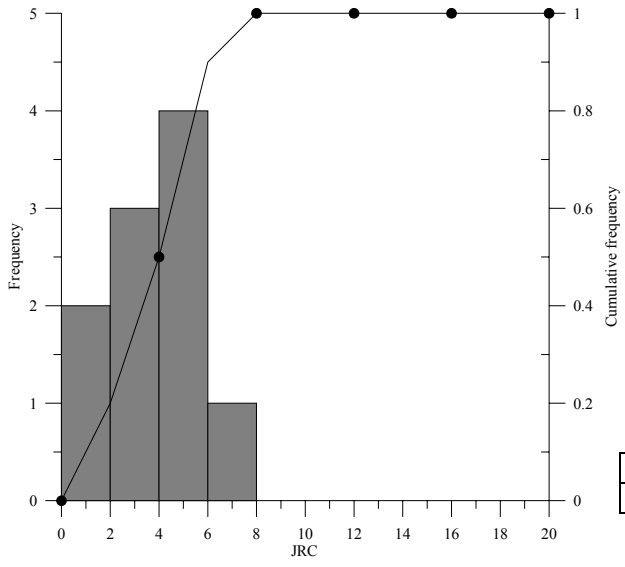

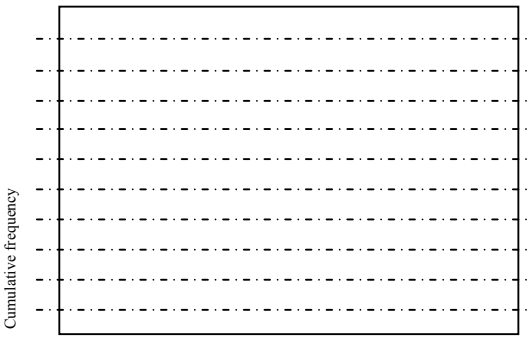

Plan of roughness profiles across surface and summary of JRC profile assessment:

Profile	1	2	3	4	5	6	7	8	9	10
JRC	2	4	8	6	4	6	2	6	4	6

Figure 3.12: Illustration of JRC_F assessment for a fracture surface measured with 10 equally spaced profiles of varying individual roughness.

Comparison of real rock profile data with the standard profile result reveals that the profile typically exhibits roughness characteristics in common with more than one

standard profile (Fig. 3.12). This observation is to be expected, since roughness can be defined by the superposition of different wavelength or scale features in creating a roughness profile e.g. roughness and unevenness (ISRM, 1978). This characteristic is also parallelled by the frequency spectra methodology evident in the Durham & Bonner (1985). In this method, increasing harmonic frequency has the effect of contributing correspondingly finer detail to the described profile. The Bendat & Piersol (1986) criterion provides a threshold for defining the completeness of the calculation, in terms of the number of harmonic frequencies that need to be incorporated within the analysis.

The observed variation of individual profiles in *JRC* should be accounted for when interpolating a coefficient to a particular profile. A histogram of *JRC* for each profile illustrates the dominant *JRC*, as well as the range of *JRC* distribution. Comparison of several parallel profiles of a natural fracture surface shows a degree of anisotropy, unless formed under special high stress conditions e.g. slickensides present on a fault or shear plane. Thus, the degree of roughness anisotropy is indicated by a plot of the roughness assessment for a number of parallel profiles across a rock fracture (Fig. 3.12). The Figure 3.12 shows a relatively homogenous roughness distribution where the average and modal *JRC* are similar. With greater roughness anisotropy, the variability in *JRC* means that the hydromechanical characteristics of the fracture will be modified, tending to the average *JRC* of the fracture. In this work, the average *JRC* based upon the Fourier analysis, JRC_F, has been used to describe the overall roughness of the profile, since this will tend to have the dominant mechanical and hydraulic impact modified to a degree by the interaction of the other sub-modal roughness groups.

3.4.3 Real rock profile analysis

Initial rock profile data was acquired from both feeler gauges and the Ferranti CMM (Indraratna et al. 2002). However, the preferred method was high resolution scanning

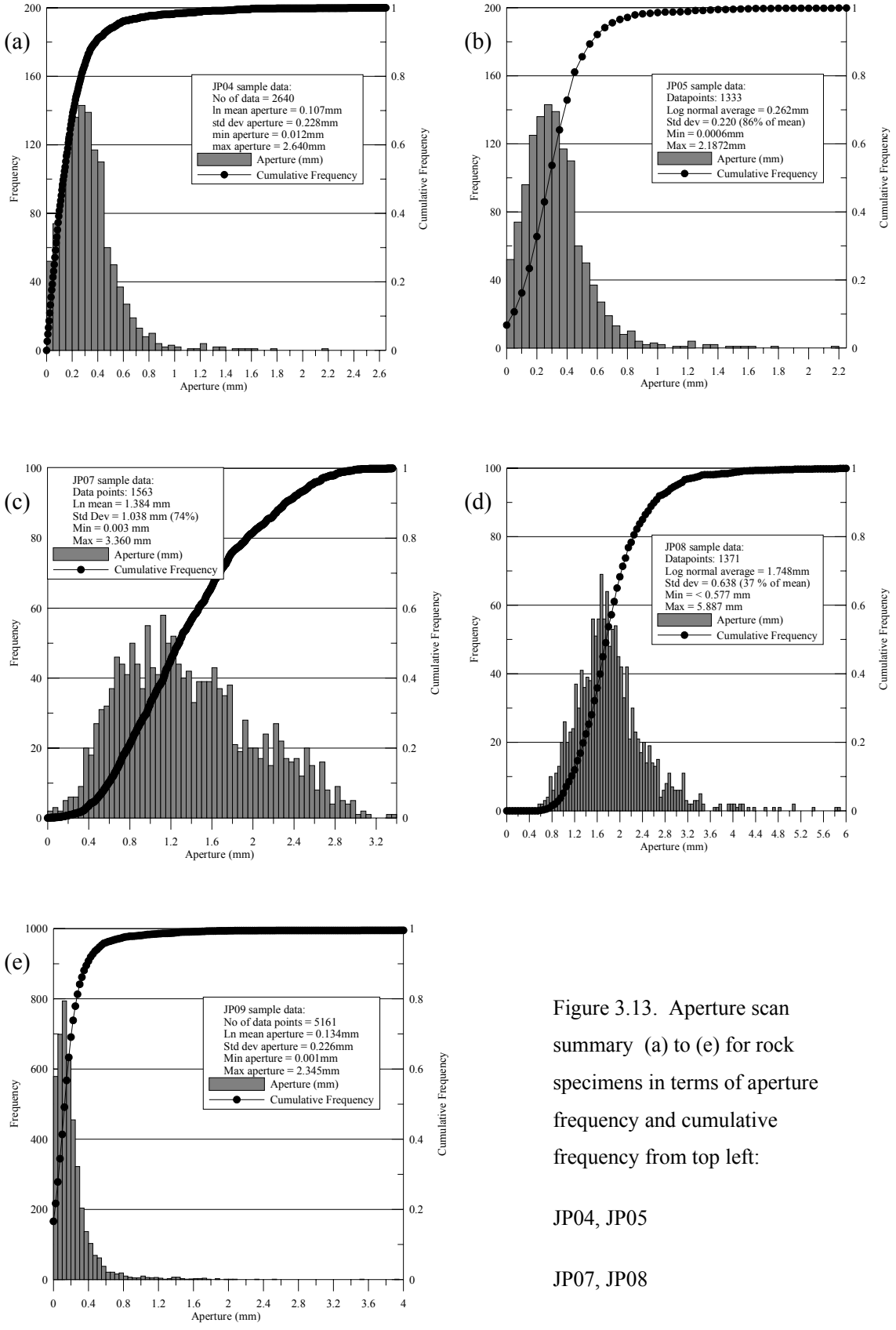

Figure 3.13. Aperture scan summary (a) to (e) for rock specimens in terms of aperture frequency and cumulative frequency from top left:

JP04, JP05

JP07, JP08

JP09

because of the greater speed of operation and the intensity of the output data. The laser scanning of fractured core specimens provided large sets of fracture surface data. The semi-automated CMM required 18hrs of measurement to capture what the Minolta Vivid could acquire in under 10 minutes. The data were reviewed and asperity height analysed by linear interpolation to provide a 2mm square grid of points across each fracture surface as per the original methodology (Indraratna et al., 2002). At each grid point, subtraction of the two corresponding fracture surface elevations defined the elemental aperture. Fourier series analysis of the fracture surface profiles was used to investigate the surface roughness. Statistical analysis was used to study the spatial distribution and variation in fracture aperture (Fig. 3.13).

The results of the high resolution laser scanning are summarised in Fig. 3.13 and 3.14. In Fig. 3.13, each sample is represented by an aperture histogram and cumulative frequency distribution with a summary of the data range and distribution. The data distribution shows a skewed normal or log normal distribution with a large standard deviation, as would be expected from the work by Hakami & Barton (1990) and Zimmerman & Bodvarsson (1996).

Table 3.2. Summary of laser scanning statistics.

Sample	**Data points**	$\bar{e}_{\log}$ **(mm)**	**Maximum aperture (mm)**	**Standard Deviation**
JP04	2640	0.107	2.64	0.228
JP05	1333	0.262	2.19	0.251
JP07	1563	1.384	3.36	1.038
JP08	1371	1.784	5.89	0.638
JP09	5161	0.134	2.35	0.226

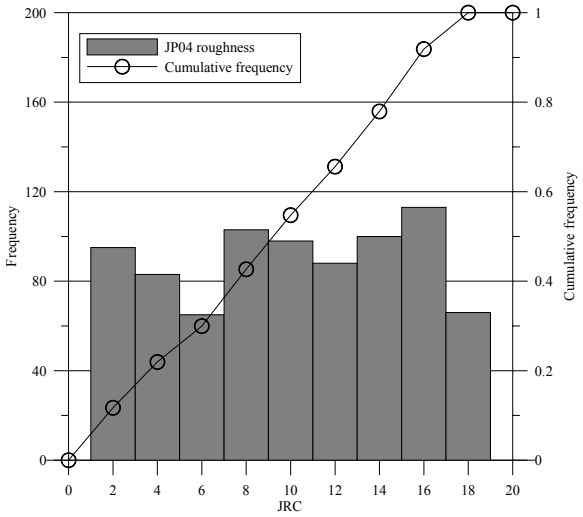

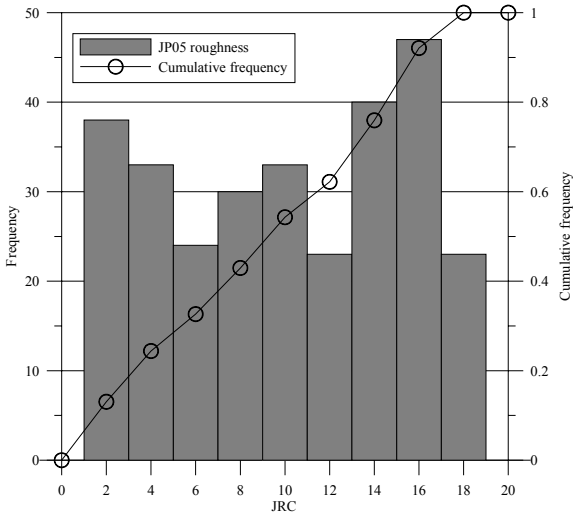

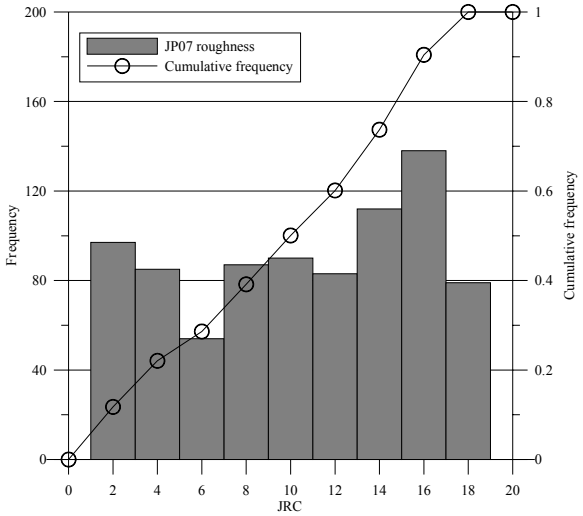

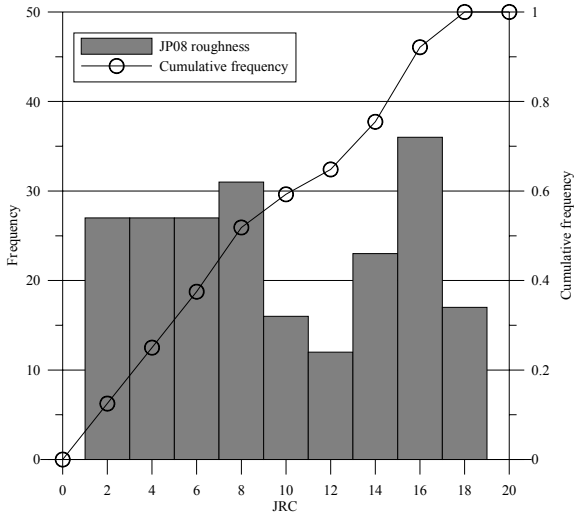

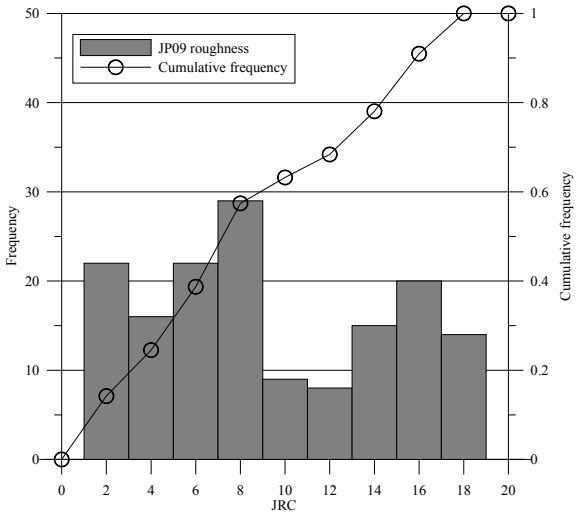

Figure 3.14: JRC_F assessment sample summary, from top left to right:

JP04, JP05

JP07, JP08

JP09

The data for each sample is also presented in Appendix C as a 3-D wire-frame model of the fracture surface with a stacked contoured layer showing the variation of fracture aperture. The scan data histogram (Fig. 3.13) and statistics (Table 3.2) indicate that for each specimen, from a sample of between 1300 and 5100 data points, there is a log-mean mechanical aperture ($\overline{e}_{\log}$) of between 0.107 mm to 1.784mm for a corresponding fracture normal stress equal to the weight of the upper fragment of the sample.

Following roughness analysis of each of the samples, Fig. 3.14 presents the *JRC* assessment. Each of the specimens were analysed using the method described in the preceding section. The interpreted *JRC* predicted from Fourier series analyses are summarised in Table 3.3. The results show roughness anisotropy developed to different degrees for each of the samples with several sub-modal roughness ranges identified by the analyses. The average JRC_F is based upon the cumulative frequency distribution of the data. The roughness assessment is best tested by comparison with the results of the TPHPTA testing using the Barton et al. (1985) correlation and Eq. [3.4]. A further simple comparison can be made using the Milne (1990) correlation discussed in Section 3.1.

In Table 3.2, the $\overline{e}_{\log}$ value represents the average mechanical aperture when the fracture is subjected to a confining stress due only to the self-weight of the upper half of the sample, i.e., a fracture normal stress of effectively zero. Thus, $\overline{e}_{\log}$ represents the $\sigma_n = 0$ point of a fracture aperture versus normal stress function such as shown by Fig. 3.6. The subsequent points that correspond to non-zero confining stress conditions are a function of the fracture normal stiffness, and must be measured under TPHPTA test conditions if fracture hydromechanical behaviour is of interest. Fracture deformation will be discussed subsequently in Chapters 6 and 7 with reference to two-phase hydromechanical triaxial testing and coupled flow computation.

The results of the Fourier *JRC* assessment for the test specimens are shown in Fig. 3.14. The JRC_F histograms show the degree of roughness anisotropy recorded on each sample. The mode and average JRC_F and sub-modal JRC_F ranges are also listed in Table 3.3. The results show the development of 2 or 3 ranges of roughness that combine to produce the measured fracture profiles.

Table 3.3: Fourier series JRC_F roughness interpretation results.

Sample	**Average JRC_F**	**Mode JRC_F**	**Sub-modal JRC ranges**
JP04	10	14 to 18	2 to 6, 8 to 12
JP05	9	12 to 16	2 to 6, 8 to 12
JP07	11	12 to 16	2 to 4
JP08	9	14 to 16	2 to 10
JP09	7	6 to 8	2 to 4, 14 to 20

The results show that the fracture profiles can be considered a composite of a number of separate JRC_F values due to the superposition of the different harmonic frequencies. No single profile was an exact replication of any of the standard profiles (ISRM, 1978). Thus, each of the fracture surfaces is a combination of different standard roughness ranges. Roughness anisotropy promotes the development of non-parallel fluid flow and anomalous localised fracture deformation. The implications of these results are discussed more in Chapters 6 and 7.

A comparison of the average JRC_F and the *JRC* calculated using the Milne (1990) and the Seidel & Haberfield (1995) relationship is shown in Fig. 3.15. The maximum amplitude (e_{max}) for each of the sample profiles was collected and analysed. The results indicated that some of the e_{max} data were affected by localised measurement error. Average and minimum e_{max} values were plotted to provide upper and lower bounds to the likely *JRC*. The average *e* value used in the Milne calculations appears unreasonable for sample JP05 (predicting $JRC > 20$). This result indicates the influence

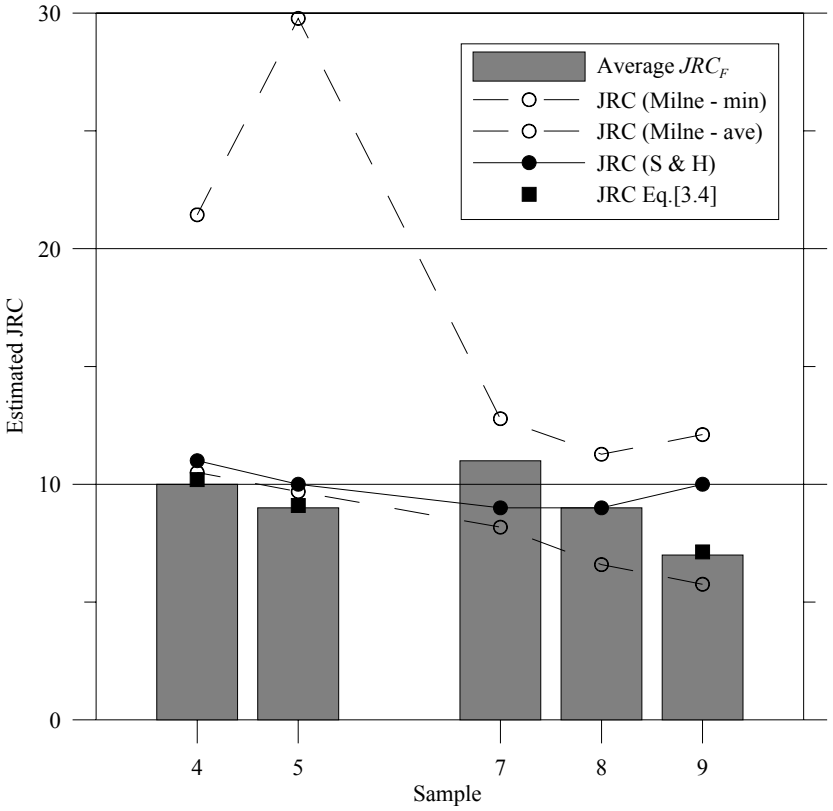

Figure 3.15: Comparison of *JRC* estimates and laboratory test data.

of localised "fly off" data points recorded during the scanning well above or below the plane, which wrongly register as asperities and influence the *JRC* estimate. Application of the Seidel & Haberfield (1995) technique (denoted as S & H on Fig. 3.15) provides a method that is less affected by erroneous data points (provided the sample size is large). The estimated *JRC* (S & H) value is generally within 1 unit of the JRC_F result and bounded by the Milne (1990) average and minimum *e* estimates. To study the validity of Fourier-based *JRC* assessment, the results of single-phase hydraulic testing and the measured average mechanical aperture e_{clip} (where $e_{clip} = e_{m0} - \delta_n$) have been plotted on Fig. 3.15. The figure shows the good agreement between the average JRC_F and the calculated *JRC* from hydraulic testing using Eq. [3.4]. Interestingly, the plotting of the available *JRC* values from single-phase hydraulic tests also confirms the good agreement between the Seidel & Haberfield (1995) and the proposed methodologies.

3.5 Summary

Fracture roughness is a crucial parameter in all engineering site investigations, particularly because of the hydromechanical consequences of fracture deformation under changing stress regimes. The ISRM (1978) standard roughness profiles represent a valuable tool to standardise fracture roughness description using Joint Roughness Coefficients (*JRC*) that are widely accepted across the geological engineering profession. It is well known that fracture roughness has implications for the shear strength of discontinuous media (Barton & Choubey, 1977; McMahon, 1985; Indraratna et al., 1995) as well as discontinuity hydraulic conductivity and groundwater seepage rates (Barton & Bandis, 1980; Witherspoon et al., 1980; Brown, 1987).

A number of different surface profiling techniques have been applied to assess fracture roughness and aperture variation. The simplest techniques presented are considered suitable for application to field–scale problems. The most accurate profiling method applied high-resolution 3-D laser scanning which has the advantage of acquiring high accuracy and high frequency data. The fine scan interval allows scope for considerable detailed analysis. The fracture aperture can be calculated to a high vertical accuracy, and the mean of natural logarithm of the aperture seems to provide a good estimation of the hydraulic parallel plate aperture under single-phase conditions.

The literature describes a variety of numerical techniques that have been previously applied to replicate surface roughness profiles e.g. fractal theory and power spectral density and in this case Fourier series analysis. The results of the standard *JRC* profile analyses show that the Fourier method allows a complex roughness profile to be produced using a limited number of n harmonics, a trace length or period ($2L$) and a reading interval Δx. The results of the calculated series show a very good fit with the original data. The close agreement between the measured and predicted roughness profiles is clearly seen in Fig. 3.10. The same degree of goodness of fit can be obtained

for physical as well as digital rock surface profiles. The surface roughness measuring approach has been developed and calibrated to measurements obtained on a 2mm grid for samples of the order of 100mm long. This methodology is effectively unaffected by scanning interval issues, since the same interval was used for calibration testing on standard JRC profiles. It is possible that this technique introduces a small error with regard to very small wavelength features, although this is not considered likely to significantly impact upon the assessed coefficient, or to have consequences affecting the subsequent derivation of other empirical parameters. It is proposed that the mathematical procedure could be used to accurately and efficiently compare specific profiles with the calculated Fourier coefficients in order to assess the appropriate *JRC*. The proposed Fourier solution provides greater confidence to *JRC* because of the increased mathematical rigour involved in the assessment. This is important when using *JRC* to select appropriate empirical geotechnical properties. The Fourier method could also be applied to fieldwork situations if minor changes were applied to extend standard discontinuity mapping procedures, so that the effect of large-scale roughness could be recorded.

A new technique for fracture roughness assessment has been proposed that can be easily calculated using a simple computer programme or a set of spreadsheet formulae. The methodology appears applicable over the full range of fracture topographies with specimen JRC_F values assessed between 7 and 11. The JRC_F can be compared to *JRC* values predicted from the Barton et al. (1985) relationship. This acceptable agreement between the two results gives confidence in the suitability of the outlined *JRC* assessment technique. The proposed Fourier series approach provides many advantages in terms of application to commercial and academic problems. The method agrees well with other available roughness estimation methods and is not over

sensitive to individual anomalous values arising from scan 'fly off'. The Seidel & Haberfield (1995) method generally provides the greatest similarity of output but the Fourier method requires less than half the data points of the other method, making data collection and interpretation less time consuming without a drop in accuracy. Overall, the results of the roughness analysis indicate that several methods should be applied for any single analysis, e.g. Milne, Seidel & Haberfield and Fourier analysis to identify any anomalous results that would affect an estimate made upon the results of a single method.

Chapter 4

Annular Two-phase Flow Model

4.1. Introduction

The general theory of isothermal, two-phase flow is well established (Wallis, 1969; Hewitt & Naylor, 1976; Govier & Aziz, 1972), although to a lesser degree in geomechanics. The complexity of the phase interaction challenges a clear analytical description of the behaviour. There are several flow pattern classifications for analogue fractures and pipes that qualify two-phase flow e.g. Mishimi & Hibiki, (1996), Fourar et al. (1993) and Golan & Stenning (1969). The flow map approach is subjective because results can be affected by the experimental conditions e.g. fracture aperture and phase injector design. However, general characteristics can still be identified and these tests provide a useful qualitative means to describe the problem to the reader.

For the conditions considered in this study, flow pattern behaviour is primarily affected by the relative velocity of the phases and the volumetric composition of the air-water mixture. Injecting air at increasing rates can lead to the development of simple two-phase flow patterns similar to Fig. 4.1. Water flows exhibit a transition from saturated (S_W = 1) to bubble flows as air phase injection pressure increases. By decreasing S_W, small, rounded and finger-shaped bubbles develop. The pattern evolves to comprise larger cap-shaped geometries with smaller rounded bubbles entrained in the intervening water slug. Progressively complex bubble patterns with relatively small volumes of intervening water phase can develop into a froth pattern. With significant drop in air pressure, continuous air flow paths can develop in an idealised fracture to

create a stratified pattern, where the denser fluid occupies the lower part of the fracture. Alternatively, denser water films can remain in contact with the fracture surfaces, whilst a core of air flows through the fracture, provided that the air phase velocity and the surface tension effects are sufficient to maintain the denser phase in contact with the upper fracture surface. Further discussion of two-phase flow pattern development can be found in Chapter 5, where the results of analogue joint experiments are described.

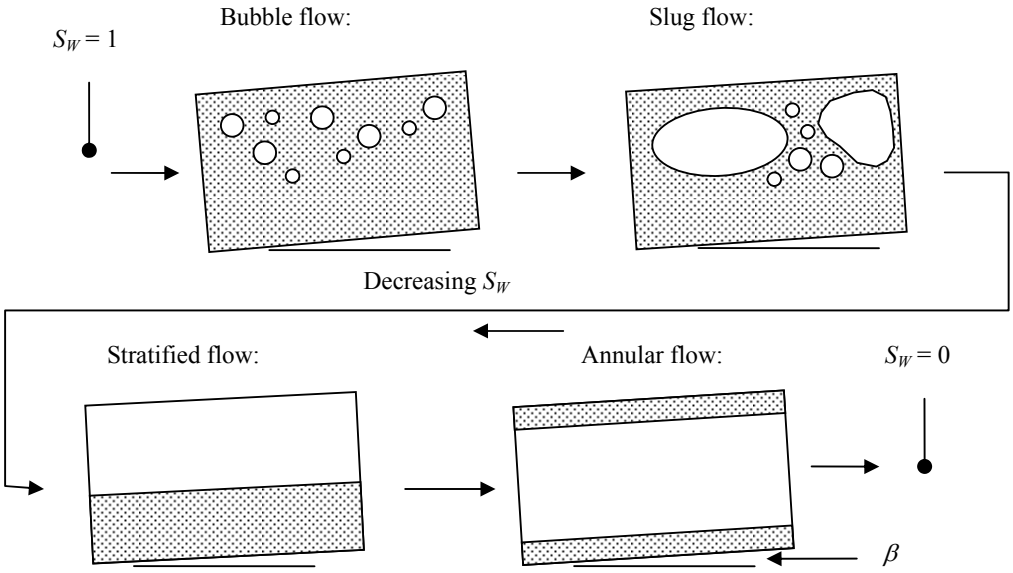

Figure 4.1: Simple smooth-walled, parallel joint elements (inclined at $\beta°$ to the horizontal) showing potential two-phase flow patterns that could be encountered in the geological environment related to variations in water phase saturation S_W. Note: flow direction is left to right and parallel to the fracture walls.

4.2. Theoretical background

Two-phase fluid hydraulics is governed by the conservation of mass, momentum and energy. Physical processes such as phase change, capillary effects and the behaviour of the phase interface can be particularly significant. The most simplistic two-phase flow model is the homogenous fluid concept, which represents each phase as a single equivalent fluid with properties related to their relative proportion. This approach can be used to approximate flow problems and Price & Indraratna (2004) apply this

approach to develop the model presented in Chapter 7. However, a more accurate solution can be achieved by considering each individual phase separately, thus allowing the interaction of the flow processes to be better explored.

Under conditions of 1-D laminar flow, a modified Darcy's Law is applicable to two-phase fracture flow calculation Eq.[4.1], where matrix (or primary) permeability is negligible.

$$Q_i = \frac{K_{ri} e_h^3 w}{12\mu_i}\left(\frac{dp_i}{dx} + \gamma_i \frac{dh}{dx}\right) \qquad [4.1]$$

The variables in Eq. [4.1] define the flow rate Q_i in terms of K_{ri}, γ_i and μ_i, the relative permeability unit weight and kinematic viscosity for a fracture aperture e_h and width w (in the y direction) acted on by a phase pressure gradient dp_i/dx. The 'i' subscript attributes the variable to either the air A or water W phase. Elevation difference (dh/dx) across the fracture can also contribute the potential driving flow, although in this case the small sample height (0.1m) is negligible when pressure gradients of 20 to 200 kPa are applied during the testing. Accordingly, the elevation gradient is neglected in the subsequent experimental analyses.

The phase pressure drop can be calculated from the principle of conservation of momentum. The general equation for the total phase pressure drop of each phase is a combination of the three respective right hand terms in Eq. [4.2]: losses due to friction (f) with the fracture walls; acceleration (a) impacts from localised unsteady flow; and changes in elevation (g) across the area of interest.

$$\frac{dp_i}{dx} = \left(\frac{dp_i}{dx}\right)_f + \left(\frac{dp_i}{dx}\right)_a + \left(\frac{dp_i}{dx}\right)_g \qquad [4.2]$$

Greater accuracy is achieved in Eq. [4.2] if losses due to phase change and interfacial shear force F_{WA} are considered. In this case, phase change is considered in a specific isothermal environment so evaporation or condensation processes do not have to be

considered. This approach is appropriate where flow is considered from a macroscopic perspective over a fracture of length *X*, rather than at a microscopic level, *dx*, since the dynamic small-scale phase behaviour is not modelled. Thus, the phase change process is a change in mass per unit flow length that is related to the change in momentum given by:

$$\Delta(momentum) = (U_A - U_W)\frac{M}{A}\frac{dx}{dz} \qquad [4.3]$$

where, U is the phase velocity, M is the fluid mass and A the cross-sectional area of flow. The frictional loss due to shear at the air-water interface can be written as the product of the interface shear stress τ_{WA} and the interface area, i.e. perimeter perpendicular to the flow direction multiplied by the joint element length. If a unit length is assumed, this can be written as:

$$F_{WA} = \tau_{WA} P_{WA} \qquad [4.4]$$

Specifically re-writing the terms in Eq. [4.2], the frictional losses can be represented as the product of the shear stress (τ_{WJ}) at the fracture wall acting around the perimeter of the fracture (P_{WJ}) and the cross sectional area (A); the acceleration losses can be replaced in terms of the phase mass (M_i) per cross-sectional area and the phase velocity gradient terms; and the elevation component of momentum losses can be represented as the product of the phase density (ρ_i) and fracture orientation (β) from the horizontal. Therefore, combining [4.3] and [4.4] with [4.2] provides the full general equation for two-phase flow:

$$\begin{aligned} A_i \frac{dp_i}{dx} &= -P_{WJ}\tau_{WJ} - \left(\rho_i U_i A_i \frac{dU_i}{dx} + A_i \frac{dU_i}{dt}\right) - A_i \rho_i g \sin\beta \\ &\pm P_{WA}\tau_{WA} - \left((U_A - U_W) M \frac{dx}{dz}\right)_i \end{aligned} \qquad [4.5]$$

The flow behaviour and phase interaction can be analysed by considering the individual phases. The specific development of the proposed two-phase flow model is presented in greater detail in the following sections. However, it is useful to precede this development with an explanation of important theoretical flow characteristics.

4.2.1. Idealised two-phase flow

Idealised two-phase fracture flow calculation usually assumes the fracture flow can be calculated using Darcy's law, written to include Poiseuille's law for flow between smooth parallel surfaces in the form of Eq. [4.1]. If continuous flow of both phases occurs, phase velocity is simply related to the pressure gradient. If one phase becomes discontinuous, phase velocity calculation is less straightforward. In some cases, the discontinuous phase can be entrained in the continuous phase with the same superficial velocity. Analogue joint testing using transparent parallel plate apparatus is an ideal way to study flow behaviour and the applicability of the proposed flow models. Two-phase flow in horizontal fractures was studied by Fourar et al. (1993) using smooth transparent plates as well as naturally rough clay brick surfaces, in order to assess the influence of a limited degree of roughness and the applicability of different two-phase flow models. Their experimental study did not consider the impact of fracture orientation on flow behaviour.

One of the aspects of this project is a more complete laboratory study of idealised two-phase flow, which is presented in Chapter 5. The work performed in this study uses an improved apparatus that incorporates a hinged frame to enable the parallel plate assembly to be rotated through 180 degrees. The writer has considered the application of the homogenous fluid concept to two-phase flow in both horizontal and inclined smooth parallel plates.

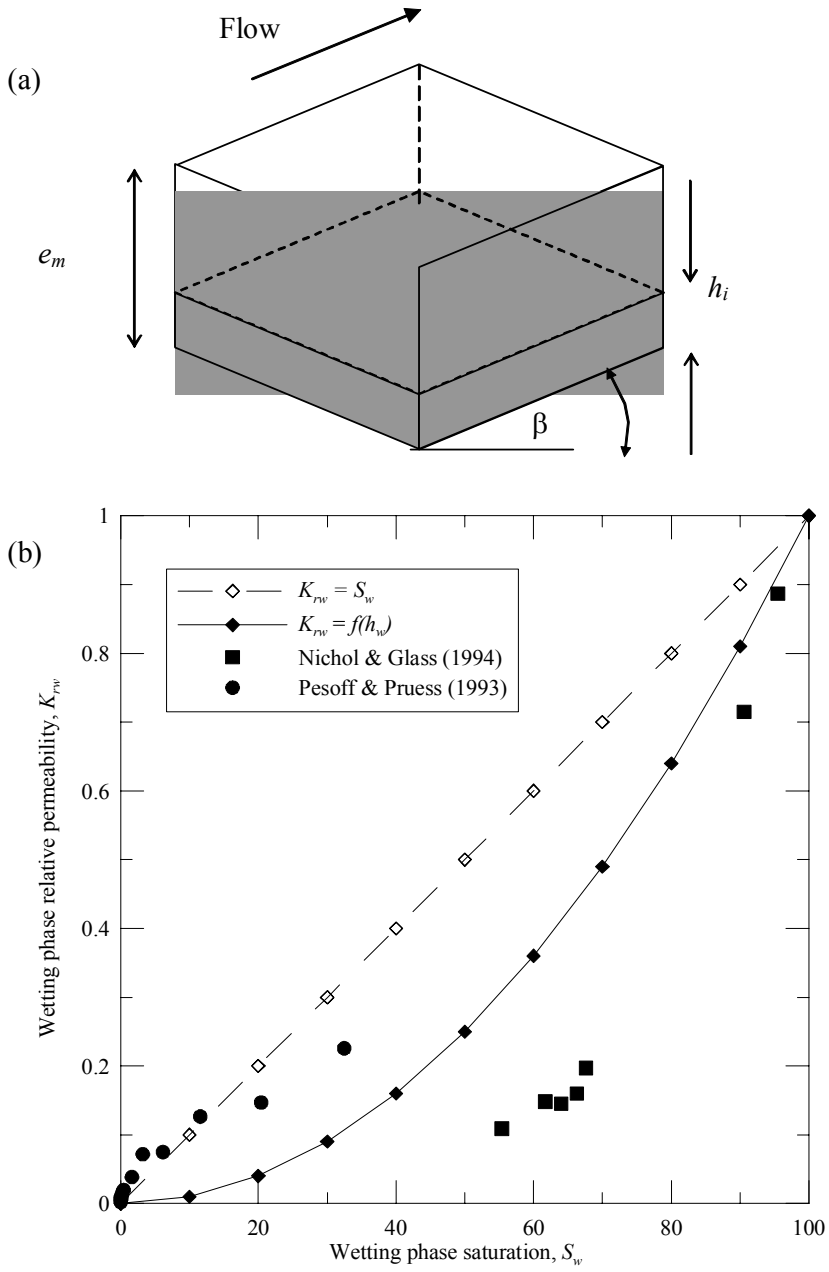

Figure 4.2: Aspects of simplified stratified flow: (a) a schematic view of an inclined idealized partially saturated joint element (aperture e_m); (b) comparison of the K_{rw} versus S_W developed from simplified model assumptions (Indraratna et al., 2003a).

A development of the simple stratified flow model (Indraratna & Ranjith, 2001; Indraratna et al., 2003a) can be applied to the optical two-phase flow results. This approach applies Darcy's law and represents the flow rate of phase *i* in relation to the phase height (h_i) flowing through the idealised fracture (Fig. 4.2).

$$Q_i = \frac{h_i^3 y}{12\mu_i}\left(\frac{dp_i}{dx}\right) \qquad [4.6]$$

This model allows a simple relationship to be developed for the relative permeability K_{ri} (Indraratna et al., 2003b). K_{ri} is the ratio of the two-phase to the single-phase intrinsic permeability (= k_i/k_{si}), and is a key parameter in the description of two-phase flow in geological media. Norton & Glass (1994) have documented the development of several relationships between the wetting phase relative permeability (K_{rw}) and the wetting phase saturation (S_W). One of the first proposed relationships equated saturation to relative permeability and has been used in petroleum engineering analyses:

$$K_{rw} = S_W \qquad [4.7]$$

The validity of Eq. [4.7] was questioned, and on the basis of analogue fracture experiments, modified by Wang & Narasimhan (1985) to include the mean aperture ($\hat{e}$), the mean aperture in contact with the wetting fluid ($\hat{e}_w$), and a tortuosity factor *(T)* to allow for non-parallel flow:

$$K_{rw} = S_W T\left(\frac{\hat{e}_w^{\,2}}{\hat{e}^2}\right) \qquad [4.8]$$

The application of the Eq. [4.8] to real fractures is problematic because the assessment of $\hat{e}_w$ and T requires detailed topographic and aperture data that is often only available as part of a specialised academic study. The writer presented an alternative approach to relative permeability assessment in Indraratna et al. (2003). The development is an extension of the stratified model and is applicable to inclined relatively smooth fractures, where capillary effects are negligible. The simplified stratified model assumed flow of both phases obeys Darcy's Law and in Eq.[4.6] replaces the aperture (e_m) and K_{ri} by the phase height (h_i). This idealisation allows K_{ri} to be written as a ratio of two phase and single-phase intrinsic permeability using Poiseuille's Law:

$$K_{rw} = \left(\frac{k_i}{k_{si}}\right) = \left(\frac{h_i}{e_m}\right)^2 \qquad [4.9]$$

Combining both the K_{ri} terms provides a new expression in terms of e_m and h_i:

$$\Sigma K_{ri} = \left(\frac{h_W}{e_m}\right)^2 + \left(\frac{h_A}{e_m}\right)^2 == 1 - \frac{2h_W h_A}{e_m^2} \qquad [4.10]$$

Consideration of Eq. [4.10] shows that $K_{rA} + K_{rW} \leq 1$ since the term $(2h_W h_A/e^2) > 0$. This outcome is illustrated in Fig. 4.2(b) and corroborates the findings of some other researchers, such as Pruess & Tsang (1990).

The proposed relationship for an idealised inclined smooth fracture with parallel flow is plotted in Fig. 4.2b to compare the results with some published experimental results from Norton & Glass (1994) and Persoff & Pruess (1993). Fig. 4.2 also shows the schematic relationship between fracture aperture e, phase height, h_i and saturation, S_i, from which it is clear that $S_i = h_i/e$. The experimental data plotted in Fig. 4.2 was obtained experimentally from horizontal analogue fractures (Norton & Glass 1994) and natural rough fractures (Persoff & Pruess, 1993). This analysis is appropriate for macroscopic steady state flow in rough fractures where capillary effects are negligible. The analysis of transient conditions, where wetted structures form under small flow rates in capillary sensitive conditions are better modelled using the approach described by others e.g. Glass (1993) or Keller et al. (2000), especially in the case of environmental problems where multiphase flow or contaminant migration occurs in a high-diffusion low-advection situation. The relationship is also applied to analysis of laboratory data acquired during this project and presented in Chapters 5 and 6. Figure 4.2 also shows the schematic relationship between fracture aperture, phase height, h_i and saturation, S_i, from which it is clear that $S_i = h_i/e_m$. The departure of expected fracture two-phase hydraulics from the theoretical response is indicated if h_A at $S_W = 0$ is not

equal to h_W at S_W = 100%. This behaviour can occur due to presence of significant roughness, partial saturation or localised fracture infill, and has been observed during laboratory testing due to the degradation of the fracture walls and formation of low permeability clay infill. The theoretical response of the fracture in the case of obstructions such as clay infill can be regained by removal of gauge from the surface.

4.2.2. Physical processes affecting fracture behaviour

The most important physical processes to affect facture flow include capillarity, phase compression and solubility, and fracture dilation in response to changes in the effective stress environment. These factors are discussed individually in the following sub-sections.

4.2.2.1 Capillary effects

In low flow or low pressure environments, where capillary flow is the dominant mechanism, water percolates between the fracture surfaces, driven in the form of dendritic fingers by the interaction of gravitational and capillary pressures (Nichol & Glass, 1994). This mechanism is different to the 'free' flow concept in the proposed simplified two-phase flow models.

The role of capillarity is increasingly significant for smaller aperture fractures, and the capillary pressure p_C is calculated by a relationship between surface tension, the fluid dependent interface contact, or 'wetting' angle, and the meniscus curvature at the air-water interface (Pruess & Tsang, 1990; Keller et al., 2000; Indraratna et al., 2003a).

$$p_C = \left(T_s \cos\theta\right)\left(\frac{1}{r_1} + \frac{1}{r_2}\right) \qquad [4.11]$$

Assuming conservatively, that the water is pure and the temperature is constant, surface tension remains unchanged (72.75mN/m at 20°C cited by Fredlund & Rahardjo, 1993). However, it is quite likely that impurities will be present in the water, significantly

reducing T_s. The terms r_1 and r_2 are the radii of curvature of the meniscus, measured perpendicular and parallel to the fracture plane, respectively. For idealised fractures, if the contact angle θ is assumed to be zero, $r_1 = e_m/2$ and r_2 is very large, the above equation simplifies further:

$$p_C = (2T_s)/e_m \qquad [4.12]$$

From Eq. [4.10] it can be seen that capillary pressure is increasingly important for narrow fractures and especially where phase pressures drops are relatively small. Further discussion of the implications of capillary effects on fracture flow is developed in Section 4.3.1.

4.2.2.2 Fluid physical properties

The proposed model considers steady state, isothermal flow conditions. This simplification is warranted because the envisaged application of the proposed model is in sub-surface environments, where temperature gradients are shallow, both spatially and temporally. The sensitivity of air and water properties to temperature is described by Table 4.1. The density of air and water varies by < 8% over the listed temperature range. The viscosity of water shows the largest sensitivity to temperature, but careful selection of the initial water viscosity value allows optimal accuracy of any calculations. The envisaged small temperature gradients would limit the variation in water viscosity to < 5%. Two-phase non-isothermal analysis becomes a more difficult problem to solve because of the variation in viscosity as well as the changes in fluid energy.

Table 4.1: Variation in density and viscosity of air and water with temperature (after Vennard & Street, 1982).

Temperature º C	**Air**		**Water**	
	Density (tm^{-3})	Viscosity (Pa s) at 101kPa	Density (tm^{-3})	Viscosity (Pa s) at 101kPa
10	1.24×10^{-3}	1.76×10^{-5}	0.9997	1.31×10^{-3}
20	1.20×10^{-3}	1.79×10^{-5}	0.9982	1.0×10^{-3}
30	1.15×10^{-3}	1.86×10^{-5}	0.9956	0.80×10^{-3}

The fluid phase compressibility in a hydromechanical model must be included in two-phase calculation for the prediction of the physical behaviour of the fluid-fracture system (Fredlund & Rahardjo, 1993). This phenomenon is most notable for the air phase because of the lower viscosity, and particularly, due to changes in phase pressure or in-situ stress. Air is known to dissolve in water, occupying a maximum of 2% of the water by volume. Following the development of unsaturated soil mechanics theory, air phase behaviour has become better understood in geotechnical engineering. The coefficient of solubility and the volumetric coefficient of compressibility for different gases could be applied if another gas, e.g. methane, was considered instead of air. This allows the application of the proposed model to broader engineering conditions, e.g. underground coal mining in gassy mines. The mechanical significance is illustrated by comparing the variation in mixture compressibility when the 2% dissolved air component is included in the calculations.

Indraratna & Ranjith (2001) identified that for an idealised fracture, the total normal deformation (Δ_T) of the aperture can be related to compressibility of air (ξ_{AC}) and water (ξ_{WC}), solubility of air in water (ξ_{AD}) and mechanical normal deformation (δ_n) due to changes in stress.

$$\Delta_T = \xi_{AC} + \xi_{AD} + \delta_n - \xi_{WC} \qquad [4.13]$$

The volumetric compression per unit fracture area ξ_{iC} of the *i* phase is related to change in volume (ΔV) in the *x*-*y* (fracture) plane. The application of the coefficient of solubility and the volumetric coefficient of compressibility within the model enables different gases to be considered instead of air. In this case, the compression of each phase can be calculated using the isothermal compressibility of air and water (C_A and C_W), and the phase volume V_i,

$$C_i = \frac{1}{V_i}\frac{dV_i}{dp_i} \qquad [4.14]$$

thus,

$$\xi_{ic} = \frac{\Delta V}{x.y} = \frac{C_i V_i dp_i}{x.y} \qquad [4.15]$$

For a fracture containing a fluid comprising bubbles of gas, the phase pressures rapidly equilibrate as the phase volume (V_i) and saturation (S_i) change in response to the phase pressure; in the case where the difference in elevation is small, and 'slip' or 'hold up' is assumed negligible, one can assume $dp_A = dp_W = dp$.

Table 4.2: Variation in solubility of different gases (after Fredlund & Rahardjo, 1993).

Temperature	**Coefficient of solubility at standard atmospheric pressure**		
º C	**Oxygen (O_2)**	**Nitrogen (N_2)**	**Air**
0	1.46×10^{-5}	2.39×10^{-5}	3.84×10^{-5}
10	1.13×10^{-5}	1.88×10^{-5}	3.01×10^{-5}
20	9.11×10^{-6}	1.55×10^{-5}	2.47×10^{-5}
30	7.55×10^{-6}	1.31×10^{-5}	2.07×10^{-5}

As shown in Indraratna & Ranjith (2001), the change in volume of dissolved air in water (V_D) can be described by the Ideal Gas law and Henry's law at certain pressure and temperature conditions. The magnitude of the solubility changes with gas composition, as can be seen in Table 4.2. Considering the specific case of a joint of length x and width y, the change of equivalent air phase height ξ_{AD} due to dissolved air may be written as follows:

$$\xi_{AD} = \frac{V_D}{x \cdot y} \qquad [4.16]$$

Air dissolves in water, and has the potential to occupy a maximum of 2% to 3% of the water by volume. Consideration of the data listed in Table 4.3 shows that the

volumetric coefficient of solubility varies slightly with temperature. Over the depth range commonly encountered in shallow Australian underground coal mines e.g. 500m, 2% is a reasonable estimate.

Table 4.3: Air volumetric solubility with temperature (after Fredlund & Rahardjo, 1993).

Temperature ºC	**Volumetric solubility coefficient**
0	2.92×10^{-2}
10	2.28×10^{-2}
20	1.87×10^{-2}
30	1.56×10^{-2}

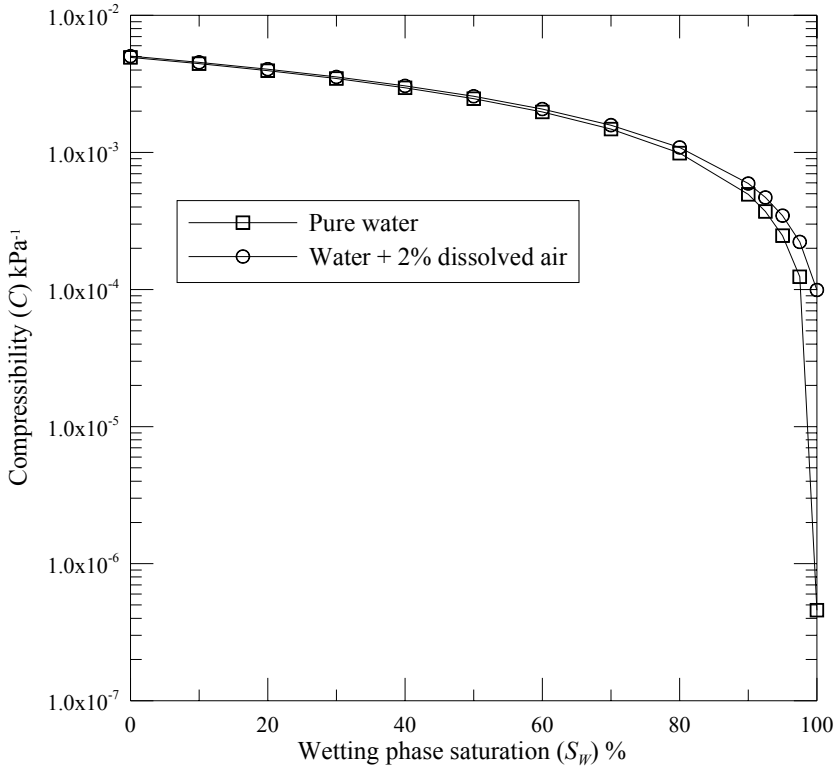

Figure 4.3: Variability of air-water mixture compressibility related to wetting phase saturation (S_W).

Adopting the 2% volumetric solubility of air in water, the implication for mixture compressibility can be contemplated. A two-phase mixture of air and water will yield increasing compressibility as the compressible (air) phase component increases.

This is shown in Fig. 4.3, emphasising the significance of dissolved air on the mechanical behaviour at high S_W values, especially where $S_W \approx 1$ and the difference in compressibility is more than 2 orders of magnitude more than for water. Further review of the mechanical aspects of a two-phase air + water mixture is contained in Chapter 7.

4.2.2.3 Mechanical dilation

The macroscopic mechanical response to fracture normal loading is accepted to be non-linear (Bandis et al., 1985; Brady & Brown, 1992; Long, 1996) over large load increments e.g. Fig. 4.4. Bandis et al. (1985) attributed a hyperbolic function to describe the normal stress:fracture closure component of the Barton-Bandis model which can be written in the form:

$$K_n = K_{ni}\left(1 - \sigma_n / \left(\delta_{\max} K_{ni} + \sigma_n\right)\right)^{-2} \qquad [4.17]$$

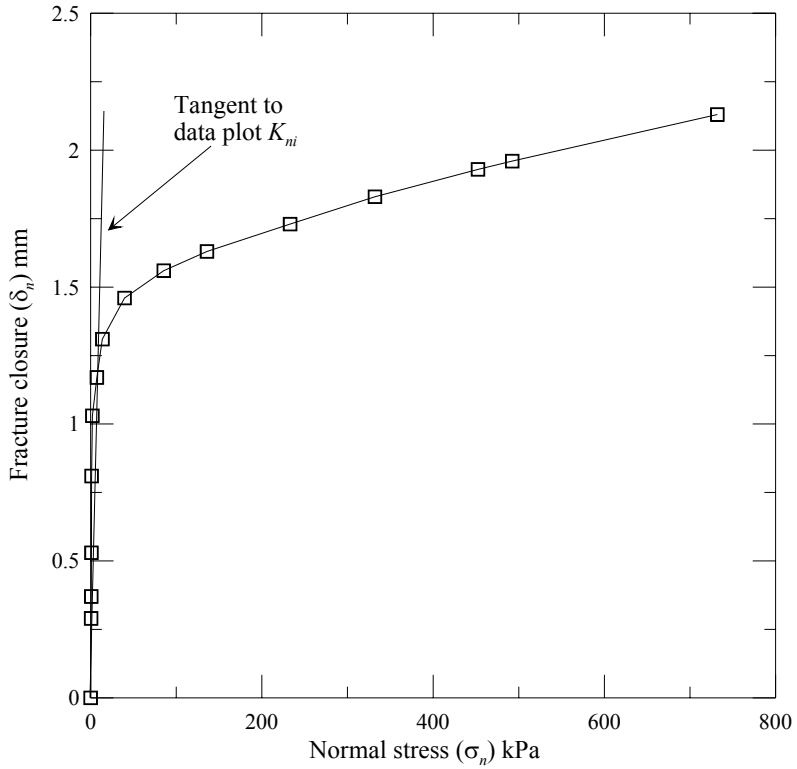

Figure 4.4: Plot of normal fracture closure versus fracture normal stress illustrating non linear closure response.

Careful selection of the normal /confining stress interval allows the curved envelope to be approximated by a piecewise, linear stress:deformation model. The change in fracture normal stiffness can be assessed from test observations of clip gauge deflection in response to changes in confining stress and pore fluid pressure. The approach used here considers an average fracture deformation because the measurement is assessed at only two locations along the fracture i.e. the clip gauge measures deformation only at that specific position on the sample. Some techniques, such as the Hertz contact theory have been proposed to consider individual asperity contacts (Sausse, 2002). The Hertz approach is better suited to analysis where many more closely spaced measurement points are available and detailed computer calculation is being performed. The method of clip gauge assessment is described in Chapter 6, with reference to the two-phase triaxial testing and will not be expanded upon further at this time.

The mechanical change in fracture aperture can be related to the normal fracture stiffness (K_n) and change in applied normal stress ($\Delta\sigma_n$). This should be written in terms of effective stress since the mechanical reaction of a water filled fracture will be mitigated by the presence of the fluid mixture with a pore pressure p, particularly where $p \approx \sigma_n$:

$$\delta_n = \frac{\Delta\sigma_n'}{K_n} = \frac{\Delta\sigma_n - p}{K_n} = \frac{\left(\Delta\sigma_1 \cos^2\beta - \Delta\sigma_3 \sin^2\beta\right) - p}{K_n} \qquad [4.18]$$

4.2.3. Two-phase flow in geological media

Despite careful development of a theoretical understanding of two-phase flow, a discontinuous geological medium is paradoxically defined by variable aperture fractures. This reality means that flow occurs between surfaces that are neither smooth nor parallel. The idealised theory works reasonably well if flow is occurring between fracture elements where aperture variation is small. In the case where fracture

roughness is significant, there is an accepted deviation from theory (Witherspoon et al., 1981). In order to analyse fluid flow in fractured rock, the spatial distribution of interconnecting fractures as well as the spatial variability of fracture apertures must be accommodated. Where apertures are assumed to be relatively uniform and the fracture network can be idealised to that of a simple geometry (Snow 1968), the analysis can be simplified for single-phase fluids. The characteristics of geological environments make such simplifications both necessary and limited in their application. For single-phase flow problems, it is often difficult to obtain sufficient field information on fracture network geometry and connectivity without access to a considerable area of rock exposure. For two-phase flow problems, the data collection is even more difficult, with most investigations restricted to collection of total flows per unit area from faces in underground excavations (Kissell & Edwards, 1975), rather than isolated detailed records of flows from a particular fracture. Sometimes borehole investigations using cross-hole techniques and relatively small borehole separation can lead to success in single-phase testing (Hsieh et al., 1983; Di Biagio, 1973), where good intersection of the fracture network has been achieved. In this paper, discussion is limited to the fracture level and does not consider fracture network flow in detail.

4.2.3.1 Fracture Roughness

The discussion in Chapter 3 established that roughness is qualified with respect to standard 100mm long profiles (ISRM, 1978) by reference to the Joint Roughness Coefficient (*JRC*) in geomechanics. In this study, the rock samples were selected to be 100mm long so that the issue of the 'scale effect' did not impact upon the interpretations. The impact of longer wavelength roughness (relative to the fracture length) is a factor that is well understood to impact upon the flow of characteristics as well as the mechanical behaviour (Barton et al., 1985). Roughness has a much smaller

impact on air flow in fractures because of the lower fluid viscosity, as can be judged from the earlier work by Di Biagio (1973).

The impact of small scale roughness relates to capillarity and surface tension effects. This is significant when applying a two-phase conceptual flow model, because the microscopic scale roughness for most medium- and fine-grained rocks tends to trap water within the intergranular pores exposed at the fracture surface. This means that the fracture surface remains wetted except under conditions of elevated temperatures or very high velocity gas flows at low S_W. This observation is a phenomenon encountered in wider engineering situations (Wallis, 1969) and not confined to geomechanics. Accordingly, stratified flow as postulated by Ranjith (2000) could only feasibly occur over relatively short fracture lengths in sub-horizontal fractures, where the rock matrix is coarse-grained with a low porosity, such as is the case for some igneous or metamorphic rocks, for example, granites, gabbros and gneiss. It is envisaged that grain or crystal size on a microscopic scale will exert a control on the distribution and size of pore throats which will control the location and extent of wetted film on the fracture surface. This phenomenon is considered in more detail in Section 4.3.1.

4.2.3.2 Aperture variability

When considering the local aperture of an individual fracture, much has been written on the potential statistical distributions applicable to real rock fractures and the relationship between statistical values and hydraulic performance. The literature, including Zimmerman & Bodvarsson (1996), provides useful reviews of the common forms of aperture distributions. Laboratory studies of sampled real fractures scanned using a microscope and micrometer showed Gaussian distributions (Yeo et al., 1998). Injection techniques were applied in separate studies published by Gale (1990) and Hakami & Barton (1990) that identified log normal distributions appropriate to their measured

data. The laser scanning results from the sampled fractures in this project tend to confirm that a log normal distribution is one of the most applicable aperture distributions and that the hydraulic aperture can be approximated by the mean of that log normal distribution ($\bar{e}_{\log} = e_h$).

Kostakis & Harrison (1999) accounted for variable apertures in their analysis of counter current flow of a gas bubble through a water-filled rough fracture. Their analytical solution provides a thorough analysis of microscopic theoretical flow behaviour, but does not assist in understanding the macroscopic response of a two-phase (co-current) flow, which is the goal of this project. Their analysis does emphasise the tendency for the denser fluid to occupy the smaller aperture elements, resulting in the lighter phase flowing around the larger aperture elements. Fracture element access is modelled as a function of the driving phase pressure gradient and the aperture element capillary number (Keller et al., 2000; Pruess & Tsang, 1990).

4.3. Proposed Two-phase Flow Model

The two-phase flow model considered in this chapter overcomes limitations of the previous simplified two-phase flow model (Indraratna & Ranjith, 2001). This model considers theoretical and experimental limitations on the development of continuous stratified flow in hydromechanical rock fracture analysis. From this study, it became clear that rough fracture surfaces are unlikely to dry out under test conditions, unless particular conditions combine, such as extremely low S_W and high p_A. This realisation has implications for the calculation of the theoretical fracture wall and interface shear forces. Consideration of the conservation of momentum allows new equations to be formulated to calculate these shear forces in terms of the phase height and also to include the JRC. Conservation of momentum no longer provides a unique analytical

solution for the case of more complex annular two-phase flow patterns, although this is achieved through application of the conservation of mass.

4.3.1. Fracture wall dry out

The proposed two-phase flow model considers potential fracture wall dry out with the passage of the gaseous phase. Observation of two-phase flow between smooth parallel plates (Chapter 5), shows that the fracture wall in contact with the air bubble usually appears dry i.e. there is no water film between the air bubble and the plate wall. This behaviour was maintained whilst phase slip conditions were negligible ($U_A \approx U_W$). However, for natural rough rock fractures, both the surfaces were observed to be wet when a test sample was separated, i.e. there were no dry spots on the surfaces where the air bubbles had been present prior to separation. To explain this fact, it is useful to consider the observation for rough surfaces in terms of capillary theory.

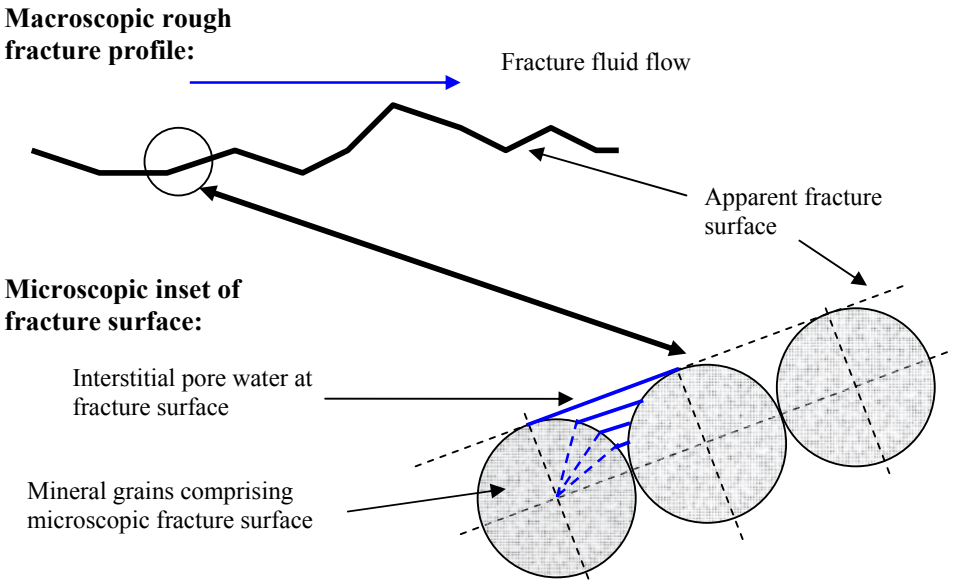

Figure 4.5: The impact of microscopic capillary forces on saturation of a rough rock fracture surface.

The example of a rough fracture is shown in Fig. 4.5 which shows the idealised physical characteristics of the fracture surface at a microscopic level. The fracture surface

comprises mineral grains or lithic fragments. The macroscopic fracture surface can be represented by a tangent to the top of the grains, and the microscopic roughness, i.e. that which would be felt by rubbing with you hand, is represented by the interstices. For this example, two adjacent grains are considered with different interstitial water levels distinguished by the intersection angle at the grain centre. The increasing interstitial saturation is associated with an increase in angle (relative to the fracture plane). A range of angles in 22.5° intervals were considered and used to calculate the corresponding S_W (Fig. 4.6 and Table 4.4).

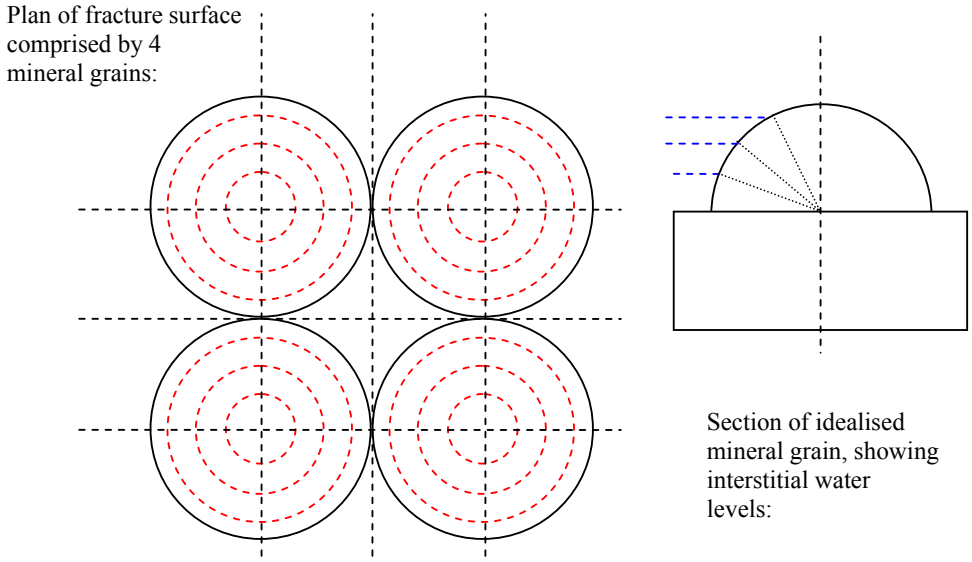

Figure 4.6: Schematic plan and section of mineral grains on a fracture surface showing idealised insterstitial saturation.

For each of the angles considered, the separation between grains is calculated, which can then be substituted as e_m in Eq. [4.10] to calculate the capillary pressure associated with that level of interstitial saturation. These calculations illustrate of the significance of capillary effects on fracture wall dry out for a range of different particle diameters shown in Table 4.5:

Table 4.4: Approximate interstitial saturation levels corresponding to intersection angles.

Angle (°)	Moisture content w (%)	Interstitial Saturation S_W (%)
1	≈ 0.00	≈ 0
22.5	7.2	21
45	18.1	53
67.5	29.8	87
90	≈ 35	≈ 100

Table 4.5: Summary of grain size descriptors.

Grain diameter, d (mm)	Particle Descriptor	
	Soil	Rock
> 2	GRAVEL	Rudaceous (of sedimentary) or coarse grained
$2 > d > 0.6$	Coarse SAND	Coarse (sandstone) or medium grained (of igneous and metamorphic)
$0.6 > d > 0.2$	Medium SAND	Medium (sandstone) or medium grained (of igneous and metamorphic)
$0.2 > d > 0.06$	Fine SAND	Fine (sandstone) or medium grained (of igneous and metamorphic)
$0.06 > d > 0.002$	Fine to coarse SILT	Siltstone or fine grained (of igneous and metamorphic)
$0.002 > d$	CLAY	Claystone or fine grained (of igneous and metamorphic)

The particle diameters in Table 4.5 can be thought of as representing decreasing fracture surface grainsizes from gravel to clay, e.g. from a pegmatite to a rhyolite, or a conglomerate to a claystone. The decreasing grain size corresponds to a reducing interstice size and volume, which are therefore related to the capillary number N_{cap} and capillary or accessibility pressure p_C of the pore volume. Using the particle diameters listed in Table 4.5, the interstitial saturation and the associated capillary pressure can be compared, Fig. 4.7. The plot indicates the accessibility pressure, or the capillary pressure that must be overcome to displace the water from the interstice. It is noted that higher displacement pressures are needed for finer grained particles for all saturation

levels and that a phase pressure greater than 1 kPa is needed to displace water even from a bed of fine sand size particles. For the case of water as the filling fluid, the associated difference in elevation (or water table inclination) across the grain that is needed to overcome the accessibility pressure is considerable. This confirms the observation that there is not significant gravity drainage of the fracture surface unless the grain diameter is ≥ 2mm (Fig. 4.8).

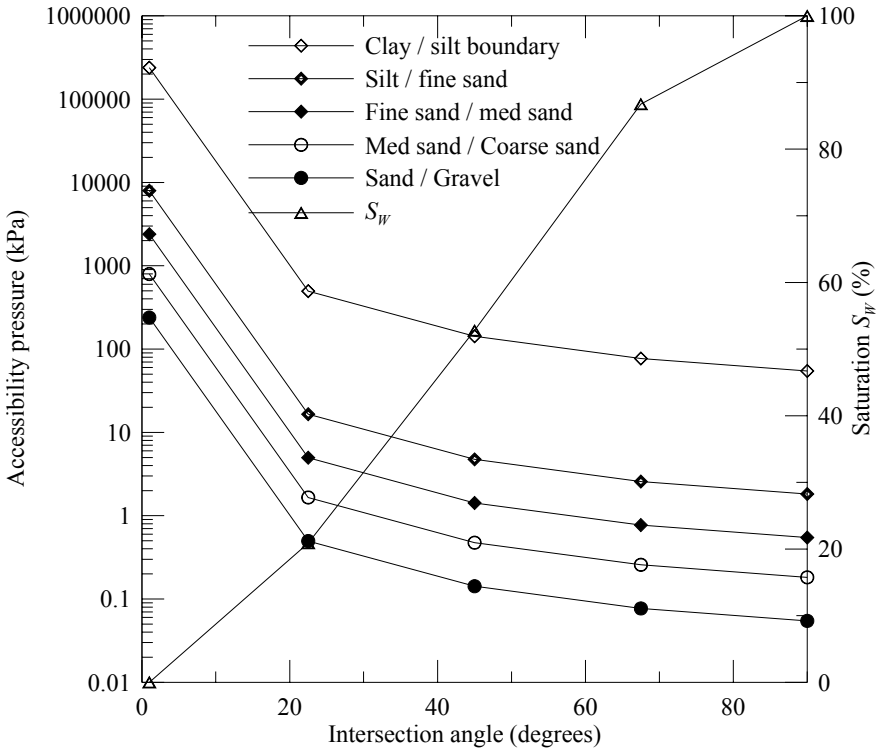

Figure 4.7: Graph comparing interstice accessibility pressure and saturation for an idealised fracture surface.

The calculations summarised in Figs. 4.7 and 4.8 show that unless coarse or very coarse grained materials comprise the fracture surface, it is realistic to assume that a water film will remain in contact with the fracture surface. Fig. 4.8 shows that for grains up to medium sand size gravity drainage will not influence a water film coating a fracture. Allowance for the presence of the wider water film distribution means that there are greater momentum losses than previously considered because of the higher magnitude shear stresses associated with the water-joint surface.

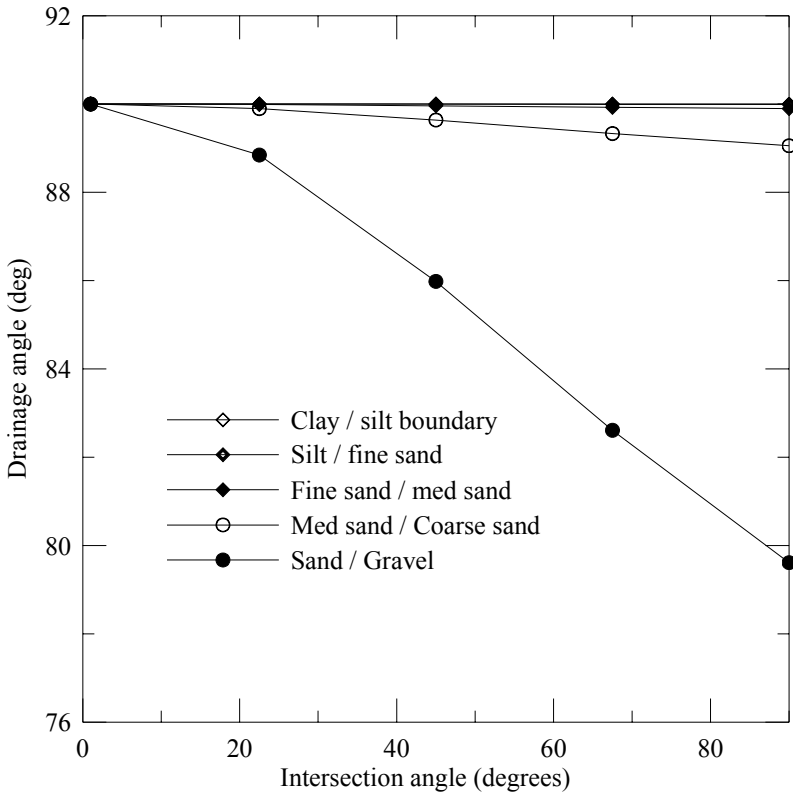

Figure 4.8: Graphical comparison of gravity drainage potential for an idealised fracture surface.

4.3.2. Fracture wall and interface shear forces

The project aim has been to devise a refined geomechanical two-phase flow model that is applicable to the isothermal macroscopic fracture flow observations. Such a model is envisaged to be equally applicable to laboratory and field testing environments and is particularly suitable given the difficulty in development of a robust microscopic flow model. This aim was also a motivation in developing optical two-phase flow testing apparatus that is discussed in greater detail in Chapter 5. A significant theoretical extension of the Indraratna et al. (2003b) stratified flow model has been carried out to consider annular flow conditions. The proposed annular flow model also conceptualises the slug flow pattern, where the air phase bubbles are separated by small volume liquid slugs, whilst a water film remains in contact with the fracture surfaces (Fig. 4.9) for the conditions where bubble volumes are relatively large. Small bubble-volume flows can also be considered with the homogenous fluid model discussed in Chapter 7.

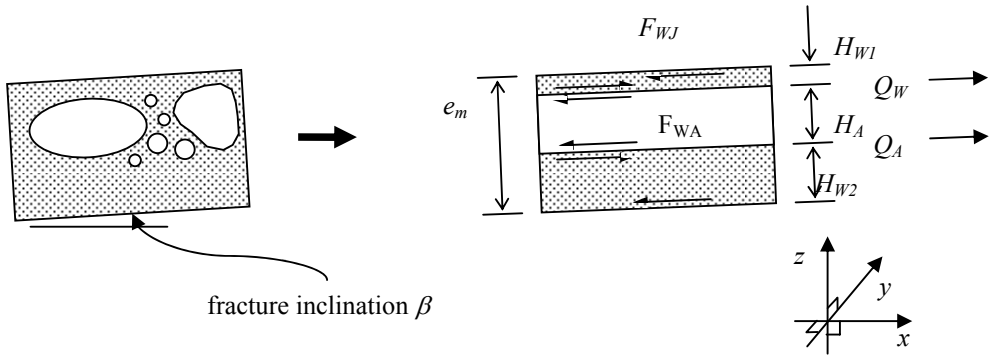

Figure 4.9: Diagram showing conceptual development of the slug flow pattern to the proposed Simplified Two Phase Annular flow model, defining interface and wall shear forces (F_{WA} and F_{WJ}), fracture aperture (e_m) and Annular Flow Phase height components (H_{W1}, H_{W2}, H_A). Note - orientation of fracture element is β^o from the horizontal.

Conservation of momentum can be applied to each of the separate phases, including allowance for phase change and shear forces corresponding to the fracture walls and the air-water interface. Re-writing Eq. [4.5] for each water and air phases provides expressions that can be combined in different forms for the relative motion or the total change in momentum, as represented by Eqs. [4.19] and [4.20].

$$\rho_W\left(U_W\frac{dU_W}{dx}-\frac{dU_W}{dt}\right)+\rho_A\left(U_A\frac{dU_A}{dx}-\frac{dU_A}{dt}\right)-\frac{dp_W}{dx}-\frac{dp_A}{dx}-(\rho_W+\rho_A)g\sin\beta$$
$$-\frac{2F_{WJ}}{H_W}+2F_{WA}\left(\frac{1}{H_W}-\frac{1}{H_A}\right)-(U_A-U_W)M\frac{dx}{dz}\left(\frac{(1-\eta)}{H_W}+\frac{\eta}{H_A}\right)=0 \qquad [4.19]$$

$$\rho_W\left(U_W\frac{dU_W}{dx}-\frac{dU_W}{dt}\right)-\rho_A\left(U_A\frac{dU_A}{dx}-\frac{dU_A}{dt}\right)-\frac{dp_W}{dx}+\frac{dp_A}{dx}-(\rho_W-\rho_A)g\sin\beta$$
$$-\frac{2F_{WJ}}{H_W}+2F_{WA}\left(\frac{1}{H_W}+\frac{1}{H_A}\right)-(U_A-U_W)M\frac{dx}{dz}\left(\frac{(1-\eta)}{H_W}-\frac{\eta}{H_A}\right)=0 \qquad [4.20]$$

where, F_{WA} is the water-air interfacial shear force $\tau_{WA}.P_A$ for unit fracture length ($x = 1$); F_{WJ} is the water joint shear force $\tau_{WJ}.P$ for unit fracture length ($x = 1$); H_A is the phase height of the idealised annular air core; H_W is the water phase height ($=H_{W1} + H_{W2}$); the fracture is defined by the aperture $e_m = H_{tot} = H_A + H_W$ and width y (in the y direction); and the total phase change momentum loss is proportioned between both phases by the

factor η. It should be explained that for each phase, the component of phase change momentum loss must be calculated from the solution of [4.17] and [4.18] and could be achieved by consideration of the conservation of energy. However, phase change related momentum loss only becomes significant where phase slip impacts on the flow, and the denser phase is 'held up' i.e., $U_A \approx U_W$ assumption no longer applicable.

If we consider the joint element to be of unit width and length Eq. [4.5] can be re-written to give for each individual phase:

$$\begin{aligned}&\rho_W\left(U_W\frac{dU_W}{dx}-\frac{dU_W}{dt}\right)-\frac{dp_W}{dx}-\rho_W g\sin\beta\\&-\frac{2F_{WJ}}{H_W}+\frac{2F_{WA}}{H_W}-\frac{\left(U_A-U_W\right)}{H_W}(1-\eta)M\frac{dx}{dz}=0\end{aligned} \qquad [4.21]$$

The corresponding air phase expression becomes:

$$\begin{aligned}&\rho_A\left(U_A\frac{dU_A}{dx}-\frac{dU_A}{dt}\right)-\frac{dp_A}{dx}-\rho_A g\sin\beta\\&-\frac{2F_{WA}}{H_A}-\frac{\left(U_A-U_W\right)}{H_A}\eta M\frac{dx}{dz}=0\end{aligned} \qquad [4.22]$$

Subtracting the expressions [4.21] from [4.22] ultimately provides a solution for the shear forces:

$$\begin{aligned}&\rho_W\left(U_W\frac{dU_W}{dx}-\frac{dU_W}{dt}\right)-\rho_A\left(U_A\frac{dU_A}{dx}-\frac{dU_A}{dt}\right)-\frac{dp_W}{dx}+\frac{dp_A}{dx}\\&-\rho_W g\sin\beta+\rho_A g\sin\beta-\frac{2F_{WJ}}{H_W}+\frac{2F_{WA}}{H_W}+\frac{2F_{WA}}{H_A}\\&-\frac{\left(U_A-U_W\right)}{H_W}(1-\eta)M\frac{dx}{dz}+\frac{\left(U_A-U_W\right)}{H_A}\eta M\frac{dx}{dz}=0\end{aligned} \qquad [4.23]$$

Combining common terms to simplify the expression gives:

$$\begin{aligned}&\rho_W\left(U_W\frac{dU_W}{dx}-\frac{dU_W}{dt}\right)-\rho_A\left(U_A\frac{dU_A}{dx}-\frac{dU_A}{dt}\right)-\frac{dp_W}{dx}+\frac{dp_A}{dx}-\left(\rho_W-\rho_A\right)g\sin\beta\\&-\frac{2F_{WJ}}{H_W}+2F_{WA}\left(\frac{1}{H_W}+\frac{1}{H_A}\right)-\left(U_A-U_W\right)M\frac{dx}{dz}\left(\frac{(1-\eta)}{H_W}+\frac{\eta}{H_A}\right)=0\end{aligned} \qquad [4.24]$$

In the case where capillary pressure and acceleration terms are small because of the steady state flow conditions, $p_W \approx p_A$; also let us assume that 'slip' is also negligible, i.e. $U_W \approx U_A$.

$$(\rho_W - \rho_A)U_i \frac{dU_i}{dx} - (\rho_W - \rho_A)g\sin\beta - \frac{2F_{WJ}}{H_W} + 2F_{WA}\left(\frac{1}{H_W} + \frac{1}{H_A}\right) = 0 \qquad [4.25]$$

For the situation of a sample under test in the TPHPTA, the change in velocity over the sample length is very small, thus:

$$2F_{WA}\left(\frac{1}{H_W} + \frac{1}{H_A}\right) - \frac{2F_{WJ}}{H_W} = (\rho_W - \rho_A)g\sin\beta \qquad [4.26]$$

The final simplification to Eq. [4.26] can be made using the relationship between phase height and saturation, i.e., $H_A / (H_A + H_W) = S_A = 1 - S_W$;

$$\frac{F_{WA}}{(1-S_W)H_W} - \frac{F_{WJ}}{H_W} = \frac{1}{2}(\rho_W - \rho_A)g\sin\beta \qquad [4.27]$$

Returning to Eqs. [4.21] and [4.22], but this time summing the formulae, generates a second expression for the total pressure drop of both phases:

$$\begin{aligned}&\rho_W\left(U_W\frac{dU_W}{dx} - \frac{dU_W}{dt}\right) + \rho_A\left(U_A\frac{dU_A}{dx} - \frac{dU_A}{dt}\right) - \frac{dp_W}{dx} - \frac{dp_A}{dx} - \rho_W g\sin\beta - \rho_A g\sin\beta \\ &- \frac{2F_{WJ}}{H_W} + \frac{2F_{WA}}{H_W} - \frac{2F_{WA}}{H_A} - \frac{(U_A - U_W)}{H_W}(1-\eta)M\frac{dx}{dz} - \frac{(U_A - U_W)}{H_A}\eta M\frac{dx}{dz} = 0\end{aligned} \qquad [4.28]$$

The simplified expression for Eq. [4.26] is developed using the same assumptions applied to Eqs. [4.23]:

$$-\frac{dp_W}{dx} - \frac{dp_A}{dx} - \frac{2F_{WJ}}{H_W} + 2F_{WA}\left(\frac{1}{H_W} - \frac{1}{H_A}\right) = (\rho_W + \rho_A)g\sin\beta \qquad [4.29]$$

The solution to the equations can proceed further, by substituting Eqs. [4.26] in [4.29]:

$$\begin{aligned}&-\frac{dp_W}{dx} - \frac{dp_A}{dx} + 2F_{WA}\left(\frac{1}{H_W} + \frac{1}{H_A}\right) + 2F_{WA}\left(\frac{1}{H_W} - \frac{1}{H_A}\right) \\ &= (\rho_W + \rho_A)g\sin\beta + (\rho_W - \rho_A)g\sin\beta\end{aligned} \qquad [4.30]$$

By expanding and collecting the phase height terms a general equation can be written:

$$\left(-\frac{dp_W}{dx}-\frac{dp_A}{dx}\right)+\frac{4F_{WA}}{H_W}=2\rho_W g\sin\beta \qquad [4.31]$$

Remembering that minimal capillary pressures are assumed in this derivation, Eq.[4.31] can be simplified to give the final equation for the phase pressure in terms of interface force water phase height and fracture inclination:

$$\frac{dp_i}{dx}=\frac{2F_{WA}}{H_W}-\rho_W g\sin\beta \qquad [4.32]$$

However, if Eq. [4.31] is re-written so that the bracketed pressure drop term is the subject, substitution can be made into Eq. [4.29] to give the equation:

$$2\rho_W g\sin\beta-\frac{4F_{WA}}{H_W}-\frac{2F_{WJ}}{H_W}+2F_{WA}\left(\frac{1}{H_W}-\frac{1}{H_A}\right)=(\rho_W+\rho_A)g\sin\beta \qquad [4.33]$$

This equation can be simplified by the collection and expansion of terms to:

$$\frac{2F_{WA}}{H_W(1-S_w)}+\frac{2F_{WJ}}{H_W}=\frac{1}{2}(\rho_W-\rho_A)g\sin\beta \qquad [4.34]$$

where, S_W is the water phase saturation ($S_W = 1 - S_A$). The Eqs. [4.27] and [4.34] can be solved simultaneously to give separate formulae for the shear forces in terms of the phase densities and heights, the saturation and the fracture inclination. Simplified equations for the air-water and water-joint surface shear forces (F_{WA}, F_{WJ} respectively) have been developed for isothermal, steady state free flow where both phases are unaffected by capillary effects or slip in a fracture of unit width ($y = 1$):

$$\frac{F_{WA}}{(1-S_W)H_W}-\frac{F_{WJ}}{H_W}=\frac{1}{2}(\rho_W-\rho_A)g\sin\beta \qquad [4.35]$$

$$\frac{2F_{WA}}{H_W(1-S_W)}+\frac{2F_{WJ}}{H_W}=\frac{1}{2}(\rho_W-\rho_A)g\sin\beta \qquad [4.36]$$

These equations can be solved to give terms for the joint wall and interface shear force as functions of the annular phase heights (H_A and H_W), the phase densities (ρ_i) and the fracture element inclination β:

$$\frac{F_{WA}}{H_W(1-S_W)} = \frac{3}{8}(\rho_W - \rho_A)g\sin\beta \text{ , and} \quad [4.37]$$

$$\frac{F_{WJ}}{H_W} = -\frac{9}{8}(\rho_W - \rho_A)g\sin\beta \quad [4.38]$$

Comparison of Eqs. [4.37] and [4.38] indicates that F_{WA} and F_{WJ} are proportional to fracture orientation β. It should also be noted that Eq. [4.37] tends to zero when S_W is zero, i.e., single phase air flow conditions. These expressions can be extended to consider fractures that are hydraulically rough, using the Barton et al. (1985) relationship:

$$e_h = \frac{e_m^{\ 2}}{JRC^{2.5}} \quad [4.39]$$

The Barton et al. (1985) expression for single-phase (water) flow can be adapted to the annular flow water phase height (H_W), which is calculated under steady state two-phase flow of air and water mixtures in rough fractures. Thus, for high and moderate S_W values, $e_h = H_W$ (i.e. $H_W = e_m^{\ 2} / JRC^{2.5}$) can be substituted in Eq. [4.38] and combined with Eqs. [4.37] and [4.38] to give the equations:

$$F_{WA} = \frac{3}{8}\frac{e_m^{\ 2}}{JRC^{2.5}}(1-S_W)(\rho_W - \rho_A)g\sin\beta \quad [4.40]$$

$$F_{WJ} = -\frac{9}{8}\frac{e_m^{\ 2}}{JRC^{2.5}}(\rho_W - \rho_A)g\sin\beta \quad [4.41]$$

The relationship described by Eq. [4.40] between F_{WA}, JRC and fracture orientation is explored in Figs. 4.10 and 4.11. The plots show that increasing inclination has the effect of increasing the magnitude of the interface shear force. Figure 4.10 also shows

that the force reduces as the fracture roughness increases, with a more noticeable reduction for relatively rough fractures (JRC > 9). Initially this outcome appears counter intuitive. However, when considering this result, it should be remembered that hydraulic aperture reduces with increasing *JRC*; this indicates that the water phase height is proportional to the interface shear force. When the graph is replotted in Fig. 4.11 for the case of constant e_h a different result is obtained; in this case it is clear that interface shear force is proportional to fracture inclination and fracture roughness.

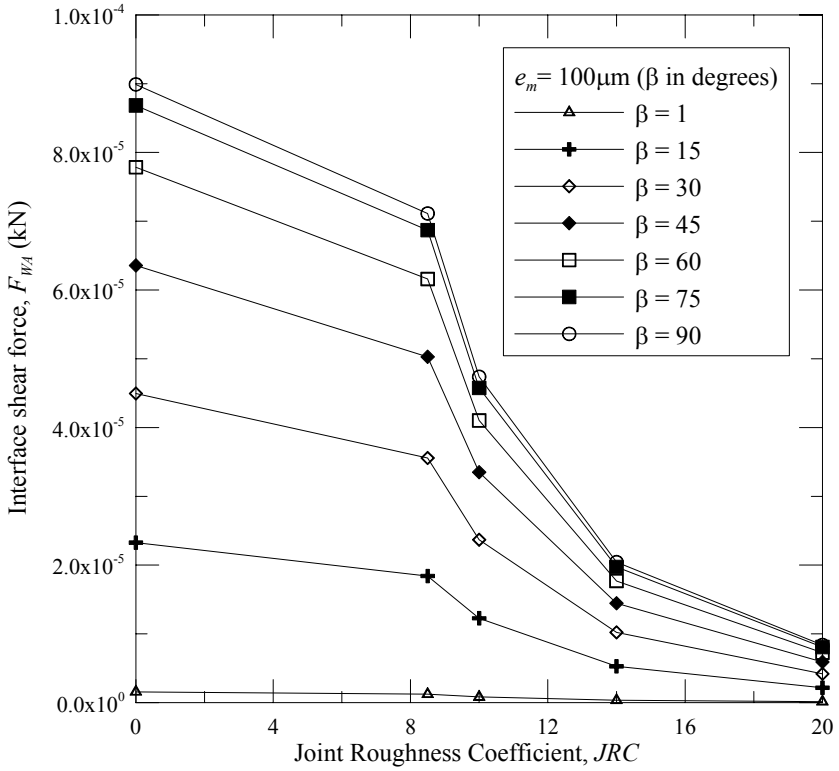

Figure 4.10: Plot showing the effect of fracture orientation on interface shear force (e_m = 100μm).

The formula in Eq. [4.41] is plotted in Figs. 4.12 and 4.13. The equation expresses the shear force at the wetted fracture wall as a function of fracture roughness and orientation, and assumes that the wall remains in contact with a film of water.

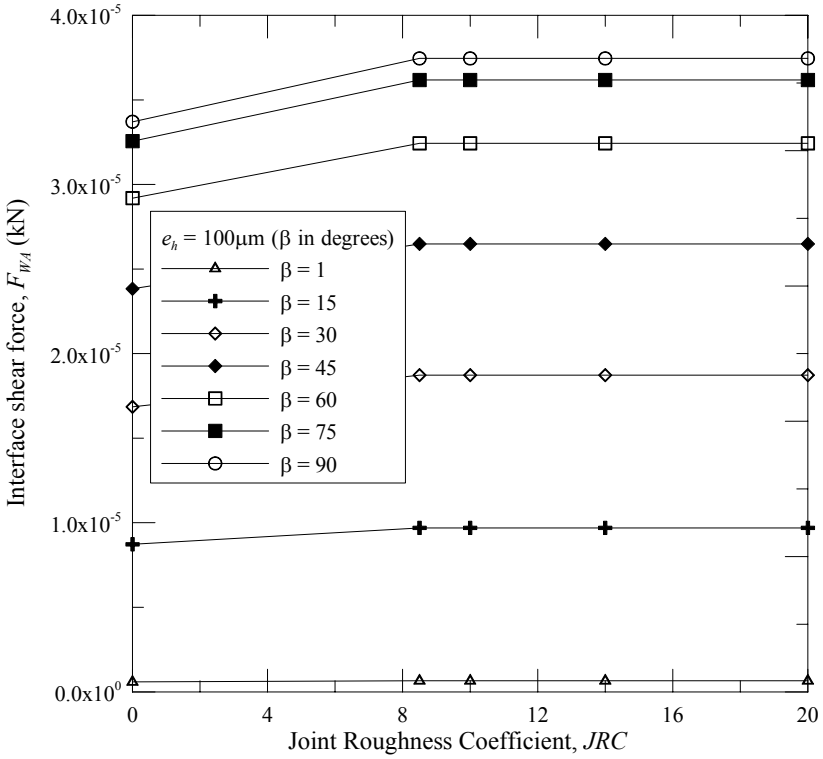

Figure 4.11: Plot showing the effect of fracture orientation on interface shear force (e_h = 100μm).

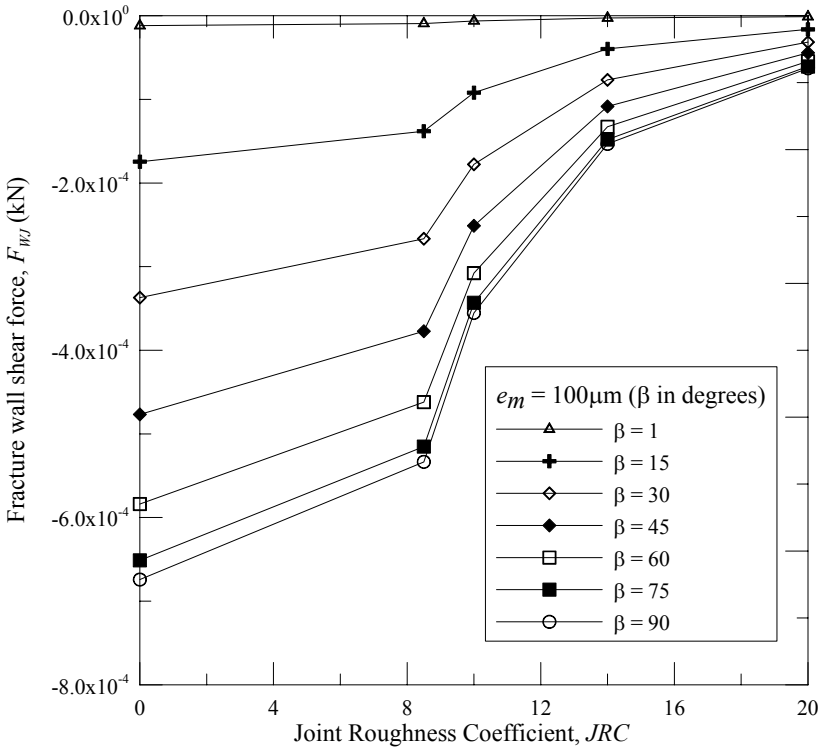

Figure 4.12: Plot showing the effect of fracture orientation on fracture wall shear force (e_m = 100μm).

Figure 4.12 shows that in absolute terms for a constant mechanical aperture, F_{WJ} is inversely proportional to *JRC* and proportional to fracture inclination. The relationship to fracture roughness and inclination is non-linear and more pronounced for relatively rough fractures (*JRC* > 9). When comparison is made with e_h constant, as is the case in Fig. 4.13, it becomes clear that inclination is the key factor is controlling the F_{WJ}, since *JRC* accounts for < 10% of the force over the entire *JRC* range.

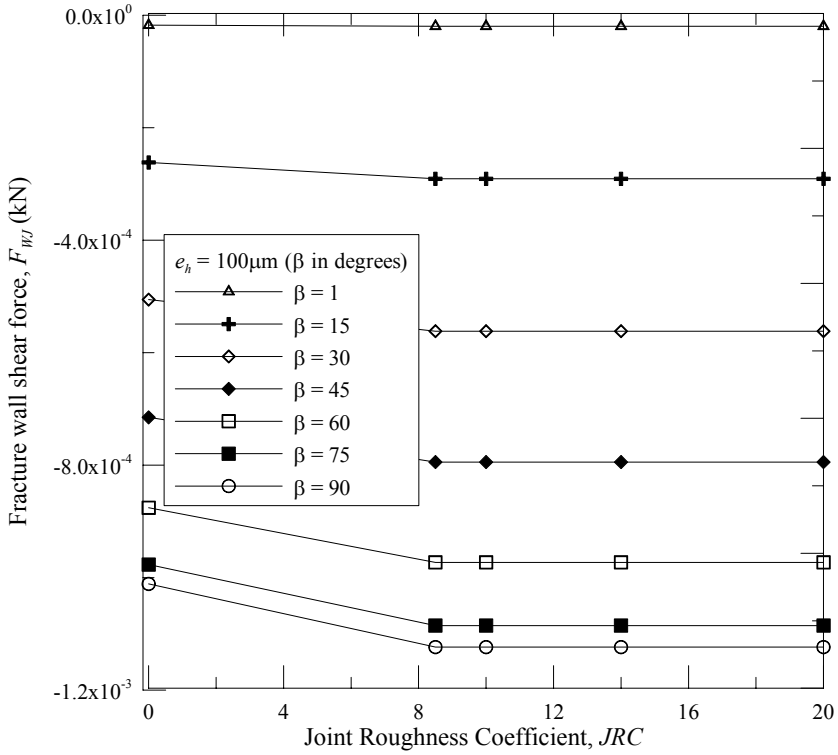

Figure 4.13: Plot showing the effect of fracture orientation on fracture wall shear force (e_h = 100μm).

Thus, a relationship between the interface and fracture surface shear forces has been developed through a detailed consideration of the impact of microscopic fracture surface roughness and the application of the conservation of momentum. This development overcomes the shortcomings that became apparent in the simple stratified model as originally proposed by Ranjith (2000). The proposed model (Fig. 4.2) is a

simplified flow model that approximates slug flow and annular flow patterns under laminar flow conditions. This new model differentiates itself from the earlier model (Indraratna & Ranjith, 2001) in that the fracture surfaces remain wet because of the intergranular surface tension effects occurring at the fracture wall.

4.3.3. Solution for annular flow phase height

A solution for the annular phase height was developed in the pressure drop expression Eq. [4.32], which relates the pressure drop to the air-water interface shear force, the phase height and elevation term. If the F_{WA} term is substituted using Eq. [4.27] an alternative formula can be developed:

$$\frac{dp_i}{dx} = 2(1 - S_W)\left[\frac{1}{2}(\rho_W - \rho_A)g\sin\beta + \frac{F_{WJ}}{H_W}\right] - \rho_W g\sin\beta \qquad [4.42]$$

This solution defines the phase pressure drop in terms of the water phase height, the water-joint wall shear force and the water saturation. Neither of these solutions provides a definitive solution for the phase height. An empirical relationship after Taitel & Dukler (1976) could be applied to estimate the interface and water-joint shear stresses. The Taitel & Dukler (1976) expression applied in the Ranjith (2000) model relies upon the two-phase Reynolds number as well as the phase velocity and density. However, this approach is not favoured on this occasion since the Reynolds number is calculated for the macroscopic two-phase flow conditions in a rough fracture, and may not necessarily represent continuous two-phase flow conditions of variable hydraulic radius. In addition, the greater interface complexity of the annular model solution within the conservation of momentum precludes the straightforward quadratic solution obtained in the Ranjith (2000) model. A recent Gradeck & Lebouché (2000) study suggests further experimental study could be accomplished by the detailed measurement of shear wall force variation and the relationship to rock fracture roughness.

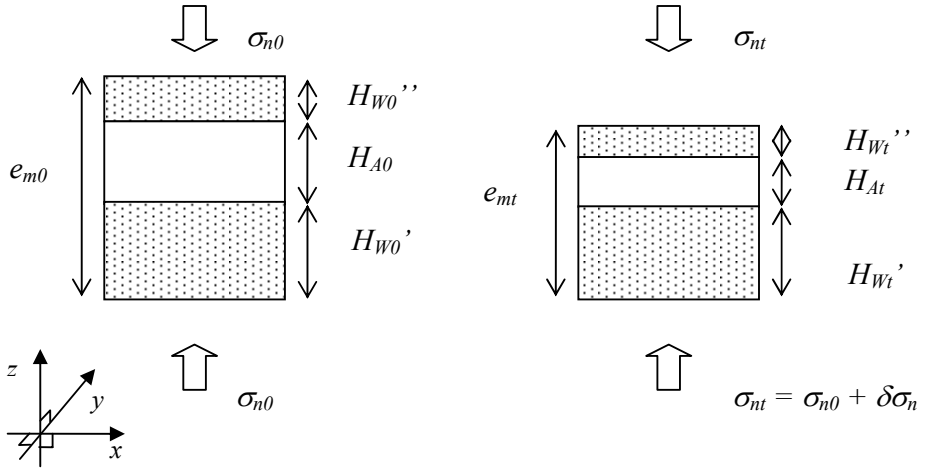

Figure 4.14: Schematic annular flow fracture element acted on by incremental stress.

An alternative solution can be developed by contemplating conservation of mass. This method is described in Fig. 4.14 and accounts for fluid phase volume compressibility related to fracture mechanical deformation.

Thus, considering the fracture element under initial stress conditions, the phase volumes can be written:

$$V_{A0} = H_{A0} x \cdot y \qquad [4.43]$$

$$V_{W0} = H_{W0} x \cdot y \qquad [4.44]$$

Phase volumes at a time t will change following a stress increment $\delta\sigma_n$ - p_i. In a linear elastic stress environment, the isothermal change in the phase volumes can be measured in terms of phase height and related to the change in fluid pressure Δp_i, and stress, enabling combination with Eqs. [4.15] and [4.18]:

$$H_{A(t)} = H_{A0} - \frac{C_{AC}(V_{A0} + V_D)\Delta p_A}{x \cdot y} + \frac{C_{WC}(V_{W0} - V_D)\Delta p_W}{x \cdot y} - \zeta \cdot \delta_n \qquad [4.45]$$

$$H_{W(t)} = H_{W0} - \frac{C_{WC}(V_{W0} - V_D)\Delta p_W}{x \cdot y} - (1 - \zeta) \cdot \delta_n \qquad [4.46]$$

The fracture normal dilation reduces the phase height for both air and water phases by the proportioning factor ζ. The relative incompressibility of water means $\zeta \approx 1$ and can be calculated using the following equation:

$$\zeta = 1 - \frac{\Delta H_W}{\delta_n} \qquad [4.47]$$

where, ΔH_W can be derived from Eq. [4.39] as $\frac{e_{m0}^2 - e_{m(t)}^2}{JRC}$, assuming that significant fracture surface degradation does not occur due to the change in stress. Thus considering the mechanical aperture at time t:

$$\begin{aligned} e_{m(t)} &= H_{W(t)} + H_{A(t)} \\ &= H_{W0} + H_{A0} - \frac{C_{AC}(V_{A0} - V_D)\Delta p_A}{x \cdot y} - \left(\frac{\left(\delta\sigma_1 \cos^2\beta - \delta\sigma_3 \sin^2\beta\right) - \Delta p_W}{K_n} \right) \end{aligned} \qquad [4.48]$$

Following a change in normal stress and fluid pressure, the fracture storage and the phase height relationships will change. Compression of the water volume will result in a corresponding expansion of the air phase, although the air phase will also compress in response to changes in pore pressure. The change in fracture aperture will be proportioned between both phases. For relatively high S_W values, it would be expected, that ζ can be estimated by relating the water phase height to the mechanical aperture using the *JRC* from Eq. [4.37]. For flow in an inclined fracture of unit width and elemental length l such as that shown in Fig.4.1, the fracture area term $x.y$ can be replaced by $l^2 cos\beta sin\beta$.

For laminar flow, the phase height concept developed in the two-phase flow new model can be incorporated into Darcy's law so that two-phase permeability testing can be analysed. Thus, considering flow calculation under linear conditions, following a stress increment occurring over a time interval from $t = 0$ to $t = t$, Darcy's law can be

re-written for each of the phases to include the new parameters in the following equations:

$$Q_{W(t)} = \frac{\left(H_{Wt}\right)^3 y}{12\mu_W}\left(\frac{dp_W}{dx}\right)_t \qquad [4.49]$$

$$Q_{A(t)} = \frac{\left(H_{At}\right)^3 y}{12\mu_A}\left(\frac{dp_A}{dx}\right)_t \qquad [4.50]$$

4.4. Summary

In this chapter, a detailed examination of two-phase flow theory has been given, exploring the common assumptions and limitations in the idealisation of flow in discontinuous geological media. Important physical factors pertaining to two-phase flow have been considered, exploring and applying capillary effects, phase solubility and compressibility to hydromechanical behaviour. The mechanical response of fracture surfaces to changes in applied normal stress have been reviewed and related to linear elastic theory using a normal stiffness function that can be measured during laboratory testing.

The significance of fracture surface roughness in preventing fracture wall dry out has been studied using capillary theory. The study concluded that only relatively coarse-grained rocks (grain size diameter ≥ 2mm) will be subject to partial dry out by fracture inclination or differential air-pressure gradient. Finer grained fracture surfaces tend to remain saturated, even under extreme inclinations because of the surface tension effects. This result implies that a water film will remain in contact with both fracture surfaces in fractures conducting two-phase air and water mixtures for many rocks, including those used in the subsequent laboratory testing (Chapter 6). This means that annular rather than stratified flow becomes a more representative flow pattern when considering a simplified two-phase flow mode, even under linear flow conditions.

The application of the theorem conservation of momentum to the two-phase flow problem enabled a simplified theoretical expression to be developed for the water-joint and air-water interface shear forces. The derived expressions take account of fracture saturation, surface roughness and fracture inclination. The fracture storativity changes with increments in normal stress because of the mechanical dilation and the change in mixture compressibility. For the situation where the viscosity contrast is large (e.g. air-water rather than water-oil) the sum of the phase heights will be equivalent to the average lognormal mechanical aperture.

The principle of conservation of mass has been applied to two-phase fracture flow resulting in the development of a macroscopic annular two-phase flow model for rough inclined rock fractures under 1-D steady state flow. The proposed model conceptualises the bubble, slug and annular two-phase flow regimes. The model is based upon Darcy's Law and allows the determination of relative permeability and saturation by relation to the phase height parameter. Fluid behaviour is coupled to changes in the stress field through the fracture normal stiffness using either linear or non-linear functions.

Chapter 5
Two-phase flow in
Analogue Joints

5.1 Introduction

An analogue joint testing programme was devised to help conceptualise two-phase rock fracture flow and to study the validity of the standard assumptions. Transparent Perspex plates were used to model fracture surfaces as smooth parallel plates and to allow observation of phase behaviour. The apparatus was instrumented using flow meters and pressure transducers. The experimental results were collected using a datalogger. The apparatus provided an illustration of the proposed simplified two-phase flow model. The laboratory data also enabled comparison of flow behaviour with existing studies of idealised two-phase flow hydraulics.

This chapter provides a short theoretical background as a context for the study. Special parallel plate apparatus was designed by the writer and fabricated by University of Wollongong Technical Staff. The apparatus design and the testing methodology is described. The observed flow behaviour is analysed and compared with several established hydraulic studies. The results are discussed in terms of the comparative studies and consequences for the proposed two-phase flow model.

5.2 Theoretical Background

Conventional analyses of fluid flow through rock fractures simplify the mechanics to a model of flow between smooth parallel plates, conveniently ignoring the effects of variable aperture (channelling) and roughness. This model is mathematically appealing because it provides a solution to the Navier-Stokes equation; this simplified model adopts Darcy's law and combines it with Poiseuille's law so that fracture aperture can be related to the permeability and flow rate by:

$$U_f = \frac{Q}{A} = K_f \frac{(h_2 - h_1)}{l} \qquad [5.1]$$

where, the fracture seepage velocity is U_f is defined by Q, the rate of discharge, and the cross sectional area A, which is taken normal to the direction of flow. The velocity can also be calculated from K_f, the hydraulic conductivity, and the hydraulic gradient Δh over the fracture length, l. Darcy's law assumes viscous linear laminar flow of an incompressible fluid. The pressure, as well as elevation differential across the test length combine to drive flow, and is relating to head difference as a product of the fluid unit weight.

It is useful to consider the intrinsic permeability when studying flow in fractured rock since this parameter is independent of fluid properties and has units of m^2. The intrinsic permeability of a discontinuity, k can be estimated using Poiseuille's law, by assuming the fracture surfaces to be smooth parallel plates with aperture of e, i.e.:

$$k = \frac{e^2}{12} \qquad [5.2]$$

The intrinsic permeability k is related to the hydraulic conductivity K_f by the fluid unit weight γ and the dynamic viscosity μ by the equation, allowing the permeation of fluids other than water to be considered:

$$K_f = \frac{k\gamma}{\mu} \qquad [5.3]$$

This allows the re-writing of Darcy's law for fracture flow U_f in a single fracture in terms of e:

$$U_f = \frac{e^2\gamma}{12\mu}\frac{(h_2 - h_2)}{l} \qquad [5.4]$$

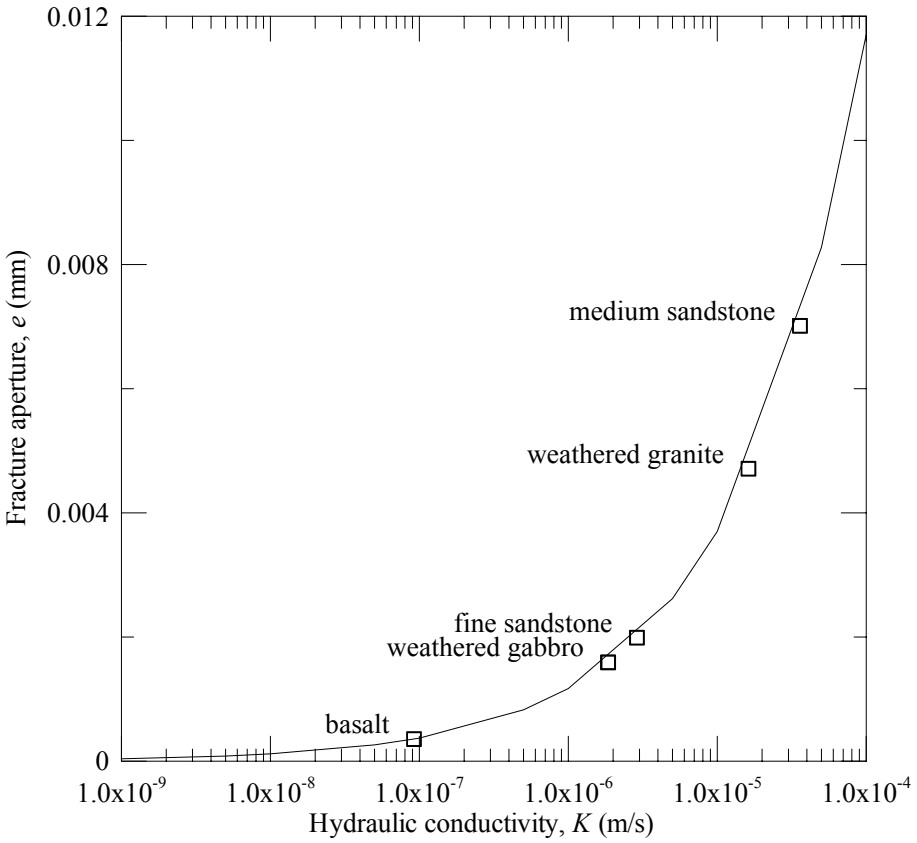

Figure 5.1: Theoretical curve showing comparison of hydraulic conductivity (unit cross sectional area) and equivalent fracture aperture (unit width). NB: Published values of rock substance hydraulic conductivity are taken from Berkman (1995).

This concept can be further extended to consider the average fracture hydraulic conductivity of a set of parallel discontinuities outcropping in a particular rock mass.

$$K_f = \frac{e^2\gamma}{12\mu b} \qquad [5.5]$$

where, K_f = fracture conductivity (ms^{-1}), e = hydraulic aperture (m), μ = dynamic viscosity (1.002 x 10^{-3} Pa s for pure water at 20°C), and b is the spacing between fractures (m).

The same mathematical approach can be applied to the analysis of flow through porous media which allows the simple comparison of the role of primary (*p*) and secondary or fracture permeability (*f*) in flow through rock fractures (Indraratna et al., 2002). For the same hydraulic gradient, the flow through a block of porous media can be related, assuming unit length, height *z* and width *w*, to the flow through a fracture element of aperture *e*. The potential total flow through a fractured rockmass can be considered as the sum of primary and fracture flows, or:

$$Q_{tot} = Q_p + Q_f \qquad [5.6]$$

For the case where Q_p and Q_f are equal, significance of fracture flow path can be illustrated by identifying the fracture aperture equivalent to the primary hydraulic conductivity of common rock types. Thus, applying Darcy's law to each of the elements gives:

$$A_p K_p I_p = A_f K_f I_f \qquad [5.7]$$

which, for water flow through an equivalent fracture reduces to:

$$K_p = \frac{e^2 \gamma}{12 \mu} \qquad [5.8]$$

Table 5.1: List of typical primary hydraulic conductivity for rock types (Berkman, 1995).

This relationship in Eq. 5.8 is illustrated in Fig. 5.1. Comparison of the graph in Fig. 5.1 with a list of typical rock type primary permeability (Table 5.1) indicates that under the same hydraulic gradient, a fracture just 0.2mm wide would be equivalent to the hydraulic conductivity of a $1m^2$ outcrop of clean sand. This example indicates the overwhelming significance of fractures and fracture networks on rock mass hydromechanics.

Two-phase air and water flows can be studied using an extension of the same approach as described in previous experimental work (Persoff & Pruess, 1993; Fourar et al. 1993; and Indraratna & Ranjith, 2001). This is achieved if the flow equation in Eq 5.2 is modified to include the relative permeability (K_r) or the phase height (h_i) and pore pressure gradient dp_i/dx where the elevation gradient is negligible:

$$Q_i = \frac{k_i K_{ri}}{12\mu_i} A \frac{dp_i}{dx} = \frac{h_i^3 w}{12\mu_i} \frac{dp_i}{dx} \qquad [5.8]$$

where, k_i is the saturated intrinsic permeability and K_{ri} is the relative permeability of phase i and w is fracture width. Laboratory investigation by Ranjith (2000) and further work presented in Indraratna et al. (2003) has shown successfully the usefulness of this approach in the consideration of low velocity, low Reynolds number flows, i.e. within the range of laminar behaviour.

The important complications when considering two-phase rather than single-phase flows are the phase interaction during flow and the impact on simple analytical hydraulic models that are typically used to calculate the flow characteristics. Analysis of two-phase flow in geological media is an area that has developed from hydraulic analysis

of flow in pipes and man-made channels. A useful technique for understanding the development of two-phase flows in the man-made environment has been the use of flow maps. These maps represent particular configurations and relate the change in observed flow behaviour to measurable physical parameters, such as phase superficial velocities. Despite the relative theoretical ease with which a two-phase flow model can be developed for flow in fractured geological media, the natural environment poses great potential for variability in the physical size, orientation and extent of the boundary conditions that govern the applicability of such a theoretical model. It is acknowledged that the flow map approach is of limited quantitative use for analysing general two-phase flow behaviour (Wallis, 1969). However, for the study of real rock fractures it does allow the consideration of the impact of fracture orientation on flow and two-phase flow pattern development behaviour. In addition, the flow map serves to test the suitability of the simplified two-phase flow models for predicting real fracture flow behaviour.

The description of two-phase flow in rock fractures is complicated by the potential variability in persistence, connectivity, topology and orientation of the fracture. The complex dependence of these factors requires a robust systematic description of flow behaviour. A review of existing work indicates that the terminology has not been developed for a range of inclinations, but rather in isolation for particular orientations. For example, Hewitt & Naylor (1976) describe patterns for both vertical and horizontal two-phase pipe flow, but comparison of the two schemes show inconsistent terminology, even originating from the same authors (Table 5.2).

Table 5.2: Comparison of two phase flow patterns for horizontal and vertical pipe flow.

Air phase velocity, U_A	**Horizontal or inclined**	**Vertical pipe flow**

It is clear from Table 5.2 that the terminology is similar for the different sets of orientations, with variants of stratified separated flow not reported in the vertical data. The simplified range of angle independent flow patterns for macroscopic conditions could be developed to include bubble, slug/plug, churn/slug and annular. For the purpose of this work it is suggested that these pattern regimes could be defined as:

(a)

(b)

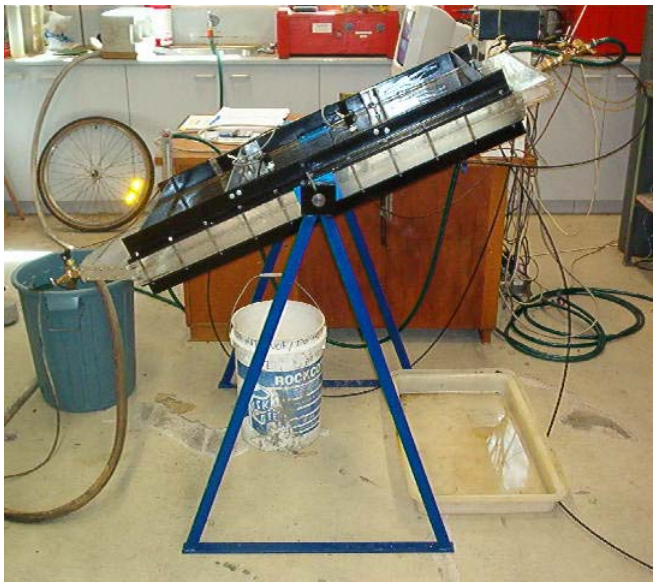

(c)

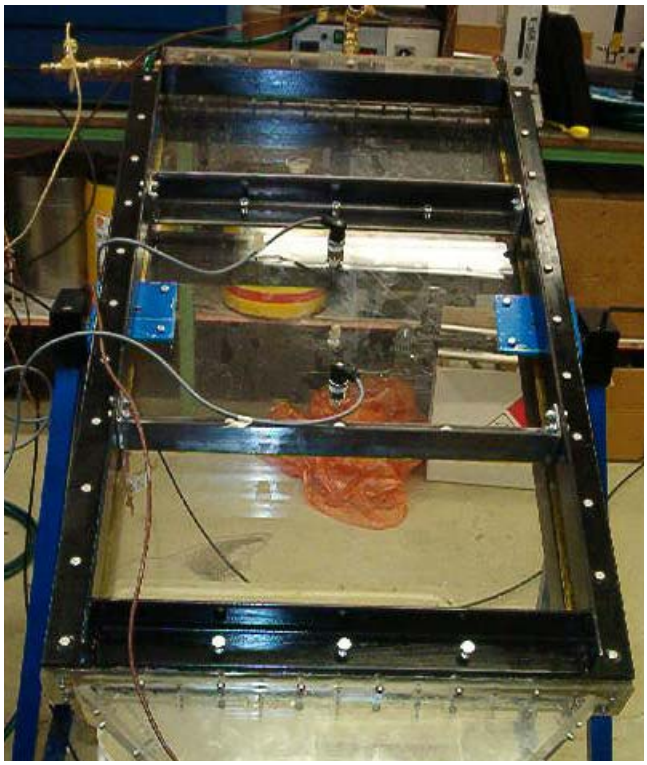

Figure 5.2: Photographs showing optical two-phase flow apparatus (a) data acquisition and flow control instruments: (b) side view analogue joint assembly in 'A'-frame: and (c) end view of the inclined apparatus

a) Bubble flow – discrete relatively small air bubbles, affected by buoyancy, in continuous water phase. Relatively high degree uniformity of bubble size and shape.

b) Slug/plug flow – discontinuous air phase in relatively large cap shaped bubbles with intervening liquid slug containing small entrained air bubbles.

c) Churn/slug flow – a degeneration of the slug pattern with a wavy lower surface interfaces coalescing with the upper bubble surface in a oscillating or churning, irregular manner.

d) Annular/annular mist flow – a development of churn/slug flow after pronounced slip or hold-up and bubble coalescence resulting in the formation of a slower upper and lower water film about a faster air core. The lower water film thickness will be greater than the upper film. The continuous central core will contain entrained particles of the slower, denser phase. The non-linear flow behaviour associated with this flow pattern differentiates this mode from that described by the annular model proposed in Chapter 4, which best represents the linear behaviour observed in (a) and (b).

5.3 Two-phase analogue apparatus

Persoff & Pruess (1993) and Fourar et al. (1993, 1995) carried out two-phase flow analyses of horizontal, replica or analogue joint apparatus. The purpose of developing new optical analogue two-phase flow apparatus was to inject two-phase mixtures between transparent smooth parallel plates so to observe flow structures over a range of phase saturations and 'joint' inclinations. Gradeck & Lebouché (2000) also used

analogue experiments and introduced rough sinusoidal mated surfaces, although visibility of the flow behaviour was distorted in this case. However, they were able to measure shear force variation with change in flow behaviour using the electrochemical technique of polarography. They found that when flow occurred normal to the fold axes, the shear force varied across a sinusoidal plate with maxima occurring at the peaks and minima in the troughs. The mated upper plate indicated shear force maxima developed at the wetted peaks, corresponding to the minima observed on the lower plate.

The Wollongong university apparatus for these experiments replicated the idealised boundary conditions using smooth planar analogue joint surfaces with flow occurring along the plate axis and no-flow boundaries along the plate edges. The equipment was designed to be supported by an 'A'-frame so that the 'joint' inclination could be varied and the effect of joint orientation on two-phase flow behaviour studied to enable more realistic flow conditions to be studied (Figs. 5.2 and 5.3).

5.3.1 Flow Apparatus and data acquisition

The apparatus comprises two 30mm thick, 1m by 0.6m Perspex plates clamped together by a fabricated metal support and held on a hinged 'A'-frame with 0.25mm bronze shim placed between the plates to maintain a constant plate separation. The aperture between the two plates was checked using a feeler gauge and maintained at the correct setting by tapped adjustment screws located in the metal frame enclosing the two plates.

Inlet and exhaust manifolds were fabricated of 10mm Perspex plate to control fluid injection and collection from between the plates. The Perspex manifold assemblies were sealed using silicon sealant and petroleum jelly on components that required adjustment or periodic re-assembly, or chloroform solution where components were fixed

permanently. Proprietary 1MPa pressure transducers made by UCC were used to measure the inlet and outlet fluid pressures. Non-return valves were placed immediately downstream of the inlet pressure transducers so that unidirectional phase flow was maintained during testing.

The water phase was injected from the domestic mains supply and the inlet flow rate was set using the precision metering valve on a 7.5 l/min Dwyer (optical) Rate Master flowmeter and controller. The air phase was injected from a compressed air source and the inlet flow rate was controlled using a Dwyer GFC 30 l/min digital flow controller. The transducers and the digital flow controller were connected to a DT500 datalogger and computer so that the test data could be recorded. The apparatus is shown photographically and schematically in Figs. 5.2, 5.3 and 5.4.

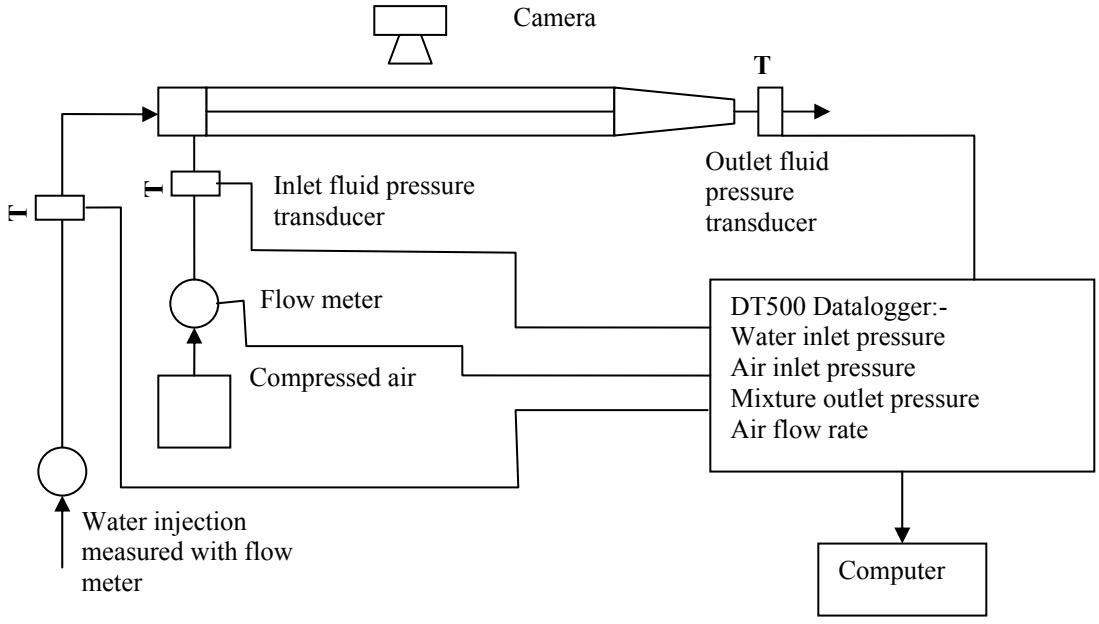

Figure 5.3: Diagram of schematic laboratory layout of optical two-phase flow apparatus.

The injection system was designed to independently monitor the phase inlet pressure and to prevent backflow through the inlet piping using non-return valves positioned in-line

between the inlet fluid pressure transducer and the inlet manifold bulkhead. The water phase was injected centrally through the inlet manifold bulkhead. The air phase was injected separately through the side of the bulkhead using high pressure 6 mm diameter copper tubing that was perforated with 0.5 mm holes drilled at 10 mm centres positioned opposite to the gap between the two Perspex plates. These details are shown in Fig. 5.4. This detail allowed for the controlled injection of air bubbles into a laminar or turbulent water flow pattern. The flow behaviour was easily observed through the Perspex so that still and video photography of the flow structures could be acquired.

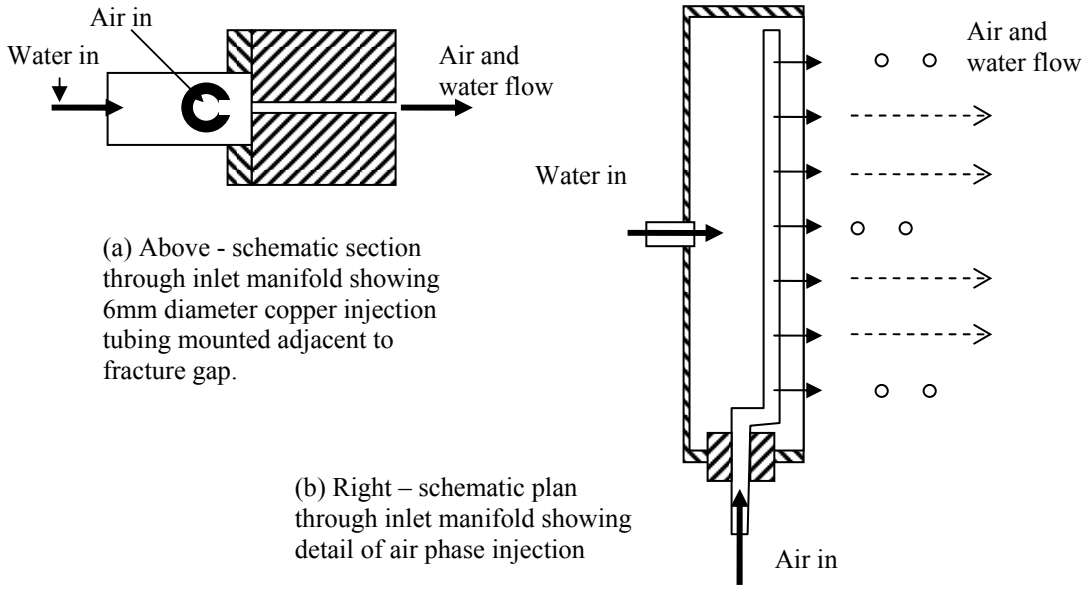

Figure 5.4: Detail of water and air injection through inlet manifold. (a) a schematic cross section through inlet manifold showing mixture injection points (b) a schematic plan showing water and air phase inlet tubing.

5.4 Methodology

Single- and two-phase flow testing was performed for parallel plate assembly orientations of horizontal, vertical and 30°, 45° and 60°. The test procedure for each orientation is

summarised by the flow chart shown in Fig. 5.5. The plate assembly was set at the required test inclination, measured with a clinometer, and then locked in place using tapping screws included in the frame hinge assemblies. Prior to commencing two-phase flow testing, single-phase water testing was performed to verify the design characteristics of the apparatus and to saturate the plate assembly. For each inclination, steady state water flow conditions were established before commencing injection of the air phase. A suite of water flow rates were tested from 0.35 l/min to 5.3 l/min. Air phase injection was conducted until air phase steady state flow conditions had been achieved. Air flow rates applied during testing were in the range 0 to 10 l/min.

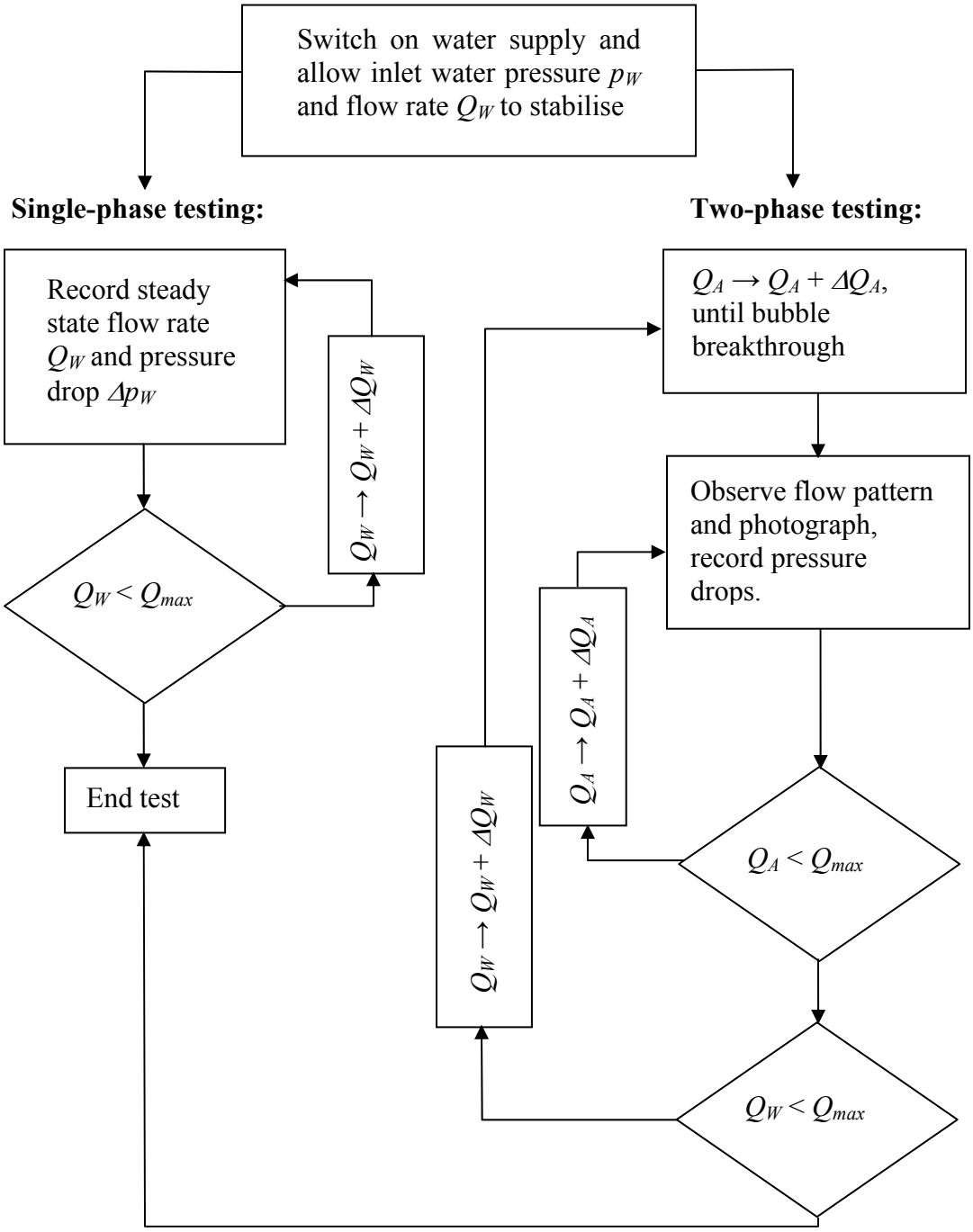

Figure 5.5: Process diagram showing analogue joint testing methodology.

5.5 Discussion of Experimental Results

The back-calculated aperture from single-phase testing was 254μm, i.e. within 1.6% of the apparatus aperture. The two-phase experimental results are discussed in terms of relative permeability and the flow pattern development.

5.5.1 Relative permeability

The experimental data was analysed in terms of the simplified two-phase flow model described in Eq. [5.8] as well as Eqs. [4.49] and [4.50]. Single-phase tests showed that the back-calculated aperture was approximately equal to the plate aperture (0.25 mm), as would be expected for Darcian conditions.

Figure 5.6: Plot showing analysis of relative permeability and water phase saturation for two-

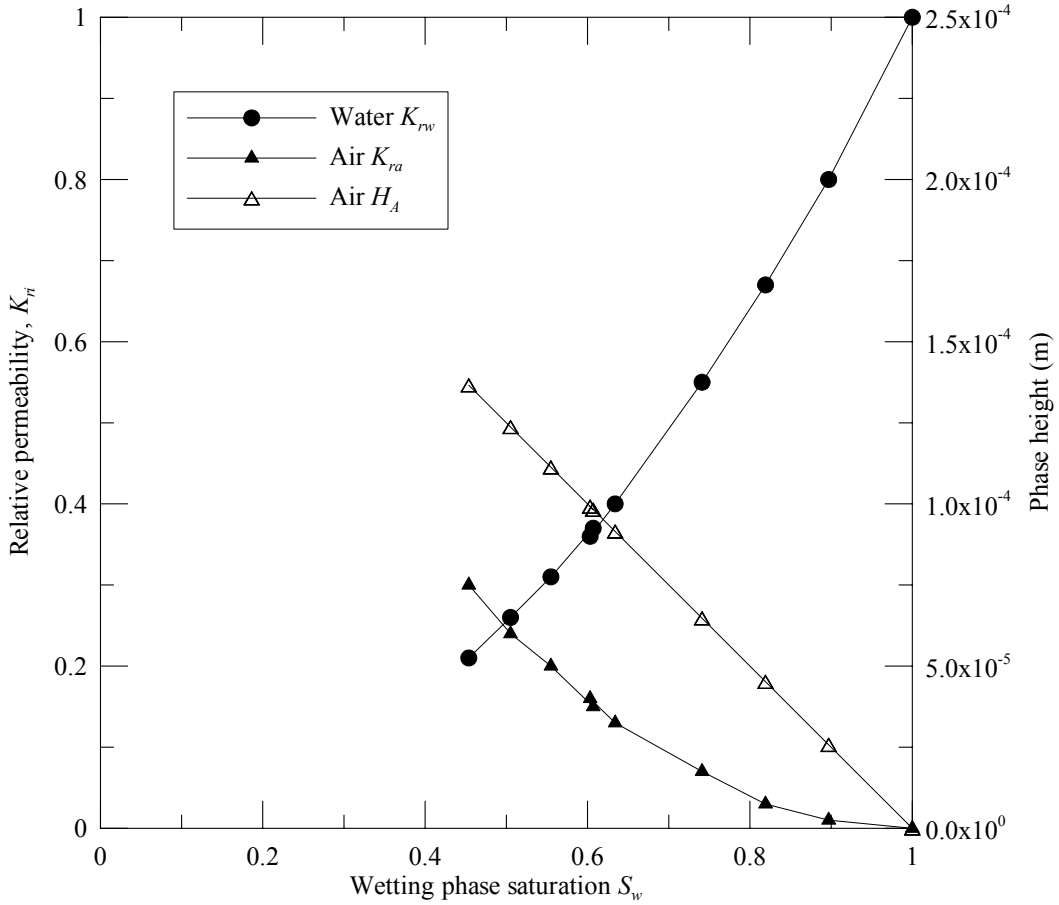

phase flow testing in the optical apparatus.

Application of the previously defined two-phase flow models showed the sum of the phase heights was equal to the plate aperture, confirming that $e_m = \Sigma H_i$, where i defines the air (A) or water (W) phase height (H). The two-phase flow data can also be interpreted in terms of the water phase saturation S_W and the relative permeability K_{ri} in accordance with Eqs. [4.7], [4.8] and the associated discussion in Chapter 4. The laboratory results in Fig. 5.6 show wetting phase saturation varied between 45% and

100%. The verification of the proposed theoretical relationship is demonstrated in Fig. 5.6 by comparison with Fig. 4.2(b). These figures show the agreement between the theoretical and experimental wetting-phase relative permeability functions. It is significant to note that, within the limits of experimental accuracy, the calculated relationship between phase height and physical aperture does not appear to be affected by the formation of localised non-stratified or annular flow patterns, and still correctly predicts the plate aperture dimension.

Please see print copy for Figure 5.7

5.5.2 Flow pattern development

The main purpose of this stage of the research project was to obtain qualitative data on the two-phase flow patterns that could be expected to occur in similar flows through real rock fractures. The study provides data on the effect of fracture inclination on two-phase flow behaviour, as well as the applicability of simplified two-phase flow models to 'fracture' specimens with a surface area some 3 orders of magnitude larger than specimens which could be tested in the TPHPTA.

Despite the specific differences in flow pattern development with orientation identified in 5.2, it is clear that two-phase flow is characterised by different phase relationships as the fracture orientation and phase saturation change. In the following discussion, Figs. 5.7 to 5.12 show pictures of flow pattern structure for different velocity and saturation conditions. These photographs depict flow from right to left, with air in the form of bubbles within a continuous water phase. A range of different flow behaviour was recognised during the testing and they have been summarised in Fig. 5.13.

This plot represents a range of flow conditions and patterns that will be discussed individually in the following sections.

(a): 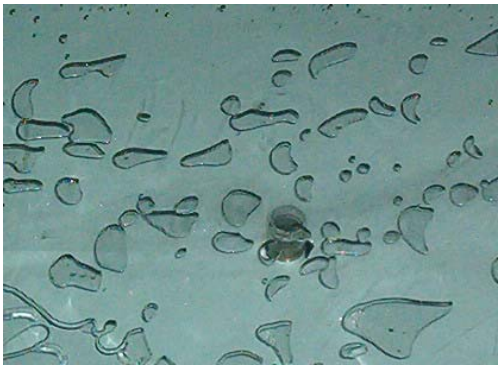 (b): 

Fig. 5.8: Lenticular and cap shaped bubbles flow in an analogue joint at the beginning of slug flow pattern, with most of bubbles fully occupy the plate aperture: (a) air bubbles in a relatively slow water phase (b) air bubbles in a relatively fast water phase.

5.5.2.1 Bubble flow

The theoretical development of two-phase flow patterns starts with a mixture of fluid bubbles within a continuous liquid phase. In bubble flow, the air phase saturation is relatively low. The bubbles tend to be geometrically simple, often round or developing to lenticular 'cap' shaped bubbles (short axis parallel to flow) with increased air flow rate. The bubbles tend to move linearly with relatively slowly. This flow pattern occurs at low air flow rates and superficial velocities as can be seen on Fig. 5.7.

With increased air phase saturation, the volumetric composition of the air phase increases, although the air phase remains discontinuous. It is clear that at low injection rates the bubbles do not necessarily contact the lower plate and flow in the upper portion of the fracture aperture (Fig. 5.7b). Higher water phase velocity increases the length:breadth ratio of the bubble, reducing the overall bubble size and increasingly the proportion of bubbles that fully occupy the aperture.

(a): 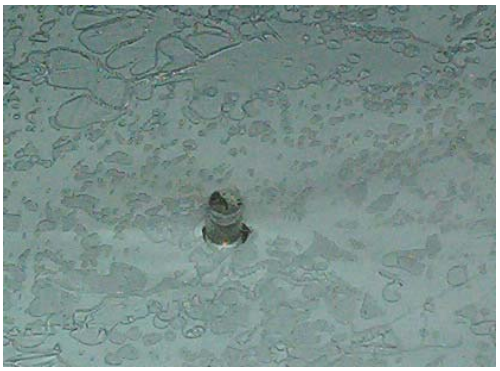 (b): 

Fig. 5.9: Larger complex bubbles develop with increased air phase flow rate. Plate (a) shows the generally smaller bubble size encountered with lower water phase flow rate. Plate (b) shows clearly formed larger bubbles in a higher velocity environment.

5.5.2.2 Slug/Plug flow

As the air phase injection rate is increased, air bubbles coalesce to form larger lenticular bubbles. In Fig. 5.8 it can be seen that as the larger bubbles move, small lower velocity air bubbles are shed from the trailing edges of the larger bubbles, whilst other slower moving small bubbles in the intervening liquid slug are absorbed at the nose of the following bubble. The larger bubbles tend to occupy the full section of the aperture. This pattern is described as the slug/plug flow pattern within this text. This behaviour marks the development of the complex flow pattern (Fourar et al., 1993) or the Golan & Stenning (1969) 'slug' pattern. With increasing S_A, air bubble size appears to increase, becoming complex and dynamic. The bubble boundaries appear to be smooth and rounded, intermixed with a variety of bubble sizes and shapes. The bubble velocity increases with air phase injection rate and S_A. This development and the impact on bubble size distribution is displayed in Fig. 5.9(a) and (b).

(a):  (b): 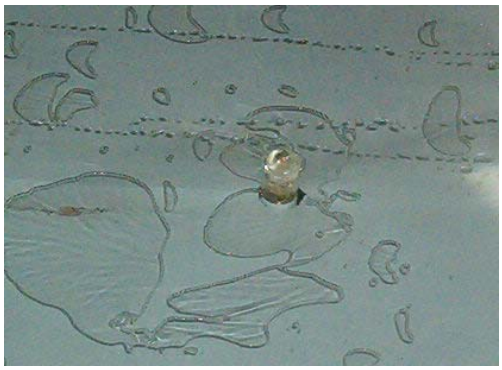

Fig. 5.10: Pulsing flow with complex cap shaped bubbles, gurgling noises associated with flow and localised formation of wavy interfaces: (a) shows intricate, large bubbles with many intervening smaller bubbles, and (b) shows higher S_W with greater proportion of large air bubbles.

5.5.2.3 Churn/slug flow

At this stage, flow comprises still higher S_A and corresponding increases in V_A. The flow pattern formed by the complex bubbles is very dynamic. This behaviour is shown in Fig. 5-10. The bubbles tend to increase in size with increasing air flow, and most of the bubbles appear larger because of coalescence associated with the bubble movement. The bubble margins do not appear as clearly defined as for previous flow patterns, indicating the onset of film intrusion at the bubble edges.

With the progression of decreasing S_W, the air bubbles arrive as periodic fronts with a cyclic range of V_A forming a surging flow (Fig. 5.11). The level of saturation and the injection pressure combine to enable coalescence to form predominantly large bubbles. The photographs clearly show differentially refracted lines representing the wavy interface below the bubble. This feature suggests that a water film is present on the underside of the bubble, flowing along the lower plate. From this stage, there is an

increasing difference in phase velocity, leading to the development of increasing phase 'slip'.

Fig. 5.11: Surging flow developed with prominent wavy interface and irregular bubble geometries in: (a) a low S_W environment; (b) a high S_W environment.

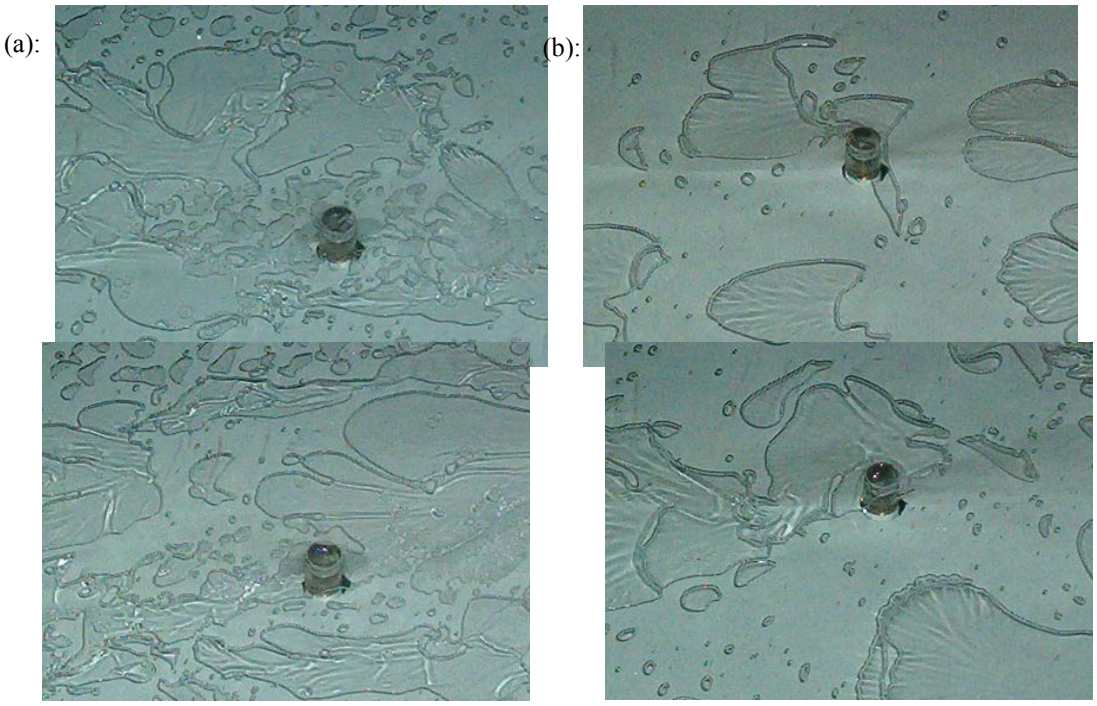

(a) (b)

Fig. 5.12: Examples of widespread surging flow with complex dendritic or billowing shapes and widely developed lower wavy interface. Increased slip conditions with an irregular leading edge to the bubble as the bubble advances through the next slower moving liquid slug in: (a) low S_W and (b) high S_W conditions.

For high V_A conditions (Fig. 5.12) the bubbles display complex plan-geometry with dynamic billowing or dendritic shapes, and a rapid and irregularly advancing nose. The wavy lower interface is present on nearly all the bubbles in Fig. 5.12 indicating the more

extensive development of slip conditions. The irregular bubble nose development is widespread in Fig. 5.12b, as well as a rippling air-water interface. Some simpler cap and lenticular shaped bubbles can also be seen entrained within the intervening slugs.

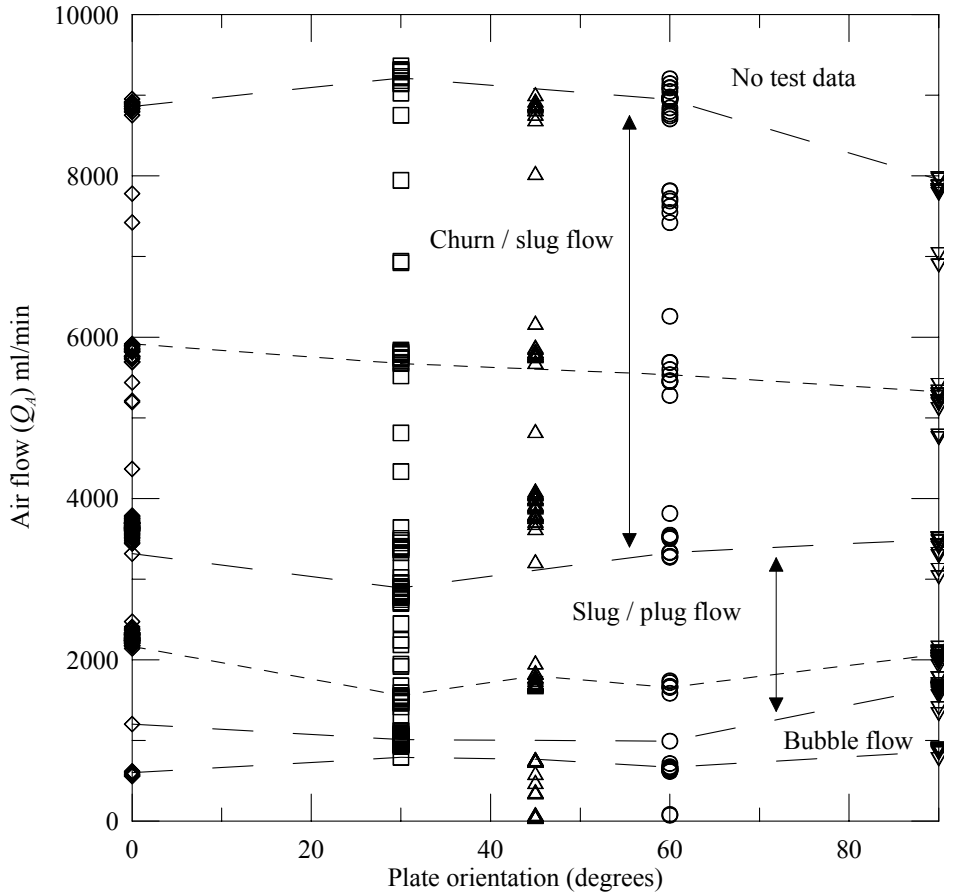

Figure 5.13: Variation in two-phase flow pattern with plate inclination and air flow rate for 250μm plate separation.

5.5.2.4 Discussion

The observed flow pattern progression with increasing air flow was repeated for tests at a range of inclinations. The test results in terms of the phase superficial velocities were plotted in Fig. 5.13 to study the effect of fracture inclination on pattern development. The same flow pattern sequence is seen for each of the inclinations indicating that plate angle has a minor effect on the formation of flow pattern and on the analysis of the flow

behaviour. The plate dimensions used in the apparatus mean that the maximum head difference is less than 15kPa. The maximum elevation potential is insignificant compared to the magnitude of the phase pressure drop used in the experiments.

Figure 5.13 shows broadly horizontal, flow pattern zones can be identified across the range of test inclinations illustrating the limited impact of fracture orientation on the test results. The flow pattern zones have been marked with the classification proposed in Section 5.2. The testing showed flow patterns become increasingly complex with greater phase pressure drop and flow rate. The bubble flow zone is associated with small rounded, finger shaped or lenticular bubbles. The bubbles do not occupy the full inter-plate gap at low air-flow and -pressure conditions.

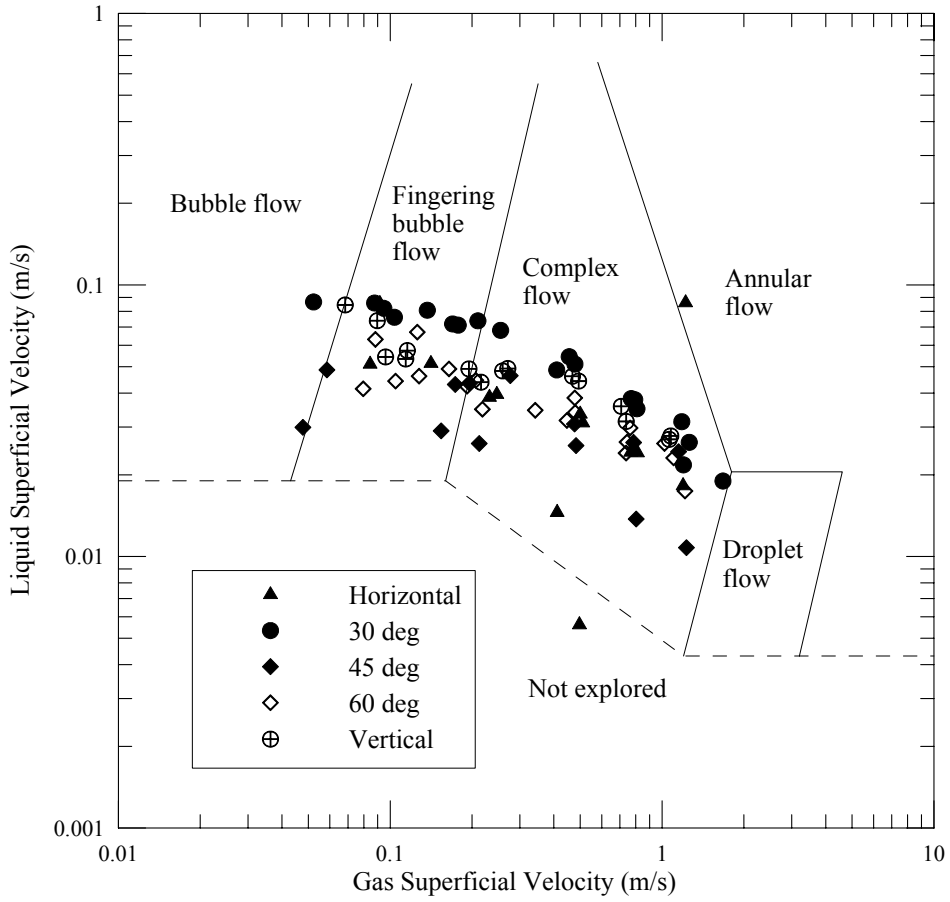

Figure 5.14: Observed two-phase flow data for 0º to 90º superimposed on Fourar et al. (1993) flow map for a horizontal glass channel.

The bubble size generally increases with air flow rate, as shown in Fig. 5.7b. The slug / plug flow regime occurs as the air phase saturation and velocity increases. These conditions result in larger bubbles that tend to occupy the full inter-plate gap and have a characteristic and predominant 'cap' shape (Fig. 5.8).

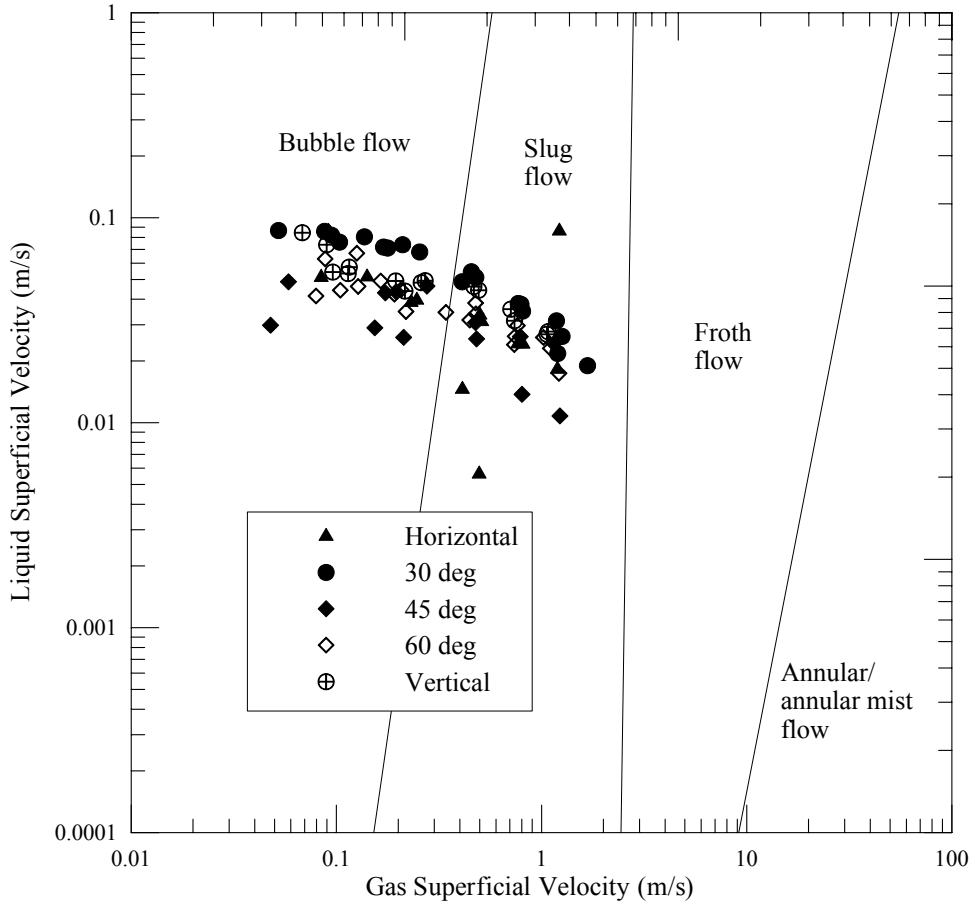

Fig. 5.15: Observed two-phase flow data for 0º to 90º superimposed on Golan & Stenning (1969) flow pattern map for flow in vertical pipes.

With greater air-phase velocity, the cap shaped bubbles begin to shed smaller bubbles from their trailing edges (Fig. 5.9). This regime is judged to represent the end of slug / plug flow. Churn / slug flow is associated with a higher energy environment where the air bubbles and the intervening liquid slugs are moving at a higher velocity than the water

film that has formed along the lower plate. Increased slip between the water film, the air bubble and water slugs leads to the formation of wavy interfaces and rapidly developing bubble noses that are captured in the sequence of Figures 5.10 to 5.12. Sustained annular flow did not develop under the test conditions.

The results show the dynamic complexity of two-phase flow patterns that develop within general flow regimes that are difficult to precisely define using a simple classification system. It is nonetheless informative to compare the observations with flow pattern maps of existing classification systems. By comparing the observations with two established classification systems proposed for horizontal analogue fractures and vertical pipes, it is possible to assess the influence of fracture orientation on flow pattern behaviour.

The horizontal flow pattern map for an analogue joint provides a good source of comparison with the observations of the testing performed in this project. The flow pattern boundaries deduced by Fourar et al. (1993) are transposed onto a superficial velocity plot of the gas- versus the water-phase. The Fourar et al. (1993) classification suggests that bubble and complex flow patterns would be expected for the range of test conditions, which is confirmed by the observed flow patterns demonstrated in Fig. 5.14. The data obtained from different test inclinations show some scatter but not a progressive trend with the increased angle of tilt, indicating the negligible influence of plate orientation on flow pattern development.

The vertical flow pattern map developed for vertical pipe flow by Golan & Stenning (1969) has also been used for flow comparison, since Fourar et al. (1993) have only reported on horizontal testing. The transposition of the Golan & Stenning (1969)

flow pattern boundaries on to the current range of test results indicates that bubble, slug and possibly froth flow may be anticipated from the plate orientations tested. The data scatter in Fig. 5.15 again shows no obvious trend in relation to orientation, reiterating the indication that fracture orientation is not a major factor on flow pattern development in a fracture system of this scale.

The relative insignificance of fracture orientation on flow pattern is important when considering flow in rough discontinuous geological media. It is clear that the simplified two-phase flow models proposed by Indraratna & Ranjith (2001) and in this work can be applied to predict the two-phase flow behaviour even where the conceptual stratified or annular flow models have not developed, especially since separate continuous flow of both phases has only developed on the microscopic scale. This is an important illustration of the application of the proposed simplified two-phase flow model presented in Chapter 4.

One difference between the conceptual annular flow model proposed in Chapter 4 and the analogue test data is the localised 'dry out' of the upper plate during the passage of the air phase bubble. This phenomenon was considered theoretically in Chapter 4 for rough fractures. Careful observation of the bubble transit through the apparatus shows that the upper contact of the air bubble is apparently with the smooth Perspex plate without an intervening water film. It appears that the lower bubble surface is also frequently in contact with the lower Perspex surface, depending upon bubble diameter and the flow conditions. The implication of this is an absence of air-water interfacial shear being replaced by air-fracture wall shear. The observed dry-out of the plate takes place because of the smooth planar Perspex surface and the surface tension properties of

the material. However, for the case of real rock fractures microscopic surface roughness maintains the water phase as a film at the fracture wall, overriding any local surface tension affects.

5.6 Summary

The significance of rock fractures in providing conducting pathways within a discontinuous rock mass has been highlighted in comparison to the mechanism of matrix seepage. A suite of analogue tests have been performed to study the two-phase flow behaviour of air-water mixtures between smooth parallel plates. The test conditions conformed to the assumed boundary conditions that are commonly applied to flow analyses in rough discontinuous geological media.

A review of existing literature indicated that there was no established flow pattern classification system that was applicable for all inclinations. This was a deficiency in the consideration of two-phase flow in geological discontinuous media, since variable inclination is a key factor in the definition of the geological environment. A flow pattern classification was proposed that is appropriate for variably inclined discontinuous geological media. This classification system has been defined in terms of observed flow behaviour recorded during testing.

As part of the study, a special apparatus was designed to enable the controlled and independent injection of both phases. Perspex plates were used so that observation of flow behaviour could be recorded. The plate assembly with an aperture of 250μm was mounted in a hinged frame that enabled the variation of plate inclination so that the influence of orientation and flow rate on two-phase flow behaviour could be examined. Analogue testing was performed for air-water mixtures with a wetting phase saturation of

between 45% and 100%, and for air phase flow rates up to 10 l/min. Tests were conducted at fixed orientations of 30°, 45º and 60°, as well as horizontally and vertically.

The testing illustrated the development of general two-phase flow patterns that change with phase saturation and phase velocity. A comparison of the test data for the different inclinations with established flow maps for horizontal and vertical flow indicates that fracture orientation has little impact on two-phase flow behaviour at the scale of the tests. However, if tests were performed with larger differential elevation, e.g. in situ testing on a regional scale or for very low injection pressures, then it is expected that elevation will have a greater influence on flow pattern.

The flow behaviour was noted to cause 'drying out' of the upper, and often the lower 'joint' surface. This is contradicts the theoretical argument presented in Chapter 4 for the capillary effects prolonging saturation of rough fracture surfaces. The particular behaviour seen in these tests is due to the smooth surface of the analogue fracture, which prevents the propagation of the water film during the passage of the air bubble. However, at increasingly elevated air phase velocity, the air bubbles were observed to first detach from the lower surface of the joint, and then form a wavy surface at the air water interface. This occurs once the phase velocities are no longer equal, and phase slip begins, whereby the air bubbles move more quickly than the liquid film and intervening slug.

The proposed annular two-phase flow model described in Chapter 4 was applied to the test data and found to correctly predict the phase height and analogue aperture relationship. It has been made clear that this model refers to linear flow behaviour and that the annular terms reflects the assumption that the water phase remains in contact with

both fracture surfaces. The current model and that previously described by Indraratna & Ranjith (2001) were found to satisfactorily relate phase height to relative permeability and illustrate the applicability of these simplified models, despite the localised development of the conceptualised flow pattern. This indicates that these models can be more widely applied to the range of laminar flow conditions outside of the original idealised flow patterns.

The two-phase flow behaviour recorded during the analogue testing illustrates the expected hydraulic behaviour through relatively smooth discontinuous geological media. The proposed simplified two-phase flow models for macroscopic conditions are relatively insensitive to flow pattern or test apparatus inclination. It can be reasonably expected that physical features particular to real fractures, such as aperture variability and flow channelling, can be considered as factors that accentuate existing flow behaviour.

The specially designed apparatus has been highly effective at illustrating the flow behaviour that occurs under two-phase conditions. The equipment has the advantage of being able to test relatively large scale fractures (surface area $0.6m^2$) as well as having the in-built flexibility to test fractures of different aperture e.g. 125μm, 375μm and 500μm using additional shims cut from existing stock. The supporting frame has been designed so that a high speed video camera can be mounted to record the dynamic flow behaviour. Careful manipulation of the spacers would enable the consideration of very fine apertures, so that the interplay between capillary and viscous two-phase flow can be studied. The equipment also has the potential to be expanded to include rough surfaced transparent casts of real fractures, or even synthetic surfaces. Alternatively different size

included elements could be placed between the plates to study the effect of contact area on flow behaviour.

Chapter 6

Two-phase Triaxial

Laboratory Testing

6.1 Introduction

The two-phase flow study that forms this chapter focuses on the performance of discontinuous geological media, i.e. a rock mass that is intersected by a number of discontinuities or fractures. The laboratory testing programme concentrates on the behaviour of a rock specimen intersected by one fracture, so that the hydromechanical characteristics of the fracture and the flow can be closely studied. This represents a different environment to a continuum-type porous, massive rock that is free of fractures through which flow takes place within the rock substance matrix, or a dual porosity type media that combines the continuum type with intersecting fractures. The aim of this part of the study is to investigate the ability of a fracture to affect the flow of two-phase mixtures of liquid and gas through a fractured rock mass, i.e. commonly encountered conditions around underground civil and mining excavations.

The rationale behind this phase of the study is set out in the following flow diagram (Fig. 6.1). The diagram summarises the stages involved during the testing and analysis of flow behaviour. The characteristics of the rock mass dictate whether:

(i) interconnected discontinuities are present,

(ii) the rock mass is massive, homogenous and isotropic, or

(iii) the rock mass is a combination of a relatively porous massive media with a superimposed fracture network.

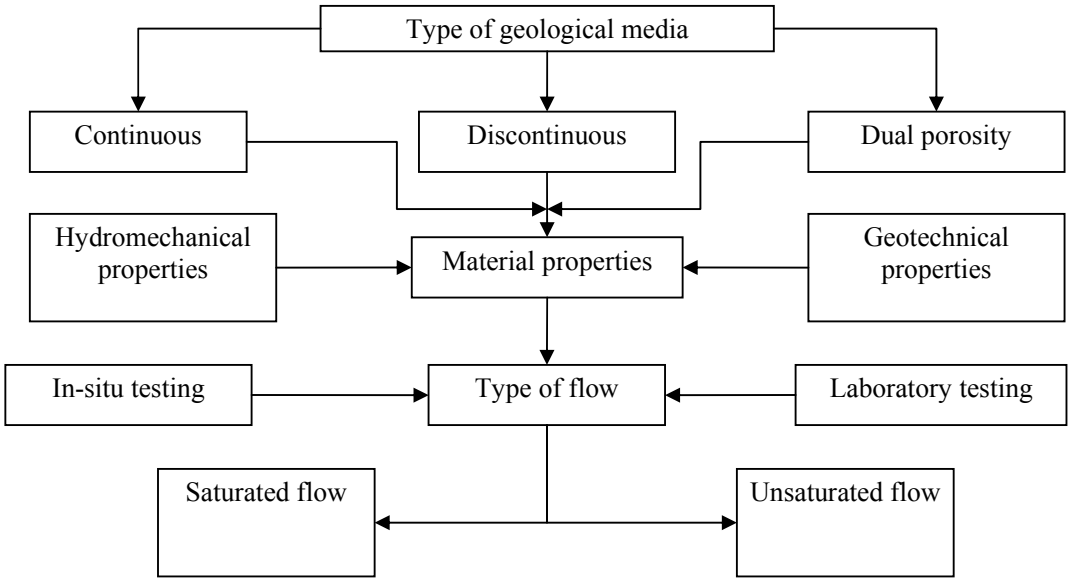

Figure 6.1: Flow chart showing sequential approach to analysis of flow through geological media.

The three above-mentioned geomechanical environments require different conceptualisation to analyse flow. The former can be represented as impermeable discontinuous rock blocks bounded by a fracture network; the latter can be hydraulically represented as a combination of a porous continuum with a fracture network. The dual porosity concept is applicable where the rock block conductivity is of a similar order to that of the bounding fractures. As the rock matrix conductivity decreases relative to the fractures, a single porosity model attributed only to secondary permeability becomes increasingly applicable.

The study has sought to establish the basic geotechnical and hydraulic properties of the rock samples being used for the study, so that the correct continuum-discontinuum model can be applied and the impact of roughness on the flow behaviour can be isolated. At this stage, the study has been limited to laboratory testing only, although the analogue joint apparatus (Chapter 5) has the potential to be used for idealised single and two-phase in-situ testing. By definition, two-phase flow where one

of the phases is gaseous, is unsaturated. This factor imposes significant constraints on the way that this problem would be usually analysed by engineers, and it is the identification and consideration of these constraints that has been the main aim of this work.

Two-phase flow behaviour has been investigated by carrying out a suite of laboratory tests using the Two-phase High Pressure Triaxial Apparatus (TPHPTA). The apparatus was originally developed and refined by researchers at the University of Wollongong (Indraratna & Haque, 1999; Indraratna & Ranjith, 2001). At the commencement of this study, further refinement to the data acquisition and flow monitoring were carried out to optimise testing capability during the current phase of testing.

The TPHPTA allows the measurement of flow and the calculation of the relative permeability of fractured rock specimens tested with air-water mixtures under a range of capillary pressures and stress regimes specifically selected to simulate those encountered in underground engineering excavations. The testing program involves the single- and two-phase steady state testing under controlled triaxial stress and capillary pressure conditions. The equipment has been modified to improve the digital data acquisition and to allow testing of relatively large volume fractures, similar to those found in the proximity of underground mining and construction projects where capillarity effects are often negligible. The previous testing used fractures (Indraratna & Ranjith, 2001) with $e_m \approx 10$ μm, which needed only a small volume dreschel bottle (250 ml) to collect and measure the mass flow rate. However, the fracture apertures tested in this current study were on average 1 to 2 orders of magnitude greater, so that the rate of flow could be up to 6 orders of magnitude higher under the same pressure

conditions. In this case, the largest available container that could be acquired and that would coordinate with the other apparatus was a 5litre flask.

6.2 Two-phase triaxial apparatus

Hydraulic testing of rock specimens is carried out in three stages, as described below. The tests are carried out at a constant axial stress, with the triaxial confining stress used to apply a normal stress to the sample fracture. For a range of inlet pressures, each fluid is injected at a constant rate until steady state flow is observed. For two-phase testing, steady state single-phase flow conditions are established for water, before air is injected at pressure increments, with steady state conditions allowed to re-establish before moving to the next increment of inlet air pressure.

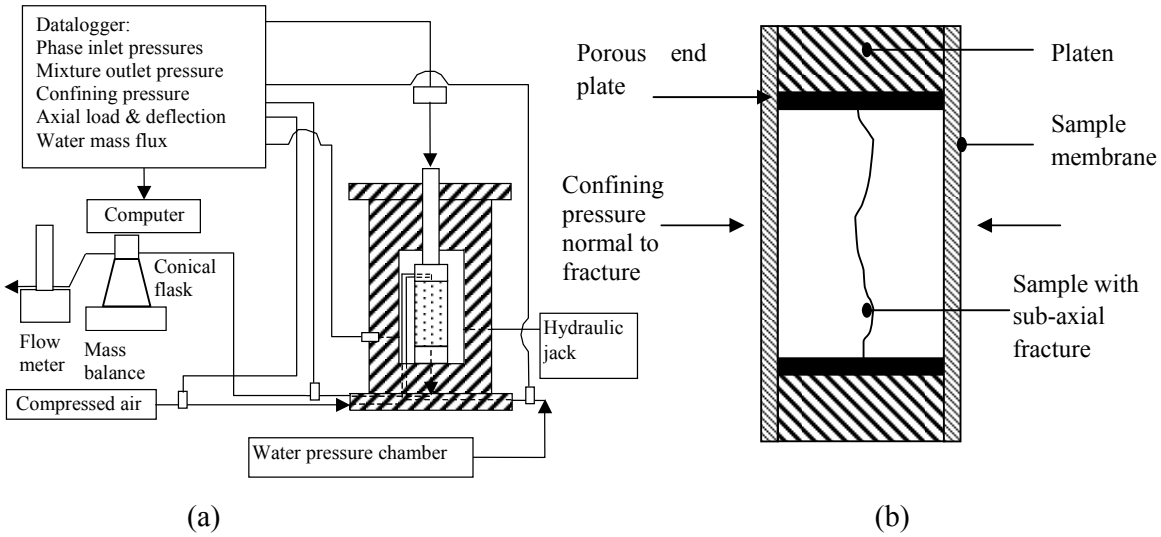

Figure 6.2: Key components of the TPHPTA: (a) Sketch diagram of Two-Phase High Pressure Triaxial Apparatus (TPHPTA) and (b) inset detail of test specimen.

The apparatus performance has been improved during this phase of the project by better use of data acquisition and flow measurement systems. The water phase mass flow measurement has been automated using a digital mass balance as well as larger capacity flasks (5 litres), so that higher permeability fractures could be tested. The air flow measurement device was replaced with more accurate and reliable digital mass flow

meters. The main advantages of the current system with the improvements are the streamlining and extension of the real time test data acquisition that enable the operator to monitor the test progress more completely without the same distractions that a more manual data collection system presents. In addition, the volume change device (Indraratna & Ranjith, 2001) has been removed to improve confining pressure regulation. This is a common limitation with hydraulic systems and the piston displacement mechanism was found to be particularly sensitive to leaks and very difficult to de-air. Sample volume change is now measured in terms of circumferential strain using two axially mounted clip gauges.

The triaxial apparatus comprises a steel cylindrical jacket and an upper and lower platen that were all machined so as to fit intimately together. When assembled as shown schematically in Fig. 6.2, neoprene 'O' rings are used to prevent leakage of confining fluid during testing. The apparatus is designed to measure sample deformation using strain gauges mounted on cylindrical spring steel clip gauges. The gauges fit around the sample when it is enclosed in a polyurethane membrane and principally measure fracture aperture dilation. This instrumentation has the capacity to measure variations in fracture normal stiffness (K_n) to be calculated over a variety of test results performed over a range of confining pressures (i.e. equivalent to joint normal stress for an axially fractured specimen).

6.2.1 Sample membrane

The sample membrane is cast from a two-part ERA TU-901 Polyurethane Resin. Injection of the compound uses two-tube combination caulking gun loaded with a 2:1 (300ml : 150ml) two tube cartridge fitted with a 235mm (24 helical element) static mixer tube to ensure uniform and thorough mixing of the two-compounds during

injection. A four component nylon (Dalrin) mould was machined so as to produce a 54mm (internal diameter) cylinder with a 3mm wall thickness.

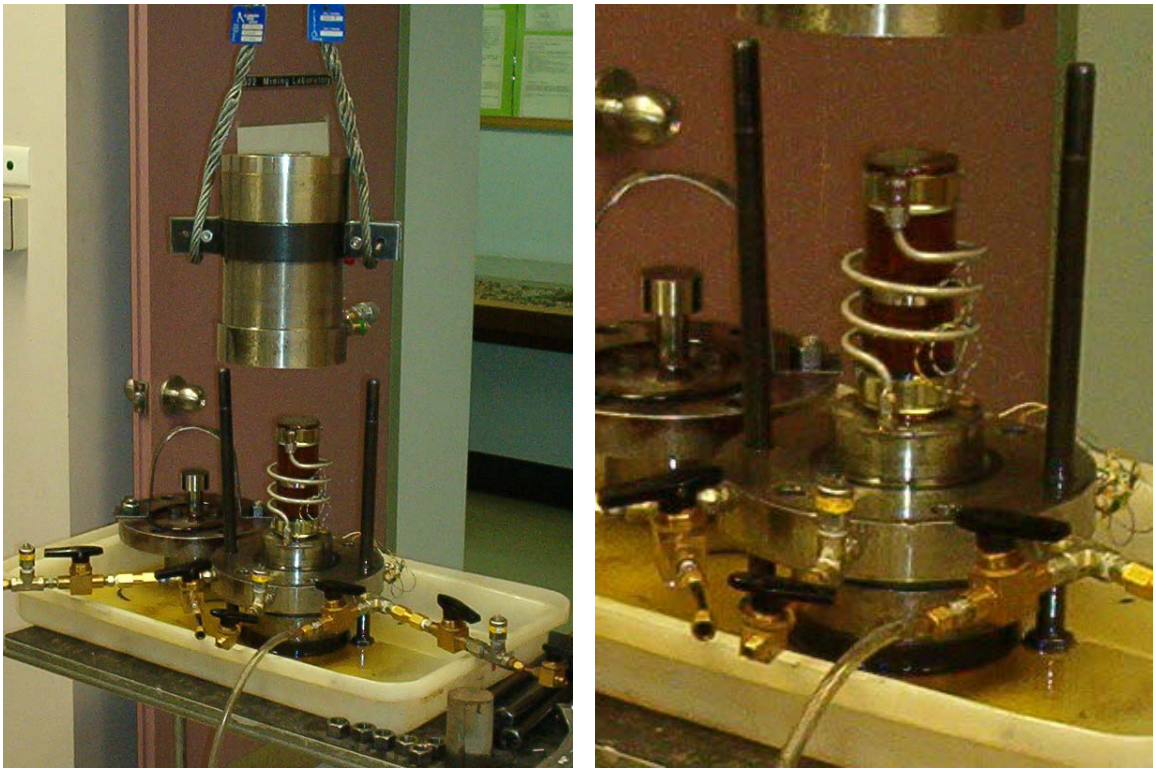

(a) (b)

Figure 6.3: Pictures showing disassembly sequence of triaxial cell. (a) Cell jacket is removed to reveal sample and membrane with clip gauge and mixture outlet tubing in place; (b) close up of lower plinth showing sample and inlet/outlet tubing.

Prior to casting, all surfaces of the mould were cleaned and smeared sparingly with a release agent. Resin was injected into the Dalrin mould at a slow and sustained rate to minimise air bubble inclusions and mix anisotropy. The membrane was cast and allowed to set for a 36hr period, before breaking the mould and trimming the cast. Membranes were only selected for testing provided the casting was free from air bubbles that could introduce localised weaknesses, leading to anisotropic strength and deformation properties during testing. A relatively stiff compound was essential so that

as wide as possible a range of confining pressures could be studied to optimise the ability of the membrane compound to bridge across the fracture trace without rupturing on potential sharp edges of the sample.

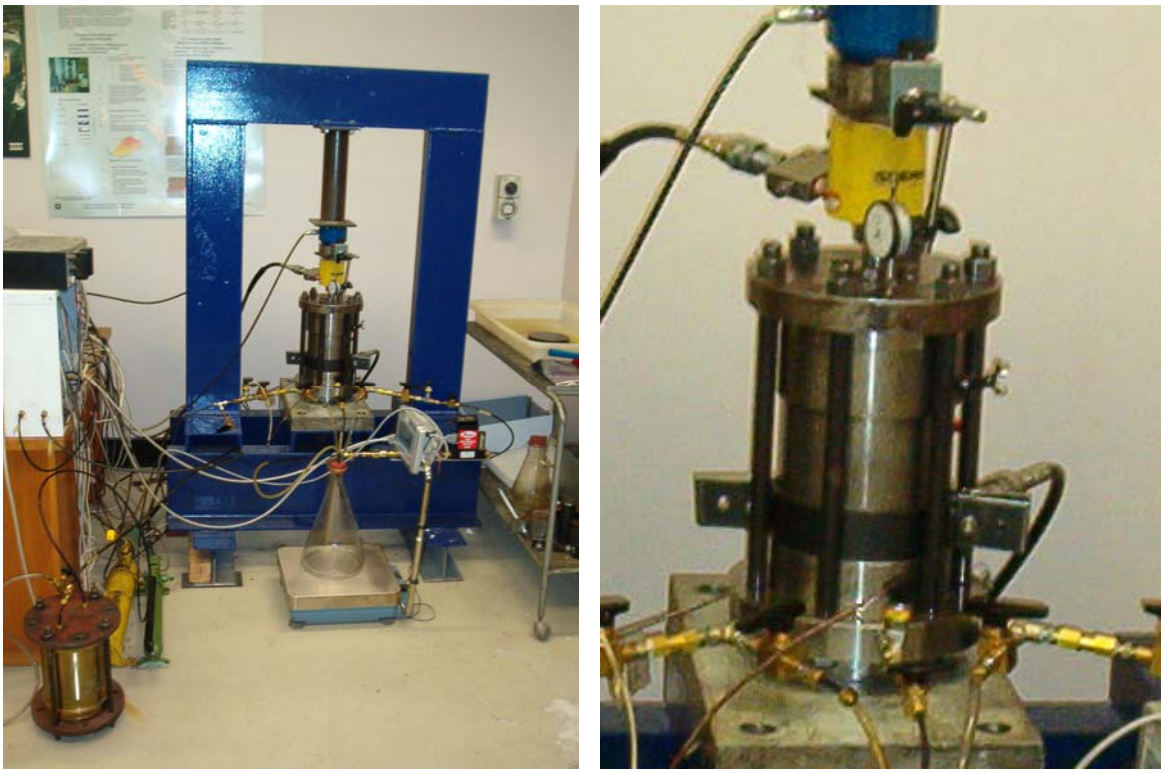

(a) (b)

Figure 6.4: Photographs showing (a) triaxial cell assembly and location within load frame relative to mass balance and digital flow meters, and (b) a close up of the inlet and outlet tubing.

Figures 6.3a and 6.3b show the sample inserted into the trimmed membrane with the fracture oriented sub-axially. Figure 6.3b illustrated the positioning of the clip gauge around the membrane (for the purpose of illustration, only one clip gauge is shown). During testing, two clip gauges are slid over the membrane and positioned equidistantly perpendicular to the sample long axis to measure the average fracture dilation. The sample ends were placed in contact with a 54mm diameter perforated and scribed bronze plates, which promote the distribution and percolation of injected fluids across

the entire face of the sample. The enveloped sample is attached to the plinth on the lower platen and secured with a 55 to 59 mm diameter high-pressure hose clamp. The clamp is tightened to prevent leakage of the test or confining fluids. The process involved in the final assembly of the sample on the lower platen can be seen in Figs. 6.4a and 6.4b.

6.2.2 Triaxial cell

A sense of the order of equipment assembly can be gained from viewing Figs 6.3b and 6.4b. The lower platen shown in Fig. 6.3b allows the details of the fluid mixture injection and outflow to be studied. The platen has 3 holes tapped to the base of the plinth, allowing air and water to be injected separately at the base of the sample; the third hole allows the mixture that emerges from the top of the sample to be directed to the flow measurement devices vis the lower platen and the helically coiled tubing seen Fig. 6.3b.

With the triaxial jacket and the upper platen lowered over the lower platen and secured in place, the apparatus can be transferred to the load frame (Fig. 6.4a). Axial load is applied to the sample using a hydraulic jack. The hydraulic jack is the yellow cylindrical object between the triaxial plunger and tubular steel spacer (Fig. 6.4). The axial deformation is monitored using a dial gauge and load recorded using a 500kg load cell (Fig. 6.4b). Axial load is maintained during the reported testing so the dial gauge is used to signal the sample failure. Confining pressure is controlled by a Sno-Trik high-pressure needle valve located at the rear of the assembled cell and applied using a second hydraulic jack, with pressure measurement made with a 0 to 10 MPa proprietary (UCC) pressure transducer. The hydraulic jacks are found in the left foreground (Fig. 6.4a), in front of the blue load frame.

Water is injected under pressure from the cylindrical pressure chamber shown in the immediate foreground at the bottom left of Fig. 6.4 (a). Compressed industrial-grade air is used for air-phase injection with inlet air- and water-phase pressures measured using two 0 to 1 MPa proprietary (UCC) pressure transducers. The fluid injection procedure is controlled by regulators on the (white) console (Fig. 6.4a). When the mixture has passed through the sample, the outlet fluid pressure passes another transducer before flow rate is measured.

6.2.3 Data acquisition and flow measurement

Flow measurement and data acquisition rely upon connection to a computer and a 10 channel Datataker DT500 data logger running DeLogger version 4.0. This configuration allows more frequent and accurate data collection during testing, compared to previous TPHPTA testing. Data is recorded at user specified time intervals (typically 30 seconds) to monitor the progression of the test.

Table 6.1: Datalogger channel configuration.

Channel	Sensor	Parameter and units
1	LVDT	Volume Change Device (mm)
2	UCC 0 – 10 bar transducer	Air phase inlet pressure (kPa)
3	UCC 0 – 150 bar transducer	Triaxial cell confining pressure
4	UCC 0 – 10 bar transducer	Mixture outlet pressure (kPa)
5	UCC 0 – 10 bar transducer	Water phase inlet pressure (kPa)
6	Load Cell	Sample axial load (kN)
7	Clip gauge (a)	Sample dilation (μm)
8	Clip gauge (b)	Sample dilation (μm)
9	GFC 0 – 500 ml/min	Air phase flow rate (ml/min)
10	GFC 0 – 30 l/min	Air phase flow rate (ml/min)

Water flow rate in terms of mass flow is reported automatically by an AND GP12K mass balance with RS2322 digital connection via a software application that downloads

Water is injected under pressure from the cylindrical pressure chamber shown in the immediate foreground at the bottom left of Fig. 6.4 (a). Compressed industrial-grade air is used for air-phase injection with inlet air- and water-phase pressures measured using two 0 to 1 MPa proprietary (UCC) pressure transducers. The fluid injection procedure is controlled by regulators on the (white) console (Fig. 6.4a). When the mixture has passed through the sample, the outlet fluid pressure passes another transducer before flow rate is measured.

6.2.3 Data acquisition and flow measurement

Flow measurement and data acquisition rely upon connection to a computer and a 10 channel Datataker DT500 data logger running DeLogger version 4.0. This configuration allows more frequent and accurate data collection during testing, compared to previous TPHPTA testing. Data is recorded at user specified time intervals (typically 30 seconds) to monitor the progression of the test.

Table 6.1: Datalogger channel configuration.

Channel	Sensor	Parameter and units
1	LVDT	Volume Change Device (mm)
2	UCC 0 – 10 bar transducer	Air phase inlet pressure (kPa)
3	UCC 0 – 150 bar transducer	Triaxial cell confining pressure
4	UCC 0 – 10 bar transducer	Mixture outlet pressure (kPa)
5	UCC 0 – 10 bar transducer	Water phase inlet pressure (kPa)
6	Load Cell	Sample axial load (kN)
7	Clip gauge (a)	Sample dilation (μm)
8	Clip gauge (b)	Sample dilation (μm)
9	GFC 0 – 500 ml/min	Air phase flow rate (ml/min)
10	GFC 0 – 30 l/min	Air phase flow rate (ml/min)

Water flow rate in terms of mass flow is reported automatically by an AND GP12K mass balance with RS2322 digital connection via a software application that downloads

were calculated within the spreadsheet for each test so that parametric relationships could be observed, in a similar fashion to that shown in Fig. 6.5, and the two-phase flow relationship of phase flow rate and pressure studied. The observed flow behaviour related to changes in hydraulic gradient or confining stress is described at length in Section 6.4.

6.3 TPHPTA testing methodology

The TPHPTA testing methodology is described in subsequent sections.

6.3.1 Sample description and preparation

Borehole core was provided from industry collaboration following a project in an underground coal mine located nearby in the NSW Southern Coalfield. The core is of a fine- to medium-grained arenaceous sandstone (belonging to the Triassic Eckersley Formation) comprising quartzitic and lithic fragments, and was drilled from the mine roof using standard geotechnical drilling techniques. The core samples contain occasional gravel-size lithic clasts and carbonaceous inclusions as expected from a 'coal measures' palaeo-environment. One of the factors that made the specimen interesting from a hydromechanical aspect was the presence of a sub-axial natural fracture that extended through a portion of the core. This provided an opportunity to test natural and induced tensile fractures within the sandstone.

The borehole was drilled using HQ equipment, yielding a nominal 64 mm diameter core. The core was cut into nominal 110mm lengths (those samples intersected by a natural fracture were taped together prior to cutting, with the two-parts in held together, to preserve their in-situ positions and prevent surface degradation and abrasion). In the laboratory, the samples were then cast in a concrete block and over-cored using an NX drill bit to provide nominally 54mm diameter samples for use in the

triaxial testing apparatus. The sample ends were lapped to ensure a smooth connection between the sample and perforated plate.

6.3.2 Membrane and clip gauge calibration testing

From the preceding description of fracture dilation measurement and Fig. 6.6, it is clear that sample deformation measurement requires calibration in order to relate the mechanical change of the clip gauge and the compression of the membrane to average aperture. To assess the deflection of the fracture aperture during loading, a correction to the gross clip gauge deflection must be made to account for the membrane deformation with changing confining stress. The relationship could be written as:

$$\delta_n = def_{clipgauge} - def_{mem} \qquad [6.1]$$

where, membrane deformation (def_{mem}) is not necessarily linear.

Membrane deformation was calibrated using the TPHPTA with a 'dummy' steel sample sheathed in a membrane. Over the stress range tested, the steel sample can be assumed incompressible when compared to the deformability of the enveloping polyurethane membrane, enabling a simple relationship between membrane deformation and confining stress can be observed. The membrane deformation can be plotted against increasing confining stress so that in subsequent tests, the actual rock sample deformation can be calculated from the recorded gross deformation value.

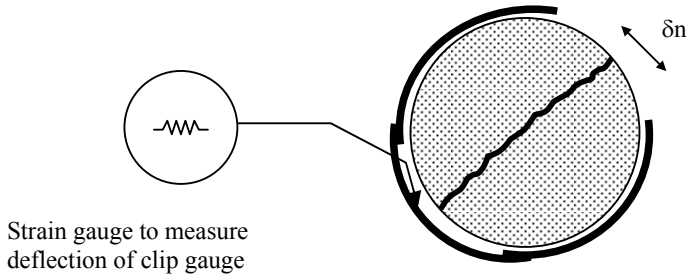

Figure 6.6: Schematic diagram showing positioning of clip gauge around membrane and sample to measure fracture normal deflection (δ_n) during triaxial testing.

Sample deformation is measured using specially developed instruments called clip gauges (Indraratna & Haque, 1999). The clip gauges are detailed in Fig. 6.6 and comprise 3 curved segments of spring steel with a 5mm long, 120 Ω foil strain gauge (gauge factor 2.13) fixed to the central portion of the gauge assembly. Flexure of the central steel gauge section due to changes in sample or membrane dimension are recorded by the strain gauge. In the course of normal testing, the sample is installed in the TPHPTA apparatus with 2 clip gauges placed around the sample to record membrane deformation whilst the confining pressure is varied similar to the arrangement shown in Figs. 6.3 and 6.4.

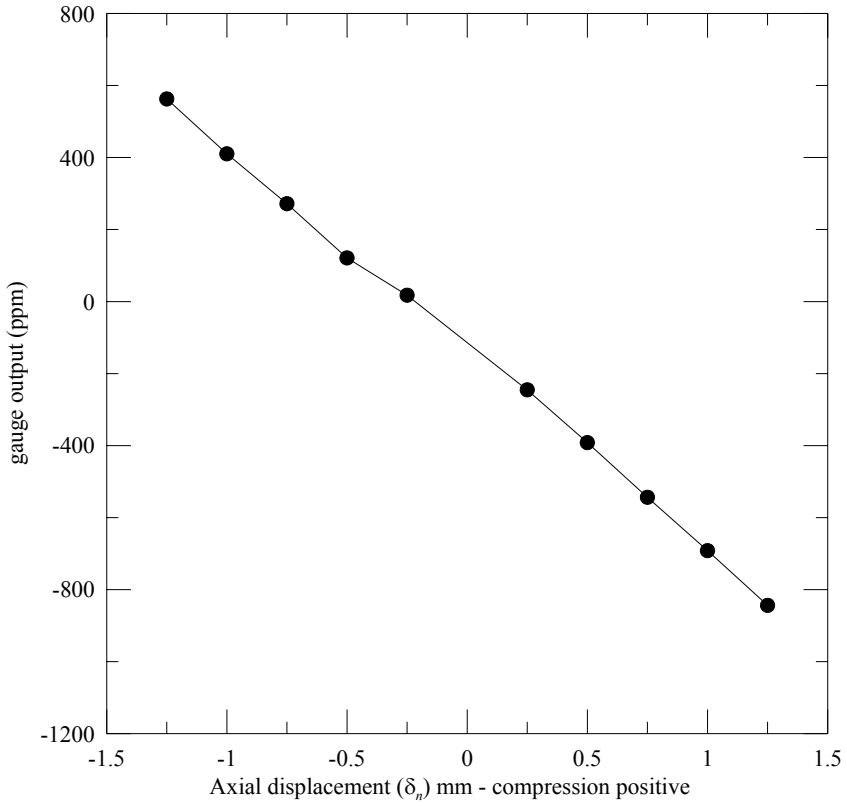

Figure 6.7: Typical results of clip gauge calibration testing.

The gauges are placed around the test specimen and membrane to measure changes in circumferential strain. The average deflection of the gauges is then used to calculate the

average change in sample fracture aperture and to estimate the fracture Normal Stiffness (K_n). Given the uneven nature of fracture surfaces and the spatial variability of fracture surface contact, the local change in aperture may not be constant across the sample, thus simple data processing was used to calculate the average change in aperture of the sample fracture.

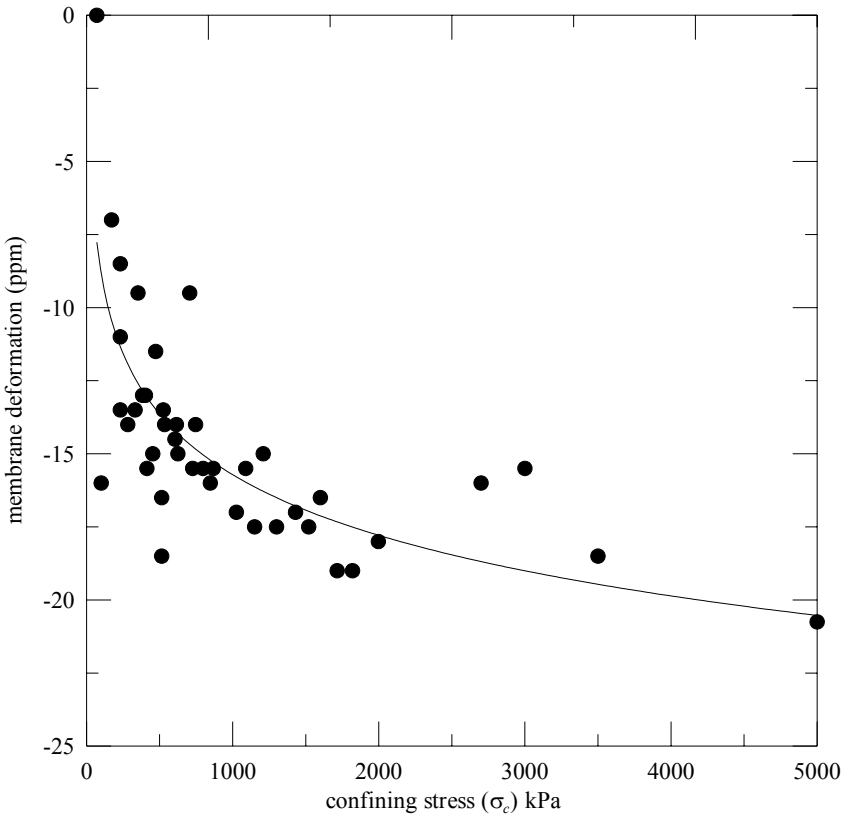

Figure 6.8: A plot of a sample of the test data showing the relationship between membrane deformation and confining stress.

The deflection of the clip gauge jaws are measured precisely with a digital vernier gauge and related to the normal deformation of the fracture using the calibration testing data. For the purposes of clip gauge calibration, the vernier calliper jaws grip the clip gauge limbs and are manually adjusted and held clamped whilst recording deflection with the datalogger. The vernier measuring axis is aligned perpendicular to clip gauge axis and the fracture plane, to directly measure fracture normal deformation. The

results of the clip gauge testing indicate similar performance of each of the clip gauges and a linear function relating physical deflection and clip gauge reading.

Figure 6.7 shows the linear relationship between nett datalogger reading (measured in parts per million or ppm) and clip gauge displacement (mm). The strain gauge signals were measured on the datalogger using the most accurate two-wire set up available. The wiring configuration used a half Wheatstone Bridge with a 2.5mA excitation. The strain gauge resistance balanced by a 120 Ω completion resistor. Analysis of the clip gauge calibration data shows the data can be interpreted to give the following relationship between deformation in a range of units – ppm as recorded by the datalogger, millimetres (mm) and micro-strain ($\mu\varepsilon$):

$$def_{mm} = def_{\mu\varepsilon} \times \frac{1}{593.58} = \left(def_{ppm} \times \frac{2.13}{2} \right) \times \frac{1}{593.58} \qquad [6.2]]$$

Once the gauge deflection is related to normal change in fracture aperture, the impact of membrane deformation can be incorporated. As can be seen from Fig. 6.8, this is achieved by analysis of the recorded membrane calibration data over the range of testing. Figure 6.8 shows a plot of confining pressure versus clip gauge reading (ppm) which can be approximated by a logarithmic regression equation to allow the membrane deformation component of any load to be calculated during TPHPTA testing:

$$def_{mem} = -3.3332 \ln(\sigma_{conf}) - 7.4338 \qquad [6.3]$$

where, def_{mem} is the membrane deformation in ppm and σ_{conf} is the confining stress acting normal to the joint surface (kPa). A sample of this data and the results of the regression analysis are shown in Figure 6.8.

6.3.3 Single-phase hydraulic testing

The design of the apparatus allows single-phase fracture testing using either the air or water phases as the permeating fluid. Typically, the single-phase testing involved

establishing steady state flow conditions for each confining pressure, for a range of different fluid injection pressures. Air phase testing was performed first so that the fracture remained free from water that could otherwise become entrapped and remain isolated in small aperture regions within the fracture plane. Entrapment would result in partial saturation for low injection pressures, causing underestimation of the fracture permeability. For relatively smooth fractures, the back-calculated apertures for air and water (single-phase) flow would be expected to be the same, unless relatively strong capillary effects were to reduce the magnitude of the water phase flow or non-linear flow was to occur. For rough fractures, back-calculated air and water (single-phase) apertures will not be the same regardless of any effects because the roughness of the fracture profiles will produce non-parallel, rotational flow within the enhanced boundary layer. However, the back-calculated single-phase air aperture for a rough fracture would still be effectively the same as the mean lognormal mechanical aperture because of the lower viscosity, i.e. $\bar{e}_{\log} = e_A$.

6.3.4 Two-phase testing

The TPHPTA equipment gives the operator total control over the injection of the two phases, as well as the application of axial and confining stress. The basic test procedure is summarised in the flow chart (Fig. 6.9). In this study for two-phase testing, steady state single-phase flow conditions are established for water injection at a pre-selected pressure. For each air pressure increment, the air phase is then injected until steady state flow conditions are established for each of the phases. This test approach was shown earlier in Fig. 6.5, where the interaction of the injected air phase increasingly impacts upon the flow of the water phase, particularly when the air phase pressure drop (p_A) exceeds 80% of the water phase pressure drop (p_W). Fig. 6.9 also shows that the water flow rapidly attenuates when air pressure is at least $p_A \approx 95\%\ p_W$.

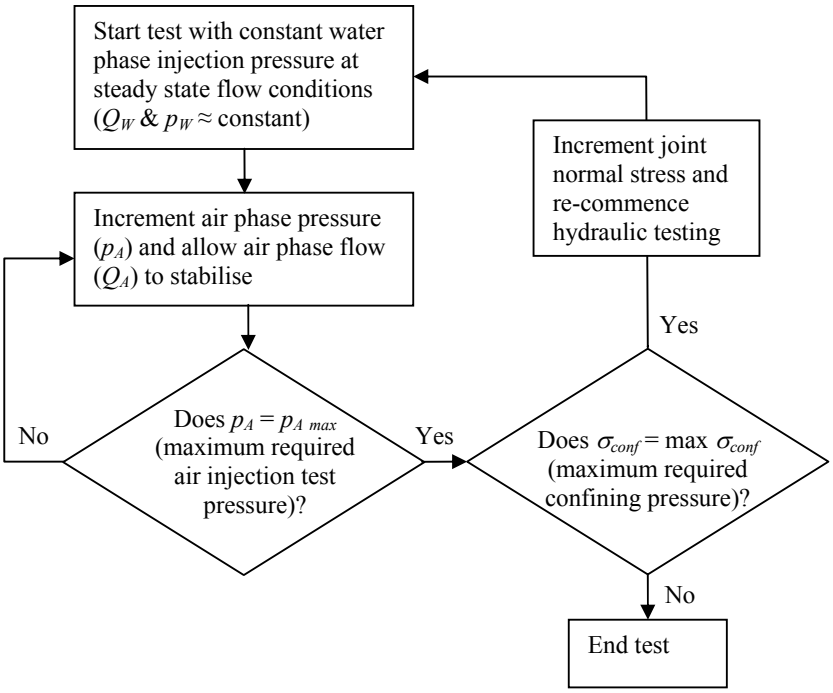

Figure 6.9: Flow chart summarising two-phase triaxial testing methodology.

6.4 Results and discussion

This section presents the results of the mechanical and hydraulic testing to characterise the two-phase flow behaviour of fractured rock samples. A limited mechanical testing regime was performed to provide information upon the density and porosity of the intact rock, the unconfined compressive strength and the Poisson's ratio. This data is used for calculating the mechanical response of the sample in subsequent sections of this document.

As described under single-phase testing, an intact sample was tested to identify the indicative matrix or primary permeability. Further single-phase testing carried out on fractured samples provides comparative data on the range of secondary permeability. The results show the contrast between the primary and secondary permeability and indicate the validity behind the assumptions applied to the analysis.

Two-phase testing was carried out on fractured samples and the results are discussed in terms of the proposed annular two-phase flow model (Chapter 4). Further examination of the observed flow behaviour is possible using the results of the roughness assessment and aperture measurement described in Chapter 3. The measured change in fracture aperture and the knowledge of the fracture roughness enables the fracture normal stiffness to be further studied in terms of the relationship between the calculated mechanical aperture and the back-calculated phase heights.

6.4.1 Mechanical and physical tests

6.4.1.1 Density and porosity

The sample dimensions and mass of the were recorded using a digital vernier gauge and electronic balance, respectively. Selected samples were weighed in both dry and saturated conditions to allow porosity and dry/saturated density to be calculated. The results are summarised in Table 6.2.

Table 6.2: Summary of TPHPTA physical sample properties.

Sample	Dry unit weight (kNm^{-3})	Saturated unit weight (kNm^{-3})	Porosity
JP08	25.65	25.95	0.146
JP09	24.40	25.44	0.106
JP10	21.39	23.40	0.103

The density testing summarised in Table 6.2 indicated that the samples have dry and saturated densities of in the ranges of 21.4 to 25.7 kNm^{-3} and 23.4 to 26.0 kNm^{-3} respectively (averages of 23.5 and 24.5 kNm^{-3}). These ranges of values would be expected for rock comprised extensively of quartz, a relatively low density mineral. The test results also show the sandstone samples to have a low effective primary porosity of between 10% and 15%. Some published empirical correlations between intrinsic permeability have been developed from the Cozeny-Karman equation (e.g.

Fisher 1977, Snow 1968). The main drawback with these relationships is the assumed idealised isotropic nature of the grain shape and packing. Observation of these samples clearly reveals anisotropy in grain shape and size as well as localised quartz rich lenses extending across the sample and parallel to the identified bedding structure. Hence application of these equations considerably overestimates the primary intrinsic permeability of the samples. The most effective way to study the primary permeability is to carry out permeability testing on the samples using the TPHPTA in single-phase mode, as further discussed in Section 6.4.2.

6.4.1.2 Young's Modulus and UCS

There were limited opportunities for destructive mechanical testing were because of the small number of samples available and the higher relative importance of the TPHPTA testing. An indicative set of mechanical and deformational properties were obtained by instrumenting JP06 with a pair of foil strain gauges during an unconfined compression test, in accordance with ISRM (1978) testing guidelines.

Table 6.3: Summary of mechanical properties from instrumented UCS testing of JP06.

Parameter	**Value**
Young's Modulus, E (MPa)	913
Poisson's ratio, ν	0.21
Unconfined compressive strength, UCS (MPa)	42

The stress and strain measurements obtained from the UCS test with strain gauge data for sample JP06 was plotted in Fig. 6.10. The plot shows an essentially linear response over more than 50% of the test. Over this linear range, the Poisson's ratio (radial to axial strain) was approximately 0.2. The sample failed at an axial stress of 42 MPa, indicating the rock to lie near the top of the medium strong range, as defined by the

ISRM guidelines (1978). The failure point corresponds to axial and radial strains of about 5%.

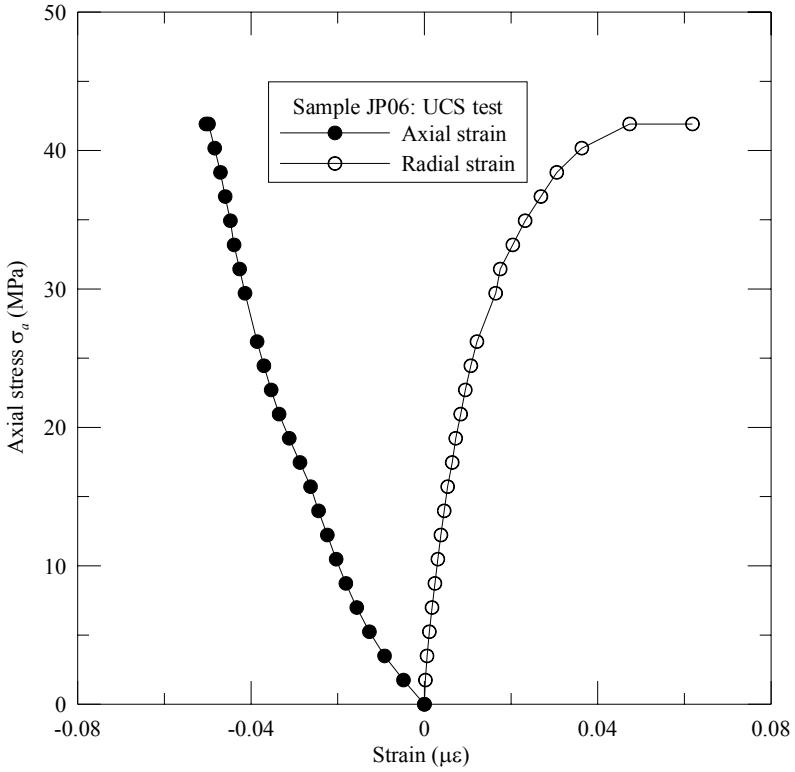

Figure 6.10: Plot of stress and strain results from unconfined compression test with strain gauges on JP06.

6.4.2 Single-phase flow

Single-phase testing was carried out using the TPHPTA apparatus by ensuring the appropriate inlet valve was closed. Although not the main area of interest, single-phase flow provides an opportunity to test the operability of the apparatus on fractured samples, allows a comparison of air and water flow, as well as providing a point of comparison to two-phase flow behaviour. In addition, intact samples can be tested to compare the role of primary and secondary permeability on the behaviour of the specimens.

6.4.2.1 Intact sample – flow behaviour

Testing of an intact sample was necessary to indicate the likely range of permeability of the sample matrix to allow comparison with the calculated fractured sample permeability. Sample JP10 was selected as representative of the specimens in terms of mineralogical texture and composition. The sample was first saturated in a water bath prior to conductivity testing with water as the permeating fluid. Tests were carried out for confining stresses of between 300kPa and 500kPa with the water injection pressure raised to 300kPa. The associated hydraulic gradient of approximately 3MPa m^{-1} was chosen to overcome the large frictional losses that would be expected in a rock mass comprising small pores. Average steady state water flow rates of about 0.01 ml min^{-1} were measured during the test, corresponding to an intrinsic permeability (k) of 3.5 x 10^{-14} m^2 (or 3.5 x 10^{-2} darcies). If this value is expressed in terms of an equivalent fracture permeability k_f, this would correspond to a smooth parallel fracture with an aperture of only 6.5 x 10^{-7} m.

Accordingly, the impact of matrix or primary permeability on the measured flows of either of the phases can be effectively ignored, given that the mean log normal fracture aperture ($\overline{e}_{\log}$) for the samples is at least 3 orders of magnitude greater for the same confining stress levels. The likely effective porosity can be estimated by comparing the measured primary permeability with the empirical porosity-permeability relationship proposed by Fisher (1977), who suggested that the intrinsic permeability k could be related to porosity n by the equation:

$$k = \frac{n^3}{180} \qquad [6.4]$$

If the matrix permeability value discussed above is substituted into Eq. 6.4 the calculated porosity value (0.02%) is much less than the bulk porosity value calculated in Section 6.4.1.1. This discrepancy indicates the difference between the gross porosity of

a material and the effective porosity, i.e. the proportion of intergranular voids that freely conduct fluid. In this case, the matrix appears essentially impermeable and can be neglected when analysing the fractured sample permeability.

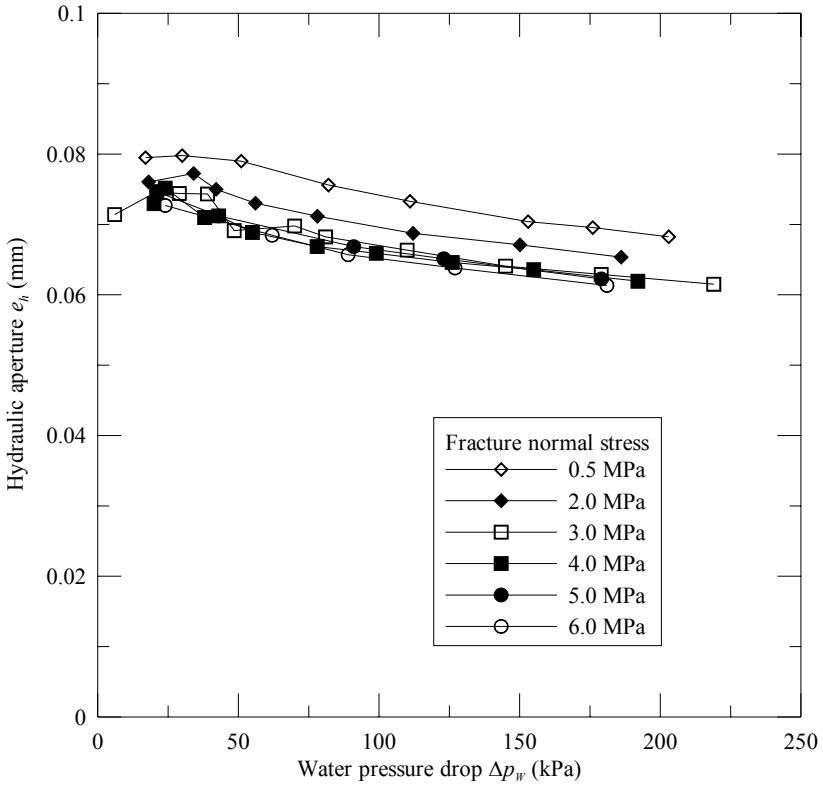

Figure 6.11: Typical single-phase test results for sample JP08, conducted over a range of confining conditions showing a plot of (back-calculated) hydraulic aperture and water phase pressure drop.

6.4.2.2 Fractured samples – flow behaviour

The single-phase tests record linear and non-linear flow conditions (Figs. 6.11 and 6.12). For a specific confining stress, back-calculation of fracture aperture using these results shows a near constant aperture occurring over the range of linear flow conditions that decreases with the onset of turbulence. When the maximum aperture is plotted for a suite of tests over a range of confining stresses, a gradual reduction in the back-calculated aperture is observed.

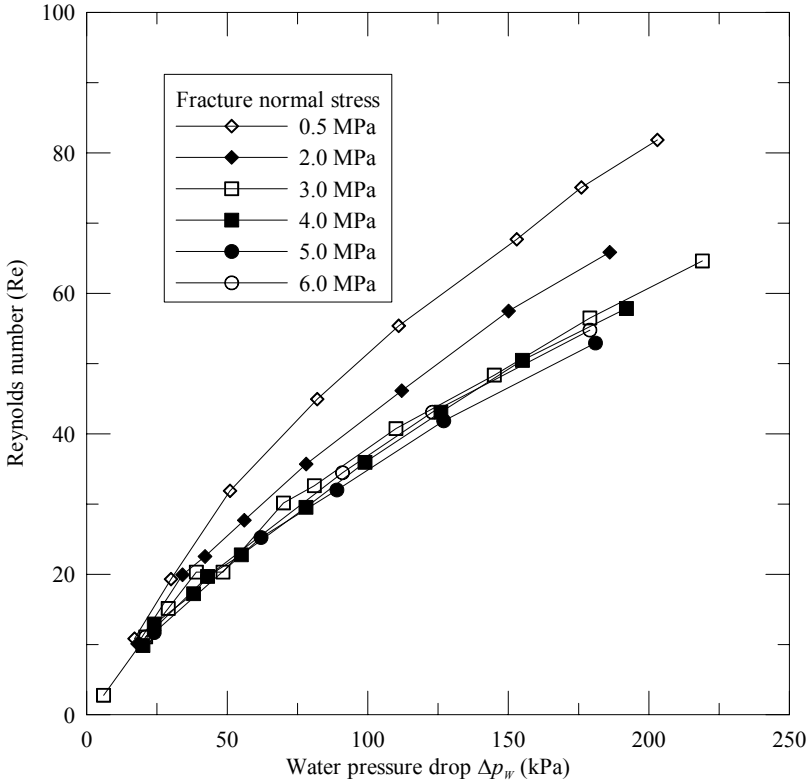

Figure 6.12: Hydraulic behaviour of rock fracture showing transitional laminar and turbulent flow for specimen JP08 for confining stress varying from 0.5MPa to 6MPa.

The fracture hydraulic response to changes in pressure gradient has been well documented (Louis, 1969; Elsworth & Doe, 1986; Lee & Farmer, 1993). The expected laminar to turbulent flow behaviour is clearly seen in the test results obtained from the current study (Fig. 6.12). The earlier work by Louis (1969) showed the transition from laminar to turbulent flow can be estimated from knowledge of the surface roughness index S and the Reynolds number is Re in Eq. [6.5]. Louis (1969) defined S as the ratio $a_{max} : 2e_m$ where, a_{max} is the maximum amplitude of the surface and e_m is the mechanical aperture. The Louis (1969) work showed that with increasing roughness, the transitional Re reduced from 2300 (S = 0.001) to 100 for S = 1.

$$\mathrm{Re} = \frac{2e \cdot V}{\nu} = \frac{2Q}{\nu y} \qquad [6.5]$$

The calculation of the surface roughness index *S* for the rock samples in this study found values >> 1 (in the range 40 to 186). The large *S* values were due to the significant fracture roughness magnitude resulting in low transitional Re (<< 100) for the samples. This was confirmed experimentally and revealed the non-linear flow transition occurred for Re between 17 and 30 (Fig. 6.12).

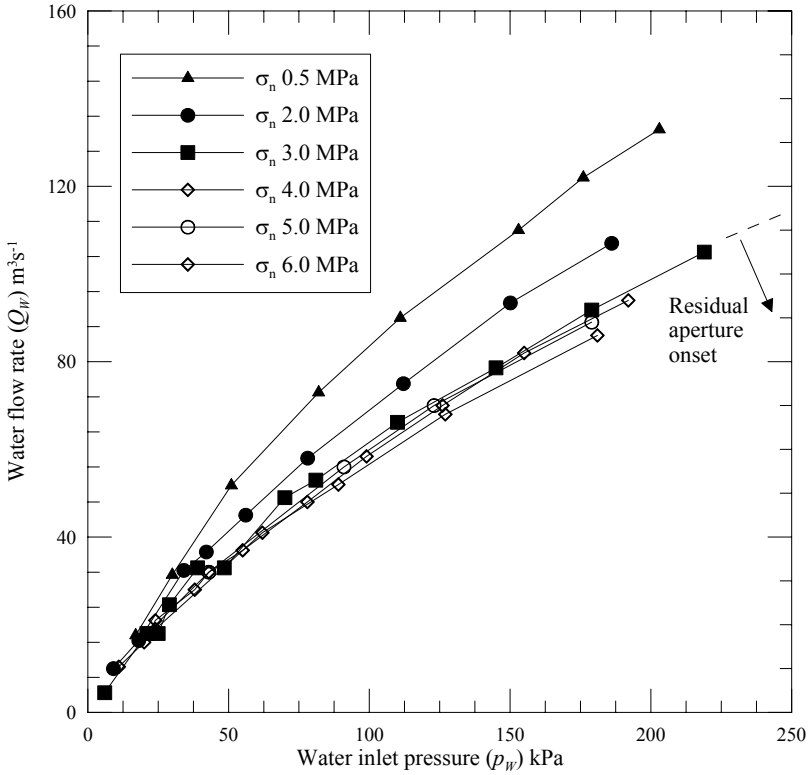

Figure 6.13: Impact of fracture normal stress and pressure drop on single-phase flow behaviour for sample JP08. Note the onset of residual aperture when normal stress exceeds 3 to 4MPa.

This study of fracture normal stress versus flow behaviour confirms established characteristics (Indraratna & Ranjith, 1999; Lee & Harrison, 2001). A plot of flow rate versus confining water inlet pressure (Fig. 6.13) shows a gradual reduction in flow as fracture normal stress (i.e. confining stress) increases. With increased stress, the proportion of fracture contact area between the surfaces rises until the residual aperture

is attained. This is signalled by a near non-reducible flow rate as shown in Fig. 6.13 beyond a confining stress of 3 MPa to 4 MPa.

Roughness has an easily identifiable impact on flow because of the promotion of non-parallel or non-linear flow through the fracture. This results in the observed divergence of the hydraulic aperture e_h that can be calculated with the 'cubic law', from the actual or 'mechanical' aperture e_m that could be physically measured as related by Barton et al. (1985) empirical relationship:

$$e_h = \frac{e_m^{\,2}}{JRC^{2.5}} \qquad [6.6]$$

where, e_h is the hydraulic aperture for $e_h/e_m \leq 1$, with apertures measured in microns. This relationship provides an important connection between the mechanical deformation of the fracture (hence, the associated rock mass) and the hydraulic performance taking account of the non-linear effects related to fracture roughness. For a stress increment $\Delta\sigma_n$ and assumed linear stiffness-deformation, Eq. [6.6] can be re-written if e_m is defined in terms of the change in aperture Δe_m, the initial mechanical aperture under zero fracture normal stress (e_{m0}) and the fracture normal stiffness, $K_{n\mu}$, in units of MPa/μm:

$$e_h = \frac{\left(e_{m0} - \Delta\sigma_n / K_{n\mu}\right)^2}{JRC^{2.5}} \qquad [6.7]$$

The relationship allows for normal loading of the fracture and assumes there is no associated degradation of the fracture surface or gouge formation that could lead to the change in the *JRC*. The estimation of $K_{n\mu}$ is based upon analysis of clip gauge deformation data gathered during laboratory testing. The applicability of Eq. [6.7] relies upon the selected stress range because of the assumed linear stress-deformation function.

6.4.3 Two-phase flow

The hydromechanical two-phase testing using the TPHPTA provides valuable data on the two-phase flow relationship to fracture normal stress. Observations from the laboratory study are discussed in terms of flow, relative permeability, and mechanical deformation.

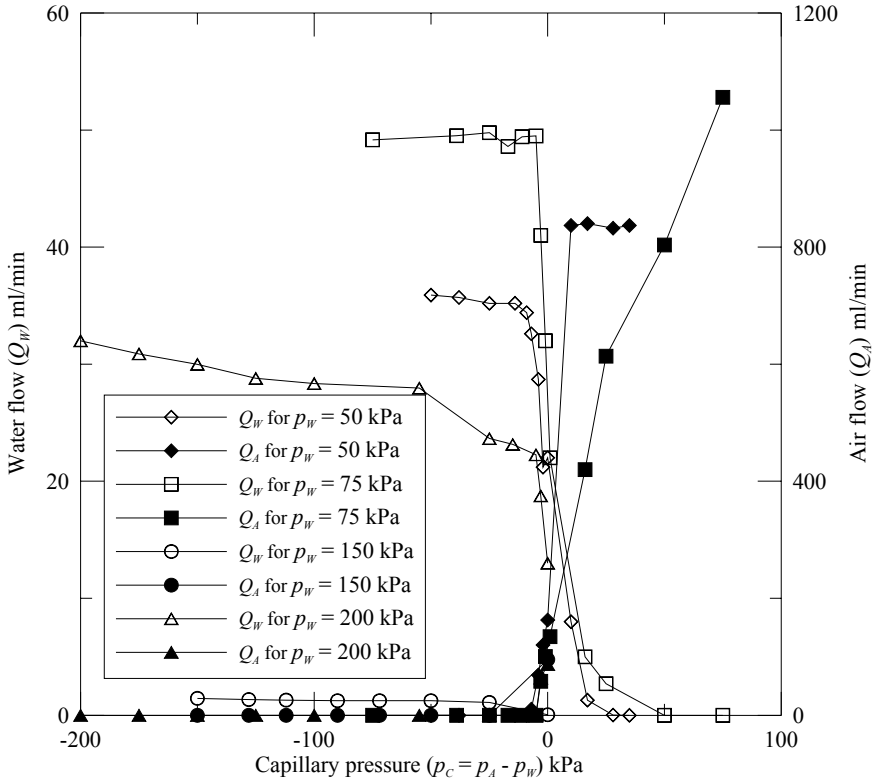

Figure 6.14: Two phase test results for JP09 at a fracture normal stress of 500kPa, and a p_W range of 50kPa to 200kPa.

6.4.3.1 Flow response to change in injection pressure gradient

The results of two-phase triaxial testing are used to illustrate the key hydraulic and mechanical features of the study. Characteristic flow and pressure data obtained experimentally are presented in Figs. 6.14 and 6.15. The plots show the fluctuations in pressure and flow rate that occur during the observed development of two-phase flow. The water flow data shows an initial gradual reduction with a corresponding increase in

air flow that is initially imperceptible. This aspect of the flow behaviour could be more clearly studied if the water flow measurement accuracy was improved.

Under steady state conditions, the two-phase flow behaviour can be studied in terms of capillary pressure. Figure 6.14 shows a gradual roughly linear reduction in water flow (Q_W) as the air phase pressure (p_A) is increased to between 80% and 98% of the water phase pressure (p_W). Over this range the corresponding air flow (Q_A) is very small (effectively zero). The transient and steady state conditions can be studied by considering the development of flow behaviour with respect to time, as is shown in Fig. 6.15. When the air phase is about 50% of the water pressure value (approx. I = 50 mins), there is a gradual increase in the air phase flow rates, which tends to oscillate with greater amplitude as the air phase pressure increases further. This suggests that the water phase is flowing continuously and the air phase flow is discontinuous.

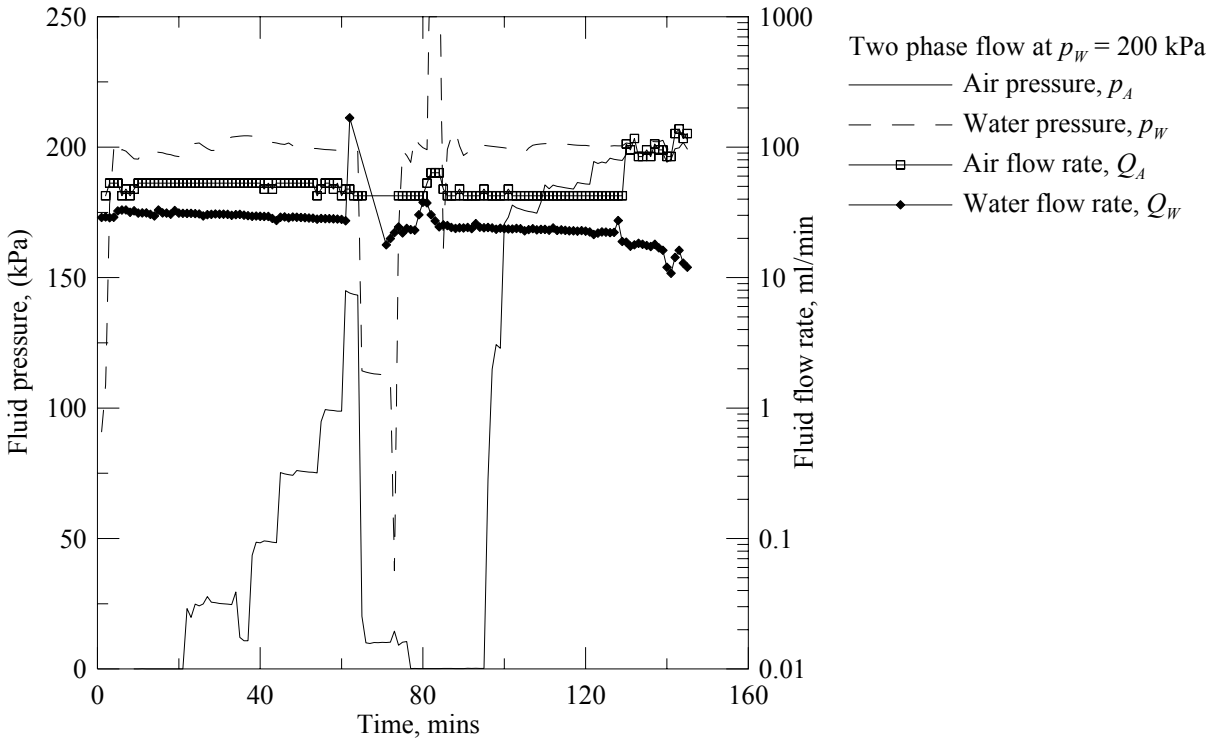

Figure 6.15: Two-phase test data plotted against time for p_W = 200kPa.

When the air phase pressure approaches about 98% (approx. t = 125 mins) of the water phase pressure, the air phase flow appears steady, suggesting that both phases are flowing continuously. By this stage, the water flow rate has dropped by one or more orders of magnitude from the initial value recorded at the start of the test. This is shown very clearly in Fig. 6.15. When continuous air phase flow occurs and the air pressure is increased, the water phase flow shows increasing fluctuation until water flow ceases. If the air pressure is maintained from the point of $p_C = 0$ and the water pressure is reduced, the water flow becomes increasingly sporadic from about p_W = 60% to 80% p_A, i.e. water flow is discontinuous. Water phase flow was observed to be only occasional for $p_W < 60\%\ p_A$.

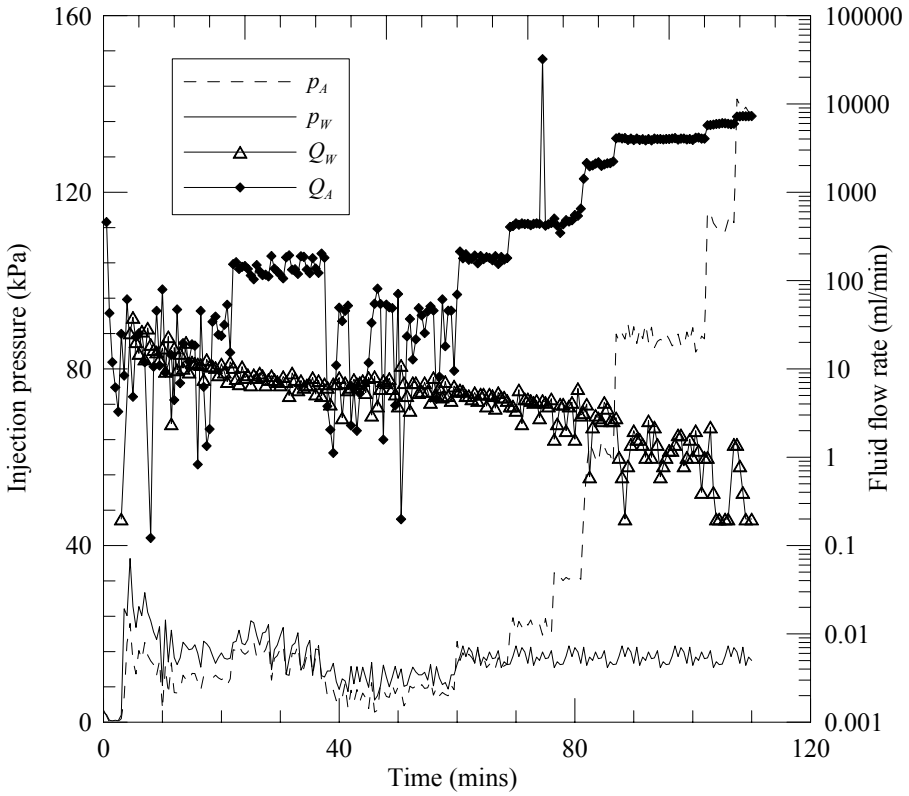

Figure 6.16: Test results for sample JP04 showing typical test behaviour - raw test data for phase flow rate and inlet pressure.

The simplified annular flow model was discussed in Chapter 4 and is defined by Eqs. [4.49] and [4.50]. The model allows the ready calculation of the phase heights H_A and H_W. Plotting fracture flow data recorded during testing reveals the inter-relationship between the phase flow rate and the pressure drop. Fig. 6.16 shows a typical test record for sample JP04 under a fracture normal stress of 500kPa. Fig. 6.16 shows the test procedure whereby, p_W is maintained at 13kPa, and p_A is injected in 6 stages from 10kPa to 140kPa. The initial water flow rate at steady state is about 8ml/min and decreases with each successive increase in p_A. The air phase flow rises in steps to 7300 ml/min.

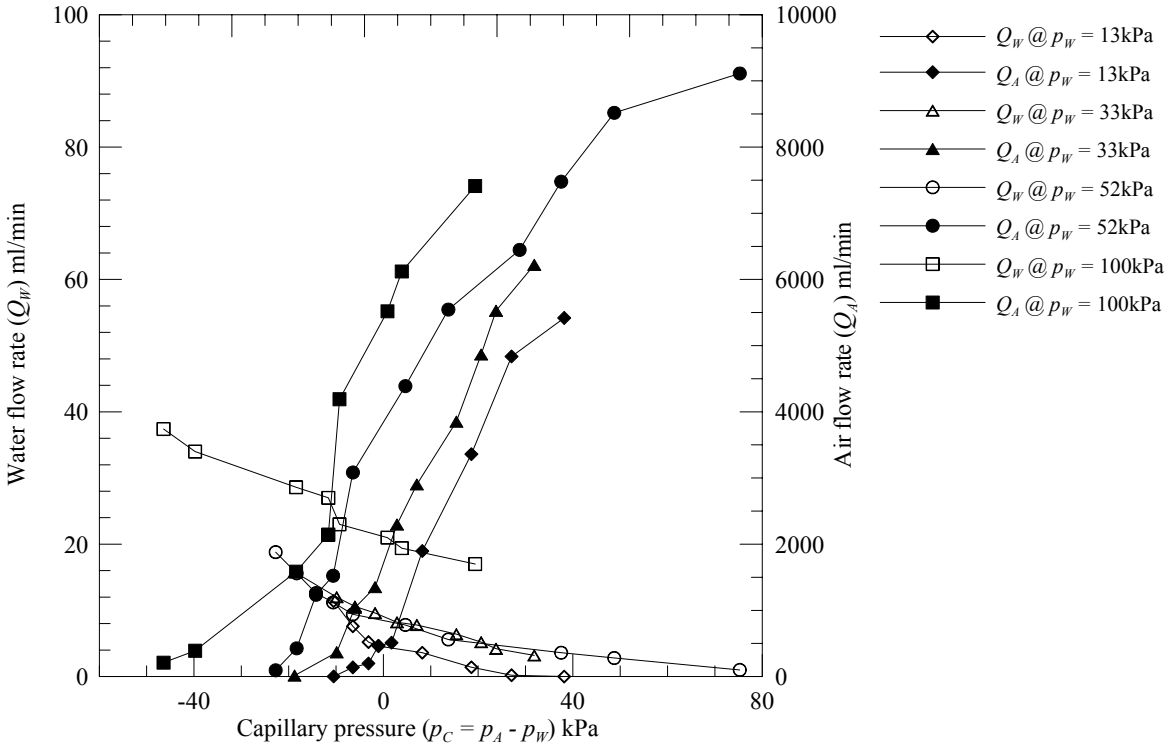

Figure 6.17: Test results for sample JP04 showing typical test behaviour - comparison of phase flow rate and phase interference.

A number of characteristics can be seen by comparing the variation in phase flow (Fig. 6.17) and phase height (Fig 6.18) during each test stage, despite the localised variations in flow and phase occupancy. As an aid to compare the two-phase flow behaviour, it is

convenient to plot data against the capillary pressure represented by the difference in phase inlet pressures or $p_A - p_W$. Fig. 6.17 plots the flow rates against the capillary pressure for each of the injection pressure tests for the two phases. The graph shows that the phase flow rate is proportional to the pressure drop, and the water flow reduces as the air pressure-drop increases. As would be expected from general hydraulics, a lower viscosity fluid flow changes much more quickly than a more viscous phase.

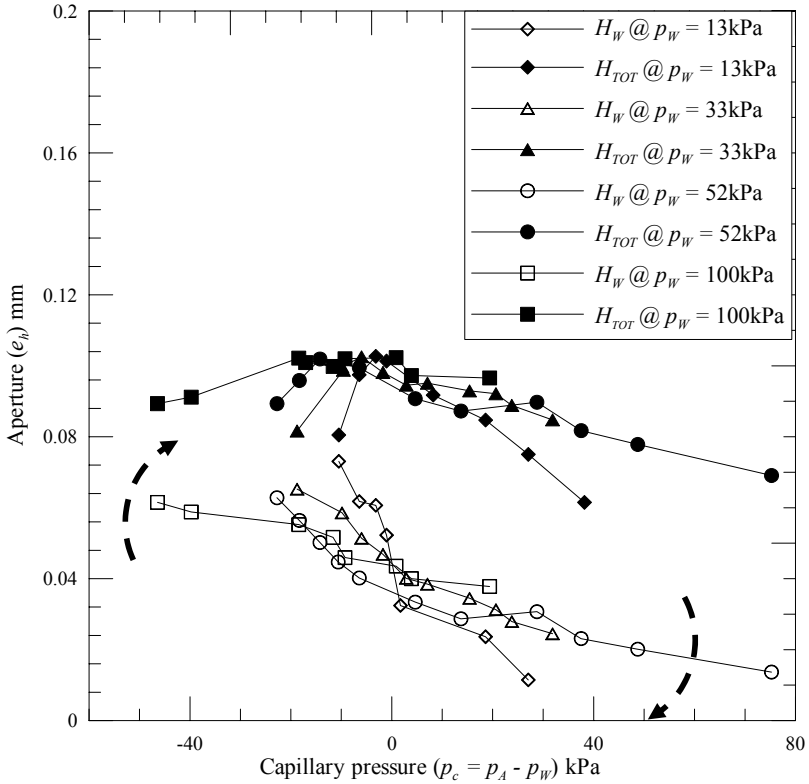

Figure 6.18: Test results for sample JP04 showing typical test behaviour - comparison of water phase height H_W and sum of phase heights ($H_{TOT} = H_A + H_W$) in terms of capillary pressure for a range of water phase pressure drops.

The air and water phase heights, H_A and H_W (Figs. 6.18 and 6.19) were calculated by applying the simplified annular flow model using Eqs. [4.49] and [4.50]. Figure 6.18 shows that the maximum H_{TOT} occurs at an incrementally lower capillary pressure (from 0 to -20kPa) as the water phase pressure is increased (from 13 to 100kPa); the same

graph also shows that the maximum H_W reduces with each increase in injection pressure. This means that the turbulent flow transition develops at decreasingly lower phase flow rates, as the phase pressure is increased. Figure 6.19 demonstrates that the total phase height increases as the air phase starts to flow more continuously, i.e. when $p_A \approx p_W$. Figure 6.19 also shows that maximum total phase height H_{TOT} increases in proportion to the capillary pressure. These conditions are expected to prevail due to increasing 'slip' between the air and the slower water phase. Ultimately, the conditions develop with the onset of greater discontinuity of phase flow with turbulence contributing to increasing momentum loss.

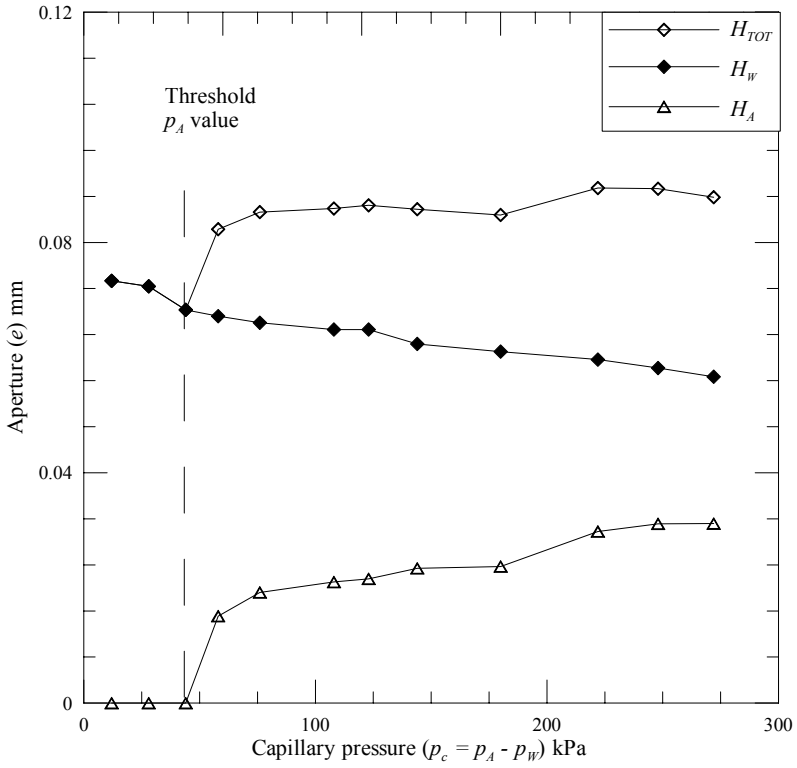

Figure 6.19: Plot showing mobilisation of air phase and impact upon calculation of the mechanical aperture.

The total phase height increases as S_W decreases linearly due to an increase in air flow. This is shown in Fig. 6.19 for $p_C \approx 180$ kPa when H_A increases 50% to 0.032mm, indicating that the water phase, rather than air, is more affected by turbulence.

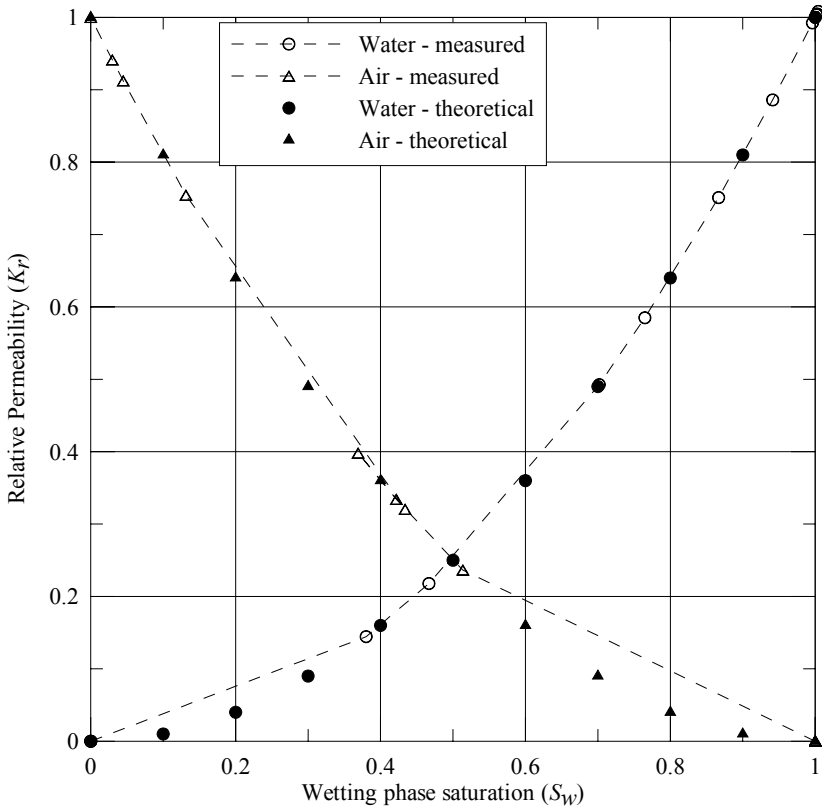

Figure 6.20: Relative permeability saturation function curve for $p_W = 75$kPa.

Differences between H_W at $S_W = 1$ and H_A at $S_W = 0$ could be envisaged where apertures and phase pressure gradients are relatively small and roughness is large, resulting in trapping of water and air pockets within the fracture, promoting diminished permeability by increased flow channelling. The presence of the lower viscosity air phase means that two-phase injection testing allows greater penetration of the phase mixture into regions of the fracture that would preclude single-phase water ingress. If two-phase flow occurs, i.e. only minimal air phase trapping, then calculation of the air phase height by measuring the air phase pressure gradient and flow rate enables the

mechanical aperture to be calculated from the sum of the phase heights, i.e., $e_m = H_W + H_A$. Laboratory results validate this observation, provided that sufficient air phase pressure drop is available to mobilise the air bubbles. This point is illustrated by plotting H_W and H_{TOT} (Fig. 6.19). H_{TOT} increases once p_A surpasses a threshold value, overcoming air phase entrapment and mobilising air phase flow.

6.4.3.2 Relative permeability analysis

The two-phase flow behaviour was analysed in terms of the relative permeability and fracture saturation for each stage of the test using Eqs. [4.7] and [4.8] and the method described in Section 4.2. Fig. 6.20 presents a sample plot of test results and shows the relationship of the phases to saturation in accordance with the phase height theory proposed in Chapter 4. The close agreement between the measured and theoretical behaviour shows validity of the assumed parallel plate conditions with minimal capillary effects throughout the range of test pressures.

The explanation of the observed variation in function geometry is of great importance and several key factors can be postulated. The flow regime of each phase is unknown: it could be linear (laminar) or non-linear (transitional or turbulent). In addition, calculation of the Reynolds number for two-phase flow is problematic since it requires careful assumption or knowledge of the fracture hydraulic diameter for each phase, as well as phase continuity. This factor depends upon both the physical fracture characteristics and also the appropriate two-phase flow regime. The relevant hydraulic radius is a quantity that changes dynamically as two-phase flow occurs, as illustrated in Chapter 5 (Figs. 5.7 to 5.12).

The complex nature and development of two-phase flow patterns will also impact upon the K_{ri}:S_w relationship. The form and extent of the air-water interface as

the p_A and p_W values approach equality will change considerably. A flow pattern transition could be envisaged, with p_A increasing relative to p_W, changing from:

- discrete air bubbles in a continuous water phase,
- two continuous air and water phases,
- continuous air phase with possibly, a small volume of film flow along fracture surfaces and maybe even some entrained water droplets.

During two-phase flow, the interface development would also be expected to compound the effect of tortuosity on phase flow behaviour, with localised and variable formation, such as was seen in Chapter 5 (Figs. 5.7 to 5.12).

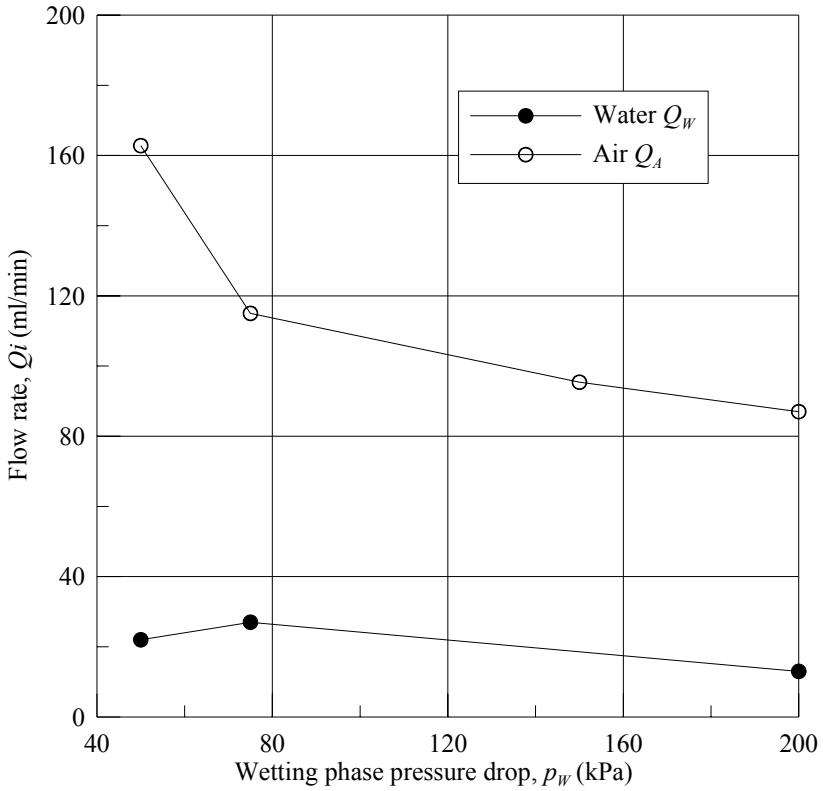

Figure 6.21: Plot of steady state two-phase flow rate (Q_i) versus wetting phase pressure (Δp_w) for sample JP09.

Plotting the two-phase flow rates against wetting phase inlet pressure (or pressure drop – Fig. 6.21) shows the peaking and/or subsidence of Q_A and Q_W as p_W increases. If we were considering single-phase water flow in a fracture, this data pattern would suggest that laminar flow conditions had been exceeded and that turbulence was occurring. This behaviour may also indicate that the assumption of linear flow may not be valid for all of the considered cases. This would suggest that a range of test pressure gradients should be studied so that the estimation of the hydraulic and pneumatic properties can be optimised, as is the case with the testing presented in Figs. 6.18 and 6.19.

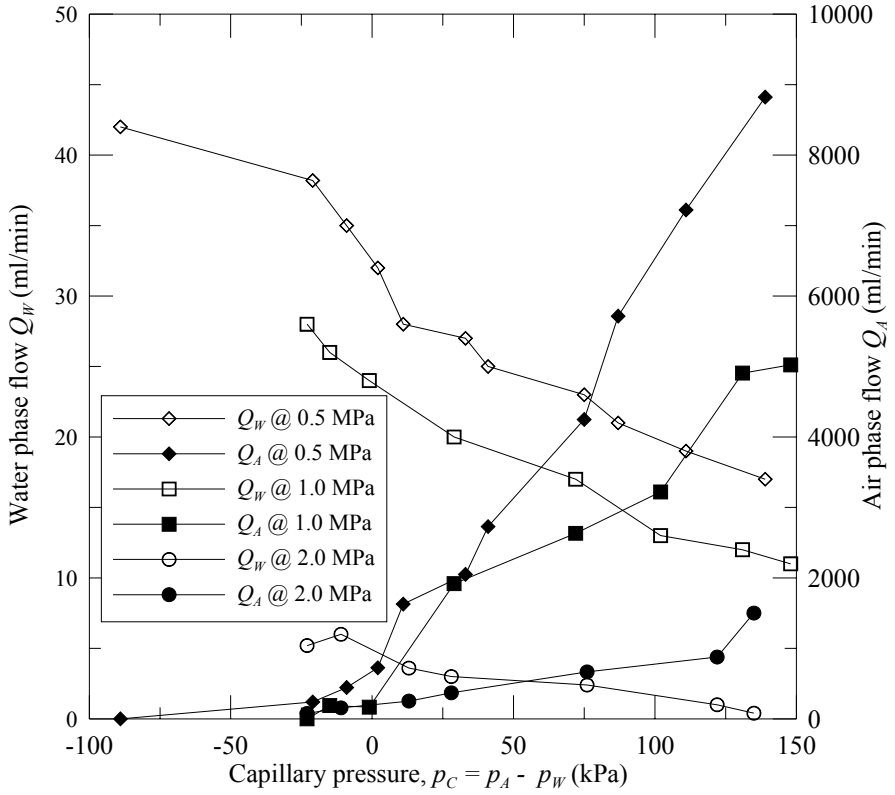

Figure 6.22: JP04 data showing phase flow rate relationship with capillary pressure and fracture normal stress.

The role of stress variation on two-phase flow behaviour is clearly illustrated by Fig. 6.22. The graph shows the reduction in phase flow associated with the progressive reduction in fracture aperture from 0.5MPa to 2MPa for sample JP04 at a near constant

water pressure drop. It is very interesting that the water flow response appears nearly proportional to stress across the range of capillary pressure, indicating that water flow is apparently uniformly affected by stress variation. The air phase response to the same stress increments differs from that observed for the water phase. The air flow relationship to stress increment appears more non-linear, but in all cases begins to rise rapidly as the capillary pressure approaches (or just exceeds) zero, and when the water flow becomes more discontinuous, as was discussed in relation to Figs. 6.14 and 6.17.

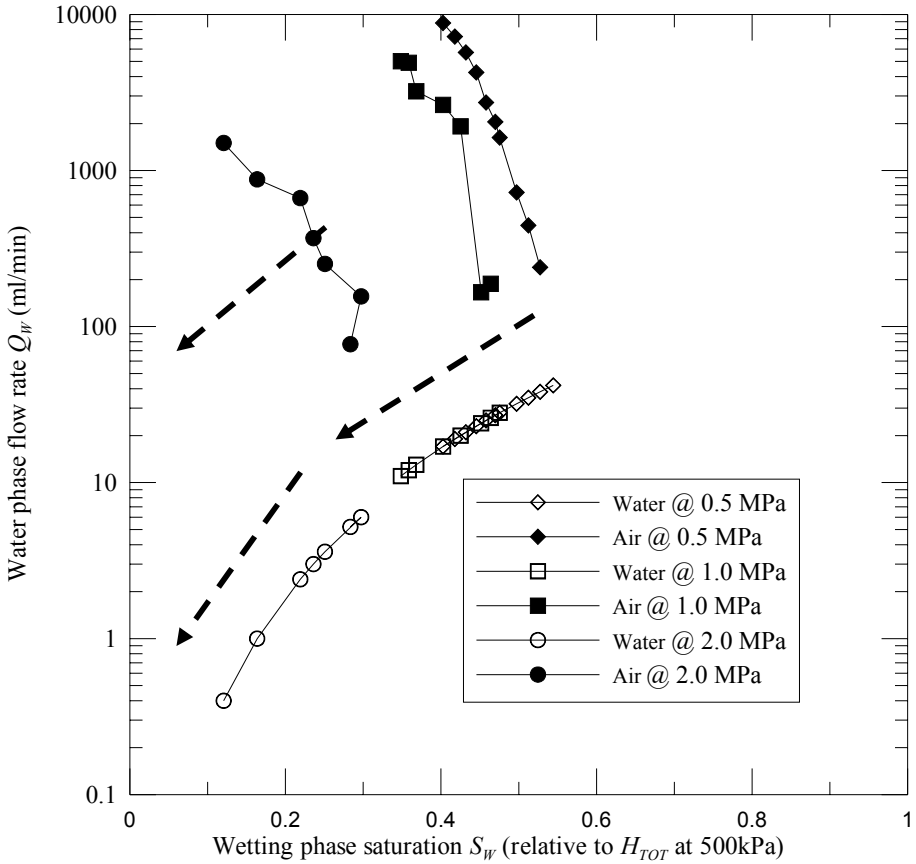

Figure 6.23: JP04 data showing change in flow rate with wetting phase saturation following increased normal stress.

The test data can also be considered in terms of the change in flow rate as a function of wetting phase saturation, as is presented in Fig. 6.23. The relative saturation at each stress increment can be related to the saturation in terms of the initial stress increment at

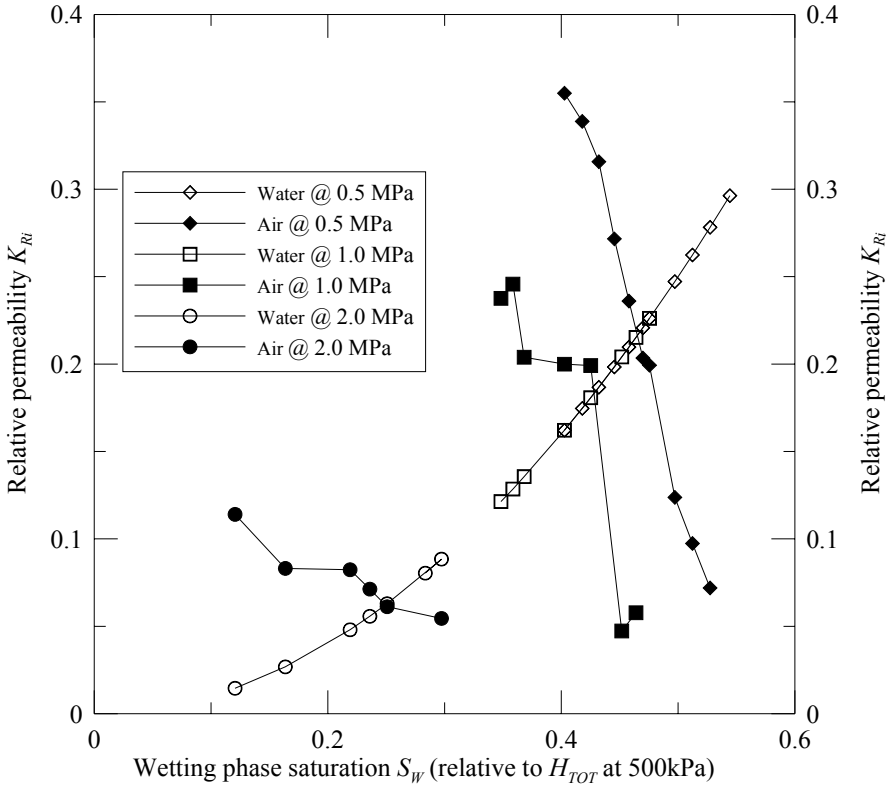

Figure 6.24: JP04 change in relative permeability with wetting phase saturation and fracture normal stress.

500kPa. The effect of increasing fracture normal stress from 0.5 to 2 MPa can be seen as the continued reduction in (relative) water phase saturation. The air flow rate reduces with reducing relative S_W as the fracture normal stress increases.

This approach can be applied to a set of results recorded over a range of confining stresses, such as depicted in Figure 6.24. For this set of tests, K_{ri} is plotted against wetting phase saturation based upon the maximum combined phase height H_{TOT} at a confining stress of 500kPa. Thus, the saturation following an increase in normal stress cannot exceed the ratio of the $H_{TOTcurrent}$:H_{TOT500}. The expected relationship can be observed in Fig. 6.24, where the water relative permeability value decreases with

reducing saturation along the theoretical trend for each subsequent normal stress rise, as predicted by Eqs. [4.7] and [4.8].

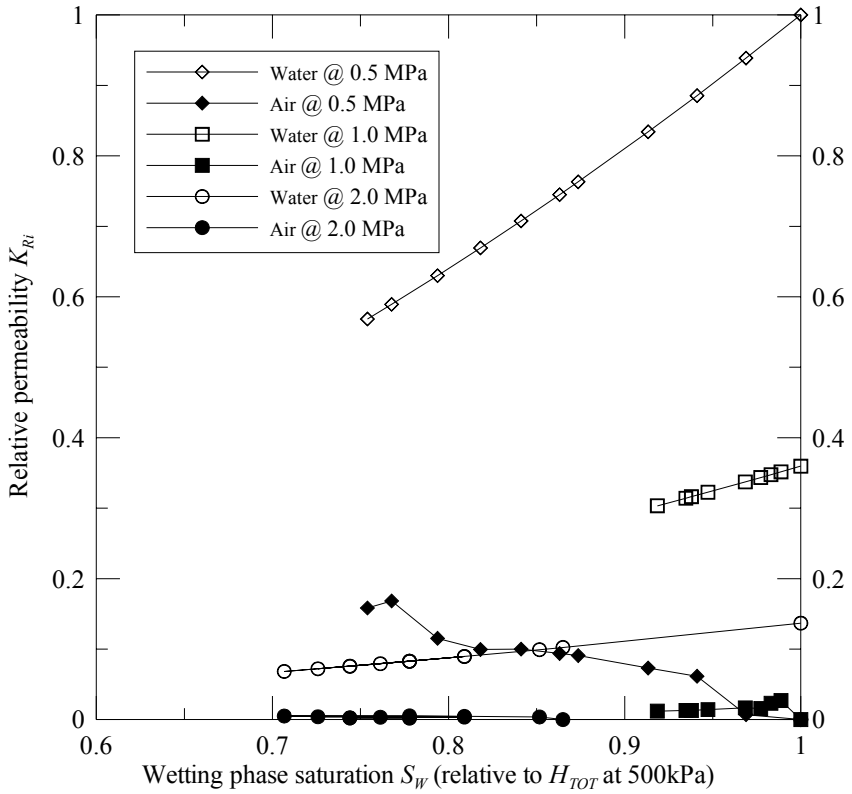

Figure 6.25. JP05 change in relative permeability with variation in S_W and fracture normal stress.

The air phase relative permeability depicts a more complex relationship that is accentuated as fracture aperture is reduced and the relative tortuosity is increased. The combined results show there is relatively little difference in fracture hydraulic behaviour between stresses of 0.5MPa and 1 MPa. The reduction in fracture aperture associated with a normal stress of 2MPa shows a considerable reduction in the fracture permeability. At low stress levels, the relatively steep inclination of the air phase relative permeability curves indicates that the air phase permeability at these mid-level saturations appears more sensitive to saturation variation and is believed to be more highly affected by fracture roughness than would be expected for a notional smooth

planar fracture. This behaviour is accentuated by the small topographic step that intersects the fracture surface at a bedding parting intersection and forms a high stress, low aperture lineament across the fracture. This feature can be seen in the photographs and wireframe model shown in Figs. C7 to C9.

The role of aperture constriction on flow behaviour can be contrasted when compared to results for further tests to sample JP05. This sample exhibits a much higher degree of large scale waviness than JP04 and shows a Kr-S_W response more closely related to the expected theoretical response as presented in Fig.6.20. Thus, greater fracture planarity promotes the theoretical flow reaction to changes in fracture aperture.

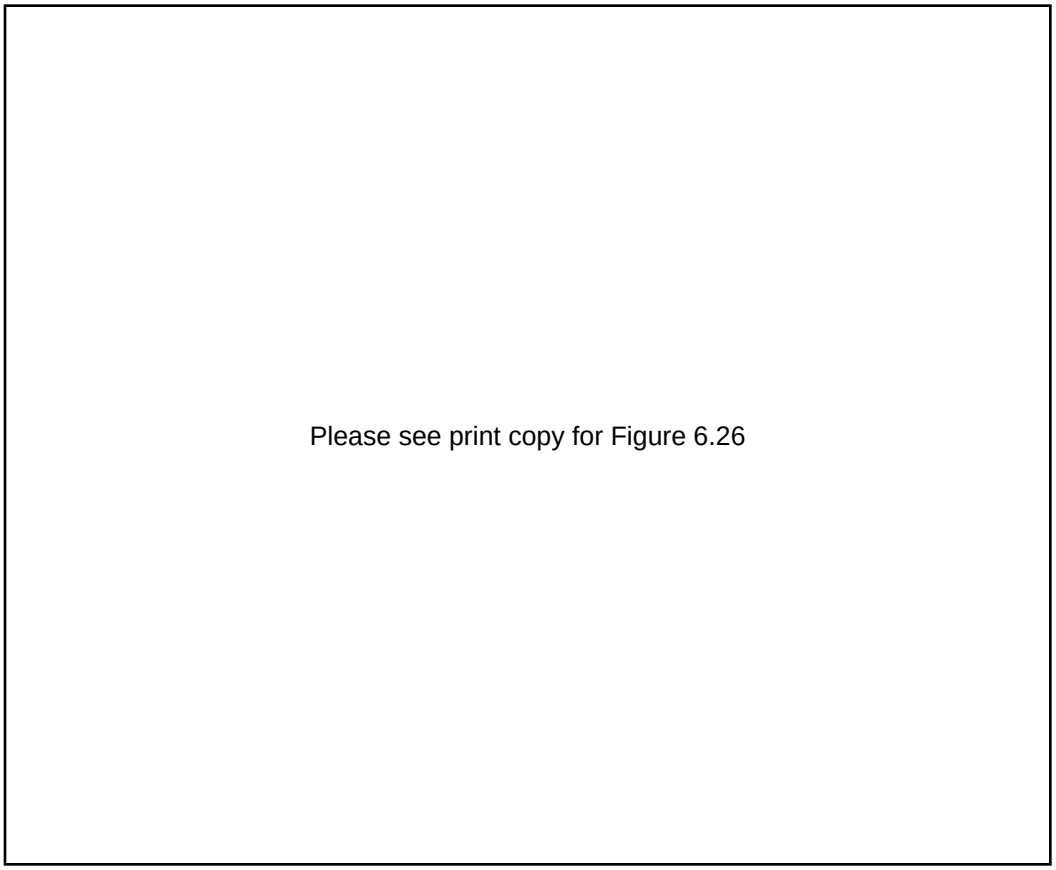

Figure 6.26. Flow map of air and water superficial velocities with Fourar et al. (1993) flow map boundaries superimposed upon the data.

Further description of two phase flow behaviour can be provided using the flow pattern descriptors that were discussed with reference to the analogue joint testing described in Chapter 5. This approach provides additional qualitative data to categorise the flow conditions (Fig. 6.26) by plotting laboratory test data in terms of the superficial air and water velocity. The flow behaviour the descriptors defined by Fourar et al. (1993) have been superimposed as lines on the plot to indicate the expected flow patterns that are occurring during the triaxial testing. From this figure (Fig. 6.26), the TPHPTA testing probably tested the full range of developed flow patterns that have been ascribed to two-phase pipe and analogue joint flow. The TPHPTA test range shown in Fig. 6.26 is similar to that investigated in Chapter 5 using the analogue apparatus. The TPHPTA data shows a higher proportion of annular flow data points, consistent with the drying out rationale advanced in Chapter 4 and the basis for the overall suitability of the simplified annular flow model. Within the limits of experimental accuracy, the simplified annular flow model correctly predicts the mechanical aperture: combined phase height relationship for the range of laboratory tests, showing the voracity and value of the proposed approach for a range of two-phase flow patterns.

6.4.3.3 Mechanical response to change in fracture normal stress

The mechanical response of the sample fractures to changes in confining stress and phase pressure gradient can be studied from the average clip gauge deformation recorded during the laboratory testing. The calculated aperture deformation derived from the clip gauges can be compared with the calculated phase heights, as is illustrated by Fig. 6.27. The laboratory data verify the arithmetic relationship between mechanical aperture and the phase height sum, $H_{TOT,}$ across a of fracture normal stresses, hence:

$$e_m = H_{TOT} = H_A + H_W \qquad [6.8]$$

Sample fracture normal stiffness can also be calculated from the clip gauge data obtained from the triaxial tests. The K_n values given in Table 6.4 represent an average value obtained over the range of compression indicated in the adjacent column. The data show that relatively planar fractures of JP04 and JP09 display similar linear stiffness responses over the test range of about 5 x 10^4 MPa/m. It is interesting that although the flow response of JP04 was affected by the presence of the previously noted step feature, the mechanical response is far less sensitive to relatively small scale physical variations. The mechanical response to such physical variations would be expected to diminish with increased normal stress because of the increasing impact of contact area stiffening the fracture deformation response, as is depicted by sample JP05 in Fig. 6.27.

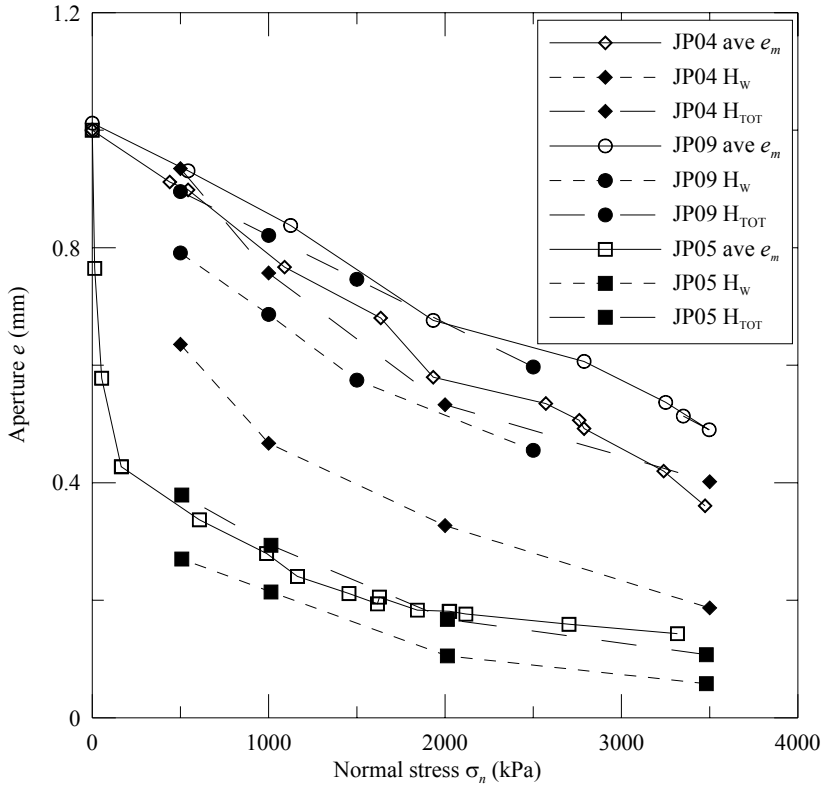

Figure 6.27: Summary plot showing average measured fracture deformation and calculated phase height.

Sample JP05 shows a noticeably non-linear response to the normal stress variation. To aid interpretation, this has been approximated in Table 6.4 to 3 linear zones identified by the relevant normal stresses of 66 kPa and 1429 kPa. The fracture topology demonstrating prominent localised large scale waviness is shown in Figs. C4 and C5. The aperture contours indicate the fracture waviness does not apparently influence the fracture aperture. The response of JP05 is believed to be related to the greater large scale waviness that is present on this sample. This more complex topology results in a much lower normal stiffness until the normal stress exceeds 1429 kPa, whereafter the fracture is some 50 times less deformable. The anisotropic response of JP05 was clearly shown in Fig. 6.27. This result shows that mechanical deformation of the rock mass is more sensitive to variations in large scale roughness, unlike the hydraulic response, and is in broad agreement with existing models of rock mass analysis (McMahon, 1985).

Table 6.4: Summary of average normal stiffness response of fractured TPHPTA samples.

Sample	**Normal stiffness K_n (MPa/m)**	**Stress range (MPa)**
JP04	5.0×10^4	0 to 3.5
JP09	5.12×10^4	0 to 3.5
JP05	4.51×10^2 2.21×10^4 1.10×10^5	0 to 0.67 0.67 to 1.43 > 1.43

One of the advantages of using the simplified two-phase flow model is that the phase height concept provides a easy to apply method to assess rock mass deformation suitable across a range of fracture normal stresses. This can be pursued by comparing H_W and H_{TOT} with the single-phase hydraulic aperture e_h and the mechanical aperture e_m estimated from the clip gauge data and related to the estimated normal stiffness. The

laboratory data indicate the single-phase hydraulic aperture is effectively the same as H_W and the addition of a regulated and measured air phase enables the calculation of the mechanical as well as the hydraulic apertures.

6.5 Summary

This chapter recounts the development and execution of a period of detailed laboratory testing using the TPHPTA. The purpose of the testing was to study the hydromechanical behaviour of sub-axially roughly fractured sandstone samples and to test the proposed annular two-phase flow model against changing in fluid pressure and confining stress conditions. The original TPHPTA was developed as described by Indraratna & Ranjith (2001), but has been improved to enable larger volume water and air flow measurement, enhanced digital flow and deformation data acquisition. These improvements allowed the apparatus to test fractures with apertures (i.e. >100μm) at least one order of magnitude larger than had been previously undertaken.

A length of arenaceous sandstone core was made available for the study which was intersected by a subaxial natural fracture. The samples were prepared for testing using the TPHPTA. Intact and fractured samples were tested to establish a representative set of physical and mechanical properties.

Two-phase flow behaviour was studied with respect to changes in phase pressure drop, relative permeability and mechanical deformation. The observed behaviour has enabled the validation of the proposed application of the conservation of mass to two-phase flow in the form of simplified annular flow. The fracture normal deformation measurement was recorded using clip gauges that were calibrated to changes in triaxial confining stress and membrane distortion over the test stress range.

The fracture deformation relationship to stress has been linked to fracture normal stiffness within defined linear elastic zones. The calculation of the air and water

phase heights has been shown to be related to the mechanical fracture aperture. Combination of the phase height relationship to the mechanical aperture allows prediction of the change in aperture when fracture roughness is known if the phase flow rates and pressure gradients have been measured. Application of the proposed annular two-phase flow model shows that for rough fractures the mechanical aperture can be related to the average log normal aperture and the total phase height, i.e. $e_m = \bar{e}_{\log} = H_{TOT} = H_W + H_A$.

Single-phase hydraulic testing of fractured and intact rock specimens has allowed the assessment of the primary permeability of the rock substance and confirmed that the matrix flow contribution in these cases was negligible compared to the typical fracture apertures used for testing (> 2 orders less than hydraulic aperture). Fractured samples tested under single-phase conditions indicated the significant level of fracture roughness of some samples, and the development of linear as well as non-linear flow behaviour. Testing over a range of fracture normal stress demonstrated the onset of non-reducible fracture flow associated with the attainment of the residual fracture aperture.

Under two-phase conditions, flow is observed to be proportional to phase pressure gradient. Under increasing air injection pressure, rough fractures act to delay the breakthrough of the air phase until the phase pressure gradients are approximately equal, when true continuous flow of both phases occurs. The air flow increases rapidly as the air phase pressure gradient exceeds that of water. This suggests that continuous 'free fracture flow' of both phases can be to a limited capillary pressure range when $p_A \approx p_W \pm 10\%$.

The proposed two-phase flow model shows flexibility, in that it can be applied across a range of linear and non-linear flow conditions to relate the flow behaviour to

changes in apparent phase height. The model has been shown to also be related to established two-phase flow parameters such as relative permeability and wetting phase saturation. Tracking the calculated total phase height indicates the stage at which non-linear flow develops for a specific injection pressure.

Comparison of the two-phase flow data with established flow maps such as those discussed in Chapter 5, indicate that the testing is expected to have occurred over nearly the full range of identified two-phase flow patterns, with a considerable proportion of the data recorded within the range attributed to annular flow by Fourar et al. (1993) and described theoretically by the analytical development presented in Chapter 4. The range of flow behaviour was also studied using the analogue joint testing described previously in Chapter 5, indicating the applicability of the model for smooth as well as rough fractures.

Chapter 7
Hydromechanical Modelling
in Discontinuous Media

7.1. Introduction

Numerical modelling of two-phase hydromechanical problems provides a crucial tool to solve the complex interactions of stress, strain, pore pressure and boundary conditions. Following the literature review presented in Chapter 2, it is accepted that simplifying assumptions are incorporated into models when resolving complicated engineering problems. Clearly, numerical solutions must be applied with some caution to ensure that the problem analysed represents the geotechnical reality. Subsequent discussion in this chapter illustrates this problem with reference to the issue of the accommodation of roughness in particular analyses. In addition, several approaches are developed to provide acceptable solutions for particular scales of problem.

In Chapters 2 and 3, there were detailed discussions were provided about the role of roughness in hydromechanics. Without repeating what has already been presented, the reader can be reminded of the hydraulic significance from reference to Fig. 7.1. The two basic equations state:

$$k = \frac{e_h^2}{12} \qquad [7.1]$$

and

$$e_h = \frac{e_m^2}{JRC^{2.5}} \qquad [7.2]$$

which can be merged together by substituting for e to create a single equation:

$$k = \left(\frac{e_m^4}{12 \cdot JRC^5} \right) \qquad [7.3]$$

The Fig. 7.1 plot relates the intrinsic permeability (k) of a fracture to the physical or mechanical aperture (e_m) for a range of smooth and rough walled fracture topographies using a derivation from Eqs. 7.1 and 7.2. Remembering that Eq. 7.2 is valid only for $e_m \geq e_h$ and apertures are measured in microns, this relationship is created by combining Poiseuille's Law and the Barton et al. (1985) empirical function.

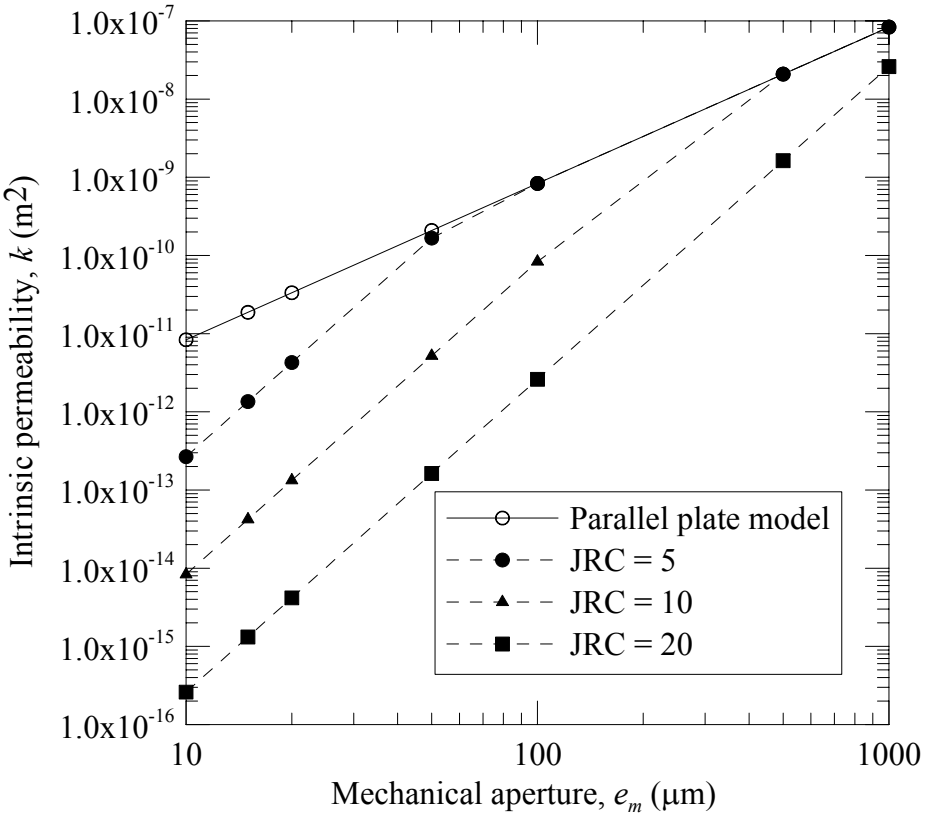

Figure 7.1: Plot of relationship between intrinsic permeability ($k = e^2/12$) and mechanical aperture, after Barton et al. (1985).

The plot emphasises the increasing impact of fracture roughness as fracture apertures decrease because of the onset of non-parallel flow conditions with change in fracture

surface contact area. This non-linear behaviour must be captured in any hydromechanical numerical analysis. Different approaches have been published for water flow through fractured rock masses (Louis 1969, Sharp 1970, Long 1983, Elsworth & Mase 1993). In this chapter, the aim is to consider two different ways of analysing flow through a single fracture developed from a single-phase and adapted to the two-phase flow environment. A simple finite difference scheme is devised to consider closely the effect of aperture variability on flow behaviour. UDEC, a commercial discrete element software package (ITASCA, 2000), is also applied to illustrate both the role of fracture roughness in flow calculation, but also the applicability of an alternative two-phase flow model to overcome the limitations of the programme code.

7.2. Theoretical background

The effect of fractures on hydromechanical behaviour depends upon the size of the rock mass element, the material properties of the rock substance or 'blocks', and rock fracture persistence and interconnectedness. The scale issue is crucial to the correct numerical analysis of rock mass interaction (Brady & Brown, 1994; Gianni et al., 1995; Carlsson et al., 1990; Geier & Hassler, 1992; Castelli et al., 2001) as shown in Fig. 7.2.

The diagram in Fig. 7.2 illustrates the effect of fracture orientation and spacing on hydromechanical analysis. The figure illustrates the major factors considered in developing effective analytical models. More detailed theoretical aspects are discussed in subsequent sections of this chapter. The general approach to modelling varies depending upon the scale of the problem. If the rock mass structure is relatively massive, then the rock substance properties alone are needed to model the rock mass response. If the rock mass comprises two blocks and one fracture, the hydromechanical properties of the fracture will have to be incorporated in the analysis. When 'free' flow

of single- or two-phase fluid through a fracture is contemplated and capillary effects are either neglected or accommodated within the calculation scheme (Pruess & Tsang, 1990; Pyrak-Nolte et al., 1992), a numerical analysis of the fracture response can be undertaken using mathematical techniques such as finite difference. This approach provides a consideration of flow and mechanical behaviour of an individual fracture. The laboratory-based research performed for this project applies easily to this scale of model.

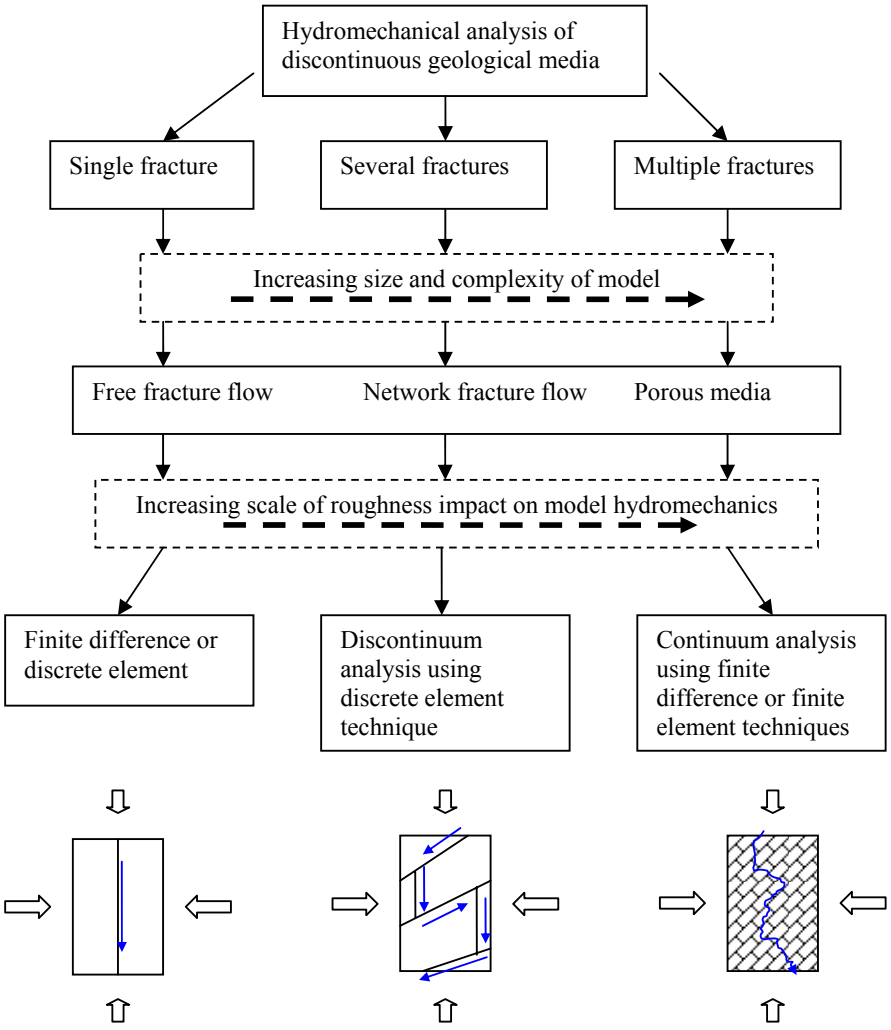

Figure 7.2: The significance of rock mass defects and scale in hydromechanical analysis.

A rock mass containing several fractures is likely to be highly influenced by the hydromechanical characteristics of the fractures with the influence gaining if rock mass damage increases. In this environment, a more complicated calculation routine is advantageous to allow the analysis of the interaction of families of discontinuities at different locations within the rock mass. Computation schemes such as the Universal Discrete Element Code, UDEC (ITASCA, 2000) provide a means of analysing models of considerable complexity. The simplified two-phase models contemplated during this project have sought to develop suitability for incorporation within such a computation code. This work is a focus of the discussion in subsequent sections of this chapter. Where the rock mass is intersected by a multitude of fractures, the relatively small size of the rock blocks relative to the model means that at this scale the model tends to behave as a granular porous medium. For this rock mass environment, analysis is applicable with a continuum approach, akin to that of soil mechanics with a different form of finite element or difference computer codes. This approach lies outside of the current study area, and is therefore deliberately discussed at a more general level in the following sections of this chapter.

The following discussion illustrates the suitability of simple numerical techniques to the hydromechanical response of fractures using models developed during this research project and aspects of more established engineering theory. Also, particular shortcomings within the UDEC code within the area of fracture hydraulics will be discussed and potential solutions will be proposed. In addition, a modelling procedure will be developed to enable the analysis of two-phase flow using the existing UDEC solution and the homogenous fluid (or equivalent) two-phase flow model.

7.3. Numerical analysis

Kostakis & Harrison (2001), Pruess & Tsang (1990) and Brown (1987) have all used numerical modelling to consider the single- and two-phase flow through variable aperture fractures. Following these studies and detailed reviews (Zimmerman & Bodvarsson, 1996) it can be concluded that for a rough discretised fracture, the parallel plate assumption is still valid, provided the change in aperture between adjacent elements is small. This fact can be tested by incorporating a simple finite difference approach to the consideration of flow through a single fracture comprising many small fracture elements.

Alternatively, more complex flow problems can be approached following the acquisition of detailed site investigation data relating to the distribution, orientation, inclination and persistence of geological features, the mechanical properties used to model perpendicular and normal deformation. In order to approximate the natural occurrence and behaviour of actual rock mass discontinuities, these geometrical and mechanical properties can be specified with regard to their mean statistical distribution and incorporated into the model in order to approximate the likely performance of the actual engineering structure.

7.3.1. Free fracture flow

Fracture flow has been studied using a relaxation technique whereby the head gradient is determined iteratively. The technique allows the calculation of the potential elemental flow, which can be used to study the development of non-parallel flow within a variable aperture fracture. The predicted outcomes are compared with the results of single-phase laboratory testing.

7.3.1.1 Fracture properties

For the purpose of this work, 2-D free fracture flow is considered to occur in the *x*-*y* plane when the driving and gravitational pressure gradient exceeds the counteracting

capillary pressure gradient, allowing mobilisation of pore fluid from one fracture element $f_{(x,y)}$ to another, e.g. $f_{(x+1,y)}$ as defined in Fig. 7.3. The finely discretised mesh means that at this scale, the 2 fracture surfaces can be considered locally 'smooth' and parallel.

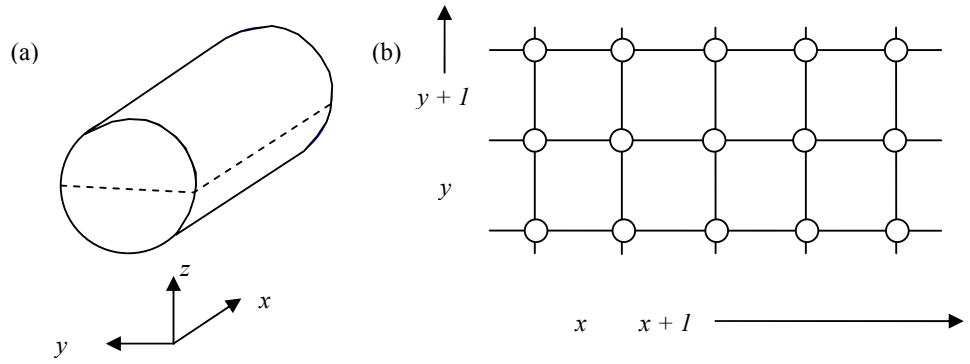

Figure 7.3: Definition of fracture for finite difference analysis. (a) Fracture orientation relative to core sample. (b) Definition of node $f_{(x,y)}$ relative to adjacent fracture elements.

Each fracture element has an associated mechanical or physical aperture $e_{m(x,y)}$. For linear laminar flow conditions at steady state, the cubic law can be applied to calculate fluid flow Q_i dependent upon the kinematic viscosity μ_i and the resultant pressure gradient dp_i/dx and dp_i/dy where element dimensions x and y are equal to the distance h.

$$Q_{i(k)} = \frac{e^3_{m(x,y)}}{12\mu_i}\left(\frac{dp_i}{dk}\right) \qquad [7.4]$$

where, k refers to the ordinate x or y and i denotes the fluid phase.

7.3.1.2 Development of Finite Difference Scheme

The finite difference method is a well established engineering technique (Tomlinson, 1989) that approximates a continuous function using discrete explicit values. The fundamental 1-D form of the finite difference equations can be written in terms of Taylor's Theorem for a function $f(z)$ with i points located a distance h apart:

$$f(z)_{x+1} = f(z)_x + h\left(\frac{df(z)}{dx}\right)_x + \frac{h^2}{2!}\left(\frac{d^2 f(z)}{dx^2}\right)_x + \ldots + \frac{h^n}{n!}\left(\frac{d^n f(z)}{dx^n}\right)_x \quad [7.5]$$

Thus, to calculate the function value at point *x*, Eq. 7.5 can be written for the location *(x – h)* and subtracted from Eq. 7.5. By considering a first order approximation a new equation is formed that can be re-arranged to give:

$$\left(\frac{df(z)}{dx}\right)_x = \frac{f(z)_{x+1} - f(z)_{x-1}}{2h} \quad [7.6]$$

Therefore, finally allowing the function to be written in the simplified form:

$$f(z) = f(z)_{x+1} - h\left(\frac{df(z)}{dx}\right)_x \quad [7.7]$$

The finite difference technique can be used to solve 2-D steady state flow problems with use of the Laplace equation (Bear & Verruijt, 1987). The most accurate form of the first derivative for 2-D flow in the *x* and *y* directions can be written in terms of the central finite difference:

$$\left(\frac{\partial f}{\partial x}\right)_{x,y} = \frac{f(z)_{x+1,y} - f(z)_{x,y}}{h} \quad [7.8]$$

$$\left(\frac{\partial f}{\partial y}\right)_{x,y} = \frac{f(z)_{x,y+1} - f(z)_{x,y}}{h} \quad [7.9]$$

Accordingly, the second derivative can be formulated:

$$\left(\frac{\partial^2 f}{\partial x^2}\right)_{x,y} = \frac{f(z)_{x+1,y} - 2f(z)_{x,y} + f(z)_{x-1,y}}{h^2} \quad [7.10]$$

$$\left(\frac{\partial^2 f}{\partial y^2}\right)_{x,y} = \frac{f(z)_{x,y+1} - 2f(z)_{x,y} + f(z)_{x,y-1}}{h^2} \quad [7.11]$$

Thus, by summing Eqs. 7.9 and 7.10 and using the Laplace identity:

$$0 = \frac{1}{h^2}\left(f(z)_{x+1,y} + f(z)_{x-1,y} - 4f(z)_{x,y} + f(z)_{x,y+1} + f(z)_{x,y-1}\right) \quad [7.12]$$

The above equation can be re-arranged to give the function approximation for the central node:

$$f(z)_{x,y} = \frac{1}{4}\left(f(z)_{x+1,y} + f(z)_{x-1,y} + f(z)_{x,y+1} + f(z)_{x,y-1}\right) \quad [7.13]$$

This formula can be applied to calculate the pressure drop across a square element forming within the grid or mesh effectively draped over the rock fracture that was defined in Fig. 7.3.

7.3.1.3 Flow analysis

The laser scanning data acquired during the study described in Chapter 3 can be used to provide the x and y coordinates for the fracture, as well as the elemental mechanical aperture values $e_{m(i,j)}$. Alternatively, the average and standard deviation can be used to statistically generate a data set according to a desired distribution. The phase pressure boundary conditions can be applied to the mesh, with a no flow boundary along the fracture edges and the laboratory measured pressure drop acting across the top and bottom of the fracture.

Contiguous fracture surface contact points or small apertures define zones within the aperture geometry of zero or negligible thickness and result in flow deviating around the inclusions and departing from the idealised parallel flow conditions. The proportion of the fracture element contact area increases with applied normal stress. On a macroscopic level, this is accommodated by considering the fracture normal stiffness (K_n). At a macroscopic level this can be explained using different theories including the fracture normal stiffness. For a smooth fracture, total closure of the fracture would eventually occur at a specific level of normal stress. For rough fractures it is common for fractures to allow small flow volumes even at very high normal stress levels, corresponding to the residual aperture back calculated from the test results (Indraratna et al., 1999).

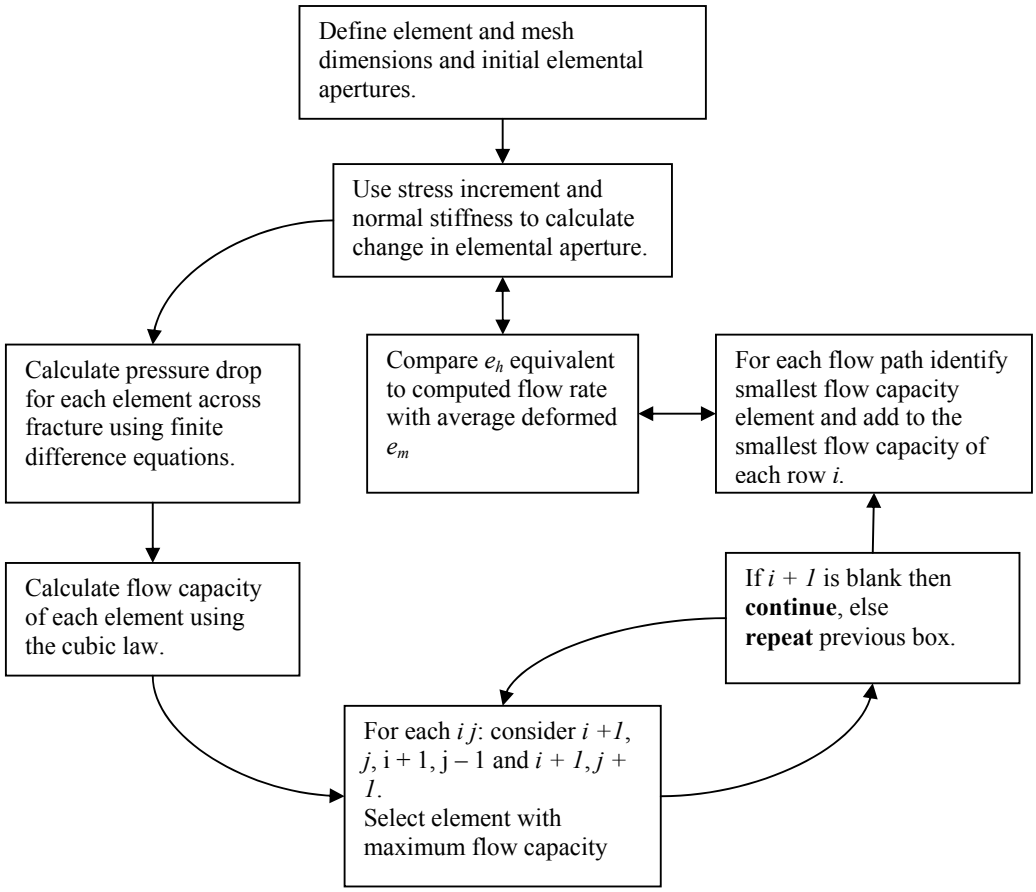

Figure 7.4: Flow chart defining stages in steady state finite difference fracture flow analysis.

The assumed stiffness behaviour should be clearly stated and calibrated with laboratory or field testing to validate the analytical model. In this model, each element aperture is considered to deform elastically according to the normal stiffness relationship. The deformed element aperture is calculated as the average of the adjacent 4 nodes. Thus:

$$\bar{e}_{mt} = \bar{e}_{m0} - \frac{(\sigma_{nt} - \sigma_{n0})}{K_n} \qquad [7.14]$$

where, $\bar{e}_{m0} = \frac{1}{4} \sum_{\substack{i=1,2 \\ j=1,2}} e_{mo}$ represents the average initial mechanical aperture for the fracture element at a time $t = 0$. The change in aperture following a stress increment ($\sigma_{nt} - \sigma_{n0}$) is calculated using the fracture normal stiffness K_n. The approach to flow analysis is summarised in the Fig. 7.4.

7.3.1.4 Discussion

Flow analysis using a single fluid was performed to develop the proposed methodology in Fig. 7.4 and to compare the calculated response with results obtained during laboratory testing. The modelling geometry was tested using the scanning data for sample JP09 to form a discretised mesh comprising 1mm square elements. The pressure drop across the fracture was defined using Eq. 7.13 with no-flow boundaries assumed to apply along the sample sides. A pressure drop was applied across the fracture to drive the flow and illustrate the presence of higher capacity flow paths. Flow through a rough fracture is controlled by the distribution of small apertures (Pyrak-Nolte et al., 1994). This leads to the development of non-parallel flow and the divergence between the mechanical aperture and the hydraulic aperture exemplified in Fig. 7.1.

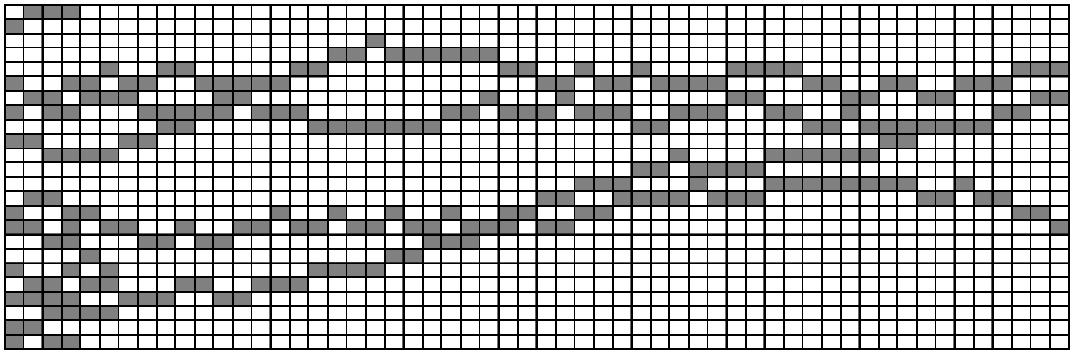

Figure 7.5: Plan of non-parallel flow development in a rough walled fracture. Coloured elements indicate high capacity flow channels with flow occurring from left to right.

The flow path tortuosity can be assessed by considering the flow capacity and distribution of each element. Flow paths develop to include the largest aperture elements and in achieving this, result in preferential non-linear flow patterns. This is illustrated in Fig. 7.5, which shows the outline of the fracture mesh and the fracture elements. The flow path can be estimated by assuming that flow from a node will preferentially follow the track of the largest apertures. The coloured squares can be imagined as ‘particles’ of the fluid, following the largest potential flow paths. It is notable that because of the presence of constricting small apertures that there is a

tendency for the flow paths to form a braided structure with confluent pathways reducing the overall number of streams from the inlet to the outlet side of the fracture.

The flow paths that develop as shown in Fig. 7.5, provide the largest contribution to fracture flow, with the minor flow volumes contributed by adjacent (smaller) elements that do not form part of the flow path, hence:

$$Q_{TOT} = \sum_{fp=1}^{fptot} Q_{fp} + \sum_{y=1}^{ytot-fptot} Q_y \qquad [7.15]$$

where, the total fracture flow Q_{TOT} is calculated using Eq. 7.4 with the minimum e_{mt} for either, flow path fp_i (for $i = 1$ to fp_{tot}), or row y (for $y = 1$ to $y_{tot} - fp_{tot}$).

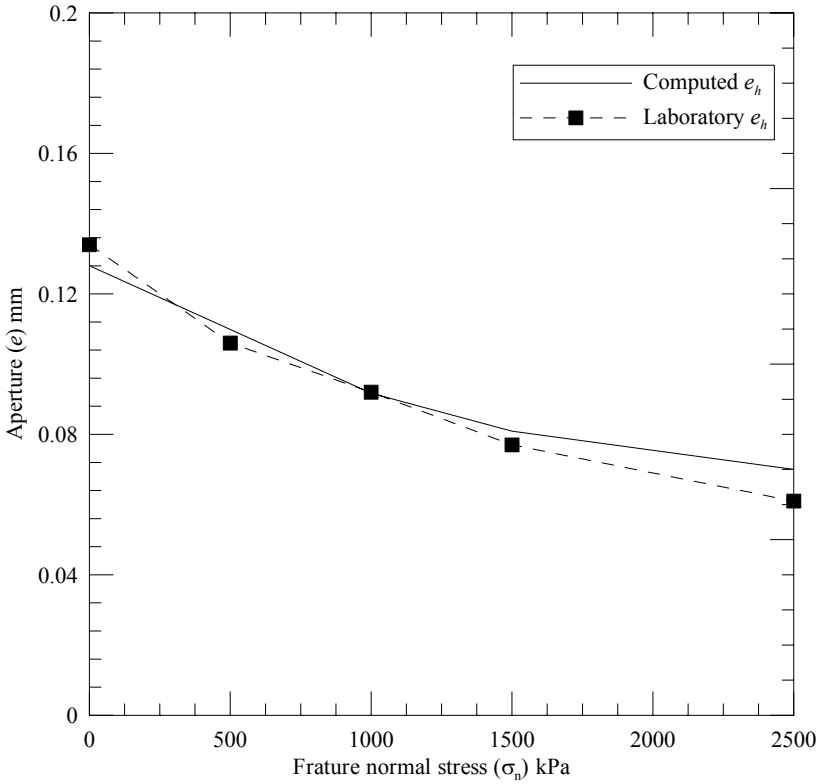

Figure 7.6: Comparison of laboratory hydraulic aperture e_h values with those computed using finite difference equations with linear elastic fracture deformation.

The sum of the minimum flow capacity of each flow path and the minimum flow capacity of the remaining $y\text{-}fp_{tot}$ rows of the fracture provides an estimate of the total flow capacity of the fracture for the applied boundary conditions. The estimate tends to

overestimate the row flow capacity, although numerical studies have shown that the magnitude of the likely error is very small (< 1%) compared to individual flow path capacity. The overestimation is small since the flow capacity of the row of elements cannot exceed the flow capacity of the smallest aperture, likely to be << 1 μm. Once the calculation has been performed it is useful to compare the result with observed flow behaviour. The relationship between mechanical aperture and the hydraulic aperture can be considered by using the cubic law to calculate the equivalent hydraulic aperture for the computed flow. The computed value can be compared with laboratory test results as is shown in Fig. 7.6. The plot shows how the consideration of 2-D flow variation due to roughness can predict the expected hydraulic performance of the fracture, even though in a conventional 1-D analysis the fracture roughness may result in a discrepancy between the mechanical and hydraulic fracture apertures.

7.3.2. Fracture Network Flow

The numerical solution to hydromechanical problems involving several fractures, or sets of fractures, creates significant additional analytical complexity, further to the issues discussed in the foregoing section. The proprietary software application UDEC (ITASCA, 2000) represents one of the leading geomechanical computer codes specifically designed to analyse the hydromechanical behaviour of discontinuous media. Far field numerical analysis can often be effectively conducted using continuum-based modelling packages, such as FLAC (ITASCA, 2000) or SIMED (Choi & Wold, 2001). The suitability of this approach requires that the rock mass is free of any discontinuities that may modify the otherwise isotropic rock mass response to changes in stress or strain. Under these conditions, numerical analyses can be reasonably assumed to incorporate materials that are approximated as continuous, homogenous, isotropic and linear elastic. The presence of geological discontinuities within a rock mass can mean

that hydromechanical analyses often exhibit very different behaviour, better described as discontinuous, in-homogenous, anisotropic and non-elastic. However, the presence of significant geological structure such as faults, joints or bedding planes requires a discrete element program, such as UDEC is required. The use of continuum-based applications in these situations is very difficult unless considerable site information and a high level of expert re-programming is undertaken (Nemcik et al., 2000) or empirical relationships are used such as the Hoek & Brown Failure Criterion (Hoek & Brown, 1982).

7.3.2.1 Theoretical basis

UDEC considers the hydromechanical interaction of user-defined rigid or deformable, impermeable rock-blocks, as well as the intervening fractures. The fluid can be considered as either incompressible or compressible and flow can be either steady state or transient flow. For rigid blocks, the block interaction can be specified by a variety of constitutive models and is controlled by the specified force-deformation law and Newton's Second Law, which for general elastic conditions can be summarised as:

$$F_i^t = F_i^0 - K_i \delta_i^t \qquad [7.16]$$

$$F_R^t = Ma \qquad [7.17]$$

where, F represents the force at time 0 and t in the i direction, either normal n, shearing s parallel to the block boundary or the resultant R. The block boundary movement during the time interval is related to the force by the stiffness K_i and the deformation δ_t. The resultant block force is related to the block mass M and the acceleration a.

The rock-block permeability can be a limitation where high primary permeability rocks are of interest. However, where fracture apertures or boundary conditions are appropriate, models can be analysed where flow dominantly acts through discontinuities. In UDEC, for edge to edge contacts, the analytical approach to

saturated fracture flow is to apply Poiseuille's and Darcy's Law for linear laminar flow conditions with fractures as approximated by smooth parallel plates using:

$$Q = \frac{1}{12\mu} e_h^3 \frac{dp}{dx} \quad [7.18]$$

where Q is flow rate, e_h is hydraulic aperture, μ is the kinematic viscosity of the fluid and dp/dx is the drop in fluid pressure across the sample length. UDEC represents the $(12\mu)^{-1}$ term as the joint permeability k_j which directly allows different fluid properties to be modelled. The saturation:permeability relationship in UDEC is defined by an empirical multiplying factor f_S that is applied to the calculated flow rate:

$$f_S = S_W^2 \left(3 - 2S_W\right) \quad [7.19]$$

where, S_W is the saturation of the fracture domain, and the function has the effect of restricting flow from domains that are not fully saturated. A further limitation to the applicability of UDEC to complex flow problems occurs where the code automatically switches the domain fluid pressure to zero where $S_W < 1$. This equation allows the calculation of an empirical relative permeability for each fracture. The applicability of the phase height approach to the theoretical analysis of fracture flow was previously illustrated in Chapter 4. Furthermore, the subsequent discussion about the application of the homogenous fluid approach illustrates the potential for extension of the code to analyse complex two-phase (air + water) flow problems.

The principal interest at this stage is the study of fluid flow and the interaction of fracture roughness applied in the general computational module (rather than specialised modules like Barton-Bandis). The contact between two adjacent blocks can be either corner to side or side to side. The impact of block contact on flow affects fluid capacity and is related to pressure differential across the fracture domain. The code is theoretically rigorous and accounts for the mechanical impact of pore pressure on the

rock blocks, the aperture related flow through fractures, the deformation of fracture aperture due to block stress and changes in fluid pressure due to flow between domains. The fluid pressure at time t p^t is defined as:

$$p^t = p^0 + K_W Q_W \frac{\Delta t}{V} - K_W \frac{\Delta V}{V_{ave}} \quad [7.20]$$

i.e., by applying the water bulk modulus K_W, the new pressure is calculated from:

- the sum of the pressure at time *0*
- the pressure change due the water flow Q_W to the fracture domain of volume V during the time interval Δt
- the change in pressure due to the change in volume ΔV relative to the average volume V_{ave} of stored water in the fracture domain.

The computational routine used by UDEC applies a conventional approach to steady state flow problems by calculating the change in fluid pressure for each domain at each time step, balancing the changes in net domain flow throughout the fracture network. The computer code uses the domain (or contact) aperture (i.e. mechanical aperture) in the flow calculations. This approach is suitable where fractures are smooth, but Fig. 7.1 illustrates that fracture roughness can lead to considerable under-prediction of fracture flow. Here, the significance of fracture roughness in the reduction of flow is clearly shown, whereby the intrinsic permeability could be reduced by up to about 5 orders of magnitude when comparing the theoretical parallel plate aperture with that calculated from the Barton et al. (1985) relationship in Eq. 7.2. Thus, it is important to accommodate the aperture reduction within the UDEC model to accurately predict rock mass hydraulic behaviour. Measuring and describing roughness has been attempted using a variety of techniques, and in this text, the writer has used Fourier series as described in detail as part of Chapter 3. The subsequent UDEC study shows that for the

case of predominantly normal fracture displacement without gouge generation, the k_j term can be re-written as:

$$k_j = \left(\frac{1}{12\mu} \frac{e_m^4}{JRC^5} \right) \qquad [7.21]$$

7.3.2.2 Flow analysis through a single rough fracture

The effect of fracture roughness on UDEC calculations was studied with a very simple two-block model (of sample length *2L*) incorporating a single horizontal fracture of aperture *e*. The basic model shown in Fig. 7.7, with the lower block fixed on rollers so that it could not move horizontally or vertically, and a pressure drop across the sample corresponding to $(p_{in}\text{-}p_{out})/2L$.

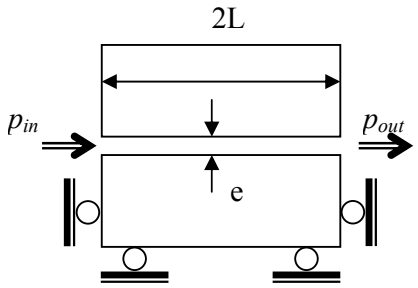

Figure 7.7: Diagram of two-block computer model used to study the effect of fracture roughness on UDEC flow calculation.

The results of the analysis presented in Fig. 7.8 shows total accord for a 300μm wide fracture, between the theoretical solution using the cubic law for smooth parallel plates and the UDEC solution. In the next stage, the standard profile corresponding to *JRC* 20 (ISRM, 1978) was digitised at 2mm intervals and incorporated into to computer data file. The same aperture e_m was maintained for the rough fracture model. The results of the computer analyses for a rough fracture with the smooth plate aperture are also plotted on Fig. 7.8 (see "UDEC uncorrected JRC = 20" series) to illustrate the potential discrepancy if fracture roughness is not incorporated. The theoretical solution when

applied to a rough profile does not account for the increased pressure drop that occurs compared to the analysis of a smooth profile. From inspection, the steady state flow rates from both models are very similar, although the rough fracture has resulted in a reduction of flow. Although this general behaviour conforms to our expectation, the magnitude of the reduction is much too small compared to what would be expected from the relationship in Eq. 7.18. This shows that for rough fractures, there is a serious risk for over-calculation of flow rate using UDEC. However, if the k_j term in Eqn. 7.21 is applied instead, then the theoretical and the computed solution are once again in agreement. This now allows the computation of fracture flow rate to correctly predict the effect of fracture roughness.

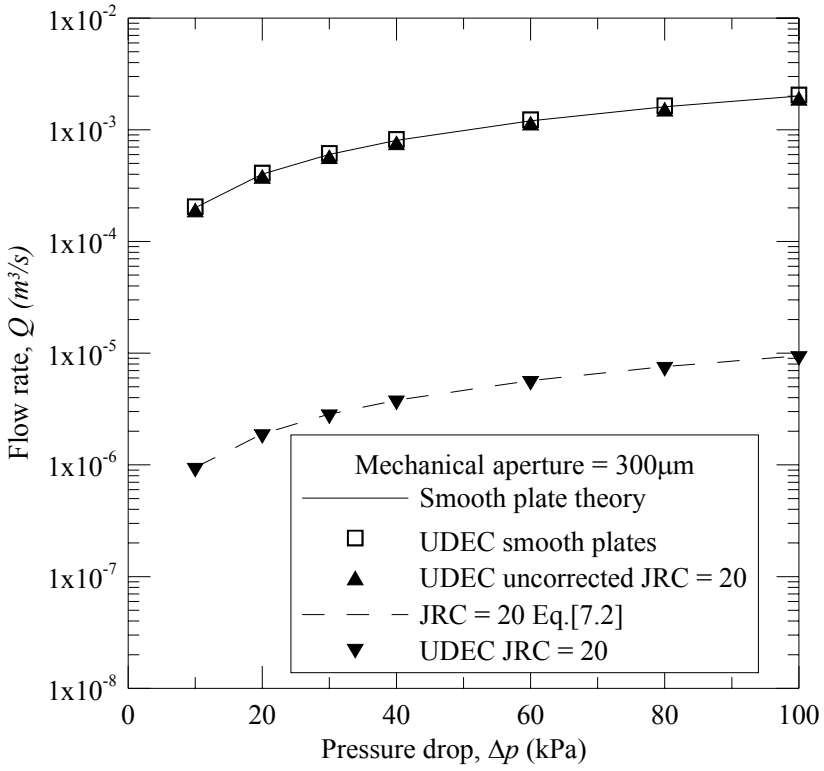

Figure 7.8: Relationship between computed and theoretical flow rate highlighting the limitation of the UDEC code.

The effect of roughness on flow was studied for the same model to consider the effect of different degrees of roughness. Analyses were conducted for models using a fracture

with 2mm discretised profiles with *JRC* of 15, 12 and 10. The plotted results for the rough profile analyses can be compared with the smooth fracture result. The results are shown in Fig. 7.9, and indicate the expected non-linear increase in flow rate with decreasing roughness. In the Fig. 7.9 graphs, it is interesting to note that the flow rate is relatively unaffected by fractures with a *JRC* of less than 10. This effect is accentuated by the linear – log plotting style. This indicates the values of careful site mapping activities to ensure a representative selection of discontinuities are recorded so that an appropriate roughness value can be assessed.

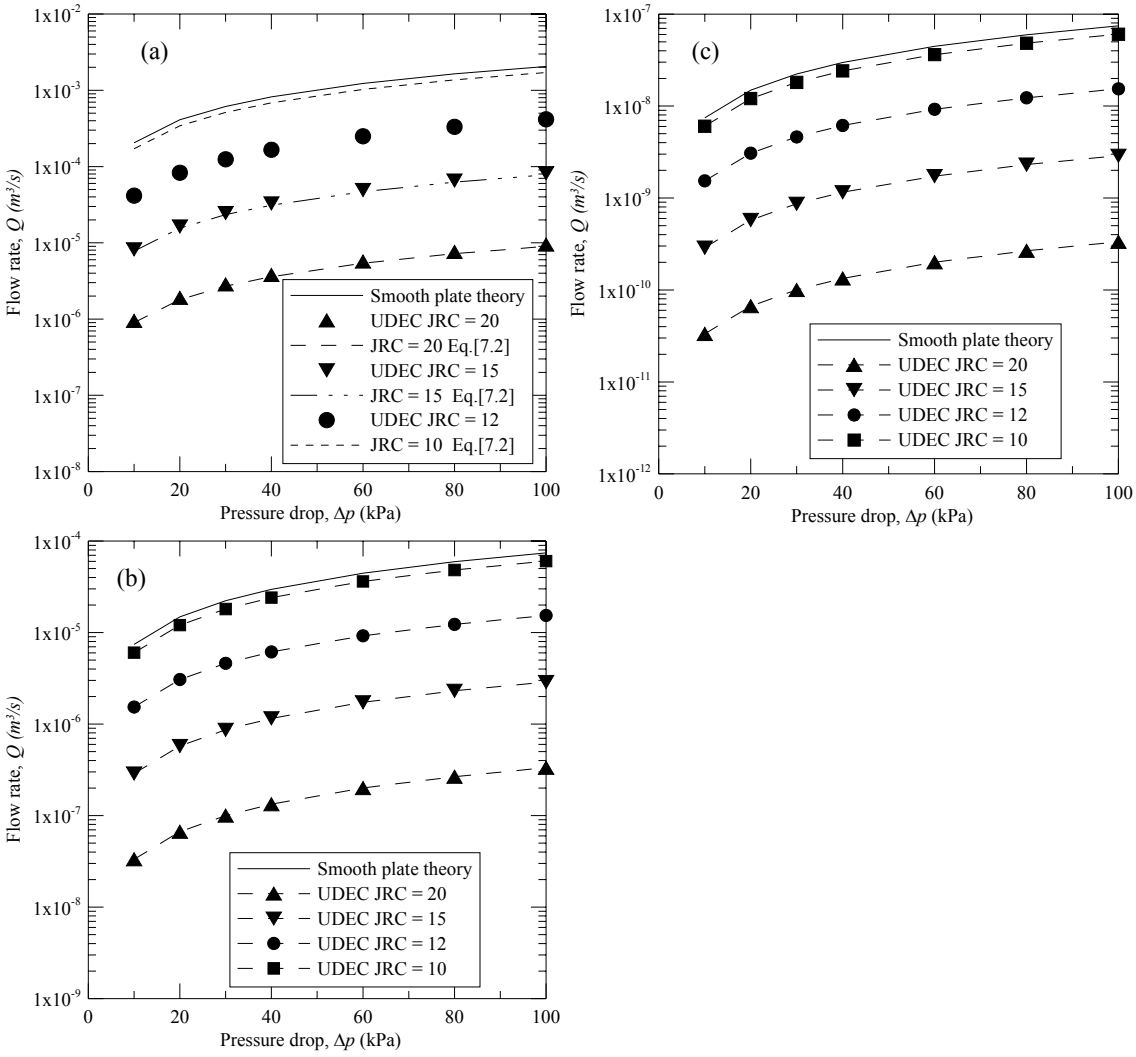

Figure 7.9: Relationship between computed flow rate and pressure drop for rough fracture – mechanical apertures (a) 300μm, (b) 100μm and (c) 10μm.

In their assessment of the cubic law, Witherspoon et al. (1980) indicated that the cubic law ceased to be appropriate for tight as well as rough fractures. To study the effect of finer apertures on the predicted UDEC result further analyses were performed for apertures of 100μm and 10μm. The plots of flow rate versus pressure drop for the additional apertures are shown as Fig. 7.9 (b) and (c) and confirmed the computations. As would be expected from Fig. 7.1, as the size of the mechanical aperture increases, the degree of sensitivity of the calculated result to roughness decreases (although it still remains significant).

7.3.2.3 Discussion

Data presented in this study indicate a shortcoming in the ability of UDEC to model flow through rough fractures. The application is limited in laminar fracture flow calculations because the routine simplifies the calculation procedure to that of flow between smooth parallel plates. However, the opportunity to specify the residual aperture does enable the analysis to replicate the observed behaviour illustrated in Chapter 6. The approximation applied to flow analysis is valid in a number of situations; the specific fracture roughness should be used at least in the early stages of hydraulic modelling, in order to establish the model sensitivity to varying fracture roughness. This shortcoming can be overcome by a manipulation of the UDEC code to include an empirical factor that correctly predicts the hydraulic aperture from the mechanical aperture and the *JRC*. The results show that the limitation is more significant when considering relatively rougher fractures where the error in flow rates could be as much as 5 orders of magnitude, if fracture roughness was neglected. Modelling could be further improved if transverse roughness was also incorporated in the model by allowing the variation of elemental aperture along the defined fracture.

This development would enable the approximation of 2-D flow within a 1-D analysis. The results presented herein indicate that fracture roughness less than *JRC* = 10 produces negligible difference with predicted flow rates based upon smooth parallel plate, i.e. $e_m \approx e_h$.

The need for further improvement in the model lies in the area of coupled flow because shear and normal displacements lead to dilation of the rock mass and change in conductivity. The resulting change in aperture leads to a change in the hydraulic characteristics of the fracture. Whilst holding to the assumption of negligible fracture degradation, and thus, the fracture roughness remains unchanged, the potential change in hydraulic properties of the fracture by change in aperture is clearly shown in Fig. 7.1. To allow for the potential change in mechanical aperture, the flow formulae need to be further changed. UDEC provides a flow logic for visco-plastic flow, e.g. consideration of grouting problems. Through careful selection of input parameters, this flow logic allows the generalized Darcy' s law to be varied using two variables in Eq. 7.22 below (ITASCA, 2000) for steady state flow of incompressible Newtonian fluids:

$$Q = \left(be^{a} / 12\mu\right)\frac{dp}{dx} \qquad [7.22]$$

All the terms in Eq. 7.22 have been defined previously, except for *a* allowing the aperture exponent to be defined by the user and *b* representing an empirical coefficient. If the aperture exponent is allowed to be 3, the hydraulic aperture and *b* can be replaced using Eq. 7.2 to provide an equation that allows for change in mechanical aperture as well as fracture roughness in the flow calculation logic.

7.3.3. Large Scale Multiple Fracture Network Flow

The analytical methodology appropriate to a large project, i.e. approaching a regional scale, can be considered as a continuum or equivalent porous medium (EPM), where the localised heterogeneity is incorporated into the bulk hydromechanical properties. The

results are pertinent to large-scale behaviour, although caution needs to be applied to the direct application of these results to near field mechanisms. The scale of this problem lies outside the focus of this work; however, a brief discussion is included for completeness. The incorporation of an anisotropic parameter such as rock fracture permeability is accepted to be in the form of a tensor (Long, 1983; Hsieh et al., 1983). Assuming that the principle permeability function is symmetrical Darcy's Law can be written in the form:

$$\begin{bmatrix} U_x \\ U_y \\ U_z \end{bmatrix} = -\begin{bmatrix} k_x & 0 & 0 \\ 0 & k_y & 0 \\ 0 & 0 & k_z \end{bmatrix} \frac{\gamma_f}{\mu} \begin{bmatrix} \partial p/\partial x \\ \partial p/\partial y \\ \partial p/\partial z \end{bmatrix} \qquad [7.23]$$

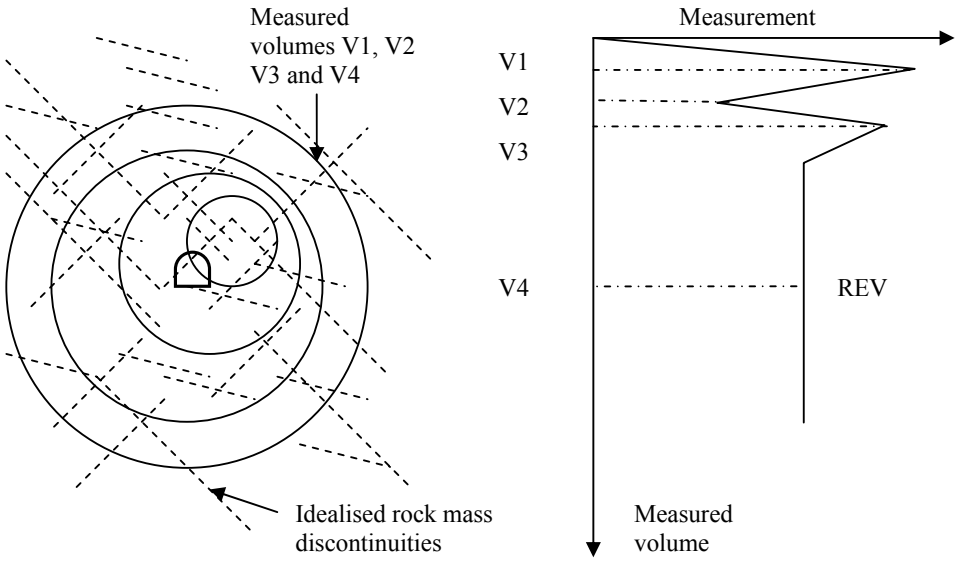

Figure 7.10: An illustration of the REV concept for a fractured rock mass (after Elsworth & Mase, 1993).

The permeability function is related to the principle permeability directions which are generally modelled as an ellipsoidal form with a set of orthogonal axes. The fundamental test for the assumption behind the EPM requires that a sufficiently large volume of rock mass is considered. This criterion is commonly called the representative

elemental volume (REV). The concept is well illustrated by Fig. 7.10, which shows that where a small number of fractures are considered within a relatively small volume, the measured result may be highly dependent upon the volume of material under consideration. Elemental volume increases result in relatively small variation in measurement, the REV has been achieved. For a problem that tests a sub-REV component, a discontinuum based analytical model is required, as previously described.

The preceding description of continua-based solutions can be theoretically extended to include a dual porosity and a two-phase analysis as explored to great effect by Bai & Elsworth (2000). The subsequent section continues with the established theme of macroscopic fracture based fracture flow. The discussion evolves to consider two-phase flow hydromechanics using a new model that could be applied to both the single fracture based finite difference routine or the more complex UDEC code.

7.4. Two phase flow analysis using homogenous fluid

7.4.1. Theoretical development

One of the most convenient approaches to the analysis of two-phase fluid mixtures flowing in natural rock fractures is that of the homogenous fluid model. The advantages of this macroscopic model include removing the need for information on the rate of phase change within the fracture, knowledge of the localised microscopic flow behaviour (e.g. individual bubble flow path) and particular knowledge of the two-phase flow pattern present under the instantaneous phase velocity and pressure drop conditions. The proposed technique considers the free flow of water and gas phases through the fracture, and is based upon estimated homogenous fluid properties calculated from the relative combination of the separate fluid phases. The model assumes:

a) aperture and fluid pressure gradients to be large enough so that interfacial capillary pressures between opposing fracture surfaces and elevation gradient across the fracture length are negligible;
b) this model is limited to the analysis of a bubble mixture and considers the motion of air bubbles entrained in a continuous water phase, such that phase velocities are effectively equal;
c) fracture walls remain wetted because of the capillary pressures associated with the rough fracture surface and the small matrix pore size;
d) rock is 'hard' with deformation approximated as linear elastic between observed normal stress ranges. In this case, fracture deformation is more sensitive to changes in normal stress than changes in fluid pressure.
e) primary permeability of the rock substance is negligible.

Figure 7.11 shows a simplified 3-D smooth joint element of aperture e (such that $e_{hom} = E_{mech}$) inclined at an angle β at time $t = 0$ and at time $t = i$, following a normal stress increment $\Delta\sigma_n$. Using the proposed approach, the basic 1-D form of the equations for continuity and the conservation of momentum for steady state isothermal flow can be written in the following forms for an inclined fracture (after Wallis, 1969) for the case of unit fracture width (y-direction):

$$M = \rho_m U A \qquad [7.24]$$

$$M\frac{dU}{dx} = -A\frac{dp}{dx} - P\tau_w - A\rho_m g\sin\beta \qquad [7.25]$$

where, M is the total mass flow rate ($M_a + M_w$) of phases a and w, ρ_m is the mixture density, A is the cross sectional fracture area, i.e. the product of fracture aperture and width ($e.y$), P *or* $2(y + e)$ is the fracture wetted perimeter, U is the flow velocity, p is the fluid pressure and τ_w is the average shear stress acting on the fracture wall.

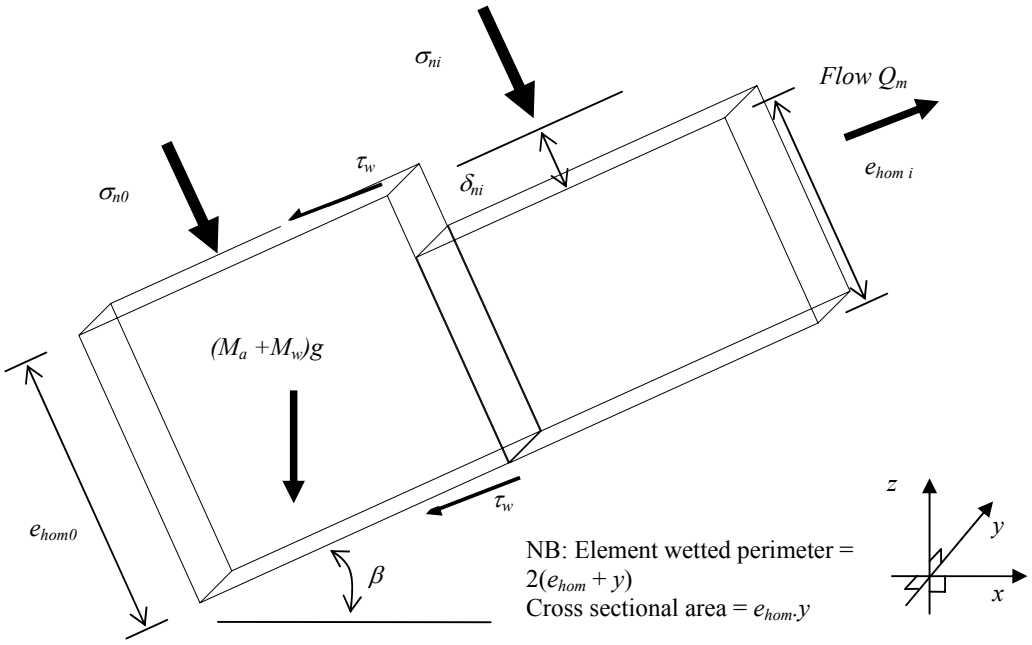

Figure 7.11. Schematic section of joint element at time zero (left) and time *t* (right) following the application of incremental fracture normal stress $\Delta\sigma_N$.

The Continuity Equation 7.24 defines the mass flux of the fluid that remains the same despite changes in phase volume that may result from the change in stress or changes in aperture. Equation 7.25 can be re-arranged to express the total pressure gradient acting across the rock fracture *(dp/dx)*, in terms of losses due to friction, acceleration and gravitational potential referring, respectively, to the three right hand terms of Eq. 7.26:

$$\frac{dp}{dx} = -\frac{P}{A}\tau_w - \frac{M}{A}\frac{dU}{dx} - \rho_m g \sin\beta \qquad [7.26]$$

In the case of the testing used in this work, it is contended that the gravitational terms can be effectively ignored since the change in elevation is equivalent to between 5% and 0.5% of the pressure drop. In the case of smaller pressure drops, gravity and capillary forces will have a greater impact on the flow and should be included in the calculations.

The average shear stress acting on the fracture wall due to the flow of the mixture can be written in terms of a friction factor (C_f):

$$\tau_w = 0.5 C_f \rho_m U^2 \quad [7.27]$$

where, C_f is defined empirically using the Reynolds number for the mixture Re_m, in accordance with Fourar et al. (1993) for laminar flow as $68.06/Re_m 1.1$ and $6.46/Re_m 0.61$ for smooth and rough fractures, respectively. This finally allows the frictional pressure gradient term for a smooth planar fracture to be written as:

$$\left(\frac{dp}{dx}\right)_F = \frac{P}{A}\tau_w = \left(\frac{1}{e}+\frac{1}{y}\right) C_f \sum_{i=a,w}(M_i)\sum_{i=a,w}(Q_i) \quad [7.28]$$

The pressure gradient due to changes in acceleration can be written as:

$$\left(\frac{dp}{dx}\right)_A = \frac{M}{A}\frac{dU}{dx} = \frac{M}{A}\frac{d}{dx}\left(\frac{M}{A\rho_m}\right) \quad [7.29]$$

Substituting 7.28 and 7.29 in 7.26 gives the following equation,

$$\frac{dp}{dx} = -\left(\frac{1}{e}+\frac{1}{y}\right) C_f \sum_{i=a,w}(M_i)\sum_{i=a,w}(Q_i) - \frac{1}{(ey)^2}\left(\sum_{i=a,w}(Mi)\right)^2 \frac{d}{dx}\left(\frac{1}{\rho_m}\right) - \rho_m g \sin\theta \quad [7.30]$$

The homogenous fluid properties used in this work are expressed in terms of the phase flows (Q_i), the mass flow rate (M_i) and corresponding phase density (ρ_i), such that the mixture density (ρ_m) is given by:

$$\rho_m = \frac{1}{\sum_{i=a,w} Q_i}\left(\rho_a Q_a + \rho_w Q_w\right) \quad [7.31]$$

The mixture viscosity (μ_m) is defined according to the work of McAdams et al. (1942), in terms of the mass fraction of the phase flows:

$$\mu_m = \sum_{i=a,w}(M_i)\left(\frac{\mu_a}{M_a}+\frac{\mu_w}{M_w}\right) \quad [7.32]$$

As often the case in hydromechanical problems, the combination of Poiseuille's and Darcy's law is considered applicable to analysing laminar homogenous fluid flows for small pressure and elevation gradients:

$$Q_m = \sum_{i=a,w} Q_i = \frac{e_{\text{hom}}^3 y}{12\mu_m}\left(\frac{dp}{dx} + \rho_m g \frac{dz}{dx}\right) \quad [7.33]$$

where, e_{hom} is the back-calculated fracture aperture based upon a homogenous fluid.

When a fracture is acted upon by a change in normal stress $\Delta\sigma_n$, the resulting change in fracture aperture δ_n, is counteracted by compression of the fluid mixture. For single-phase flows of compressible liquids, the fluid can be regarded as effectively incompressible, whilst the relative velocity of the two phases is small (Vennard & Street, 1982). When considering a homogenous fluid comprising gas and liquid, it is assumed that the resulting mixture has a compressibility related to the relative proportions of each of the individual phases and the changes in stress at the macroscopic mechanical level.

Indraratna & Ranjith (2001a) related the total normal deformation *(ΔT)* of the fracture aperture to the compressibility of air (ξ_{AC}) and water (ξ_{WC}), the solubility of air in water (ξ_{AD}) and the mechanical normal deformation (δ_n) due to changes in stress. Hence,

$$\Delta_T = \xi_{AC} + \xi_{AD} + \delta_n - \xi_{WC} \quad [7.34]$$

When considering a homogenous fluid, this expression simplifies to:

$$\Delta_T = \delta_n - \xi_{mc} \quad [7.35]$$

where, ξ_{mc} is the volumetric compression *(ΔV)* of the homogenous fluid mixture per unit fracture area. The compressibility of the mixture comprises the compression of the air and water phases under the local phase pressure. The water phase is relatively stiff, so that most of the compression is accommodated by the air phase. The negative sign for ξ_{WC} allows for the air phase to expand to occupy any compression of the water. Hence, for a fracture of length l and unit width, inclined at β to the horizontal, the compression can be written as:

$$\xi_{mc} = \frac{\Delta V}{l^2 \cos\beta \sin\beta} \quad [7.36]$$

The isothermal compressibility of air and water (C_A and C_W) can be used to calculate the compressibility of an air-water mixture based upon the volumetric composition of both phases. The compressibility of the individual phases can be written in the form of,

$$C_W = -\frac{1}{V_W}\frac{dV_W}{dp_W} \quad [7.37]$$

Thus, for an air-water mixture, the compressibility is given by:

$$C_{AW} = -\frac{1}{V_A}\frac{dV_A}{dp_A} - \frac{1}{V_W}\frac{dV_W}{dp_W} \quad [7.38]$$

If the total fracture volume, $V = V_A + V_W$, and then considering the wetting phase saturation (S_W) to make the air phase volume $V_A = V(1 - S_W)$, Eq. 7.38 can be re-written to include the change in pore phase pressure with respect to total stress change ($dp_i/d\sigma$), after Fredlund & Rahardjo (1993):

$$C_{AW} = -\frac{1}{V_W + V_A}\left(\frac{dV_A}{dp_A}\frac{dp_A}{d\sigma} + \frac{dV_W}{dp_W}\frac{dp_W}{d\sigma}\right) \quad [7.39]$$

The differential can be expanded so that compressibility is a function of the water phase saturation and the phase compressibility, whereby:

$$C_{AW} = -C_A(1 - S_W)\frac{dp_A}{d\sigma} - C_W S_W \frac{dp_W}{d\sigma} \quad [7.40]$$

Re-writing Eq. 7.35 with the preceding terms gives:

$$\xi_{mc} = -\frac{\Delta V}{y.x} = -\frac{C_{AW}\Delta p_{AW}.V}{l^2 \cos\beta \sin\beta} = -\frac{V_A + V_W}{l^2 \cos\beta \sin\beta}\left(C_A(1 - S_W)\frac{dp_A}{d\sigma} + C_W S_W \frac{dp_W}{d\sigma}\right) \quad [7.41]$$

The fluid under test is conceptualised as gas bubbles mixed within a continuous water phase. In the test fracture, the independently injected air and water pressures are envisaged to rapidly equilibrate through localised changes in phase saturation (S_i). In

this case, where the difference in elevation across the fracture is small and inter-phase slip is negligible, one can assume $dp_A = dp_W = dp$.

The change in fracture aperture is related to the normal fracture stiffness (K_n) and the change in applied normal stress ($\Delta\sigma_n$). An equation could be written in terms of the effective stress, since the mechanical reaction of a water filled fracture will be mitigated by the presence of the fluid mixture with a pore pressure p. In the case of non-linear fracture deformation an alternative stiffness function can be used in Eq.[19], although in this case a linear elastic condition is considered. For a coordinate system where principal maximum and minimum stresses are parallel to the z and x axes respectively, the expression is:

$$\delta_n = \frac{\Delta\sigma_n'}{K_n'} = \frac{\Delta\sigma_n - p}{K_n'} = \frac{\Delta\left(\sigma_1 \cos^2\beta - \sigma_3 \sin^2\beta\right) - p}{K_n'} \qquad [7.42]$$

The change in fracture normal stiffness can be assessed from test observations of clip gauge deflection with changes in confining stress and pore fluid pressure. The fluid mixture within the fracture will respond to the change in stress by a change in volume defined by the fluid mixture compressibility. The mixture compressibility was expressed in Eqs. 7.35 and 7.36, and is equivalent to the change in solubility of the air phase within the water, the change in the dissolved air content of the water, and the compression of the air and water phases. This allows rewriting of the expression for the total fracture deformation (ΔT) in Eq. 7.35 as:

$$\Delta_T = \frac{\Delta\sigma_n - p}{K_n'} - \frac{V_A + V_W}{l^2 \cos\beta \sin\beta}\left(C_A\left(1 - S_W\right)\frac{dp_A}{d\sigma} + C_W S_W \frac{dp_W}{d\sigma}\right) \qquad [7.43]$$

7.4.2. Results and discussion

Two-phase hydraulic testing of the samples using the TPHPTA can deliver large volumes of test data, giving detailed information on the steady state and transient flow conditions, as illustrated in Figs. 7.12a and b. Samples containing fractures with

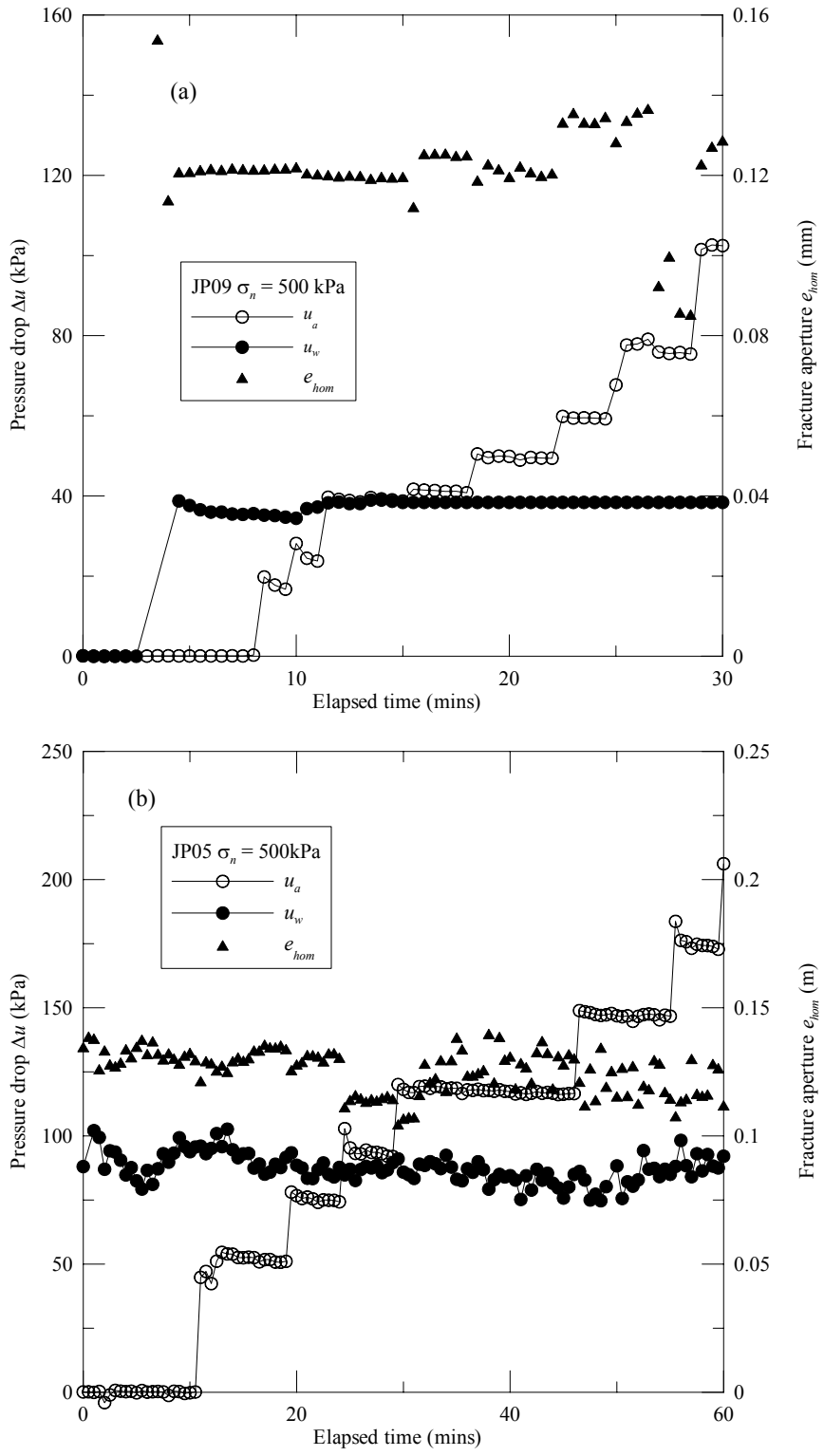

Figure 7.12. Two phase test results: (a) sample JP09 confined at 500kPa with water phase pressure drop 40kPa; (b) sample JP05 confined at 500kPa with water phase pressure drop 95kPa.

apertures of this order of magnitude achieve steady state conditions within a few minutes. Figure 7.12a presents one of a variety of tests, and describes a test on JP09 that in this instance commenced with a water phase inlet pressure of about 40kPa. Air phase injection pressures were increased stepwise to a final pressure of about 95kPa. Analysis of the test data using Eqs. 7.32 and 7.33 enables the fracture aperture (e_{hom}) corresponding to the homogenous fluid properties to be evaluated. The calculated value increases slightly with the air inlet pressure, although the value of the aperture remains within about 5% to 10% of the initial magnitude throughout most of the test. There is increased variability in the calculated aperture for air inlet pressures greater than 60kPa, which is attributed to the onset of higher air velocities and the development of slip under the dynamic flow conditions. The same approach applied to the data shown in Fig. 7.12b, shows the test response for sample JP05 subjected to a fracture normal stress of 500kPa and a sustained water phase inlet pressure of about 95kPa.

The localised increases in calculated aperture are believed to correspond to improved air phase flow path connectivity, resulting in this apparent aperture dilation and the dynamic behaviour of the air and water phase. In reality, no physical increase in aperture would be expected, but rather there has been an improvement in the mixture conductivity due to the increase in phase pressure drop and the reduction in mixture viscosity associated with the reduction in water phase saturation, S_W. When Δp_a exceeds Δp_w there is potential for an increase in calculated aperture i.e. $e_{hom} > e_h$, where the increased air pressure acts to drive the mixture flow and mobilises trapped air phase. The greater variability of the calculated aperture values when $\Delta p_a >> \Delta p_w$ is understood to represent the onset of increasing slip conditions where the model assumptions are no longer applicable.

Comparison with the laboratory data published by Fourar et al. (1993) suggests that froth and annular two-phase flow patterns tend to deviate from the linear trend that defines laminar flow. Hence, the two-phase flow patterns encountered during this particular testing probably correspond to bubble, some annular flow and possibly complex flow patterns, located within the laminar flow regime, possibly tending to complex or froth patterns at very high air phase test pressures. The assumed largely laminar flow conditions also appear reasonable if the experimental mixture flow rates are plotted against pressure drop. A sample of the test data is shown in Fig. 7.13. This graph shows a mainly linear trend occurring during two-phase testing for pressure drops up to 100kPa.

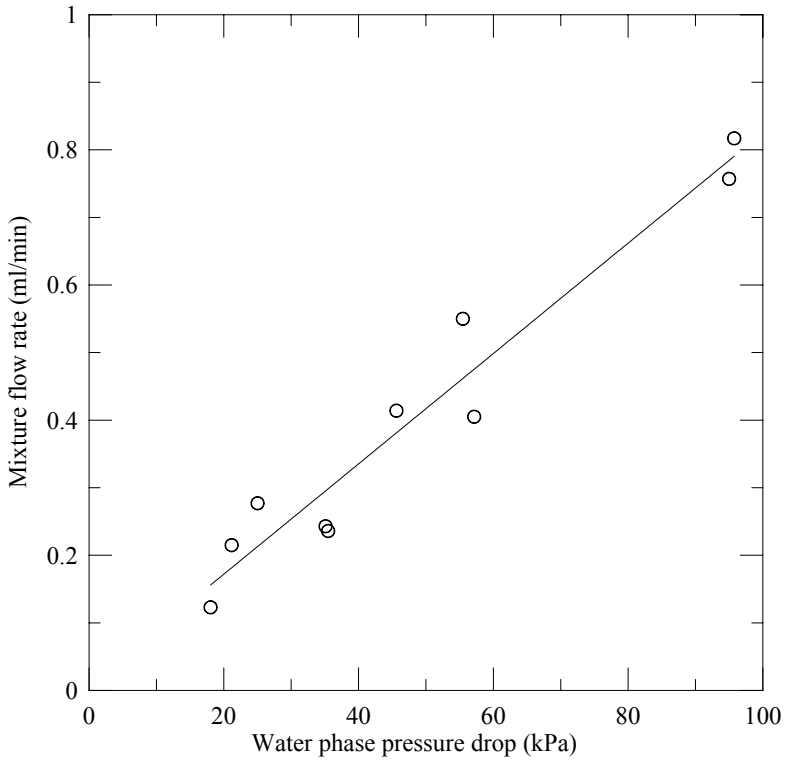

Figure 7.13. Selected test data for sample JP09 showing variation in mixture velocity with water phase pressure drop.

Figure 7.13 demonstrates some scatter, reflecting the difficulty in recording "steady state" flow data from dynamic behaviour. Digital filtering techniques or refined data sampling frequency may improve the repeatability of the results. This behaviour is discussed subsequently.

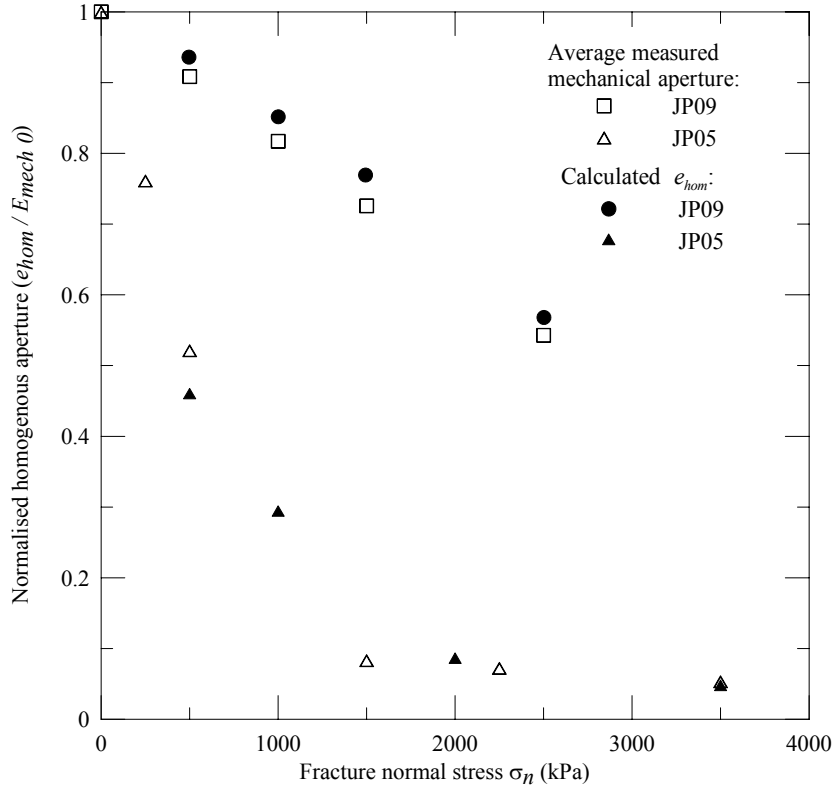

Figure 7.14. Comparison of the average calculated homogenous fluid fracture aperture with the recorded fracture dilation data obtained from analysis of the clip gauge readings.

It is interesting to plot the average calculated e_{hom} values (normalised by the initial mechanical aperture) for each of the fracture normal stresses and to compare them with the measured normalised fracture normal stiffness functions based upon the clip gauge data (Fig 7.14). From this plot, there is clearly a strong similarity between the e_m versus σ_n data, and that for e_{hom} versus σ_n. This relationship suggests that the homogenous fluid provides a good technique for assessing rock mass dilation and fracture aperture estimation. It is especially noteworthy that this approach overcomes the single-phase

testing problem of increased pressure drop due to fracture roughness, and therefore, over the range of roughness investigated, dispenses with the need for empirical correlation, such as that by Barton et al. (1985). Where both single-phase water and two-phase air-water testing can be applied to the same fracture, allowing an assessment of the single-phase (water) hydraulic aperture and the fracture roughness. Therefore, this additional testing provides valuable hydromechanical rock mass properties using the proposed testing and calculations.

It is informative to test the validity of the proposed roughness assessment. This can be done by comparing the homogenous fluid test data and the corresponding single phase water testing results obtained at a particular confining stress (Table 7.1). Using the assessed roughness JRC_F, the mechanical aperture e_m can be calculated using Eq. 7.2. The assessed JRC_F and the measured single-phase hydraulic aperture e_h are used to calculate the mechanical aperture e_m with Eq. [7.2]. For comparison, the measured mechanical aperture e_{clip} and e_h can also be used to calculate the empirical JRC with the same equation. Table 7.1 shows that the assessed roughness and the empirical roughness are very similar. In addition, the homogenous fluid aperture e_{hom} is shown to be very close to the measured mechanical aperture i.e. within 5% to 10%. Improved accuracy and reduced data scatter could be achieved for tighter or rougher fractures through testing with larger datalogger time increments. The e_{hom} value is based upon a range of test results calculated over a range of different pressure gradients, yet despite this, shows acceptable agreement with the measured and calculated values. This outcome gives confidence to the applicability of the proposed JRC assessment technique since the assessed JRC_F agrees well with the empirical JRC calculated from the single-phase hydraulic aperture e_h and the measured mechanical aperture e_{clip}.

Table 7.1. Comparison of aperture and JRC values at 500kPa confinement.

Sample	**Average** JRC_F	**Empirical** JRC **[Eq. 7.2]**	e_h (μm)	e_m (μm)	e_{hom} (μm)	e_{clip} (μm)
JP05	9 to 8.5	9.1	75	135 to 126	122	137
JP09	7 to 7.5	7.1	115	122 to 133	121	125

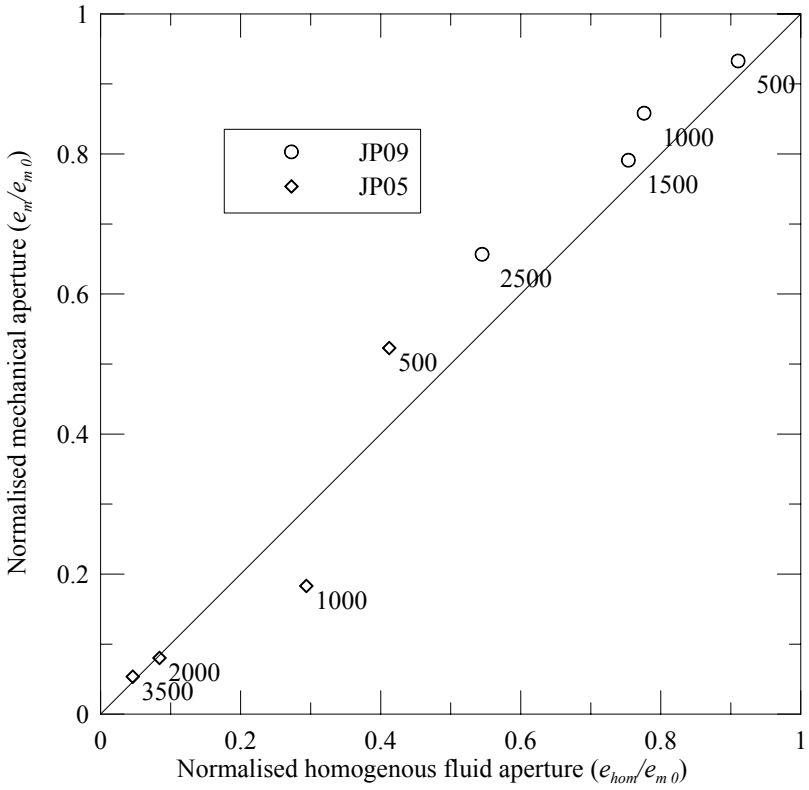

Figure 7.15. Plot of normalised homogenous fluid and mechanical apertures for samples JP05 and JP09. (Note: data points labelled with corresponding fracture normal stress.)

To extend the e_{hom} versus e_m comparison, a graph plotting normalised e_{hom} (= $e_{hom}/ e_{m\,0}$) versus normalised e_m (= $e_m/ e_{m\,0}$) was prepared (Fig. 7.15). The test data for the three samples are plotted together. The points plot close (within about 10%) to the 45° line in all cases and confirm the proposition that e_{hom} is a good predictor of e_m. This variability of data was also discussed regarding Fig. 7.13. The dynamic behaviour involving the

passage of air bubbles and liquid slugs can complicate instantaneous measurement of pressure and flow.

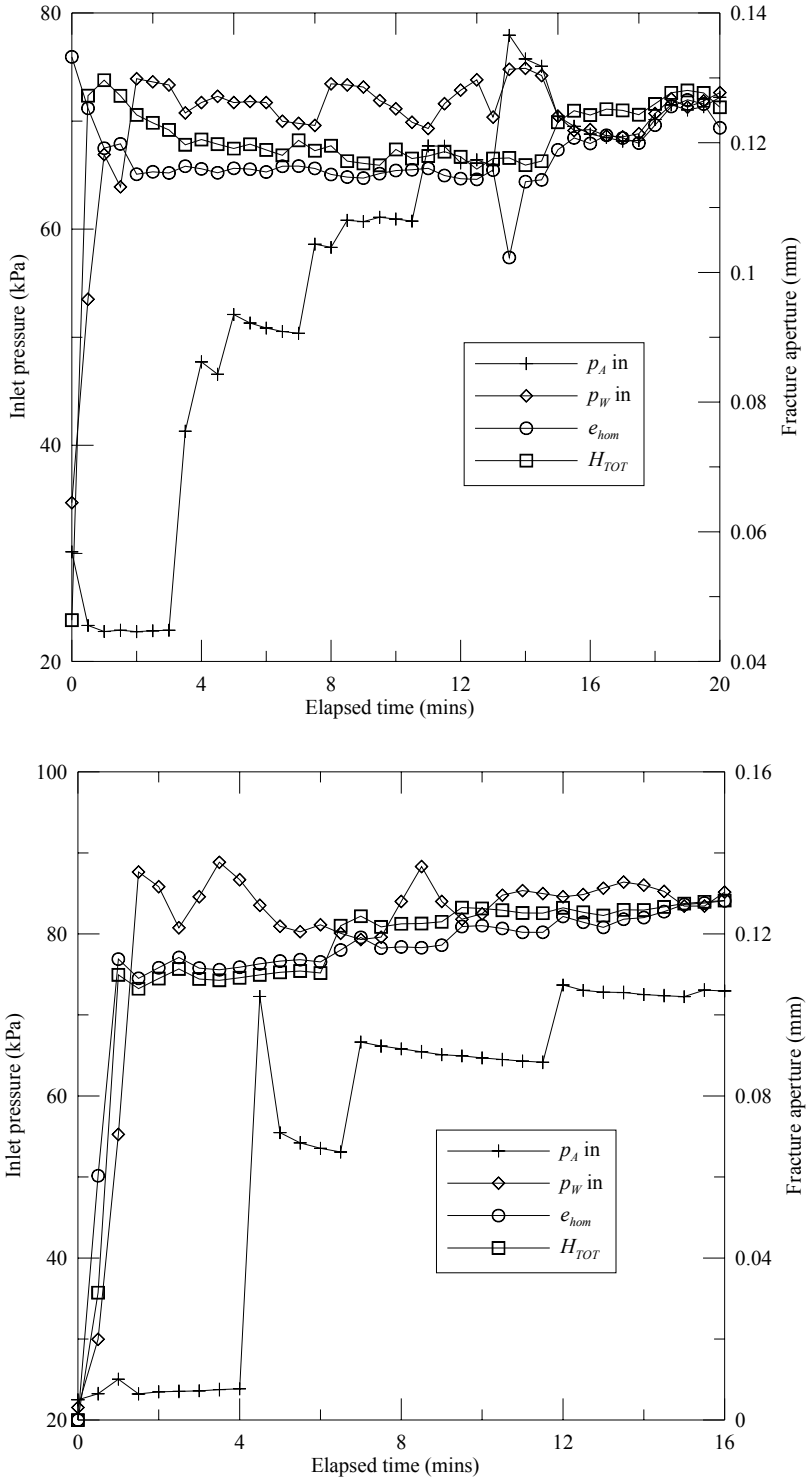

Figure 7.16. Comparison of calculated homogenous aperture e_{hom} with phase height sum H_{TOT}.

The calculated homogenous aperture can be compared against the sum of the air and water phase height (Fig. 7.16). The two aperture values show very good agreement indicating the compatibility of both proposed two-phase flow models for the assumed linear flow conditions.

7.5. Summary

The key outcomes from the study of hydromechanical modelling in this chapter can be summarised as follows:

- Representing the hydromechanical behaviour of rough fractures is crucial in accurate numerical analysis of rock mass behaviour. Different scales of application are best represented by specific modelling approaches because of the varying impact of geological discontinuities on solutions. Different approaches are contemplated within this chapter to consider the role of discontinuities and fracture roughness in single- or two-phase flow.
- The macroscopic analytical approach applied in previous chapters is initially replaced to consider 2-D flow through a variable aperture fracture. A relaxation approach using a finite difference scheme has been developed. The finely discretised mesh illustrated how non-parallel flow develops when fractures are rough, instead of the commonly assumed smooth parallel plate conditions. Linear laminar flow conditions were assumed in the model and the majority of calculated flow was observed to originate from a few high flow capacity pathways.
- The computed flow based upon laser scan surface roughness data was used to estimate the representative hydraulic aperture for the whole fracture. The computed aperture closely compared to the back-calculated hydraulic aperture from single-phase laboratory testing results for a range of fracture normal

stresses. This outcome verifies the modelling and illustrates the potential for 2 - D analyses to be reduced to 1-D calculations to provide engineering solutions, i.e. from the microscopic to the macroscopic. This approach has the flexibility to be expanded to consider the intersection of a network of fractures using the approach proposed by Priest (1993).

- In this study, the UDEC code waas applied to a rough fracture in a simple two-block model for particular *JRC* roughness profiles. The results show that this important computer code does not accommodate fracture roughness during hydraulic analyses, approximating calculations to the smooth parallel plate flow. Whilst unrecognised, this approximation can have important analytical limitations, especially where fracture $JRC > 10$.
- One part of the project has demonstrated that UDEC is sufficiently flexible to enable a visco-plastic flow code to be modified to correctly incorporate the impact of roughness in reducing the flow capacity of rough fractures. This proposal assumes that roughness is unaltered by changes in the in-situ stress, but provides a useful solution to the identified limitation for modelling single-phase flow in rough fractures.
- The inability of UDEC to accommodate two separate phases again limits the suitability of the code for the analysis of two-phase 'free' fracture flow in geological discontinuities. This problem is addressed by the homogenous fluid model, representing the two fluids as one equivalent fluid and satisfying conservation of mass. A theoretical model is developed that incorporates phase compressibility and solubility to replicate two-phase flow behaviour.
- The model is validated using Two-phase High Pressure Triaxial testing and clip gauge data and the calculated apertures compared to those from analysis using

the annular flow model. The results verify that for linear flow and 'no slip' conditions, the homogenous fluid model correctly predicts the mechanical aperture, and the results are unaffected by fracture roughness. The homogenous fluid model is found to predict similar aperture values to those calculated using the simplified annular model presented in Chapters 4 and 6. One of the advantages of the homogenous fluid model is that the fracture roughness does not need to be identified to estimate the single-phase hydraulic aperture, provided the flow rate and pressure drop are measured for each phase.

Chapter 8

Conclusions

&

Recommendations

8.1 Summary of main outcomes

This research project has considered the impact of roughness on two-phase (air + water) flow in discontinuous geological media. The anisotropic nature of fracture orientation, aperture topology and persistence can be limitations on coupled single- and two-phase flow. The research has been driven by the need for improvements in the prediction of two-phase flows in underground mining development and civil engineering infrastructure to better manage the hazards of outburst and in-rush events that can catastrophically influence worker safety and mine production. There are available far-field modelling techniques but the link between fracture roughness, conductivity and stress is often empirical or assumed. The aim of the work has been to develop robust coupled two-phase flow models to improve near-field hydromechanical rock fracture analysis. The key findings are discussed below:

8.1.1 Theoretical background

A critical review of single- and two-phase hydraulics using available literature has established the significance of fracture roughness in predicting flow behaviour. The review identified the 'cubic' law is applicable for hydraulic fracture analysis except for the case of tight, rough fractures. The rate of change and the degree of roughness are

important in analyses. The study established that inclusion of 2-D variability in fracture aperture requires simplifying assumptions for flow analyses and identifying an opportunity for better definition of macroscopic coupled two-phase flow models.

An accurate study of fracture aperture and variability was necessary to analyse laboratory testing of real rock fractures and a review considered an array of analytical techniques for roughness assessment in terms of industry standard terms. High resolution laser scanning was used to acquire detailed digital information on fracture topography. An innovative technique using Fourier series was developed as an objective, reproducible method to assess fracture roughness and roughness anisotropy in relation to the Joint Roughness Coefficient, JRC_F. The Fourier technique uses the harmonic frequency signature for standard *JRC* profiles to interpolate an average JRC_F that can be applied to subsequent hydromechanical analyses, and is verified against single-phase testing data. The technique shows the combination and interaction of different roughness wavelengths present in fracture profiles. The methodology appears applicable over a range of fracture topographies with specimen JRC_F values assessed as 11 and 7. The calculated joint roughness coefficient, JRC_F can be compared to the one that would be predicted from the Barton et al. (1985) relationship. This acceptable agreement between the two results gives confidence in the suitability of the developed *JRC* assessment technique. The methodology has been related to the standard roughness profiles ensuring that the technique will relate to the full range of *JRC* (0 – 20), as well as the range of roughness studied in the current investigation.

8.1.2 Two-phase Model development

Rock fractures comprise rough irregular surfaces that could be considered parallel only at very small scales. Theoretical examination of capillary effects in rough rock fractures illustrates that the drying out of rough discontinuity surfaces is unlikely except where

the grain or crystal size is larger than 2mm and fracture walls are near vertical or subject to displacement high pressures.

Consideration of coupled two-phase hydraulics has enabled expressions to be developed for interface and fracture wall shear forces using conservation of momentum, assuming that fracture wall 'dry out' does not occur. These equations are written in terms of *JRC*, saturation, fracture inclination and phase height. A simplified annular flow model has been proposed based upon the wall 'dry out' theory and conservation of mass. The macroscopic 1-D model includes phase compressibility, solubility and elastic fracture deformation and is based upon linear laminar flow, and 'no slip' conditions. The proposed phase height parameter replaces the relative permeability and fracture aperture that are often applied in two-phase flow analyses. This study illustrates how the complexity of two-phase flow, when taken at the macroscopic level, can be investigated with relative simplicity using an adaptation of the 'cubic' law.

8.1.3 Analogue hydraulic testing

The idealised smooth parallel plate fracture flow model was studied using two-phase analogue joint apparatus to replicate the common boundary conditions. The equipment was specially designed with 1m long transparent plates to study inclined, horizontal and vertical flow under linear and non-linear conditions. The testing programme allowed the development of a qualitative flow pattern classification related to phase saturation and velocity. It was noted that smooth surfaces, unlike rough fractures, dry out during air phase flow and that large scale continuous two-phase flow did not occur. Nonetheless, the proposed annular flow model was found to correctly predict the parallel plate aperture, indicating the wider applicability to additional flow patterns, and calculation of the relative permeability and saturation relationship.

8.1.4 Rough fracture hydraulic testing

Having validated the model for two-phase flow in analogue smooth fractures, the proposed model was applied to two-phase coupled flow in roughly fractured rock fractures. The Two-phase High Pressure Triaxial Apparatus (TPHPTA) was used to test the rock matrix and single-phase fracture hydraulic conductivity. The TPHPTA was refined to improve the data acquisition and boundary condition monitoring. The key improvements were:

a) More accurate and efficient data collection using a Datataker DT500 data logger.
b) Improved water flow measurement in terms of discharge collection capacity and digital data monitoring.
c) Improved air flow measurement with digital flow meters to control and monitor flow data.
d) Improved fracture dilation measurement as a function of fracture normal stress and relation to the two-phase hydraulic behaviour using the phase height parameter.

The single-phase testing of intact samples established that the primary (or matrix) permeability was several orders of magnitude less than the fracture permeability values calculated from the laboratory testing with an effective porosity of < 0.02. The equivalent fracture aperture corresponding to the matrix permeability is 0.7μm, typically less than 1% of the hydraulic apertures tested at 500kPa confining stress. Thus, for the range of fluid pressure gradients applied during this testing, it was acceptable to disregard the impact of primary permeability on the two-phase flow behaviour.

The study of the linear and non-linear fracture response using the single phase Reynolds number indicated that the fractured samples used for testing were significantly rough, in terms of the Surface Roughness Index (S) defined by Louis (1969). The

conclusion to be drawn from this observation is that the Darcy to non-Darcy flow transition would occur for Re <<100. The single phase testing confirmed this expectation with the laboratory transition occurring at Re values as low as 30 to 15.

The TPHPTA results related the phase height parameters wetting-phase function relative permeability and saturation using an extension of the proposed two-phase flow model. The results indicated a strong relationship between phase height, fracture saturation and relative permeability across a range of test pressures.

The testing showed that the maximum water phase height H_W was equal to the single-phase hydraulic aperture e_h and the phase height sum H_{TOT} was equal to the mean log normal mechanical aperture. The annular model appears applicable for laminar flow of the envisaged flow pattern, but also for other high S_W combinations involving bubble and slug flow patterns. Two-phase injection testing could be applied to back-calculate the mechanical and hydraulic apertures. Theoretically, this information could be used to estimate rock mass deformation as well as *JRC*, where a single fracture was intersected. This development could be accommodated with only a small modification to traditional packer test equipment.

8.1.5 Hydromechanical analysis

The purpose of this section of the chapter has been to discuss techniques that are available for geomechanical analysis and to indicate where limitations exist that need to be accounted for when the more complex two-phase flow problem is considered. The role of flow path tortuosity in single-phase water flow for a single fracture has been studied using a 2-D finite difference scheme. The study showed how the hydraulic aperture can be calculated from a discretised mesh of fracture elements. The results illustrated that the flow is controlled by a small number of high conductivity channels that form in the fracture plane. This approach could be extended to consider two-phase

and fracture network flows using established simple computational schemes (Priest, 1993) using the simplified models presented in this research.

Discrete element modelling is an effective numerical technique to simulate the behaviour of a discontinuous rock mass by assuming the discontinuity properties within the model to reproduce field behaviour. Limitations have been identified in the UDEC flow calculation routine that over-predict flow through rough fractures. A simple block model has been used to demonstrate the limitation and to develop an empirical solution to accommodate rough fracture flow analysis under normal loading conditions where shear deformation and gouge formation are negligible. This refinement theoretically allows the user to carry out hydro-mechanical modelling with the flow code logic taking account of the change in mechanical aperture as well as fracture roughness.

To enhance the applicability of UDEC to two-phase flow problems, a coupled homogenous fluid model has been presented to predict two-phase flow of air and water mixtures through rock fractures. The homogenous fluid model can be applied to UDEC analyses by modification of the k_j term to incorporate μ_m. The suitability of the proposed model has been verified against laboratory data that has been acquired from TPHPTA testing and analysis of high resolution surface roughness investigation of the test specimen fracture surfaces. Using the homogenous fluid model there is good agreement between the calculated fracture aperture e_{hom} and the measured average mechanical aperture e_{clip}. Laboratory data also verified that the homogenous fluid model and the simplified annular model predict similar apertures, i.e. $e_{hom} \approx H_{TOT}$.

The calculation method adopted in homogenous fluid approach indicates the results are not influenced by roughness and flow path tortuosity, once a sufficient volume of air is present, unlike for single-phase water flow. This would be expected

because, for low viscosity fluids, the mechanical aperture e_m approximates the hydraulic aperture e_h.

8.2 Benefits to Industry

One of the main motivations of this research project has been to develop theories that have applications to field situations to achieve improvements to our analytical capabilities. The following research outcomes are perceived to have particular benefits to industry.

- The proposed roughness assessment method using Fourier series is computationally simple to calculate using spreadsheets and the technique will work satisfactorily with a total of 50 data points whereas other methods require many more e.g. Seidel & Haberfield (1995) require 128. The method allows an objective assessment of the roughness, removing the opportunity for *JRC* variations arising from differences in individual judgement. Repeatability in roughness assessment is very important when using rock mass rating schemes are carrying out preliminary rock engineering assessments. The relative simplicity of the data collection makes the technique time efficient and suitable for field and laboratory applications at a range of scales, from < 1m to >> 100m. The method has inherent flexibility to incorporate the appropriate scale of roughness that is related to the dimensions of the project.
- The proposed annular two-phase flow model enables the fracture permeability to be calculated and the mechanical response or roughness estimated. The benefit of the analysis at a macroscopic level using the proposed coupled model is that near-field rock mass behaviour can be analysed without the need to revert to complex computed solutions. This technique would be highly suited to rapid assessment or conceptual analyses of proposed engineering development for the

estimation of the mechanical response or the anticipated gas or water flows. For example, the efficiency of a developed coal bed methane production well can be monitored to check for progressive obstruction of fractures by deposited minerals. The simplified two-phase flow models allow a analysis of the producing fracture network and an estimate in the change in fracture apertures.

- The hydromechanical behaviour revealed by the laboratory results could be incorporated into two-phase borehole testing to investigate the hydraulic and mechanical properties of identified fractures. Di Biaggio (1972) reported on borehole testing for an underground cavern study whereby water and air were separately injected into a borehole to compare fracture conductivity between the injection and monitoring wells. In a similar situation, equipment development to enable independent simultaneous phase injection would enable not only conductivity assessment, but also fracture roughness or mechanical aperture through comparison of the maximum air and water phase heights.
- The study of the UDEC flow calculation has highlighted a potential for the over-estimation of single-phase flow through a fractured rock mass. The analytical review has identified a modification to the flow code that corrects the computed flow volume with respect to the fracture *JRC*. The variation to the code assumes that there is negligible shear deformation or gouge development. The result of the modification enables sensitivity testing to identify the range of likely inflows that could be anticipated for particular rock fracture characteristics. In addition, the development of a two-phase homogenous fluid model has allowed the prediction of observed laboratory two-phase flow behaviour. The study has identified the suitability of this model for application of UDEC to two-phase hydromechanical steady state analyses.

8.3 Study Limitations

The complexity of hydraulic analysis and rock mass anisotropy require the incorporation of simplifications and assumptions to any theoretical development. The proposed coupled two-phase flow models in this work are principally constrained by the following conditions:

- The two-phase flow models have assumed linear laminar flow conditions. The results have demonstrated the suitability of a technique to objectively assess and accommodate fracture roughness, a factor that detracts from many hydromechanical studies. The models could be adapted to non-linear flow if Darcy's law were replaced with accepted non-linear flow laws such as Forcheimer or Missbach. Such a development would require the identification of fracture specific constants that would limit the model applicability compared to the linear flow models. The results show that the onset of non-linear flow can be identified from the sum of the phase heights H_{TOT}.
- The study has considered the flow of air and water through 'open' fractures where capillary and gravitational pressure gradients are negligible compared to the phase pressure gradients acting to drive flow. The model also assumes that fracture surfaces remain wetted due to surface tension and the fine grain and pore size of the rock substance. These simplifications do not invalidate any of the reported conclusions and the flow models could be expanded to consider capillary pressure as a modifying rule to fracture element accessibility. This limitation means that the models in this form are more suited to higher pressure gradient conditions, e.g. underground mining rather than methane migration from a small landfill.
- The models are limited to hydraulic conditions where the air and water phase superficial velocities are similar, i.e. slip is negligible. The testing demonstrated

that this condition is valid for much of the range of test conditions. However, at high air velocity, such as that seen during some of the analogue testing, slip can develop and limit the model applicability. Under these conditions an alternative solution would be required incorporating non-linear, compressible flow.

- The study has been limited to small finite fractures and has not considered larger fractures or fracture networks where scale effects could influence the hydraulic and mechanical properties. These phenomena could be incorporated into the proposed models using established empirical correlations. The aim of this research has been to obtain information about coupled two-phase flow at a fracture level, independent of the increased complexity of an anisotropic rock mass.
- A larger set of natural fractured samples should be studied to assess the impact of roughness anisotropy on the roughness assessment. The influence of profile spacing over the fracture surface should also be studied further.

8.4 Recommendations for future research

The milestones that have marked the progress of this project have highlighted a number of areas of further research. The particular areas for future research include:

- The proposed model in this project assumes that flow is linear and the phase 'slip' or 'hold up' is negligible. The laboratory results show that the phase height: mechanical aperture relationship model under-predicts the mechanical aperture once non-linear flow of the water phase occurs. A logical extension of this approach is to consider environment low wetting phase saturation conditions where gas phase 'slip' is significant. This environment could be analysed by adapting established single-phase non-linear and transient flow laws to emulate the increased momentum losses associated with high-pressure gradient flows.

- Recent advances in the economics of sustainable and renewable energy projects in Australia present several opportunities related to components of this project. The existing development of coalbed methane extraction to supply mine-site power at Tower Colliery near Wollongong or residential gas at Cawdor southwest of Sydney, present two potential extensions of this project. Additionally, with the rise in significance of Hot Dry Rock projects within Australia, as well as worldwide, it is theoretically attractive to extend this approach to non-isothermal modelling. In both areas of development, borehole stability is critical to the maintenance of project viability. Given the existing progress, there is considerable potential for field-based crosshole trials of the existing models and potential for further development in thermal and non-linear flow.
- During this research project, the development and availability of surface scanning technology has enabled considerable advance in surface profiling. Accurate and affordable computer controlled scanning and milling machinery used in industrial design and component manufacturing could be applied to scan and replicate existing rock fracture specimens. The availability of a wide range of natural rough profiles would enable sustained hydromechanical investigation using the TPHPTA. Currently this study is restricted by the limited reproducibility of real fractured samples.
- Two-phase hydromechanical fracture behaviour under shear loading using a large-scale shear box is a topic that could be studied using a specialised rock mechanics shear box. The variation of fracture aperture during shear deformation is known to affect fracture permeability (Chen et al., 2000). The impact of fracture topography and shear deformation on two-phase flow would

provide improved understanding of near-field rock mass behaviour in the mining or petroleum fields and promote understanding of gouge formation.

- The documented advances in two-phase hydromechanics have emphasised the relationship between phase flow and fracture deformation across a range of two-phase flow patterns. The more sophisticated understanding of hydromechanics could be incorporated into a detailed near-field computational code. There is a need for improved prediction and analysis to hazardous geotechnical environments encountered in underground mining and construction.

Bibliography

Archambault G., S. Gentier, J. Riss & R. Flamand (1997). The evolution of void spaces (permeability) in relation with rock joint shear behaviour. Int. J. Rock Mech. & Min. Sci. 34:3-4, paper No. 014 (on CD Rom).

ASTM (1993). Standard test method for permeability of rocks by flow air. American Society of Testing Methods. Annual Book of ASTM Standards, Section 4 – Construction - D 4525-90, pp. 825 – 828.

Bai, M. & Elsworth, D. (2000). Coupled processes in subsurface deformation, flow, and transport. ASCE Press, Reston VA (USA), 334p.

Barton N. & de Quadros E. F. (1997). Joint aperture and roughness in the prediction of flow and groutability of rock masses. Int. Journ. Rock Mechs. Min Sci., vol 34 no 3-4, Paper No.252.

Barton N. & Lingle R. (1982). Rock mass characterisation methods for nuclear waste repositories in jointed rock. Rock Mechanics: Caverns and Pressure Shafts, ISRM Symposium, Aachen, pp. 3-18.

Barton N. & S. Bandis (1980). Some effects of scale on the shear strength of rock joints. Int. J. Rock Mech. Min. Sci. & Geomech. Abstr., Vol. 17, pp. 69-73.

Barton N. & V. Choubey (1977). The shear strength of rock joints in theory and practice. Rock Mechanics, 10, pp. 1-54.

Barton N., Bandis S., Bakhtar K. (1985). Strength deformation and conductivity coupling of rock joints. Int. Journ. Rock Mechs. Min. Sci. & Geomech. Abs. vol. 22 no. 3 pp. 121-140.

Bawden, W. F. & Roegiers J. C., (1985). Two phase gas escape from gas storage caverns. Proceedings of the International Symposium on the Fundamentals of Rock Joints, ed Stephansson O., Björkliden, 15-20 Sept 1985, pub Centek pp. 503-514.

Bear J. & Verruijt A., (1987). Theory & Application of Transport in Porous Media: Modelling Groundwater Flow & Pollution. Pub. D. Reidel Dordrecht NL., Chap. 9, pp.225-242.

Bendat J. S. & Piersol A. G. (1986). Random Data: Analysis and measurement procedures. 2nd Edition pub. John Wiley & Sons Inc., 566p.

Berkman D.A. (1995). Field Geologists Manual 3rd rev edition 1995 Monograph 9, Section 7.8.2; pub AusIMM Carlton Vic Australia, 390 p.

Brace W. F. (1980). Permeability of crystalline and argillaceous rocks. Int. Journ. Rock Mech. Min. Sci. and Geomech. Abs. vol. 17, pp. 241-251.

Brady B. & Brown E.T. (1994). Rock Mechanics for Underground Mining, 2nd Edition, pub. Chapman-Hall, London pp.571.

Brown S.R. (1987). Fluid flow through rock joints: the effect of surface roughness. Journ. Geophys. Research, Vol. 92, No. B2 pp. 1337-1347.

Carlsson A. Gustafson G., Lindblom U. & Olsson T. (1990). Scale effects in the determination of hydraulic properties of rock masses. In: Scale effects in rock masses, ed. Pinto da Cunha, pub. Balkema Rotterdam, pp 103-117.

Castelli M., Re F., Scavia C. & Zaninetti A. (2001). Experimental evaluation of scale effects on the mechanical behaviour of rock joints. In *Rock mechanics a challenge for society*, eds. Sarkka & Eloranta, pub. Balkema, pp 205-210.

Chen D. W., Zimmerman R. W. & Cook N. G. W. (1989). The effect of contact area on the permeability of fractures. Rock mechanics as a guide for efficient utilisation of natural resources, ed. Khair, pub. Balkema, Rotterdam, pp. 81-88.

Chen Z., Narayan S. P., Yang Z., Rahman S. S. (2000). An experimental investigation of hydraulic behaviour of fractures and joints in granitic rock. Int. J. Rock Mech. Min Sci., 37, pp. 1061–1071.

Choi, S.K. & Wold M.B. (2001). Advances in simulation of gas outburst conditions in underground coal mines. 2001 International Coal Bed Methane Symposium, university of Alabama, Tuscaloosa, 14-18 May 2001, pp.1-12.

Cook A. M., Myer L. R., Cook N. G. W. and Doyle F. M. (1990). The effect of tortuosity on flow through a natural fracture. pp. 371-378 Rock Mechanics Contributions and Challenges, Proc 31st US Symp Rock Mechs, pub. Balkema.

Cook N. G. W. (1992). Natural joints in rock: mechanical hydraulic and seismic behaviour and properties under normal stress. Int. Journ. Rock Mechs. & Min. Sci. & Geomech. Abstr. (Jaeger Lecture) vol 29, no 3 pp. 198-223.

Cornwell D. K. & Murphy H. D. (1985). Experiments with non-Darcy flow in rock joints with large scale roughness. In: Proc. Int. Symp. Fundamentals of Rock Joints, Bjorkliden, Sweden, ed. Stephansson O., pub. Centek, Lulea Sweden, pp.323-332.

DiBiagio E. (1973). Leakage of gas from underground storage facilities in rock. NGI Report No.97, p.15-30.

Durham W.B. & B.P. Bonner (1985). Closure and fluid flow in discrete fractures. Fractured and jointed rock masses, eds. Myer, et al., pp. 441-456, Rotterdam, Balkema.

Elsworth D. & Doe T.W. (1986). Application of non-linear flow laws in determining rock fissure geometry from single borehole pumping tests. Int. J. Rock Mechs. Min. Sci. & Geomech. Abstr., 23, pp. 245-54.

Elsworth D. & Mase C.R. (1993). Groundwater in Rock Engineering. Chapter 8 in *Comprehensive Rock Engineering, principles Practice & Projects*, Vol. 1, ed. Hudson J.A. pub. Pergamon Press, Oxford, UK, pp.201-224.

Ertekin T.W., Sung W. & Schwerer F.C. (1988). Production performance analysis of horizontal drainage wells for the degasification of coal seams. J. Petroleum Technology, 40, pp. 625-632.

Fell R., Stapledon D. & Macgregor P. (1992). Geotechnical Engineering of Embankments Dams, pub. Balkema, pp. 202-210.

Fisher, H.N. (1977). An interpretation of pressure and flow data for the two fractures of the Los Alamos hot dry rock (HDR) geothermal system. Proc. 18th US Symp. On Rock Mech., Golden, Colorado, pp. 1B41-1B48.

Fourar M, Bories S, Lenormand R, Persoff P. (1993). Two-phase flow in smooth and rough fractures: measurements and correlation by porous medium and pipe flow models. Water Resources Research, 29:11 pp.3699-3708.

Fourar M. & Bories S. (1995). Experimental study of air water two-phase flow through a fracture (narrow channel). Int Journ Multiphase Flow, 21:4 pp 621-637.

Fourar M. & Lenormand R. (2001). A new model for two-phase flows at high velocities through porous media and fractures. Journ Petroleum Science & Engineering, 30 pp 121-127.

Fredlund D. G. & Rahardjo H. (1993). Soil mechanics for unsaturated soils. John Wiley & Sons Inc, New York, 517p.

Gale J. (1990). Hydraulic behaviour of rock joints. Rock Joints eds. Barton N. & Stephansson O., pub. Balkema, Rotterdam. pp. 351-373.

Geier J. & Hassler L. (1992). Scale effects in estimating fractured rock block conductivity from packer tests. In *Rock mechanics*, eds. Tillerson & Wawersik, pub. Balkema, Rotterdam, pp. 551-560.

Giani G.P., Ferrero A.M., Passarello G. & Reinaudo L. (1995). Scale effect evaluation on natural discontinuity shear strength. In *Fractured and jointed rock masses* eds. Myer L., Cook N.G.W., Goodman R.E. & Tsang C.S.F, pub. Balkema Rotterdam, pp 447-452.

Glass R. J. & Norton D.L. (1992). Wetted region structure in horizontal unsaturated fractures: water entry through the surrounding porous matrix. Proc 3rd Annual International High Level Radioactive Waste Management Conference, La Grange Park, Ill: American Nuclear Society, pp. 717-726.

Glass R.J. (1993). Modelling gravity-driven fingering in rough walled fractures using modified percolation theory. Proc 4th Annual International High Level Radioactive Waste Management Conference, La Grange Park, Ill: American Nuclear Society, pp. 2042-2052.

Golan L. P. & Stenning A. H. (1969). Two-phase vertical flow maps. Proc. Inst. Mech. Eng., Fluid Mechanics and Measurements in Two-phase Flow Systems, 184:3c, pp.108-114.

Govier G. W. & Aziz K. (1972). The Flow of Complex Mixtures in Pipes. pub. Van Nostrand Reinhold Company, New York, USA 792p.

Hakami E., (1995). Joint aperture measurements - an experimental technique. Fractured and jointed rock masses, eds. Myer, Cook, Goodman & Tsang, pub. Balkema, Rotterdam, pp. 453-456.

Hakami E., Barton N. (1990). Aperture measurements and flow experiments using transport replicas. Rock Joints, eds. Barton N. & Stephansson O. pub. Balkema, Rotterdam pp. 383-390.

Hardisty P. E., Wheater H. S., Birks D. & Dottridge J. (2003). Characterisation of LNAPL in fractured rock. Quart Journ Eng Geol Hydrogeol, vol 36, part 4 pp. 343-354.

Harpalani S. & Chen G. (1999). Positive impact of gas production induced stress and strain on coal permeability. Proc. 9th ISRM International Conference Paris, France. pp. 291-295.

Harpalani S. & Zhao X. (1989). The unusual response of coal permeability to varying gas pressure and effective stress. Rock mechanics as a guide for efficient utilisation of natural resources, ed. Khair, pub. Balkema pp. 65-72.

Hewitt G. F. & Naylor N. S. (1976). Annular two-phase flow. Pergamon Press, Oxford UK, 307p.

Hoek E. & Bray J.W. (1981) Rock Slope Engineering Revised 3rd Edition, pub. IMM London, pp. 358.

Hoek E. & Brown E. T. (1982). Underground Excavations in Rock, Revised 2nd Edition, pub. IMM London, 527p.

Houlsby A.C. (1971). Routine interpretation of the Lugeon water test. Quarterly J. Engineering Geology, Vol.9, pp. 303-312.

Hsieh P. A., Neuman S. P. & Simpson E. S. (1983). Pressure Testing of Fractured Rocks – A Methodology Employing 3-D Cross Hole Tests. Topical Technical Report NUREG/CR-3213, Dept. Hydrology & Water Resources, University Arizona, USA, 176p.

Hvorlsev M.S. (1951). Time lag and soil permeability in groundwater measurements. U.S. Corps of Engineers Waterways Experiment Station, Bulletin No. 36, pp. 50.

Indraratna B & Ranjith P (2001). Unsaturated behaviour of jointed rock. Balkema, Lisse 286p.

Indraratna B, Price J & Gale W. (2003). Laboratory Measurement of Relative Permeability under Two-Phase flow conditions in Jointed Rocks. 39th US Rock Mechs Symp, Cambridge Ma., USA, Jun 2003, pp. 1603-1611.

Indraratna B, Price J, Gale W (2002). Fourier description of fracture roughness. Proc 5th North American Rock Mechs Symp, Toronto, Canada, 7 - 10 July 2002, eds. Hammah et al., pub. University of Toronto Press, pp.35 – 44.

Indraratna B, Price J, Ranjith P, Gale W (2002a). Some aspects of unsaturated flow in jointed rock. Int. J. Rock Mech. Min. Sci., 39, pp 555-568.

Indraratna B, Ranjith P, Price J, Gale W (2003b). Two-phase flow of air and water through rock joints – Analytical approach and experimental verification. ASCE Journal of Geotechnical and Geo-Environmental Engineering, Oct 2003, 129(10): pp.918-929.

Indraratna B. & A. Haque, (2000). Shear behaviour of Rock Joints. Rotterdam, Balkema, 164p.

Indraratna B. & Haque A., (1999). "Triaxial equipment for measuring the permeability and strength of intact and fractured rocks". Geotechnique 49(4):515-521.

Indraratna B. & Ranjith P. (2001). Hydromechanical Aspects and Unsaturated Flow in Jointed Rock. A. A. Balkema, Lisse, 286 p.

Indraratna B. & Ranjith P. G. (2001). Laboratory measurement of two-phase flow parameters in rock joints based on high pressure triaxial testing. ASCE Journ Geotechnical and Geoenvironmental Engineering, vol. 127(6) pp. 530-542.

Indraratna B., A. Herath & N. Aziz (1995). Characterisation of surface roughness and its implications on the shear behaviour of joints, Mechanics of Jointed and Faulted Rock, ed. H.P. Rossmanith, pp. 515-520, Rotterdam, Balkema.

Indraratna B., Price J. & Gale W. (2002b). Fourier Description of Fracture Roughness. NARMS-TAC 2002, "Mining & Tunnelling Innovation & Opportunity," Toronto, pub. Uni of Toronto, Canada, 7 – 10 July, pp.35-44.

Indraratna B., Price J. & Gale W. (2003a). Laboratory Measurement and Analysis of Relative Permeability under Steady State Two-phase (air-water) Flow. 39th US Rock Mechs Symp, Cambridge MA, USA, Jun 2003 pp.1603-1611.

Indraratna B., Rambanda P. & Singh R. N. (1994) Numerical analysis of water inflows to underground excavations - current status and future trends. 5th Int Mine Water Congress, Nottingham UK. pp. 339-354.

Indraratna B., Ranjith P. G. & Gale W. (1999a). Single phase water flow through rock fractures. Geotechnical and Geological Engineering vol 17, pp. 211-240.

Indraratna B., Ranjith P. G. & Gale W. (1999b). Deformation and permeability characteristics with interconnected fractures. 9th ISRM Int Congress on Rock Mechs, Paris, France, 01-Jan-99 pp. 755-760.

Indraratna B., Ranjith P., Price J. and Gale W. (2003b). Two-phase flow of air and water through rock joints – Analytical approach and experimental verification. ASCE Journal of Geotechnical and Geo-Environmental Engineering Oct 2003, 129(10): pp.918-929.

Indraratna, B.I., Haque, A. & Gale, W., (1999). Evaluation of jointed rock permeability using a high pressure triaxial apparatus. *Mechanics of Jointed and Faulted Rock*. Rossmanith (ed), Rotterdam: Balkema, pp. 561-566.

Isherwood D. (1979) Geoscience Data Base Handbook for Modelling Nuclear Waste Repository, Vol 1 NUREG/CR-0912 VL, UCRL-52719, V1

ISRM (1978). Suggested Methods for the Quantitative Description of Discontinuities in Rock Masses, Part 1, Site Characterisation, Rock Characterisation Testing and Monitoring, ISRM Suggested Methods. Ed. E.T. Brown, Commission on Testing Methods, Int. Soc. Rock Mechs., Pergamon Press.

ISRM (1981). Rock Characterisation Testing and Monitoring: ISRM suggested methods. The Committee for the Commission on Testing Methods, ISRM, ed. Brown E. T., pub Pergamon Press, London.

ITASCA (1999). FLAC (ver 3.4) User's Guide, First Edition, Vols. 1-10.

ITASCA (2000). UDEC (ver. 3.1) User's Guide, First Edition. Vols. 1 - 8.

Iwai, K (1976). Fundamental studies of fluid flow through a single fracture. PhD Thesis, University of Berkeley, California - (WRL 532.519)

Jermy C. A. (1995). A laser scanning device to measure joint surface roughness, Mechanics of Jointed and Faulted Rock, ed. H.P. Rossmanith, pp. 169-174, Rotterdam, Balkema.

Jing L., C.F. Tsang, O. Stephansson & Kautsky F. (1996). Validation of mathematical models against experiments for radioactive waste repositories – DECOVALEX experience. In: *Coupled Thermo-Hydro-Mechanical Processes of Fractured Media, Developments in Geotechnical Engineering*, vol.79, pub. Elsevier, Amsterdam, p.25-56.

Keller A. A. (1997). High resolution CAT imaging of fractures in consolidated materials. Int Journ Rock Mech Min Sci. vol 34 no 3/4 paper 155.

Keller A. A., Blunt M. J., Roberts P. V. (1997). Micro-model observation of the role of oil layers in three phase flow. Transport in Porous Media, no.26, pp.277-297.

Keller A. A., Blunt M. J., Roberts P. V. (2000). Behaviour of non-aqueous phase liquids in fractured porous media under two-phase flow conditions. Transport in Porous Media, no. 38 pp.189-203.

Khor S. H., Mendes-Tatsis M. A. & Hewitt G. F. (1997). One-dimensional modelling of phase hold ups in 3 phase stratified flow. *Int Journ Multiphase Flow.* Vol 23 No 5 pp 885-897.

King G.R. & Ertekin T. (1984). A comparative evaluation of vertical and horizontal gas drainage wells for the degasification of coal seams. Paper SPE 13091, presented at the 59th Annual Technical Conference and Exhibition of the SPE, Houston, Texas, US. Sept. 16-19.

Kissell F. N. & Edwards J. C. (1975). Two-phase flow in coal beds. USBM, Report on Investigations 8066, 16p.

Körner St. & Friedel L. (1999). Phase distribution and bubble velocity in two-phase slit flow. *Int Journ Multiphase Flow.* 25, pp.1181-1194.

Kostakis K. & Harrison J. P. (1999). Numerical analysis of gas bubble flow in water filled fractures. Computers & Geotechnics, 24 pp. 3-28.

Krahn J. & Morgernstern N. R. (1979). The ultimate frictional resistance of rock discontinuities. Int. Journ. Mech. Min. Sci. & Geomech. Abstr. vol 16 pp. 127-133.

Kulatilake P.H.W.S., Um J., Panda B.B., & Nghiem N. (1998). Accurate quantification of joint roughness and development of a new peak shear strength criterion for anisotropic rock joints. Proc. Int. Conf. On Geomechanics and Ground Control in Mining and Underground Construction, Wollongong, Australia, eds. B. Indraratna & N. Aziz, Vol 1, 33-48

Lama R.D. (1995). Effect of stress, gas pressure and vacuum on permeability of Bulli coal samples. Int. Symp. cum Workshop on Management & Control of High Gas Emission & Outbursts, Wollongong, 20-24 Mar 1995, pp. 293-301.

Lama, R. D. & Bodziony J. (1996). Outbursts of gas, coal and rock in underground coal mines. Pub. R.D. Lama & Associates, Mt Pleasant NSW Australia, 499p.

Lee C-H. & I. Farmer (1993). Fluid Flow in Discontinuous Rocks, Chapman-Hall, 169p

Lindblom U. E. (1997). Design criteria for the Brooklyn Union gas storage caverns at JFK airport, New York. Int. J. Rock Mech. & Min. Sci. Vol. 34, No. 3-4, Paper 179.

Lomize G. M. (1951). Water flow through jointed rock. Gosenergoizdat, Moscow. In Russian, cited in Cook (1992).

Long J. C. S. (1983). Investigation of equivalent porous medium permeability in networks of discontinuous fractures. PhD Thesis, University of Berkeley, Ca, USA, 276p.

Long J.C.S & Witherspoon P.A. (1985). The relationship of the degree of interconnection to permeability of fracture networks. J. Geophys. Res., 90 (B4), 3087-98.

Long J. C. S. (1996). Rock Fractures and Fluid Flow: Contemporary understanding and applications. US National Research Council, Committee on Fracture Characterisation and Fluid Flow, pub National Academic Press, Washington, pp. 550.

Louis C. & Maini Y.N. (1970). Determination of in situ hydraulic parameters in jointed rock. Proc 2nd Congress ISRM, pp.1-32.

Louis C. (1968). Etudes des écoulements d'eau dans les roches fissures et des leurs influences sure la stabilité des massifs rocheux. Bull. De la Direction des Etud. Et Rech. EDF, sér. A, 3, T2-F.

Louis C. (1969). A study of groundwater flow in jointed rock and its influence on the stability of rock masses, Rock Mechanics Research Report No. 10, Imperial College, London.

Louis C. (1976) Introduction à l'hydraulique des roches, PhD Thesis, Paris.

Maini Y.N. T., Noorishad J., Sharp J. (1972). Theoretical and field considerations on the determination of insitu hydraulic parameters in fractured rock. Proc. Symp. Percolation Through Fissured Rock, ISRM & IAEG, T1-E, pp. 1-8.

Mandlebrot, B. B. (1983). The fractal geometry of nature, Freeman, San Francisco, USA.

McMahon B.K. (1985). Some practical considerations for the estimation of shear strength of joints and other discontinuities. Proceedings International Symposium on Fundamentals of Rock Joints, Björkliden, Sweden, 15-20 September, ed. O. Stephansson, 475-485, Luleå, Centek.

Meaney K., Paterson L., Pinczewski W.V. & Stevenson M.D. (1995). Advances in coal seam reservoir simulation for mine gas drainage. Int. Symp. cum Workshop on Management & Control of High Gas Emission & Outbursts, Wollongong, 20-24 Mar 1995, pp. 277-285.

Milne D. (1990). Standardised joint descriptions for improved rock classification. In: Rock Mechs. Contributions & Challenges, Proc. 31st US Symp Rock Mechs., Colorado Sch of Mines, Golden Colorado USA eds. W. A. Hustrulid & G. A. Johnson, 18 June 1990, pub. Balkema Rotterdam pp 35-41.

Mishimi K. & Hibiki T. (1996). Some characteristics of air:water two-phase flow in small diameter vertical tubes. Int. Journ. Multiphase Flow 22(4): pp.703-712.

Moye D.K. (1967). Diamond drilling for foundation exploration. Civil Eng. Transactions, J. I. E. Aust.

Muskat M. (1982). The flow of homogenous fluids through porous media. Pub. International Human Resources Development Corporation, Boston, Ma., USA 763p.

Nemcik, J.A., Indraratna, B. & Gale W. (2000). Floor failure analysis at a longwall mining face based on multiple sliding block model. Geotechnical & Geological Engineering, 18 pp.175-192.

Neuzil C.E. & Tracy J. V. (1981). Flow through fractures. Water Resources Research, 17, 191-199.

Nguyen T. S., Borgesson L., Chijimatsu M., Rutqvist J, Fujita, T, Hernelind J., Kobayashi A, Ohnishi Y., Tanaka M., Jing L (2001). Hydro-mechanical response of a fractured granitic rock mass to excavation of a test pit – the Kamaishi mine experiment in Japan. Int Journ Rock Mech Min Sci. vol 38 pp 79-94.

Nichol M. J., Glass R. J. (1994). Wetting phase permeability in a partially saturated horizontal fracture. Proc 5th Annual International High Level Radioactive Waste Management Conference, La Grange Park, Ill: American Nuclear Society, pp. 2007-2019.

Nichol M.J., Glass, R.J., Nguyen H.A. (1993a). Wetting front instability in an initially wet unsaturated fracture. Proc 4th Annual International High Level Radioactive Waste Management Conference vol 2, La Grange Park, Ill: American Nuclear Society pp. 2042-2052.

Nichol M.J., Glass, R.J., Nguyen H.A. (1993b). Small scale behaviour of single gravity-driven fingers in an initially dry fracture. Proc 4th Annual International High

Level Radioactive Waste Management Conference Vol 2, La Grange Park, Ill: American Nuclear Society, pp. 2023-2032.

Persoff P. & Pruess K. (1993). "Flow visualisation and relative permeability measurements in rough walled fractures." In: Proc. 4th Annual International High Level Radioactive Waste Management Conference, Las Vegas, Nevada USA: American Nuclear Society, pp.2033-2041.

Piggott A.R. & D. Elsworth (1995). A comparison of characterising fracture surface roughness. Fractured and Jointed Rock Masses, eds. L. Myer, N. G. W. Cook, R. E. Goodman & C. S. F. Tsang, pub. Balkema Rotterdam, pp. 331-336.

Power W. L. & Tullis T. E. (1991). Euclidean and Fractal models for the description of rock surface roughness. Journ Geophys. Res., No. B1, Vol. 96, pp. 415-424.

Priest, S. D. (1993). Discontinuity analysis for rock engineering. Chapman Hall, London UK, 473p.

Pruess K. & Tsang Y. W. (1990). On two-phase relative permeability and capillary pressure of rough walled rock fractures. Water Resources Research. Vol 26 No 9 pp. 1915-1926

Pyrak-Nolte L. J., Myer L. J., Cook N. G. W. & Witherspoon P. A. (1987). Hydraulic and mechanical properties of natural fractures in low permeability rock. 6th International Congress on Rock Mechanics, Montreal Canada, Vol 1 pp. 225-231.

Pyrak-Nolte L. J., Nolte D. D., Myer L. R., Cook N. W. (1990). Fluid flow through single fractures. Rock Joints eds. Barton, N. & Stephansson, O. pub. Balkema Rotterdam pp. 405-412.

Pyrak-Nolte L.J. & Montemagno C., (1994). The effect of critical path on fluid flow through a fracture. In *Rock Mechanics*, eds. Nelson & Laubsch, pub. Balkema, Rotterdam, pp. 81-87.

Pyrak-Nolte L.J., Helgeson D. & Haley G. (1992). Immiscible fluid flow in a fracture. In *Rock Mechanics*, eds. Tillerson & Wawersik, pub. Balkema, Rotterdam, pp. 571-578.

Ranjith, P. G. (2000). Analytical and experimental modelling of coupled water and air flow through rock joints. *PhD. Thesis*, University of Wollongong, pp. 405.

Rasmussen, T. (1991). Steady state fluid flow and travel times in partially saturated fractures using a discrete air water interface. Water Resources Research Vol. 27 No. 1 pp. 67-76.

Raven K.G. & Gale J.E. (1985). Water Flow in a Natural Rock Fracture as a Function of Stress and Sample Size. Int. J. Rock Mech. Min. Sci. & Geomech. Abstr., 22, pp. 251-61.

Richardson, L. F. (1961). The problem of contiguity: an appendix of statistics of deadly quarrels. General Systems Yearbook 6, pp.139-187.

Rissler P. (1977). Determination of permeability of jointed rock. Institute for Foundation Engineering, Soil Mechanics, Rock Mechanics and Waterways construction, RWTH Aachen, Vol.5.

Romm E.S. (1966). Flow Characteristics in Fractured Rock (in Russian), Nedra, Moscow. (cited in Ziegler T.W. (1976). Determination of Rock Mass Permeability, Tech Report S-76-2, US Army Corps Engineers, Waterway Experiment Station, Vicksburg MS.)

Rouse H. (1961). Engineering hydraulics. pub. J. Wiley & Sons Inc, New York, London 1038p.

Sausse (2002). Hydromechanical properties and alteration of natural fracture urfaces in the Soultz granite (Bas-Rhin, France). Tectonophysics 348 (2002) 169– 185.

Schrauf T.W. & Evans D.D. (1986). Laboratory study of gas flow through a single natural fracture. Water Resources Research, Vol.22, No.7 pp. 1038-1050.

Seidel J.P. & Haberfield C.M. (1995). Towards an understanding of joint roughness. Rock Mechanics and Rock Engineering, 28 (2): pp. 69-92.

Snow D.T. (1968). Fracture deformation and change in permeabilility and storage upon changes in fluid pressures. Quarterly of the Colorado School of Mines, 63(1): pp.201-244.

Somerton W.H., Soylemezoglu I.M. & Dudley R.C. (1975). Effect of stress on permeability of coal. Int. J. Rock Mech. Min. Sci. Geomech., Vol.12, No.5, pp. 129-145.

Spiegel M.R. (1974). Theory and Problems of Fourier Analysis with Application to Boundary Value Problems. Schaum's Outline Series, McGraw-Hill Inc., 191p.

Thiel K. (1989). Rock Mechanics in Hydro-engineering, Developments in Geotechnical Engineering Vol.51 pub. Elsevier, Netherlands, pp. 261-272

Tomlinson M.J. (1989). Foundation Design and Construction. 5th Edition, pub. Longman, Harlow UK, pp. 151-155.

Tsang Y. W. (1984). The effect of tortuosity on fluid flow through a single fracture. Water Resources Research, 20, pp. 1209-1215.

Tse R. & Cruden D. M. (1979). Estimating Joint Roughness Coefficient. Int. J. Rock Mech. Min. Sci. & Geomech. Abstr. Vol. 16, pp. 303-307.

Vennard J.K & Street R.L. (1982). Elementary Fluid Mechanics. 6th Edition, John Wiley & Sons, New York, 689p.

Wallis, G.B. (1969). One dimensional two-phase flow. McGraw-Hill Inc., USA 408p.

Walsh J.B. (1981). Effects of pore pressure and confining pressure on fracture permeability. Int. J. Rock Mechs. Min. Sci. & Geomech. Abstr. 18:429-435.

Wang J.S.Y. & Narasimhan T. N., (1985). Hydrologic mechanisms governing fluid flow in a partially saturated, fractured porous medium. Water Resources Res., 21, 12, pp.1861-1874.

Wei Z. Q. & Hudson J.A. (1988). Permeability of jointed rock masses. In: Rock mechanics and power plants, ed. Romana pub. Balkema pp.613-626.

Witherspoon P. A., J.S.Y. Wang, K. Iwai, & J. Gale (1980). Validity of cubic law for fluid flow in a deformable rock fracture. Water Resour. Res., Vol. 16, No. 6 pp. 1016-1024.

Yamatomi J., Mogi G., Adachi T. & Sugiura K. (2001). Modeling and analysis of fluid flows through a rock fracture with wall roughness, Rock Mechanics in the National Interest, eds. D. Elsworth et al., pp. 705-712, Lisse, Swets & Zeitlinger.

Yang Z. Y. & Di C. C. (2001). A directional method for directly calculating the fractal parameters of joint surface roughness. Int. J. Rock Mech. Min Sci., 38, pp. 1201-1210.

Yang Z. Y., Di C. C. & Lo S. C. (2001a). Two-dimensional Hurst Index of Joint Surfaces. Rock Mechanics & Rock Engineering, 34 (4), pp.323 – 345.

Yang Z. Y., Di C. C. & Yen K. C. (2001b). The effect of asperity order on the roughness of rock joints. Int. Journ. Rock Mechs. & Min. Sci. 38, pp.745 – 752.

Zimmerman R. W., & Bodvarsson G. S. (1996). Hydraulic conductivity of rock fractures. Transport in Porous Media, 23: pp 1-30.

APPENDIX A

DEVELOPMENT OF CONSTITUTIVE EQUATIONS

FOR STRATIFIED TWO-PHASE FLOW

A1. INTRODUCTION

The development of the simplified stratified model for two-phase flow was published in Indraratna & Ranjith (2001). Following a period of ongoing study a revised model has been proposed. The revisions to the model include the removal of the original terms referring to in-situ stresses and the careful re-definition of the fracture perimeter terms. The stress terms were removed since neither the shear nor normal stress acting on the joint plane was envisaged to contribute to the momentum loss equation since a Newtonian liquid will not sustain or transmit a stress unless it is confined and no flow can occur. The revised model still accounts for stress related change in aperture through the joint wall normal displacement term δ_n which is related to the joint normal stiffness and joint normal stress. The fracture perimeter terms were clarified and simplified so that they were easier for the reader to interpret.

A2. THEORETICAL DEVELOPMENT

The following revisions were published in Indraratna et al., (2003). The model analyses two-phase flow in terms of a simple stratified model as was originally proposed in Indraratna & Ranjith (2001). This approach has since been refined and superseded by the work presented within the main chapters of this thesis. It is suggested that two-phase flow through a single rock joint can be analysed by reformulating the momentum conservation equation, as previously done by Wallis (1969) to include the joint inclination. The variables are defined in Fig. A1 below:

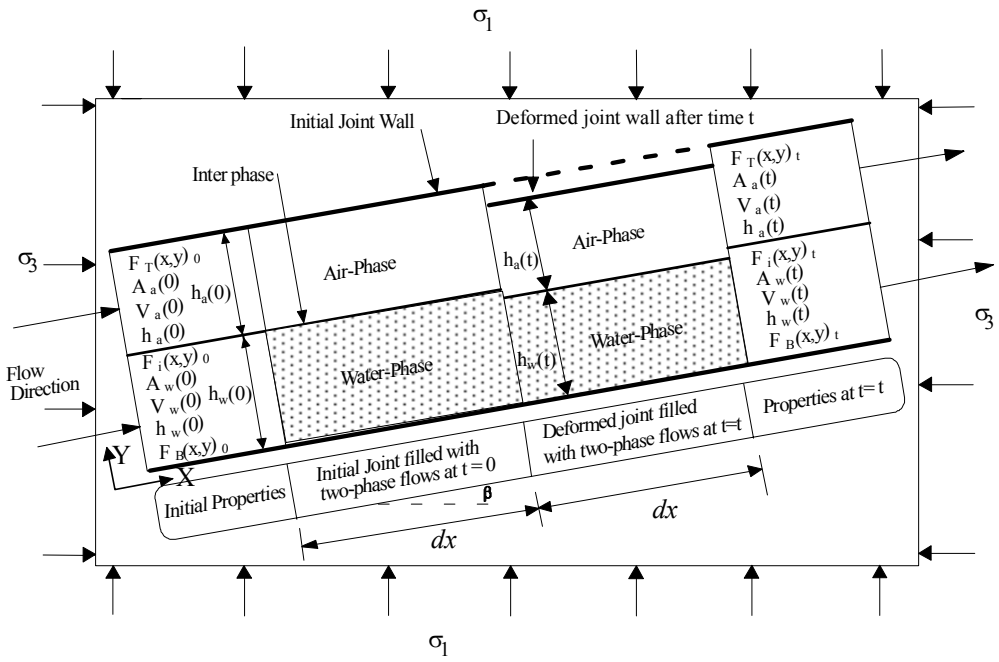

Fig. A1: A typical inclined joint filled with two-phase flows indicating change of interface and deformation of joint wall associated with change of stress level. Note: at the limit of negligible phase height, $S_{jw} = S_{ja} = S_{wa}$

The revised momentum equation considers the factors affecting fluid flow alone. Based on a unit width of rock element, for water flow only:

$$(\rho_w v_w A_w)\frac{dv_w}{dx} - (\rho_w A_w)\frac{dv_w}{dt} - (A_w)\left(\frac{dp}{dx}\right)_w - (\rho_w g \sin\beta A_w) + (\tau_{wa} S_{wa}) - (\tau_{jw} S_{jw}) -$$

$$(v_a - v_w)(1-\eta) M\frac{dR}{dx} = 0 \qquad [A1]$$

where,

a = the subscript represents air phase

w = the subscript represents water phase

A_i = cross sectional area of the fluid *i* (m^2)

ρ= density of fluid (kg/m^3)

v = velocity of fluid at time *t* (m/s)

dx = length of fluid element (m) along the joint length, *x*

y = width of fluid element (m), later assumed as unit width

S_{wa} = air-water interface perimeter = y (m)

S_{jw} = fracture perimeter length in contact with water phase = $2h_w + y$ (m)

$\tau_{wa} = \frac{f_I (v_a - v_w)^2 \rho_a}{2}$ = shear stress acting on the water-air interface (N/m^2). It is convenient to express the interfacial and joint wall shear stress in terms of friction factors (Taitel et al. 1976), where f_I is the friction factor between two phases.

$\tau_{jw} = \frac{f_w \rho_w v_w^2}{2}$ = shear stress acting on the wall (N/m^2), where f_w is the friction factor between wall and water.

$f_k = c.(R_e)^{-n}$, where R_e is the Reynolds number determined by:

$R_e = \frac{4 v_k A_k \rho_k}{S_k \mu_k}$, where, k takes 'a' and 'w' for air and water, respectively. Note that the typical friction coefficients, c = 0.0046, n=0.2 for turbulent flow, and c=16 and n=1 for laminar flow may be assumed (Cohen and Hanratty, 1968).

μ = dynamic viscosity (Pa.sec)

M = total mass rate (kg/s) = $(Q_a \rho_a + Q_w \rho_w)$

Q = volumetric phase flow rate (m^3/s)

R = fraction of the total mass flow across the interface = $M_1 / M = Q_a \rho_a / (Q_a \rho_a + Q_w \rho_w)$

η = fraction of the force taken by air phase associated with phase change

β = orientation of the joint (degrees)

p = fluid pressure inside the joint (N/m^2)

Similarly, for the air-phase (subscript 'a' represents the air phase)

$$(\rho_a v_a A_a)\frac{dv_a}{dx} - (\rho_a A_a)\frac{dv_a}{dt} - (A_a)\left(\frac{dp}{dx}\right)_a - (\rho_a g \sin\beta\, A_a) - (\tau_{wa} S_{wa}) - (\tau_{ja} S_{ja}) -$$

$$(v_a - v_w)\,\eta\, M\frac{dR}{dx} = 0 \qquad [A2]$$

where,

S_{ja} = fracture perimeter length in contact with air phase = $2h_a + y$ (m)

$\tau_{ja} = \frac{f_a \rho_a v_a^2}{2}$ = shear stress acting on the wall (N/m^2), where f_a is the friction factor between joint wall and air, which depends on the Reynolds number determined for air.

Equations (A1) and (A2) can be further extended to incorporate the phase heights of water and air in stratified flow, as well as to model the factors influencing these phase heights. The cross-sectional area of the water phase may be written in terms of the phase level (h_w) and width of the wetted joint wall (y). In nature, rock fractures can extend for considerable distances and occupy large surface areas. In the case of the fractures used in the test specimens the fracture surface area of each joint wall is approximately the product of the sample height and width ($0.00594m^2$). The fracture perimeter in contact with the air and water phases can be simplified if the phase level component (h_w or h_a) is neglected (introduces an error of < 0.05% even when fracture is fully saturated, assuming a 10μm aperture). The perimeter length of the interface and the joint walls can be then be assumed to be approximately the same (i.e. $S_{wa} = S_{ja} = S_{jw}$) as width across flow. When capillary forces are negligible (compared to viscous forces) the pressure gradient in both phases are equal $\left[ie. \left(\frac{dp}{dx}\right)_w = \left(\frac{dp}{dx}\right)_a = \left(\frac{dp}{dx}\right) \right]$.

Eliminating the pressure drop $\left(\frac{dp}{dx}\right)$ from the above 2 equations in order to attain a solution for the interface level, and assuming unit width (i.e. y =1):

$$\frac{1}{h_w(t)}[\tau_{wa} - \tau_{jw} - (v_a - v_w)(1-\eta) M \frac{dR}{dx}] + \frac{1}{h_a(t)}[\tau_{wa} + \tau_{ja} + (v_a - v_w)\eta M \frac{dR}{dx}] =$$

$$- \rho_w v_w \frac{dv_w}{dx} + \rho_a v_a \frac{dv_a}{dx} + \rho_w \frac{dv_w}{dt} - \rho_a \frac{dv_a}{dt} - g \sin\beta[\rho_a - \rho_w] \quad [A3]$$

where, M is now considered as total mass flow per unit width.

The mechanical and hydraulic behaviour of discontinuities in rocks depends strongly on the topography of the contacting surfaces and the degree of correlation between them. The topography of joint walls has been studied using various techniques including profilometers (Pyrak-Nolte et al., 1987; Brown & Scholz, 1985). The initial surface profiles of top and bottom joint walls are taken as $F_T\ (x,y)_0$, and $F_B\ (x,y)_0$, respectively. Once they are subjected to deformation associated with external stresses and fluid pressure, they are assumed to take the form of $F_T\ (x, y)_t$, and $F_B\ (x,y)_t$, respectively, after time, t. The interface between the two phases is described by $F_I\ (x,y)_0$, and $F_I\ (x,y)_t$ at t = 0 and after time t, respectively.

If ξ_{wc} is the change of interface between two phases due to the compressibility of water, then the height of water-phase, $h_w(t)$, can be represented by:

$h_w(t) = F_I\ (x,y)_0 - F_B\ (x,y)_0 - \xi_{wc}$, or

$$h_w(t) = F_I\ (x,y)_0 - F_B\ (x,y,\Delta_B)_t \qquad [A4]$$

where $F_B\ (x,y,\Delta_B)_t$ is given by the expression, $F_B\ (x,y)_0 + \xi_{wc}$.

Factors, which control the height of air-phase, are (a) mechanical deformation of joint, (b) compressibility of air, (c) rate of solubility of air in water, and (d) effects of change of fluid properties and temperature. The height of air-phase, $h_a(t)$, at time t is given by:

$$h_a(t) = F_T\ (x,y)_0 - F_I\ (x,y)_0 - \Delta_T \qquad [A5]$$

where, Δ_T is the deformation of wetted wall in contact with the air-phase. The total deformation, Δ_T, includes the effects of compressibility of water (ξ_{wc}), compressibility of air (ξ_{ac}), solubility of air in water (ξ_{ad}), and the elastic deformation of the joint wall (δ_n) on the height air-phase $h_a(t)$. Hence,

$$\Delta_T = \xi_{ac} + \xi_{ad} + \delta_n - \xi_{wc} \quad [A6]$$

The evaluation of the functions ξ_{ac}, ξ_{ad}, δ_n and ξ_{wc} will be discussed later.

If $F_T\ (x,y,\Delta_T)_t$ is represented by the expression $[F_T\ (x,y)_0 - \Delta_T]$, Eqn (A5) can now be re-written as:

$$h_a(t) = F_T\ (x,y,\Delta_T)_t - F_I\ (x,y)_0 \quad [A7]$$

Substituting Equations (A4) and (A7) into the Equation (A3) will yield:

$$\{F(x,y,\Delta)] + \tau_{wa}\ [\ F(x,y,\Delta)] - [\tau_{jw}\ ]\ F_T(x,y,\Delta_T) - \tau_{ja}\ F_B(x,y,\Delta_B) -$$

$$(v_a - v_w)\ (1-\eta)\ M\frac{dR}{dx}\ [(1-\eta)\ F_T(x,y,\Delta_T) + \eta\ F_B(x,y,\Delta_B)] +$$

$$F_I\ (x,y)_0\ [\tau_{jw} + \tau_{ja} + \ (v_a - v_w)M\frac{dR}{dx}\ ]\} = \{F_I\ (x,y)_0\ [F_T(x,y,\Delta_T) + F_B(x,y,\Delta_B)] -$$

$$F_I^2\ (x,y)_0 - F_T(x,y,\Delta_T)\ F_B(x,y,\Delta_B)\ \}\{A - g\ \sin\beta\ (\rho_a - \rho_w)\} \quad [A8]$$

In the above, $F(x,y,\Delta) = F_T(x,y,\Delta_T) - F_B(x,y,\Delta_B)$ [A8a]

The above expression may be rearranged in a simplified form to give:

$$F_I\ (x,y)_0\ [\ A\ \sum_{k=1}^{2}\Delta_k - \sum_{i=a,w}\tau_{J\,i} - C] - A\ F_I^2\ (x,y)_0 =$$

$$F(x,y,\Delta)\ \tau_{wa}\ - [\sum_{\substack{k=1\\ i=a,w}}^{2}\tau_{J\,i}\ \Delta_k\ ] - \sum_{\substack{N=1-\eta,\eta\\ k=1}}^{2} C\ N\ \Delta_k + A\ \Delta_1\ \Delta_2 \quad [A9]$$

where, $A = [B - g\ \sin\beta\ (\rho_a - \rho_w)]$ [A9a]

$B = [\rho_w\ v_w\frac{dv_w}{dx}\ - \rho_a\ v_a\frac{dv_a}{dx}\ + \rho_w\frac{dv_w}{dt}\ - \rho_a\frac{dv_a}{dt}\ ]$ = force per unit area associated with unsteady effects of flow; [A9b]

$$C = [\ (v_a - v_w)M\frac{dR}{dx}\ ]; \quad [A9c]$$

$\Delta_1 = F_T(x,y,\Delta_T)$, and [A9d]

$\Delta_2 = F_B(x,y,\Delta_B)$ [A9e]

The Equation (A9) can also be simplified to write the main governing equation as follows:

$$F_I\,(x,y)_0\,\Delta_3 - A\,F_I^{\,2}\,(x,y)_0 - D = 0 \qquad [A10]$$

$$\text{where, } \Delta_3 = [\,A \sum_{k=1}^{2} \Delta_k - \sum_{i=a,w} \tau_{Ji} - C], \qquad [A10a]$$

$$\text{and } D = F(x,y,\Delta)\,\tau_{wa} - [\sum_{\substack{k=1\\ i=a,w}}^{2} \tau_{Ji}\,\Delta_k\,] - \sum_{\substack{k=1\\ N=1-\eta,\eta}}^{2} C\,N\,\Delta_k + A\,\Delta_1\,\Delta_2 \qquad [A10b]$$

The Equation (A10), which is of quadratic form, has a definite solution to determine the interface level. A simplified analytical solution for the interface height for steady state flow in a horizontal joint can be obtained by neglecting the gravity effects of associated with the air phase. Eqn. A9 will then lead to the following simplified form:

$$F(x,y,\Delta)\,[\tau_{wa}] - \sum_{\substack{k=1\\ i=a,w}}^{2} \tau_{Ji}\,\Delta_k + F_I\,(x,y)_0 \sum_{i=a,w} \tau_{Ji} = 0 \qquad [A11]$$

$$F_I\,(x,y)_0 = \frac{\sum_{\substack{k=1\\ i=a,w}}^{2} \tau_{Ji}\Delta_k - F(x,y,\Delta)\,[\tau_{wa}]}{\sum_{i=a,w} \tau_{Ji}} \qquad [A12]$$

$$F_I\,(x,y)_0 = \frac{\tau_{Ja}\,F_B\,(x,y,\Delta_B) + \tau_{Jw}\,F_T\,(x,y,\Delta_T) - \tau_{wa}\,F(x,y,\Delta)}{\tau_{Ja} + \tau_{Jw}} \qquad [A13]$$

where, $F(x,y,\Delta) = F_T(x,y,\Delta_T) - F_B(x,y,\Delta_B)$

$\Delta_1 = F_T(x,y,\Delta_T)$, and

$\Delta_2 = F_B(x,y,\Delta_B)$

$\tau_{Ji} = \tau_{Ji}$

where 'i' takes subscripts 'a' and 'w' for air and water, respectively.

The Eq [A13] models the interface between air and water phases for steady state flow through a single horizontal joint. The quadratic solution to the equation is available because of the simple fluid phase configuration. The problem becomes more complicated when an annular configuration is considered, as is discussed in Chapter 4.

APPENDIX B

ROUGHNESS MEASUREMENT AND CALCULATION

B1. INTRODUCTION

This appendix presents the operating sequence developed for roughness measurement using the Ferranti U900 CMM and the formulae developed for the Fourier series analysis. The instructions use the available keypad macro facility to make data recording more efficient. The formulae were developed to operate within a MS Excel spreadsheet.

B2. FERRANTI COORDINATE MEASURING MACHINE (CMM)

Data acquisition using the Ferranti CMM was developed so that the gathering exercise was as efficient as possible. These instructions are part of the discussion relating to Section 3.4.2 (Chapter 3). The equipment is shown in Fig. 3-7. The principal stages of the process were as follows:

1. Position and lightly clamp sample in position using the fixtures and fitting s provided.
2. Align axes of the sample so that coincident with the 2 horizontal perpendicular axes of the instrument (by eye).
3. Switch on the instrument at the back of the microprocessor and check the positioning of the sample, adjusting the sample position as needed before tightening screws.
4. Move the probe tip to above the leading edge of the sample; switch microprocessor off and on again to reset the coordinate datum and macro memory.
5. On the U900 keypad, from the main menu select SET and toggle the AUTO option; press OK (green button) to accept.

6. Press CLEAR (red button) to return to main menu.
7. Select POS and manually set the probe at the desired starting position (lock the axes when finished).
8. Select CLEAR and then MEAS.
9. Select POINT NC (i.e. effectively 2 presses of the same button) to arm the probe tip ready for a non-calibrated reading.
10. Manually lower probe to contact the sample surface (probe will beep when contact is made and lost) and reading will be displayed as X Y and Z.
11. Press OK then CLEAR to return to main menu.
12. Select RON to set record to ON so that a keystroke macro is recorded for the following operations.
13. Select PRINT, followed by ACTUALS, and then press the white keys next to X, Y and Z (left side of microprocessor). Command executes and returns to main menu.
14. Select ROFF to stop recording keystroke macro.
15. Go to step 7 to select the next point. It is recommended to work in x lines or profiles along the sample (same Y) and work from the back of the sample towards the operator.

If Hyper-Terminal is to be used the following options must be selected so that data from the print command can be sent to the computer:

1. use direct connection to appropriate communications port (File-Properties)
2. use ANSI (back scroll buffer lines 500) under File-Properties
3. use 9600 bps baud rate, data bits 7, parity – even, stop bits – 2

Application of the keypad macro facility permits a 100mm profile of 50 data points to be measured in about 20 minutes (as quick as some of the automated CMMs).

However, where many profiles are to be measured, the time involved in acquiring the data becomes significant unless an automated system is available. The Minolta Vivid 910 records data points at a 25μm interval over the entire sample area in less than 15 minutes, even allowing for equipment set up and scanning optimisation.

B3. FOURIER SERIES ANALYSIS

The theory behind the Fourier series approach has been discussed in Section 3.3.4. The roughness analysis is described with respect to the particular methodologies in Sections 3.4.1, 3.4.2 and 3.4.3. The digital data was analysed in a spreadsheet format using user-defined formulae based upon Eq. [3.20] to [3.22].

The calculation considered each segment of the function in piecewise fashion, and therefore integrated each *y*-pair in turn, to give the expressions:

$$a_n = \frac{1}{2L}(z_2 + z_1)\left(\frac{L}{n\pi}\right)\left[\sin\left(\frac{ny\pi}{L}\right)\right]_{y_1}^{y_2} \qquad [B.1]$$

$$b_n = \frac{1}{2L}(z_2 + z_1)\left(\frac{L}{n\pi}\right)\left[-\cos\left(\frac{ny\pi}{L}\right)\right]_{y_1}^{y_2} \qquad [B.2]$$

These coefficients are summed for each data point and for $n = 1$ to n_{max} over the period T to provide the unique a_n and b_n coefficients for each harmonic frequency. When $n = 0$, a can be calculated in Excel using the formula:

$$a_0 = (2/\text{COUNT}(b_n: b_{max\text{-}1}))*\text{SUM}(b_n:b_{max\text{-}1}) \qquad [B.3]$$

The accuracy of the solution can be assessed using the Correlation coefficient ρ to compare the measured z_{meas} and predicted z_{pred} asperity values. The correlation can be calculated in terms of the covariance $cov(z_{meas},z_{pred})$ and the mean μ, standard deviation σ using the Eq. [B4]:

$$\rho\,(z_{meas},z_{pred}) = (\text{cov}(z_{meas},z_{pred}) / \sigma_{Zmeas}.\sigma_{Zpred}) \qquad [B.4]$$

where,

$$(\sigma_{Zmeas})^2 = (1/n_{max}) \Sigma(z_{meas}(i) - \mu_{Zmeas})^2 \quad [B.5]$$

$$(\sigma_{Zpred})^2 = (1/n_{max}) \Sigma(z_{pred}(i) - \mu_{Zpred})^2 \quad [B.6]$$

$$\text{cov}(z_{meas},z_{pred}) = (1/n_{max}) \sum_{i-1}^{n} \{(z_{meas}(i) - \mu_{Zmeas})(z_{pred}(i) - \mu_{Zpred})\} \quad [B.7]$$

The results showed a high positive correlation, in the region of > 0.9987, indicating the suitability of the technique and the number of harmonic frequencies in performing the analysis.

APPENDIX C:

ANALYSIS OF ROCK SAMPLE LASER SCANNING DATA

C1. INTRODUCTION

This appendix contains graphical output from the statistical analysis of the rock fracture specimens. It should be noted that all wireframe and contour figures are measured in millimetres. The data was obtained with a Minolta Vivid 910 High Resolution Laser Scanner, as discussed in Section 3.4.1 and shown in Fig. 3.9. The roughness and aperture analyses are summarised in Figs. 3.13 and 3.14.

C2. SAMPLE JP09

Sample JP09 (Figs. C1 and C2) was intersected by a planar fracture with the right end of the sample containing relatively large apertures > 0.25mm. The left end of the sample has typically smaller apertures < 0.125mm.

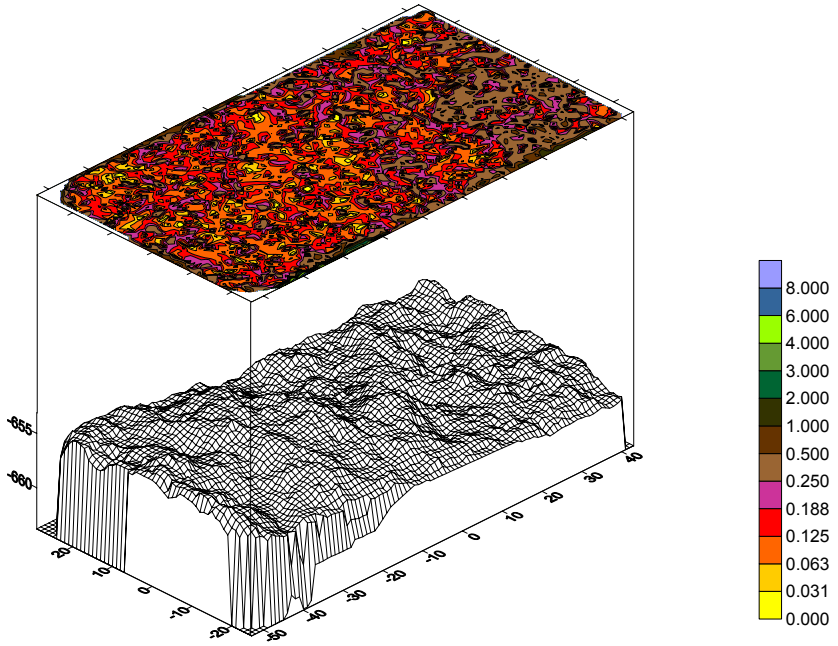

Fig. C1: Sample JP09 wireframe and aperture contour plot.

The presence of a number of finer apertures (< 0.03mm) in this portion of the fracture will act to constrict the flow despite the number of localised aperture elements > 0.125mm.

Fig. C2: Sample JP09 - photograph of fracture plane.

C3. SAMPLE JP08

Sample JP08 is intersected by a natural fracture that is characterised by significant apertures, typically > 1mm.

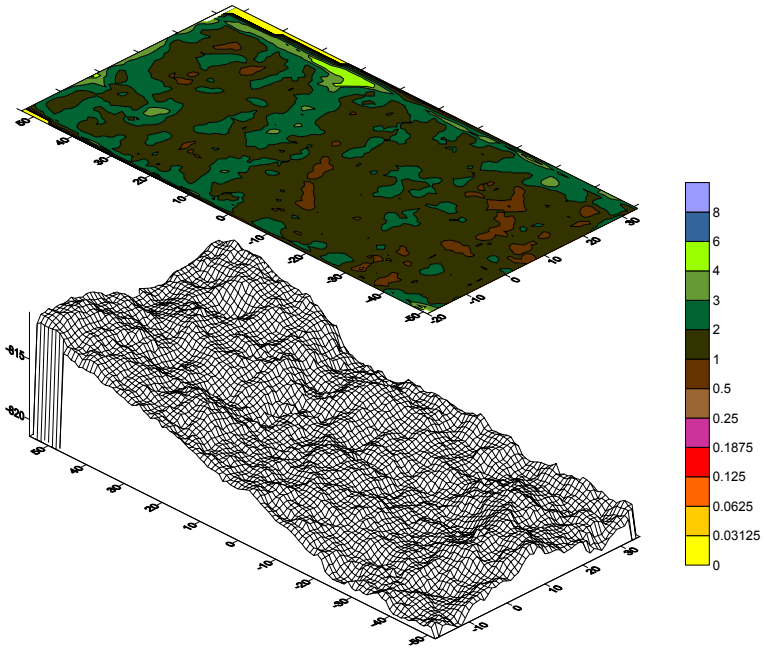

Fig. C3: Sample JP08 wireframe and aperture contour plot.

C4. SAMPLE JP07

Figure C4 shows sample JP07 also contains a natural fracture with generally large apertures > 1mm. The surface is characterised by low small scale roughness, compared to JP08.

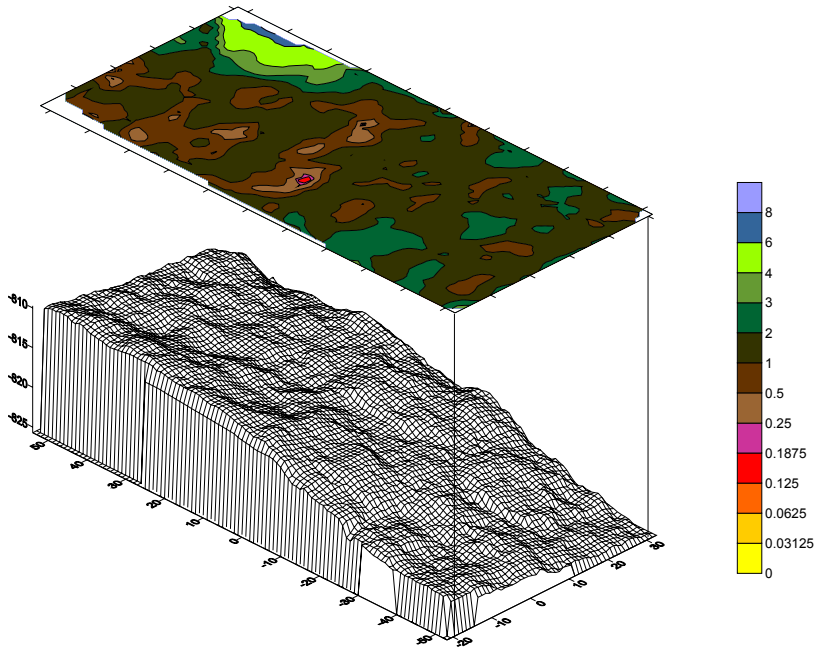

Fig. C4: Sample JP07 wireframe and aperture contour plot

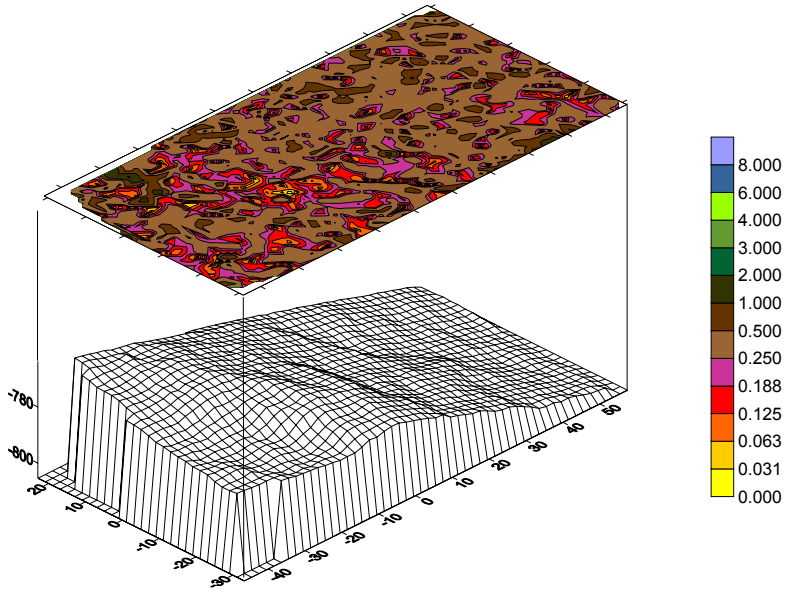

Fig. C5: Sample JP05 wireframe and aperture contour plot.

C5. SAMPLE JP05

Figures C5 and C6 show that sample JP05 is intersected by a generally inclined planar fracture. The left end of the sample contains a localised large wavelength roughness feature. A large proportion of the surface has an aperture > 0.25mm.

Fig. C6: Sample JP05 showing roughness feature on photograph of fracture plane.

C6. SAMPLE JP04

The sample intersects an inclined planar fracture with the left end of the sample characterised by a zone of relatively large apertures > 0.25mm (Fig. C7). The left end of the sample represents relatively finer apertures between 0.063mm and 0.185mm. Figure C7 also shows the bedding plane step that intersects and offsets the fracture plane. This feature is shown in greater detail in the photographs in Figs. C8 and C9. The step feature picked out by limonite staining coincides with a flat lying bedding parting and is shown clearly in Fig. C9.

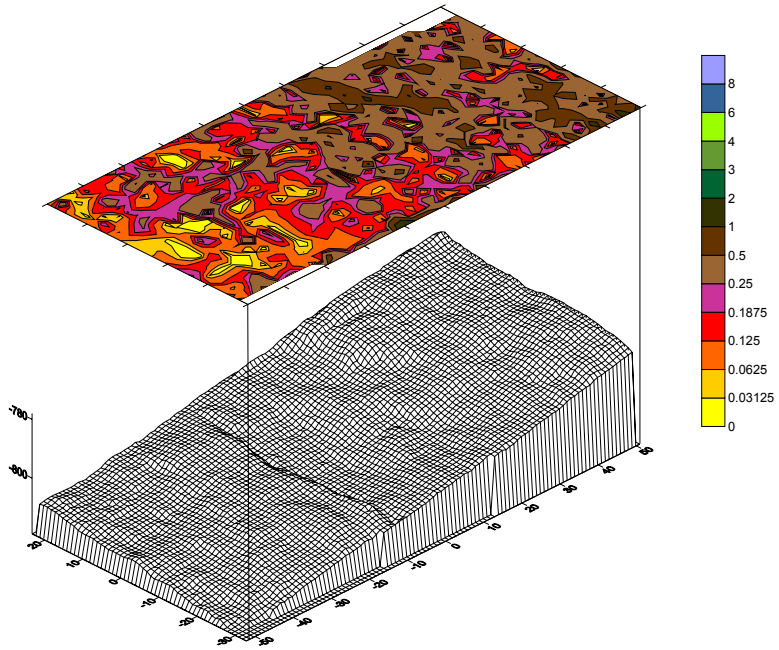

Fig. C7: Sample JP04 wireframe and aperture contour plot.

Fig. C8: Sample JP04 photograph of fracture plane.

Fig. C9: Sample JP09 photograph of fracture plane plan showing bedding parting intersection.